Ion Beam Applications

Edited by Ishaq Ahmad and Malik Maaza

ION BEAM APPLICATIONS

Edited by **Ishaq Ahmad** and **Malik Maaza**

Ion Beam Applications
http://dx.doi.org/10.5772/intechopen.71589
Edited by Ishaq Ahmad and Malik Maaza

Contributors

Marek Schmidt, Hiroshi Mizuta, Masashi Akabori, E.A Dawi, Vladimir Egorov, Evgeniy Egorov, Sokeng Ifriky Tadadjeu, Balla Diop Ngom, Robert Van Zyl, Shane Martin, Malek Maaza, Tania Tsvetkova, Nina Khuchua, Marina Tigishvili, Nugzar Dolidze, Zurab Jibuti, Revaz Melkadze, Roland Diehl, Changzhi Shi, Ishaq Ahmad, Fabian Ezema

© The Editor(s) and the Author(s) 2018
The rights of the editor(s) and the author(s) have been asserted in accordance with the Copyright, Designs and Patents Act 1988. All rights to the book as a whole are reserved by INTECHOPEN LIMITED. The book as a whole (compilation) cannot be reproduced, distributed or used for commercial or non-commercial purposes without INTECHOPEN LIMITED's written permission. Enquiries concerning the use of the book should be directed to INTECHOPEN LIMITED rights and permissions department (permissions@intechopen.com).
Violations are liable to prosecution under the governing Copyright Law.

Individual chapters of this publication are distributed under the terms of the Creative Commons Attribution 3.0 Unported License which permits commercial use, distribution and reproduction of the individual chapters, provided the original author(s) and source publication are appropriately acknowledged. If so indicated, certain images may not be included under the Creative Commons license. In such cases users will need to obtain permission from the license holder to reproduce the material. More details and guidelines concerning content reuse and adaptation can be foundat http://www.intechopen.com/copyright-policy.html.

Notice

Statements and opinions expressed in the chapters are these of the individual contributors and not necessarily those of the editors or publisher. No responsibility is accepted for the accuracy of information contained in the published chapters. The publisher assumes no responsibility for any damage or injury to persons or property arising out of the use of any materials, instructions, methods or ideas contained in the book.

First published in London, United Kingdom, 2018 by IntechOpen
eBook (PDF) Published by IntechOpen, 2019
IntechOpen is the global imprint of INTECHOPEN LIMITED, registered in England and Wales, registration number: 11086078, The Shard, 25th floor, 32 London Bridge Street
London, SE19SG – United Kingdom
Printed in Croatia

British Library Cataloguing-in-Publication Data
A catalogue record for this book is available from the British Library

Additional hard and PDF copies can be obtained from orders@intechopen.com

Ion Beam Applications
Edited by Ishaq Ahmad and Malik Maaza

p. cm.

Print ISBN 978-1-78923-414-5

Online ISBN 978-1-78923-415-2

eBook (PDF) ISBN 978-1-83881-585-1

We are IntechOpen, the world's leading publisher of Open Access books

Built by scientists, for scientists

3,600+
Open access books available

113,000+
International authors and editors

115M+
Downloads

151
Countries delivered to

Our authors are among the
Top 1%
most cited scientists

12.2%
Contributors from top 500 universities

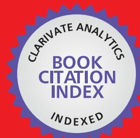

WEB OF SCIENCE™

Selection of our books indexed in the Book Citation Index
in Web of Science™ Core Collection (BKCI)

Interested in publishing with us?
Contact book.department@intechopen.com

Numbers displayed above are based on latest data collected.
For more information visit www.intechopen.com

Meet the editors

Ishaq Ahmad joined the National Centre for Physics in 1999 and currently holds the positions as the director of the Experimental Physics Department, National Centre for Physics, Islamabad, and as an adjunct faculty member of Pakistan Institute of Engineering and Applied Sciences (PIEAS), Islamabad. He has coauthored over 100 publications in SCI journals and supervised several master's, PhD and postdoctoral degree students. He has published numerous books and book chapters. His research interests focus on ion implantation, radiation-induced modification of materials/nanomaterials, synthesis of nanomaterials/thin films and ion beam analysis of materials. He is an editorial board member and a reviewer of several well-known journals. He was a TWAS-UNESCO-iThemba LABS research associate from 2014 to 2016. He obtained his PhD degree from the University of Chinese Academy of Sciences, China.

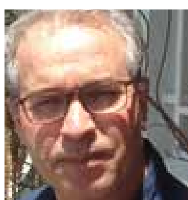

Prof. M. Maaza holds his PhD degree in Quantum Neutron Optics from the University of Pierre and Marie Curie and the Commissariat à l'Energie Atomique, respectively. He is currently a permanent joint staff member of the National Research Foundation of South Africa and in charge of the Africa's International Relations desk at iThemba LABS and the University of South Africa (UNISA). He is the chair of reputed international organizations and commissions. His expertise is in the multidisciplinary field of nanosciences, photonics and solar energy. Within the STI and RDI landscapes, with a Hirsch index of 33, he has published more than 300 ISI international publications and supervised several postgraduates from all over Africa and South Africa.

Contents

Preface XI

Section 1 Introduction 1

Chapter 1 **Introductory Chapter: Ion Beam Applications 3**
Ishaq Ahmad and Fabian I. Ezema

Section 2 MeV Ion Beam Applications 13

Chapter 2 **Ion-Nanoscale Matter Interactions 15**
Elmuez A. Dawi

Chapter 3 **Ion Beams for Materials Analysis: Conventional and Advanced Approaches 37**
Vladimir Egorov and Evgeny Egorov

Chapter 4 **Ion Beams for Space Applications 73**
Sokeng Ifriky Tadadjeu, Balla Diop Ngom, Shane Martin, Robert Ryk Van Zyl and Malik Maaza

Section 3 Focused Ion Beam Applications 87

Chapter 5 **Ion Beams for Nanoscale Optical Data Storage 89**
Tania Tsvetkova

Chapter 6 **Nitrogen Ion Microscopy 113**
Marek E. Schmidt, Masashi Akabori and Hiroshi Mizuta

Section 4 Ion Implantation 137

Chapter 7 **Ion Implantation as a Tool for Controlled Modification of Photoelectrical Properties of Silicon 139**
Nina Khuchua, Marina Tigishvili, Nugzar Dolidze, Zurab Jibuti, Revaz Melkadze and Roland Diehl

Chapter 8 **Characterization and Simulation of p-Type Ion Implantation in MCT 161**
Changzhi Shi

Preface

Ion beam is a well-known versatile tool, which is being used frequently across the world in various applications. This book is aimed to provide a brief introduction of different approaches and recent development in ion beam application.

The first section provides a brief introduction into the topic.

The review in the second part of the book covers the ion beam with the MeV energy range. Furthermore, this book contains the popular research interests regarding the interaction of nanoparticles with MeV-ranged ion beam. Coalescence of nanoparticles to form nanowires with swift heavy ions is discussed in this section. Ion beam in MeV energy range is helping the material scientists to perform material characterization from the last 60 years. Unique and advanced ion beam analysis techniques are also presented in this section. The effects of space radiation on spacecraft body and shielding materials are very severe, sometimes causing the operation failure. To overcome these issues, shielding materials are being developed, and ground-based radiation testing of these shielding materials using MeV ion beams is addressed in this book.

The third part of the book defines the recent achievements on focused ion beam generation and its applications. The focused ion beam techniques have been discussed as a novel approach for property modification and optimization of wide-bandgap materials for high-density data storage application. This section covers focused ion beam application in new digital memory as a data-writing tool in bits of nanometer diameter into new-generation storage materials and photon near-field technology was discussed. Additionally, advancement in focused ion beam with molecular nitrogen source gas instead of atomic source gases is also discussed here. This new nitrogen focused ion beam source is very useful for imaging and patterning.

The final segment of the book addressed the most important applications of ion implanter. Ion implantation is one of the key technologies for the fabrication of electronic devices in a controlled manner. Hereby, the modifications of the photoelectrical properties of n-Si and silicon-on-insulator structures due to B^+ ion implantation are explained concisely. On the same line, the ion implantation of group V dopants, such as P, As and Sb, in HgCdTe and the computer simulations on the collision of incident ions and lattice atoms are also tried to be incorporated in this book. This approach will help to understand the distributions of ions and recoil atoms numerically.

The authors are very thankful and want to acknowledge all those who potentially contribute in this book, namely, Prof. Dr. E.A. Dawi, Prof. Dr. V.K. Egorov, Prof. Dr. E.V. Egorov, Prof. Dr. S.I. Tadadjeu, Prof. Dr. B.D. Ngom, Prof. Dr. Shane Martin, Prof. Dr. R.R Van Zyl, Prof.

Dr. Tania Tsvetkova, Prof. Dr. Marek E. Schmidt, Prof. Dr. Masashi Akabori, Prof. Dr. Hiroshi Mizuta, Prof. Dr. Nina Khuchua, Prof. Dr. Marina Tigishvili, Prof. Dr. Nugzar Dolidze, Prof. Dr. Zurab Jibuti, Prof. Dr. Revaz Melkadze, Prof. Dr. Roland Diehl, Prof. Dr. Changzhi Shi and Mr. Julian Virag, Publishing Process Manager.

Regards

Ishaq Ahmad
National Centre for Physics
Islamabad, Pakistan

Malik Maaza
UNESCO-UNISA Africa Chair in Nanosciences/Nanotechnology
UNISA and Nanosciences African Network
iThemba LABS-National Research Foundation
South Africa

Section 1

Introduction

Introductory Chapter: Ion Beam Applications

Ishaq Ahmad and Fabian I. Ezema

Additional information is available at the end of the chapter

http://dx.doi.org/10.5772/intechopen.78966

1. Overview

Ion beam instruments such as particle accelerators, focused ion beams (FIB), and ion implanters are versatile instruments which are broadly applied almost in all field of physics from nuclear physics to particle physics, condense matter physics, and atomic physics. These are also an important tool in other areas of science and technologies such as chemistry, environment sciences, biology, space science and engineering, and semiconductor technology. Its applications are substantially being extended for generating cluster ions, synchrotron radiations, focused ion beams with molecular nitrogen source gas, and proton-proton colliders. Progress in nuclear and particle physics originated from studies with ion beam is playing now a determining role in astrophysics and cosmology. Similarly, low energy ion beam, such as ion implanters and FIB, are also useful instruments for device fabrication and microscopy.

This chapter aimed to present a brief review of a broad range of applications of the ion beam in diversified fields which will be useful for the common reader to understand ion beam science and technology. Finally, the latest research using MeV ion beam, focused ion beam, and ion implanter is compiled in this book in three respective sections. For a further concise review of ion beam applications, electron beams are excluded from this review chapter and book, even though electron microscopes and other useful applications are being emerged in different areas of fields. For example, focused electron beam was used in patterning and cutting of nanowires [1]. **Figure 1** shows the patterning of ZnO nanowires using focused electron beams at transmission electron microscopy (TEM).

IntechOpen

© 2018 The Author(s). Licensee IntechOpen. This chapter is distributed under the terms of the Creative Commons Attribution License (http://creativecommons.org/licenses/by/3.0), which permits unrestricted use, distribution, and reproduction in any medium, provided the original work is properly cited.

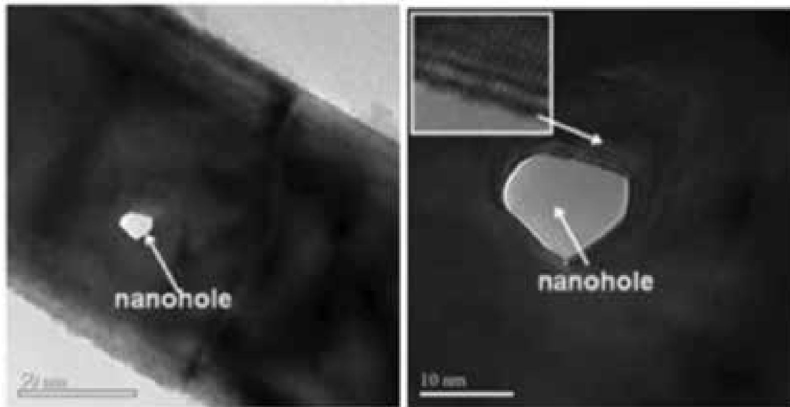

Figure 1. Focused electron beam to create nanoholes in ZnO nanowires [1].

2. Applications

2.1. Materials science

This section introduces to the materials scientists, chemists, and physicists about the ion beam techniques for materials analysis, modification of materials, and development of new materials using ion beam. MeV ion beams for materials analysis techniques are being used as complementary techniques in materials analysis. These are the group of non-destructive analytical techniques such as particle induced X-ray emission (PIXE), particle-induced gamma-ray emission (PIGE), nuclear reaction analysis (NRA), Rutherford backscattering (RBS), and ion channeling, which are being used to analyze composition and depth profiling of solids. Almost all elements from hydrogen onward can be probed by ion beam analysis (IBA). IBA techniques are discussed in detail in Section 2. Focused or collimated beam into micron and submicron (Microprobe) is now developed, which is useful for mapping of lateral elemental distribution over a specimen. These microbeams are useful for high-resolution imaging by measuring density variations through scanning transmission ion microscopy (STIM) technique.

Ion beam modification of materials is an important application of ion beam. Recently, boron carbonitride nanotubes were synthesized from boron nitride nanotubes using C ion beam irradiation [2]. Similarly, phase transformation of thin film and nanostructured materials by ion beams is another important application. Ion beam-induced controlled modification of physical properties is possible in thin film and nanostructured materials [2–8]. Phase segregation and separation is another unique application of ion beam [9].

Ion implantation is an exceptional surface treatment method to implant N-type and P-type dopants into semiconductors to make solid-state electronics. Moreover, dilute magnetic semiconductor devices could be synthesized through direct implantation of magnetic elements into nonmagnetic semiconductors [10, 11]. After developed FIB, now it is also possible to

implant required elements into required depth to make semiconductor devices. Section 3 describes the advantages of ion implantation process with emerging new applications.

Focused ion beam in keV energies is also used for microscopy of materials [12]. FIB instrument can be utilized for microstructure tomography in the range from ~100 nm to 10 μm. Advanced FIB microscopy has been described in detail in Section 3.

2.2. Environmental sciences

IBA techniques such as PIXE are widely used for environmental studies. Trace element measurement in aerosol samples is an important application of MeV ion beam. After developed microprobe, now it is possible to measure or mapping of heavy metals in various samples like trees, fish, deposit mining dust on trees leaf, glacial melting study, etc., which give valuable seasonal and historical information of pollution to the particular area of study. Many authors have proven the diagnostic usefulness of hair analysis in assessing pathological elemental concentrations in the body. Hair has been shown to reflect environmental and occupational exposure to lead, mercury, aluminum [13], and a combination of multiple metals. Microanalysis of hair to assess the toxic metals in scalp hair of artisanal miners are important environmental studies using micro PIXE. The PIXE technique has been proven as a high accurate, sensitive, and nondestructive method to determine concentration and composition of chemical elements. Beside these, PIXE technique has been successfully used in many other environmental studies like elemental mapping, source appointment, and chemical characterization of various pollutants.

2.3. Device fabrications

Focused ion beam either in MeV or keV energies is a considerable tool in science and technology for micro and nanodevice fabrications using both bottom-up and top-down approaches. In the bottom-up approach, individual nano-objects such as nanowires and nanotubes can be assembled directly together in form of functional welded networks using ion beam induced nano-welding technique. Ion beam-induced nanowelding is another option to make nanowire/nanotube-welded junctions and to make nanodevices or integrate nanodevices. Recently, researchers used ion beam as a tool to weld carbon nanotubes, silver nanowires, Ni nanowires, and SiC nanowires to make junctions and large-scale welded networks [14–21] (**Figure 2**).

In top-down device fabrication approach, 3D MeV proton beam writing is an important technique to make micro and nanodevices [22]. Whereas, keV energy FIB is now an essential tool to use for TEM sample preparation and device fabrication and to fabricate complex nanoscale structures/patterns. It is a tool that directly makes a 3D and 2D pattern without masks from a few nanometers to hundreds of micrometers in size. Compact FIB instruments are developed and being used to fabricate microelectromechanical systems (MEMS)-based devices, microfluidic chips, photonic devices, and DNA sequencing nanopore membranes [23, 24]. More detail FIB applications are described in Section 3.

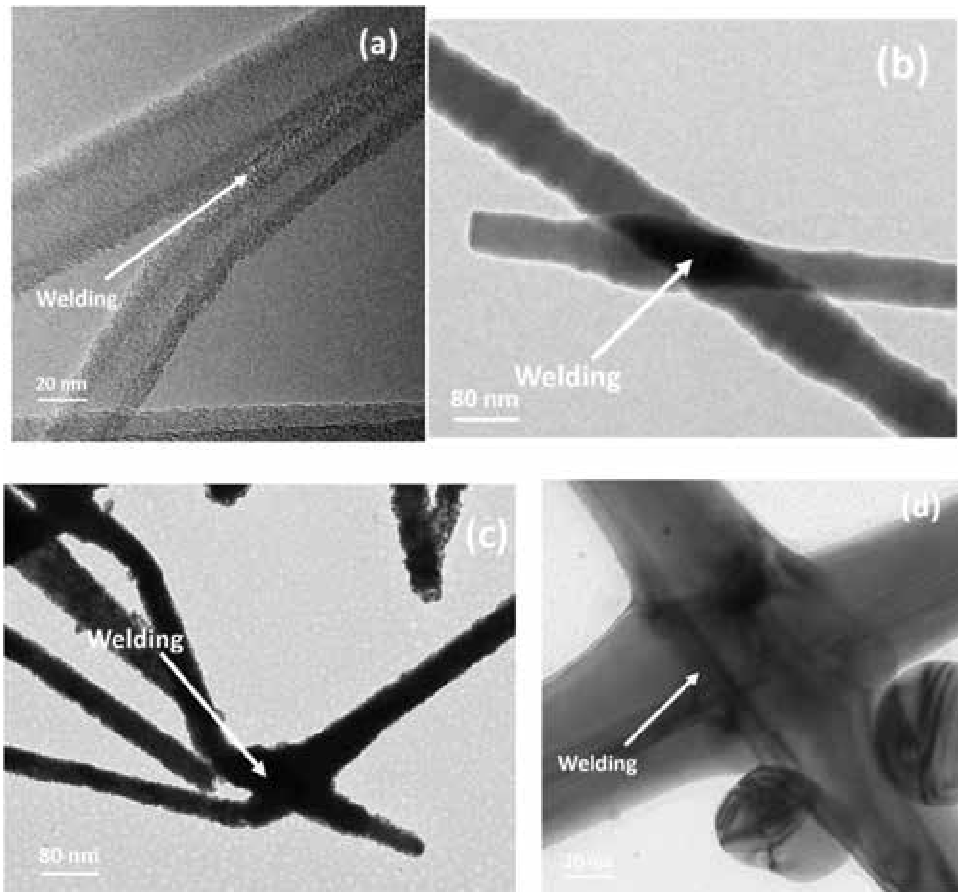

Figure 2. Ion beam-induced welding of (a) multiwalled carbon nanotubes [21], (b) SiC nanowires [14], (c) Cu nanowires, and (d) silver nanowires [18].

2.4. Atomic physics

Excitation and ionization of atoms by ion beam is another application of ion beam technology to study atomic structure. Ion beam-induced X-ray emission is a rich phenomenon to study the complicated process during ion beam interaction with matter. The fundamental parameter such as ionization cross section is a pure quantum mechanical phenomenon. When an ion passes through the target atom, the target atom becomes ionized due to columbic interaction of ions with target atom. The target atom is ionized by absorbing ion beam energy and rest of the energy is utilized in ejaculation of auger electron in case of atomic collision and heating.

When an atom deionized, it released the absorbed energy in the form of photon, and its excess energy ejaculates the auger electron and rest of the energy loss goes in the heating of sample. The probability of emission of x-rays or photon from particular due to electron transition from upper shell to lower shell is called the fluorescence of particular shell. We can measure the

X-ray production cross section of particular shell using fluorescence yield of shell of target element. For K-shell, X-ray production cross-section data are available so far to support PIXE technique for materials analysis, whereas a lot of discrepancies exist in L-shell and M-shell of X-ray production cross section measurement. As it had become complicated due to fluorescence and auger electron transition between levels and sublevels.

The fine and hyperfine lines originating from s, p, d and f orbitals and its suborbitals (from levels and sublevel) can be studied and explore the fluorescence and auger electron transition and Coster-Kronig transition for L- and M-shell X-ray production cross section. The relative intensity ratios of K-shell, L-shell, and M-shell transition lines can be explored from light and heavy ion in advanced studies. Decreasing and increasing trend of intensity ratio of transitions lines $K\alpha/K\beta$ and $L\beta/L\alpha$ can also be explored as a function of ascending order of elements Z, respectively.

The stopping power or energy loss of projectile in the matter is another research area. Due to lack of correct knowledge of stopping power, error in cross-section measurement is large. Bethe formalism and Ziegler, the founder of TRIM/SRIM software for heavy ions stopping power, may deviate from the experimental results at different energy ranges. The study reveals that there are many discrepancies exist in the theoretical models. Using heavy ion for cross section and stopping power studies can improve the theoretical models.

The multi-ionization effect by heavy ion is an open research field and a once need to explore the complicated physics exit behind it. PIXE using heavy ion lead us to find the fact for corrections of theoretical Models.

2.5. Nuclear physics

Study of nuclear structure and nuclear reaction using ion beam is another application of ion beam technology. As the diameter of the nucleus is less than 10^{-14} m, the nuclear structure study with microscopy technique is hard to investigate. Therefore, high energy ions which have a size comparable to a nucleus are another option to investigate the structure of the nucleus. Scattering cross section could be measured by energetic ions interacting with target nucleus. Ion-induced nuclear reaction could be possible to emit secondary particles such as neutrons, alpha particle, gamma-rays, and beta particles. Once energies and angular distribution of secondary particle emission observe, then size and shape of the nucleus and the forces existing inside the nucleus could be deduced. Large range of ion beam-induced nuclear reactions is possible.

Proton beams with different energies are very useful for various aspects of research, such as proton beams with energies between 1 MeV and 1 GeV are almost always used for nuclear structure studies. Proton beam with energy between 1 and 100 MeV could be made to interact with whole nuclei or with several nucleons, while proton beam with energy between 100 and 1000 MeV could be interacted with individual nucleons in the nucleus which giving more precise information about each nucleon. Ion beam energies greater than 1 GeV are useful to produce short-lived particles such as mesons [25].

2.6. Biology

Ion beam could be applied in biology for probing, damaging and modifying the biological samples. Ion beam accelerators have advanced further by the introduction of nuclear microprobes. These microprobes have opened up new areas of research in biological science by allowing elemental microanalysis, with imaging capabilities, particularly suitable for the measurement of trace elements in biological tissues. Whereas ion beam-induced mutation of crops, vegetables and fruits are matured method. Micro PIXE is continuously applied in life science for comprehensive food crops analysis to determine traces of toxic heavy metals.

2.7. Particle physics

High-energy ion beams produced by particle accelerators also have vast applications in particle physics as it is a tool to study extreme states of matter. In high energy physics, particle colliders have taken part in a key role in scientific discoveries for last many decades. Particle colliders are basically ion beam accelerators where particles are accelerated up to relativistic speed to collide with a stationary target or head-on collision with each other like proton-proton colliders. At sufficiently high energy, relativistic particles smash into other high energy particles. Energies of the colliders continuously increase over time for exploring new physics/particles. Moreover, advanced high energy particle detectors are being developed for understanding the properties of high energy particles such as mass, energy, charge, spin, and isospin, which are being created during collision of relativistic particles.

Large Hadron Collider (LHC) is the world's largest accelerator built at Swiss-French border in Geneva, Switzerland. It is also used to accelerate the heavy ion beams. It is capable of accelerating Pb ions with the beam energy of 2.76 TeV/nucleon, which yield to 1.15 PeV in total, with the luminosity of 1.0×10^{27} cm^{-2} s^{-1}. Heavy ion beam focuses on study of quantum-chromo-dynamics (QCD), the strong interaction sector of Standard Model (SM). It allows to study physics of strongly interacting matter and the quark-gluon plasma at extreme values of energy density and temperature in nucleus-nucleus collision.

2.8. Medical application

Medical radioisotopes for medical applications are well established for diagnostic and therapy. Ion beams are also being used to produce radioisotopes that are used for the mentioned uses. Further research is also going on to produce high-quality radioisotopes through the series of investigation into production of radioisotopes and its decay characteristics in medical applications such as cross-section measurement of ion beam with target atom to monitor nuclear reactions, compilation of nuclear reaction data for therapeutic radionuclides production, and Beta decay nuclear reaction cross-section measurement for positron emission tomography.

Ion beam therapy is another unique application of ion beam, which provides cutting-edge cancer treatment. Ion beam therapy is a newly emerging treatment for cancer, which is more effective than any other old techniques. In ion beam therapy, ion beam is offering the possibility of excellent dose localization and thus maximizing cell killing within the tumor. Proton therapy for cancer treatment is a matured technology to damage cancer cells while producing the least

damage to the surrounding uninfected tissues. Radiotherapy with carbon ion beam is also developed and is popular in the world, while heavy ion therapy research is going on by understanding fundamental damage mechanisms of cancer cells under heavy ion irradiation [26].

2.9. Nuclear astrophysics

The production of radioactive ion beam and studying its properties are currently a hot research area in accelerator scientific community and for nuclear astrophysicists. Energetic radioactive ion beam, a beam of short-lived nuclei, opens up a new research direction to study nuclear reactions and nuclear structures. Nuclear reaction with radioactive ion beam provides information on reactions that occur at our sun and other stars in our universe. For astrophysics point of view, scientists have produced short-lived halo nuclei in radioactive ion beam facilities to study nuclear astrophysics. Further research is going on for a generation of short-lived neutron-enriched nuclei in next-generation radioactive ion beam facilities, which are required to understand the existence of heavy elements in the universe by the astrophysics rapid neutron-capture process. Through this short-lived radioactive ion beam, it may be possible to explore the secrets of the universe as these nuclei beams play a vital role in understanding the origin of the elements and the dynamics of stellar objects. Moreover, short-lived nuclei (radioactive ion beam) are essential for useful studies of astrophysical objects such as neutron stars, super novae, X-ray bursters, and supernovae. In conclusion, short-lived halo nuclei in radioactive ion beam facilities will provide us with the information that how the chemical elements had formed our world in the cosmos [27].

3. Conclusion

Recent researches in ion beam applications that are mentioned in this introductory chapter are so detailed that it is not possible to cover them in this book. Therefore, this book only has selected special chapters from distinguished authors that cover various aspects of:

1. MeV ion beam applications
2. Focused ion beam applications
3. Ion implantation

Author details

Ishaq Ahmad[1]* and Fabian I. Ezema[2]

*Address all correspondence to: Ishaq@ncp.edu.pk

1 National Centre for Physics, Islamabad, Pakistan

2 Department of Physics and Astronomy, University of Nigeria, Nsukka, Nigeria

References

[1] Ahmad I, Dee CF, Husnain G, Rafique HM, Yan L, Naseem S. The use of high intensity electron beam to form nanohole, induce bending and fabricate nano-contact on a ZnO nanowire. Micro and Nano Letters. 2012;**7**:122-124

[2] Ahmad I, Naqvi SR, Iqbal JI, Lu B, Yan L, Dee CF, Aslam B. Substitutional carbon doping of hexagonal multiwalled boron nitride nanotubes (h-MWBNNTs) via ion implantation. Journal of Nanoparticle Research. 2014;**16**:2170-2178

[3] Bushra B, Shehla H, Madhuku M, Ahmad I, Khan R, Arshad M, Alamgir K, Naseem S, Maaza M. MeV carbon ion irradiation-induced changes in the electrical conductivity of silver nanowire networks. Current Applied Physics. 2015;**15**:642-647

[4] Usman M, Naeem M, Hassan NU, Maqbool M, Iftikhar A, Ahmad I, Zahid H. Structural, optical, and electrical characteristics of AlN:Ho thin films irradiated with 700 keV protons. Applied Surface Science. 2015;**357**:179-183

[5] Ishfaq M, Rizwan Khan M, Bhopal MF, Nasim F, Ali A, Bhatti AS, Ahmad I, Bhardwaj S, Cepek C. 1.5 MeV proton irradiation effects on electrical and structural properties of TiO_2/n-Si interface. Journal of Applied Physics. 2014;**115**:174506

[6] Khan S, Husnain G, Ahmad I, Khan K, Usman M, Saira R. Structural characteristics of Ni-implanted AlN. Surface Topography. 2014;**2**:035007

[7] Shah A, Husnain G, Ahmad I, Arshad M. Cu ions irradiation impact on structural and optical properties of GaN thin film. International Journal of Modern Physics B. 2013;**27**:1350020

[8] Yan L, Zhou G, Ahmad I, Zhou X. Improving the electrical conductivity of multi-walled carbon nanotube networks by H ion beam irradiation. Carbon. 2011;**49**:2141-2144

[9] Ahmad I, Madhuku M, Adeela S, Khan S, Javaid H, Ali A, Wang D, Ilyas SZ, Mola G, Waheed A, Rasheed MA. Tailoring the structural and optical characteristics of InGaN/GaN multilayer thin films by 12 MeV Si ion irradiation. Materials Science in Semiconductor Processing. 2017;**64**:95-100

[10] Husnain G, Yao SD, Ahmad I, Arshad RHM, M M. Characterization of n-GaN dilute magnetic semiconductors by cobalt ions implantation at high-fluence. Journal of Magnetism and Magnetic Materials. 2012;**324**:797-801

[11] Husnain G, Yao SD, Ahmad I, Rafique HM. Structural and magnetic impact of Cr+– implantation into GaN thin film. Solid State Sciences. 2012;**14**:735-738

[12] Munroe PR. The application of focused ion beam microscopy in the material sciences. Materials Characterization. 2009;**60**:2-13

[13] Kempson IM, Lombi E. Hair analysis as a biomonitor for toxicology, disease and health status. Chemical Society Reviews. 2011;**40**(2011):3915-3940

[14] Khan R, Khan MAR, Ahmad I, Khan MA, Iqbal T, Ezema FI, Maaza M. Joining of individual silicon carbide nanowires via proton beam irradiation. Current Nanoscience. 2018;**14**:1-6. DOI: 10.2174/1573413714666180328153514

[15] Honey S, Naseem S, Ahmad I, Maaza M, Bhatti MT, Madhuku M. Interconnections between Ag-NWs build by argon ions beam irradiation. Journal of Nanomaterials & Molecular Nanotechnology. 2017;**6**:1000213

[16] Honey S, Ishaq I, Madhuku M, Naseem S, Maaza M, Kennedy JV. Nickel nanowires mesh fabricated by ion beam irradiation-induced nanoscale welding for transparent conducting electrodes. Materials Research Express. 2017;**4**:075042

[17] Shehla H, Naseem S, Ishaq A, Maaza M, Bhatti MT, Wan D. Large scale silver nanowires network fabricated by MeV hydrogen (H^+) ion beam irradiation. Chinese Physics B. 2016;**25**:046105

[18] Shehla H, Ishaq A, Yaqoob K, Javed I, Saira R, Shahzad N, Maaza M. Ion beam irradiation-induced nano-welding of Ag nanowires. Micro and nano Letters. 2016;**11**:34-37

[19] Shehla H, Khan S, Javed I, Madhuku M, Ahmad I, Shahzad N, Maaza M. Protons irradiation induced coalescence of silver nanowires. Current Nanoscience. 2015;**11**:792-796

[20] Ishaq A, Ni Z, Long Yan L, Gong J, Zhu D. Constructing carbon nanotube junctions by Ar ion beam irradiation. Radiation Physics and Chemistry. 2010;**79**:687-691

[21] Ishaq A, Yan L, Zhu D. The electrical conductivity of carbon nanotube sheets by ion beam irradiation. Nuclear Instruments and Methods in Physics Research B. 2009;**267**:1779-1782

[22] Sum TC, Bettiol AA, Kan JA, Watt F, Pun EYB, Tung KK. Proton beam writing of low-loss polymer optical waveguides. Applied Physics Letters. 2013;**83**:1707-1709

[23] Steve R, Robert P. A review of focused ion beam applications in microsystem technology. Journal of Micromechanics and Microengineering. 2001;**11**:287-300

[24] Chih JL, Thomas A, Alexey B. Fabrication of symmetric sub-5 nm nanopores using focused ion and electron beams. Nanotechnology. 2006;**17**:3264-3267

[25] Clark DJ. Accelerators for nuclear physics. Reports on Progress in Physics. 1972;**35**:1007-1075

[26] Hirohiko T. Overview of carbon-ion radiotherapy. Journal of Physics: Conference Series. 2017;**777**:012032

[27] Karlheinz L, Hendrik S. The role of radioactive ion beams in nuclear astrophysics. Physica Scripta. 2013;**T152**:014011

Section 2

MeV Ion Beam Applications

Chapter 2

Ion-Nanoscale Matter Interactions

Elmuez A. Dawi

Additional information is available at the end of the chapter

http://dx.doi.org/10.5772/intechopen.76862

Abstract

Irradiation of spherical gold (Au) nanoparticles confined within a silica matrix with swift heavy ions induces their shaping into prolate nanorods along the beam direction. In this review, spherical colloidal Au nanoparticles with a diameter in the range of 15–30 nm (±3 nm) are irradiated at normal incidence with Ag ions with a kinetic energy in the range of 18–54 MeV to fluences between 10^{13} and 10^{15} ions/cm^2 at 300 K. For example, under irradiation with 18 MeV Ag^{+4} ions to a fluence of 6.4×10^{14} ions/cm^2, the originally spherical nanoparticles of 15 nm diameter are shaped into prolate nanorods with a length of 40 nm and a width of 8 nm. An aspect ratio of the major to the minor axis of the nanorods of about 5.0 ± 0.4 at constant volume is achieved. Saturation of the variation of the aspect ratio is reached at a fluence of 8.7×10^{14} ions/cm^2. Irradiation of samples containing 15 nm Au particles with 25 and 54 MeV Ag ions has shown further lengthening of the Au nanorods, increasing with the increasing ion energy. Similar ion-shaping behavior is reported for 30 nm Au particles under irradiation with 18, 25, and 54 MeV Ag ion energies, respectively. By systematically monitoring the experimental data, we put in evidence the existence of a threshold fluence of Au nanoparticle elongation. The value of the threshold fluence is found to depend on both the ion energy and nanoparticle size.

Keywords: ion beam, electronic stopping, Au nanoparticles, ion track, nanorods, nanowires

1. Introduction

The use of ion beams as effective tools for changing the material properties has gained increasing interest during the past few decades. In particular, emphasis is given to ion implantation [1] and focused ion beam [2] processes which have received an enormous amount of attention in semiconductor technology applications.

IntechOpen

© 2018 The Author(s). Licensee IntechOpen. This chapter is distributed under the terms of the Creative Commons Attribution License (http://creativecommons.org/licenses/by/3.0), which permits unrestricted use, distribution, and reproduction in any medium, provided the original work is properly cited.

When an ion penetrates a solid, it dissipates its kinetic energy in collisions with the target atoms. Ion implantation is performed in the energy regime where electronic stopping dominates the minimal sputtering mechanism. Implanted ion profile and the concentration of impurity atom are affected by sputtering. As the target material is being bombarded with energetic ions, some of the incident beam ions are implanted and retained in the target, while the surface that is exposed to the ion beam is simultaneously receding due to sputtering. Schematic diagram of the ion-solid interaction is illustrated in **Figure 1** (adopted from Nastasi et al. [3]). The basic mechanisms characterizing the interactions of ions with solids can be summarized as follows:

1. Nuclear energy loss. This is the main mechanism of energy losses at low ion velocities (kinetic energy, corresponding to ~1 keV/a.m.u.). The bombarding particle transfers its energy to the nucleus of the target atom in elastic collisions, which causes the atoms to be displaced from their equilibrium positions.
2. Electronic energy loss. This is the predominant mechanism of energy loss for fast ions (≥ 1 MeV/a.m.u.). In this regime the ions lose their kinetic energy by electronic excitation and ionization of target atoms.
3. Photon radiation. Stopping through photon generation becomes significant only at relativistic velocities (bremsstrahlung, transitional Vavilov-Cherenkov radiation).
4. Nuclear reactions. Nuclear reactions of the projectile ion and target atoms occur when the two collision partners have sufficient kinetic energy that the Coulomb barrier can be overcome

Taking into account the fact that most attention is paid to ion-induced structural changes of materials within nuclear and electronic energy loss regimes, we shall only discuss the two first mentioned mechanisms of the ion-matter interactions. A good approximation is the assumption that nuclear and electron energy losses are uncorrelated and can therefore be discussed separately and independently.

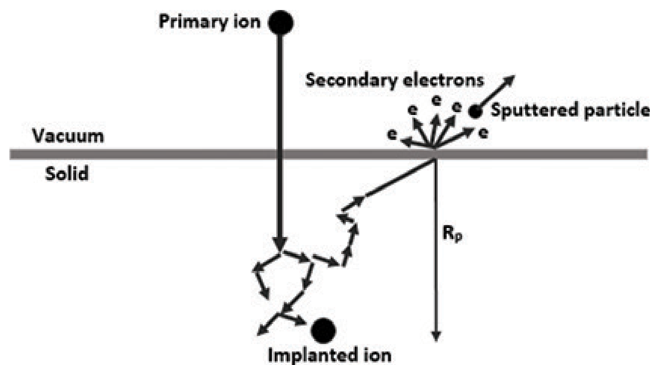

Figure 1. Schematic diagram of the ion solid interactions (adopted from Nastasi et al. [3]).

In the case of nuclear stopping, elastic collisions cause the ions to change their velocity, but the total kinetic energy of the colliding atoms remains constant. On the other hand, inelastic collisions involving electrons are not accompanied by large changes in the direction of the ion, and here several processes are possible: excitation and ionization of atoms with electron exchange in the colliding atoms. A typical evolution of the energy loss as a function of the ion kinetic energy is presented in **Figure 2** for a beam of xenon ions (Xe ions) in amorphous SiO_2. From the figure, one can, for instance, infer that the electronic stopping power for an energy of 370 MeV is more than two orders of magnitude larger than the nuclear stopping power.

1.1. Ion beam-induced deformation

i. Anisotropic plastic deformation of colloidal silica particles

Heavy ions with ~MeV/a.m.u. kinetic energy predominantly lose their energy in a solid target material by electronic excitation and ionization of the target atoms. It is now well established that during irradiation with such ions, amorphous materials are subject to irreversible anisotropic changes of their specimen dimensions [4, 5]. Detailed description of the mechanism governing the anisotropic deformation is reported by the viscoelastic model. The latter presumes the deposition of energy by the incident ion into the electronic subsystem of the material. Through electron–phonon coupling, this energy is transformed in a cylindrical molten-like transient heating around the path of the particles. In a very short time interval (few femtoseconds), and as a result of the cylindrical molten expansion, shear stress relaxation induces freezing anisotropic stress as cooling of the heated regions is taking place. In this way,

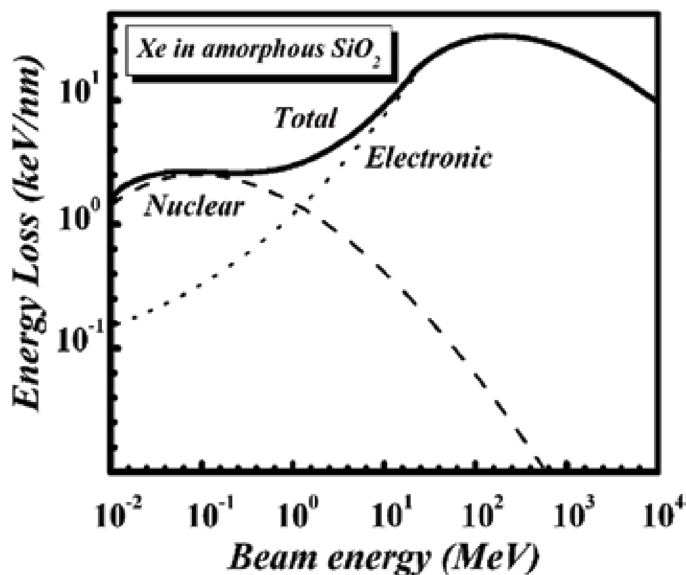

Figure 2. Nuclear, electronic, and total energy loss versus the ion energy for typical ion energy of 370 MeV Xe in amorphous SiO_2. The figure is reproduced with permission from M. Toulemonde [8].

the deformation mechanism is governed by electronic energy loss and most efficiently with ions in the MeV/a.m.u. energy range. Extrapolation of experimental high-energy to lower-energy data has suggested that the deformation is not expected to occur below a minimum irradiation energy of 1 MeV [6, 7]. The concept of the thermal spike is generally invoked to interpret the damage induced in amorphous materials such as metallic or silica glasses when they are traversed by ions with a kinetic energy in the electronic stopping regime.

ii. Anisotropic plastic deformation of embedded metal nanoparticles

Metal nanoparticles (NPs) are subject of large scientific and technological interest because of their specific properties which are different from those of the corresponding bulk material [9, 10]. When light impinges on (nano)-metal, the free conduction electron clouds respond collectively by oscillating in resonance, which excitation is known as a surface plasmon (SP). For a number of (noble) metals, the resonance behavior is noticeable in a single band in the visible range of the electromagnetic spectrum. One of the interesting aspects is the possibility to shift the surface plasmon resonance (SPR) peak of metal NPs into the infrared region by modifying their aspect ratio [11]. The SPR peak characteristics depend on the size, the shape, and the chemical environment of the metal NP; thus, modification of one of these parameters represents a way to control the optical properties of the material containing the NPs. In this respect, the ion beam-shaping technique is becoming a powerful tool to manipulate matter at the nanometer scale, allowing spherical dielectric particles to be transformed into prolate nanostructures, i.e., to elongate in direction perpendicular to the incident beam direction. Meanwhile, metal NPs embedded within a dielectric matrix are transformed into nanorods and/or nanowires that are aligned along the direction of the incident ion beam [12]. The latter is becoming an increasing scientific interest specially in tailoring the optical properties of plasmonic-active materials which could be widely used in applications within nanophotonics and nanoplasmonics [13].

2. Method

Compared to conventional surface science techniques, such as gas-phase synthesis and deposition of NPs under ultrahigh-vacuum condition, the self-assembly of NPs by means of electrostatic coupling is a scientifically and economically interesting alternative [14]. In the following, charge-stabilized spherical colloidal gold NPs, which have been derivatized with (3-aminopropyl)triethoxysilane (APTES), are deposited on the surface of thermally grown silicon oxide substrates. The thickness of the thermal oxide amounts to 200 nm. Two sets of samples with the different NP size of 15 and 30 nm diameter are prepared. Dispersion in size is deduced from atomic force microscopy (AFM) technique. AFM analysis of the particle heights is measured and found to amount to about ±3 nm. Each set consists of a number of identically prepared samples for each NP size.

At present AFM is one of the important techniques for analysis of surface morphology [15, 16]. The size and shape of Au NPs have been inspected by a Nanoscope® IIIa tapping mode atomic force microscope (TM-AFM) operating in air. **Figure 3** shows AFM images of Au NPs, distributed on the sample surface after immersion for 5 minutes into a solution containing Au NPs

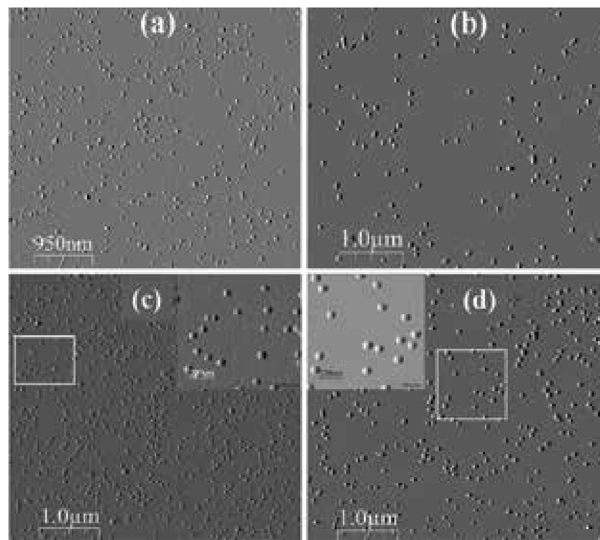

Figure 3. AFM images of 15 and 30 nm Au particles deposited on the SiO_2 surface after immersion into Au solution for 5 minutes, (a) and (b), respectively, and 40 minutes, (c) and (d), respectively.

with 15 and 30 nm diameter (a) and (b), respectively, and after immersion for 40 minutes into Au solution containing 15 and 30 nm diameter NPs, (c) and (d), respectively. These AFM images which were taken before sputter deposition of the second oxide layer show the uniformity of the Au NP distribution over the surface of the samples.

A silicon dioxide layer with thickness of about 150 nm is reactively sputtered to cover the Au NPs. Subsequently, the layer structure is annealed at 900°C in an open furnace. To provide a good thermal contact during the irradiation treatment, the samples are mounted on a massive copper holder using conductive paste. For better understanding of ion energy and NP initial size dependence, irradiations with 18, 25, and 54 MeV Ag ions are performed on the first set of the samples. This first set is composed of three identically prepared NPs of 15 and 30 nm diameter each. The additional set of samples composed of the same NP size is prepared at higher NP areal density as to investigate the role of NP density within the resulting deformation characteristics of embedded NPs. The variation in Au NP areal density is established by variation of the immersion time of the samples into the Au-containing solution, between 5 and 40 minutes. The resulting density of the 15 and 30 nm Au NP samples obtained following the deposition scheme between 5 and 40 minutes is estimated in **Table 1**. The average interparticle distance is calculated based on a square array of particles. The ion beam is electrostatically scanned to homogeneously irradiate the entire sample area of 2 × 2 cm. Irradiations are performed at room temperature (300 K) for fluences ranging from 10^{13} to 10^{15} ions/cm^2 applying normal incidence. Beam currents are sufficiently stable during irradiations as measured on a spot of 1 mm^2 using a micro-Faraday cup. The beams are delivered by the Utrecht 6.5 MV EN tandem accelerator. The values for the electronic stopping powers in SiO_2 and the projected range of the silver ions in SiO_2 at the energies applied are deduced from the SRIM program [17] and shown in **Table 2**.

Deposition time (±1 min)	5 minutes	10 minutes	20 minutes	30 minutes	40 minutes
15 nm Au NP concentration (particles/cm^2) (±10%)	2.5×10^9	7.5×10^9	1.4×10^{10}	1.7×10^{10}	4×10^{10}
Interparticle distance (±10 nm)	200	115	85	76	50
30 nm Au NP concentration (particles/cm^2) (±10%)	—	9×10^8	2.3×10^9	2.8×10^9	3.2×10^9
Interparticle distance (±10 nm)	—	333	208	188	176

Table 1. NP concentration and the corresponding interparticle distance of Au NPs with average size of 15 and 30 nm diameter deposited on SiO_2 substrate by immersion of the substrate into colloidal Au-containing solution for time intervals of 5, 10, 20, 30, and 40 minutes.

These ranges are far beyond the thickness of the oxide layers containing the metal nanoparticles. Hence, the irradiation is only used to deposit energy into the SiO_2-Au layers. The Au nanoparticle size and shape before and after irradiation are studied by using (tapping mode) atomic force microscopy (AFM), Rutherford backscattering spectrometry (RBS), and transmission electron microscopy (TEM).

Analysis of the samples has been carried out by different techniques. Rutherford backscattering spectrometry (RBS) is used to measure the density of Au species as it penetrates into the SiO_2 matrix. With respect to the latter, RBS is regarded as a faster tool to bring information about Au NP depth distribution before and after irradiation with heavy ion beams. The depth distribution of the Au NPs is estimated from the corresponding full width at half maximum (FWHM) of the Au peak in the RBS spectra. It is worth mentioning that under swift heavy ion (SHI) irradiation, the vast majority of the Au species will not be confined to their NPs due to melting; therefore, the FWHM of the Au peak cannot bring qualitative estimation of the exact NP size. However, a qualitative trend of the NP elongation can be followed. RBS analysis was carried out applying an incident $^4He^+$ ion beam with energy of 2 MeV at normal incidence geometry. The backscattered ions were analyzed in situ using two detectors at angles of 120° and 170°, respectively. In the "Results" section, we will only discuss the data analysis obtained from one detector of our selection (120° detector), assuming that the data obtained from the 170° are essentially identical. After RBS analysis, samples containing the metal NPs are analyzed by transmission electron microscope (TEM) for cross-sectional imaging of the size and shape of Au NPs before and after irradiation. For that purpose, a 300 keV Philips/CM30 microscope is used. The micrographs obtained from X-TEM analysis are processed with a slow scanning camera applying digital micrograph program.

	S_e (SiO_2) (keV/nm)	S_n (SiO_2) (keV/nm)	S_e (Au) (keV/nm)	S_n (Au) (keV/nm)	R_p (μm)
18 MeV^{+4}	5.4	0.23	11	0.9	5.8
25 MeV^{+5}	6.7	0.18	14	0.7	6.9
54 MeV^{+8}	9.7	0.10	24	0.4	10.3

Table 2. Values for electronic (S_e) and nuclear (S_n) stopping power for SiO_2 and gold and projected range (R_p) obtained for the applied ion beams (18, 25, and 54 MeV Ag ions). All the values are obtained using the code SRIM 2008 [17].

3. Results

Au NPs with average size of 15 and 30 nm diameter are prepared with different NP concentrations and/or areal densities (10^8–10^{10} particles/cm^2) embedded within a single plane parallel to the surface of a SiO_2 matrix. In this section, we will report a detailed investigation of swift heavy ion irradiation effects on these NPs. A selective range on incident ion energy of 18, 25, and 54 MeV Ag ions is applied. Influence of the ion energy, NP size, and areal density on the process of ion-induced elongation of spherical Au NPs will be discussed. For clarity of presentation, the "Results" section is divided into two subsections. The first subsection discusses the role played by embedded NP size and ion energy within the deformation characteristics at almost constant NP areal density and/or concentration. For that purpose, NP size range between 15 and 30 nm diameter is selected of which its samples are identically prepared and successively irradiated with ion beam energies in the range of 18–54 MeV Ag ions. In the second subsection, for the two NP sizes, the ion beam-induced deformation is investigated considering two extreme regions of NP areal density (low concentration and high concentration) applying single ion energy of 54 MeV Ag^{+8} ions.

3.1. Elongation as a function of the initial NP size and the ion beam energy

3.1.1. Evolution of 15 nm Au NPs

The first set consisting of three identically prepared samples, containing 15 nm Au NPs with an average areal density amounting to 1.7×10^{10} particles/cm^2, is irradiated with 18, 25, and 54 MeV Ag ions, respectively. **Figure 4a–c** shows the Au RBS peak as obtained from the 120° detector for several fluence values for the three energies. The relatively sharp peak of the unirradiated regions corresponds to 15 nm particles which are embedded in a SiO_2 matrix in a plane at a depth of approximately 150 nm below the surface. RBS analysis in **Figure 4a–c** shows broadening in Au NP peak with increasing the irradiation fluence. The broadening in the Au RBS peak indicates that the depth distribution of the Au is penetrating into the hosting SiO_2 matrix. The latter indicates that the pristine Au NP is transformed into aligned nanorods parallel to the ion beam direction. The evolution of the FWHM with fluence from the 120° and 170° detectors is shown in **Figures 5(a)** and **5(b)**, respectively.

From inspection of the data in both figures, two facts are deduced for irradiations of 15 nm Au NPs with 18 and 25 MeV Ag ions, as follows:

- **i.** No elongation appears for fluences lower than ~5.0×10^{13} and 3.0×10^{13} ions/cm^2, respectively.
- **ii.** The RBS peak width reaches saturation for fluences larger than ~$6–8 \times 10^{14}$ and 4.5×10^{14} ions/cm^2, respectively.

The X-TEM micrographs in **Figure 6a**, **b** correspond to the highest 18 MeV irradiation fluence (8.7×10^{14} ions/cm^2). Clearly, under 18 MeV Ag^{+4} ions, the originally spherical NPs of 15 nm diameter are all shaped into prolate nanorods with a length of ~40 nm and a width of ~8 nm, thus, with an aspect ratio of about 5. The volume of each nanorod corresponds approximately

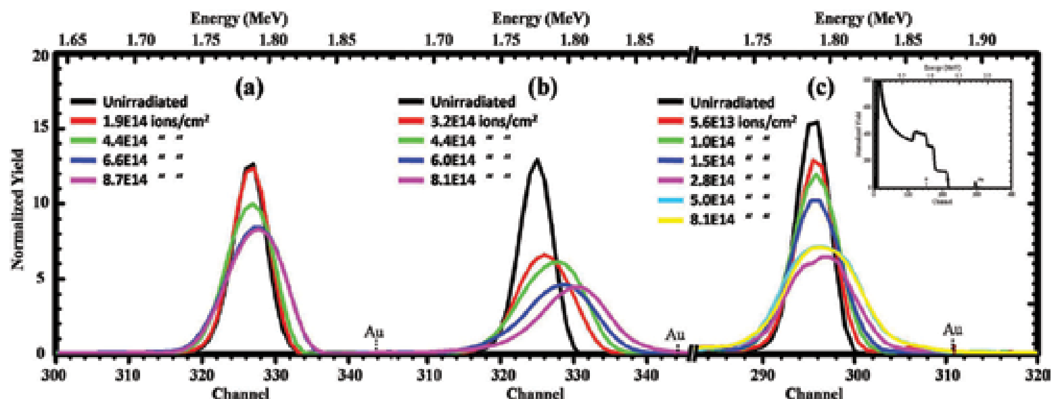

Figure 4. Normalized RBS spectra of three identically prepared samples containing Au NPs with 15 nm diameter with an average areal density of 1.7x10^{10} particles/cm^2 after being irradiated with energies of 18 MeV Ag^{+4} ions, 25 MeV Ag^{+5} ions, and 54 MeV Ag^{+8} ions, (a), (b), and (c), respectively. The inset shows total normalized spectra for all samples. The Au surface channel is indicated. The scale is (a), and (b) is the same; however, for (c), the experimental condition is slightly different.

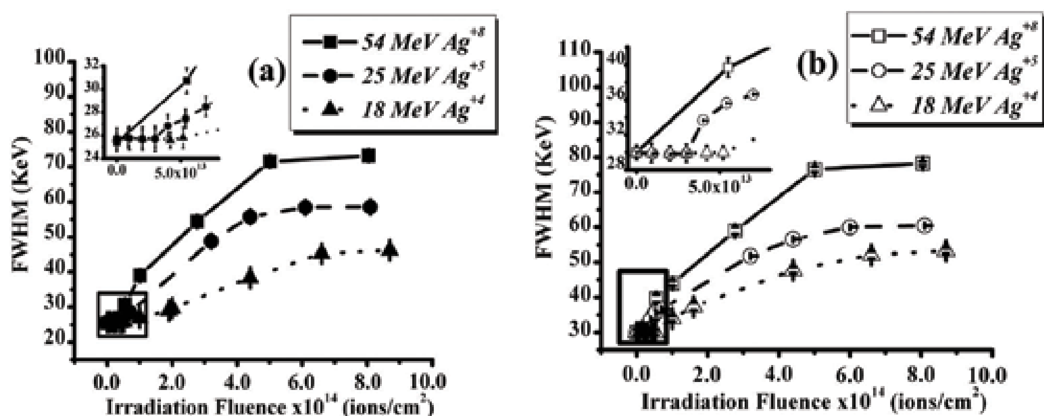

Figure 5. The FWHM of the Au peak as function of irradiation fluence determined simultaneously for the 120° and 170° scattering angles, (a) and (b), respectively. The figures are for 15 nm Au NPs irradiated with 18 MeV Ag^{+4} ion energy (triangles and dot line), 25 MeV Ag^{+5} ion energy (circles and dash line), and 54 MeV Ag^{+8} ion energy (squares and solid line). A magnified view of the region identified by the black square and the black rectangle is included in the inset of figure (a) and (b), respectively.

to that of the pristine spherical NP (V_{NR}~V_{NP}). This indicates that the ion-shaping process for these irradiation conditions is an individual process, i.e., each NP deforms into a similar prolate nanorod.

The broadening of the Au RBS peak for the sample irradiated with 54 MeV Ag^{+8} ions is also represented in **Figure 5a**, **b**. At this energy the elongation of 15 nm Au particles starts without detectable threshold fluence in these measurements. After irradiation to a fluence of 1.0 × 10^{14} ions/cm^2, the broadening of the Au RBS peak has already reached the value attained under irradiation with 18 MeV Ag^{+4} ions to the maximum fluence of 8.7 × 10^{14} ions/cm^2. The latter observation confirms the influence of the ion energy on the elongation characteristics of Au NPs.

http://dx.doi.org/10.5772/intechopen.76862

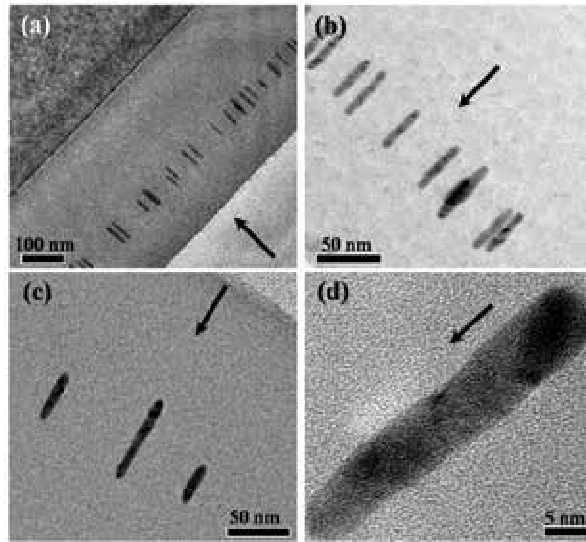

Figure 6. High-resolution X-TEM images of (i) 15 nm Au NPs under 18 MeV Ag^{+4} ions to a fluence of $8.7\text{x}10^{14}$ ions/cm^2 (a) and (b). (ii) 15 nm NPs under 54 MeV Ag^{+8} ions to a fluence of 1.0×10^{14} ions/cm^2 (c) and (d). The direction of the ion beam is indicated by the black arrows.

Strikingly, X-TEM micrographs corresponding to the irradiation with 54 MeV Ag^{+8} ions to a fluence of 1.0×10^{14} ions/cm^2 reveal almost similar nanorod morphology as those given in **Figure 6a**, **b**. These micrographs are given in **Figure 6c**, **d** showing aligned Au nanorods of approximately 40 nm length and ~8 nm width parallel to the ion beam direction. With increasing the irradiation fluence above 1.0×10^{14} ions/cm^2, the Au RBS peak continues to broaden until its width becomes constant for fluences larger than 5.0×10^{14} ions/cm^2.

3.1.2. Evolution of 30 nm Au NPs

A second set of three identically prepared samples containing 30 nm Au NPs with a areal density of about 2.8×10^9 particles/cm^2 are irradiated with 18, 25, and 54 MeV Ag swift heavy ions. The series (a–c) in **Figure 7** represents the evolution of the Au RBS peak with irradiation fluence at these energies. **Figure 8** shows the change in FWHM with fluence derived from the RBS spectra for the three energies using the 120° detector. From the figure, two facts are deduced similar to the case for 15 nm Au NPs under irradiations with 18 and 25 MeV Ag ions, as follows:

i. Elongation threshold fluences are observed, amounting to about $7.0\text{x}10^{13}$ and $5.0\text{x}10^{13}$ ions/cm^2, respectively.

ii. Saturation in FWHM of the Au RBS peak is reached at fluences $6.0\text{x}10^{14}$ and $5.0\text{x}10^{14}$ ions/cm^2, respectively.

For irradiation with 54 MeV Ag^{+8} ions, the ion-shaping effect starts again without detectable threshold fluence. At the same time, no saturation is visible up to a fluence 2.0×10^{14} ions/cm^2.

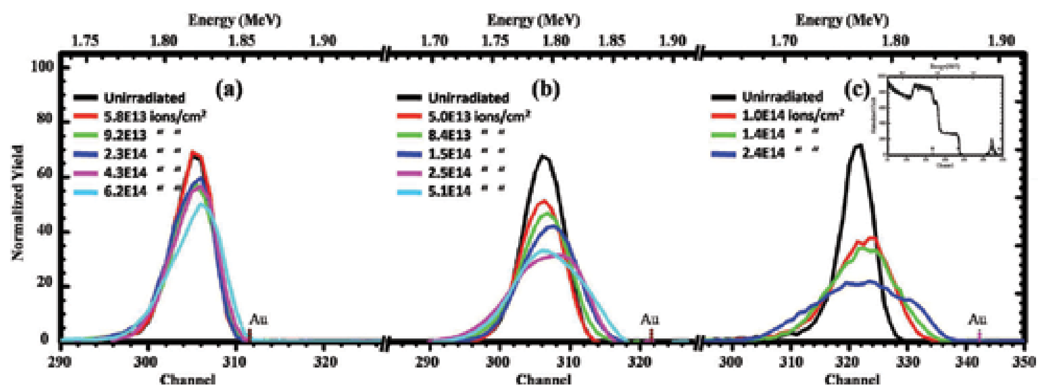

Figure 7. Normalized RBS spectra of 30 nm Au particles under (a) 18 MeV Ag^{+4} ions, (b) 25 MeV Ag^{+5} ions, and (c) 54 MeV Ag^{+8} ions for samples prepared with an average areal density of 2.8×10^9 particles/cm^2.

AFM analysis in **Figure 3** points to a good uniformity of Au NP distribution over the surface and the absence of agglomeration, i.e., clustering of individual NPs. This allows us to investigate the role of interparticle distance on the ion-shaping mechanism. Thus, in the following subsection, we will focus on the elongation phenomenon by varying the initial areal density of the Au NPs.

3.2. Elongation as a function of the initial NP size and initial NP concentration

3.2.1. Evolution of 15 nm Au NPs

Samples containing spherical Au NPs with diameter of 15 nm prepared with areal density between 0.25 and 4×10^{10} particles/cm^2 were irradiated with 54 MeV Ag^{+8} ions. The series

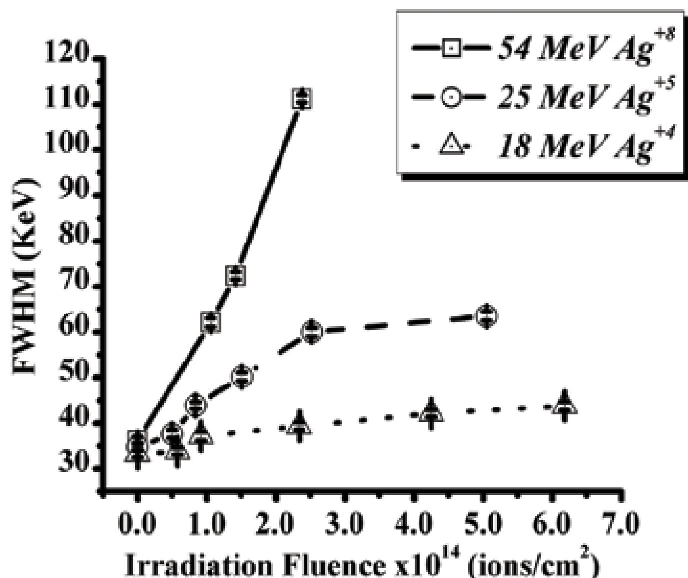

Figure 8. The relative change of Au peak width determined for the 120° scattering angle as a function of fluence for 30 nm Au particles under irradiation with 18 MeV Ag^{+4} ions (triangles and dot line), 25 MeV Ag^{+5} ions (circles and dash line), and 54 MeV Ag^{+8} ions (squares and solid line).

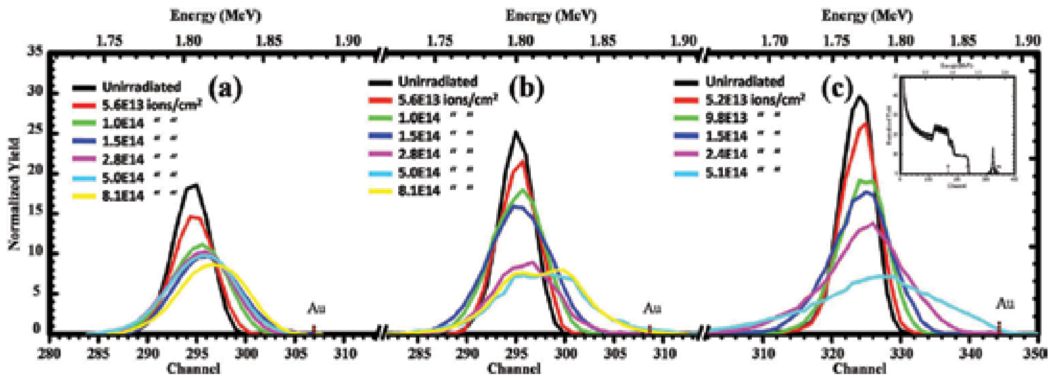

Figure 9. The Au RBS peak of 15 Au NPs for various irradiation fluences of 54 MeV Ag^{+8} ions for different areal densities of 2.5×10^9, 1.4×10^{10}, and 4×10^{10} particles/cm^2, (a), (b), and (c), respectively. Normalized RBS spectra are presented in the inset of plot (c).

(a–c) in **Figure 9** show the 15 nm Au RBS peak for various fluences for NP at areal density of 2.5×10^9, 1.4×10^{10}, and 4×10^{10} particles/cm^2, respectively. **Figure 10** shows the evolution of the FWHM of the RBS Au peak as a function of the fluence, for various values of the areal density. From the inspection of the figure, two regions clearly appear as follows: (i) For low irradiation fluences, the relative broadening of the RBS peak is almost the same for all samples irrespective of their areal density. We define this region as A. (ii) Above a critical fluence of about $1–2 \times 10^{14}$ ions/cm^2, the broadening of the RBS peak becomes significantly a function of the NP areal density. This region is denoted as region B. Apparently, all the curves tend to evolve toward a saturation value. The larger the initial NP areal density, the larger the saturation value of the FWHM appears to be.

We presume that in region A, Au NPs elongate into nanorods conserving their original volume (V_{NR}~V_{NP}). This is confirmed by X-TEM analysis as is shown in **Figure 11a–d**. To understand correlations between NP areal density and/or concentration and the broadening within the Au RBS peak observed in region B in **Figure 10**, we have selected two X-TEM micrographs of extreme NP densities (lower/higher) for comparison. As for the lowest NP density of 2.5×10^9 particles/cm^2, TEM micrographs in **Figure 11a**, **b** which correspond to irradiation fluence of 8.0x10^{14} ions/cm^2 is shown. The X-TEM micrograph in this figure shows aligned Au nanorods with major to minor axes of 100.8 nm. Calculation of the corresponding volume of these nanorods indicates that the volume for each nanorod is about twice the volume of the original pristine NP (V_{NR}~2V_{NP}). Then, we consider the TEM micrographs corresponding to the highest areal density (4×10^{10} particles/cm^2) at a fluence of 5.0×10^{14} ions/cm^2 (see **Figure 11**). These micrographs are given in **Figure 11c–e** and show long nanowires with their major axis varying from 150 to 180 nm and minor axis of 8 nm. It is obvious that these wires are not the result of the deformation of a single particle because their Au content exceeds that of the initial NPs by at least a factor of 5 to 6, i.e., V_{NR}~ (5–6) V_{NP}. We attribute that multiple Au NPs must have contributed to the growth of such nanowires. Seemingly, under swift heavy ion irradiation, some NPs deliver their species by disintegration, and through lateral transport, the disintegrated particles contribute to the growth of other particles. In this way, further lengthened nanostructures will appear in account of shorter ones. The latter hypothesis has been confirmed by X-TEM analysis where we observed smaller aligned particles, likely resulting from the fragmentation of some

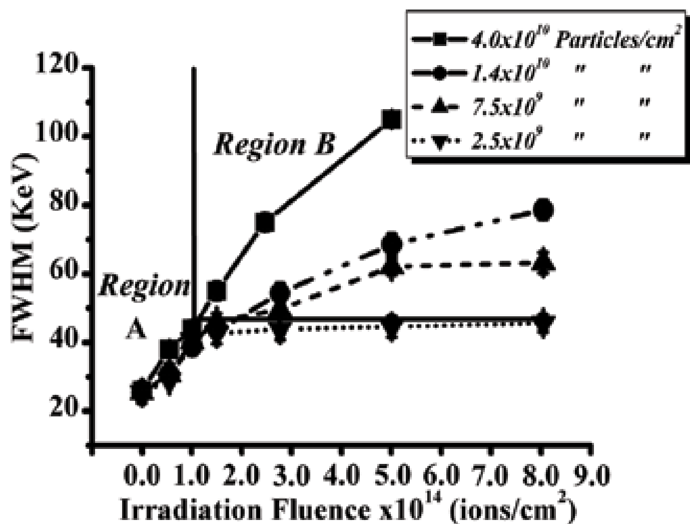

Figure 10. The FWHM of Au RBS peak obtained from the 120° detector as a function of 54 MeV Ag^{+8} irradiation fluence for different areal densities of 15 nm Au particles.

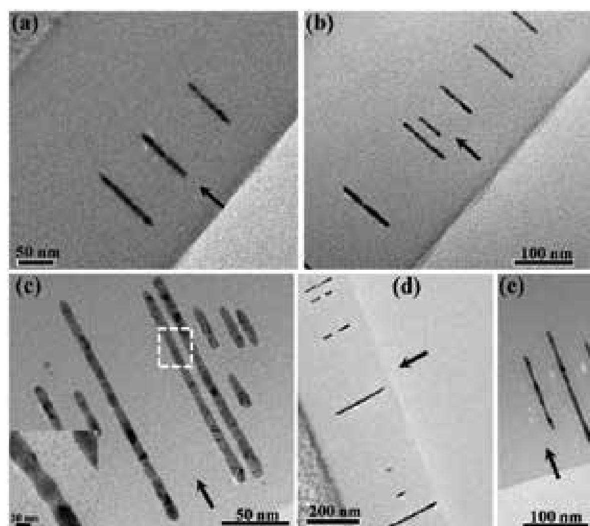

Figure 11. HR-XTEM images of (i) 15 nm Au particles with initial areal density of about 2.5×10^9 particles/cm^2 after irradiation with 54 MeV Ag^{+8} ions to a fluence of 8.1×10^{14} ions/cm^2, (a) and (b), respectively. (ii) 15 nm Au particles with an initial areal density of 4.0×10^{10} particles/cm^2 irradiated with 54 MeV Ag^{+8} ions to a fluence of 5.0×10^{14} ions/cm^2, (c), (d), and (e), respectively. The direction of the ion beam is indicated by the black arrows.

ion-deformed nanorods or nanowires. It emerges that the variation of NP areal density, and the concomitant variation of the interparticle distance, results in a strong variation in the shaping characteristics of the spherical Au NPs. For the areal density larger than 2.5×10^9 particles/cm^2

and above the critical fluence of 1.0 × 10^{14} ions/cm^2, Au NPs start to disintegrate, while others continue to grow by accumulation of atoms and/or fragments from the disintegrating particles. The latter is assumed to occur by means of a process that is well known as Ostwald ripening. Interestingly, in some regions of TEM micrographs, tiny satellite particles surrounding shorter particles were seen (inset of **Figure 11c**). These satellite particles were not visible before irradiation. It is clear that the relative increase in Au peak width of the lowest areal density sample has already attained its maximum value just above the critical fluence. This might imply that there exists a threshold areal density for nanowire formation for 15 nm diameter Au particles, at an areal density of ~5.0 × 10^9 particles/cm^2, under 54 MeV Ag^{+8} ion irradiation. This corresponds to an interparticle distance of about 150 nm. Presumably, the mass transport process is effectively limited by a too large distance between the Au NPs.

3.2.2. *Evolution of 30 nm Au NPs*

Au NPs having an average diameter of about 30 nm and areal density ranging between 0.9 and 3.2 × 10^9 particles/cm^2 were irradiated with 54 MeV Ag^{+8} ions up to a fluence of 5.0 × 10^{14} ions/cm^2. The Au RBS peaks and the evolution of the FWHM of Au peak with the fluence for each NP areal density are shown in **Figure 12a–c** and **Figure 13**, respectively.

Again, we report the existence of two separated regions as in **Figure 10**. At lower irradiation fluences, the Au NP broadening evolves the NP size (region A). However, for fluences larger than a certain value (estimated for this NP size of about 1.0 x 10^{14} ions/cm^2), the broadening in Au NPs in region B evolves the NP areal density. As can be seen in **Figure 14a**, **b**, X-TEM micrographs show Au nanowires of a length of about 150~200 nm and a width of 8 nm aligning as a result from irradiation of the 30 nm Au NPs with areal density of 3.2 × 10^9 particles/cm^2 with 54 MeV Ag^{+8} ions to a fluence of 5.0 x 10^{14} ions/cm^2 (see **Figure 3.5**). From the data in this figure, we deduce a threshold interparticle distance near 250 nm for nanowire formation, i.e., at an areal density of approximately 9.0 x 10^8 particles/cm^2.

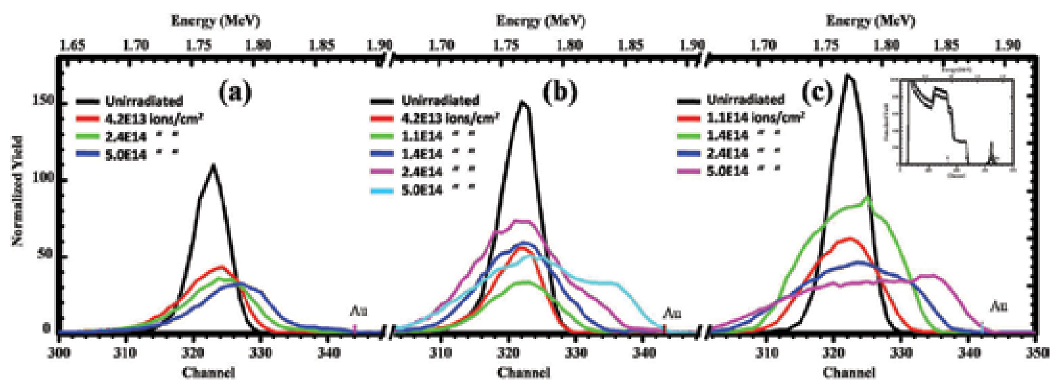

Figure 12. The Au RBS peak of 30 Au NPs for various irradiation fluences of 54 MeV Ag^{+8} ions for different areal densities of 9.0 × 10^8, 2.8 × 10^9, and 3.2 × 10^9 particles/cm^2, (a), (b), and (c), respectively. Normalized RBS spectra are presented in the inset of plot (c).

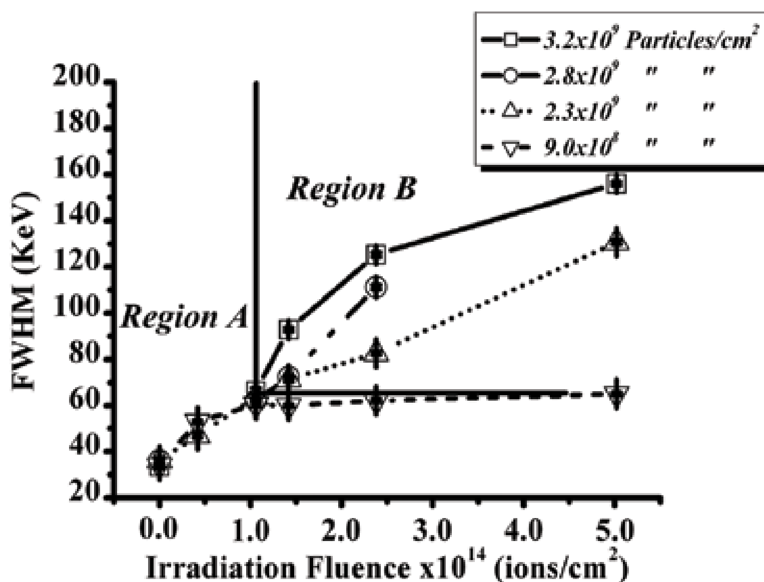

Figure 13. The FWHM of Au RBS peak obtained from only the 120° detector as a function of 54 MeV Ag^{+8} irradiation fluence for different areal densities of 30 nm Au particles.

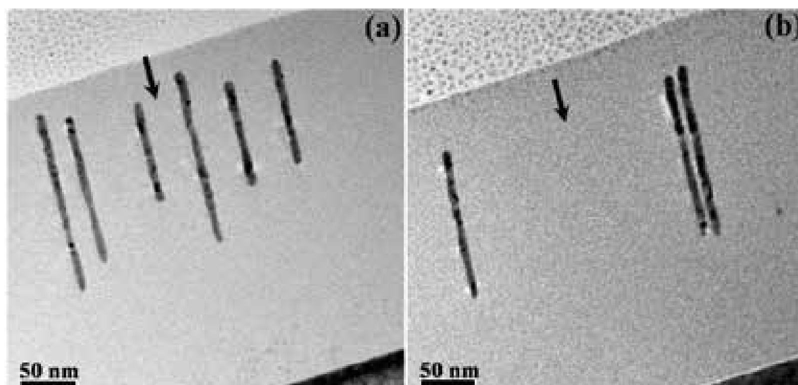

Figure 14. HR-XTEM images of 30 nm Au particles with initial areal density of 3.2×10^9 particles/cm^2 irradiated with 54 MeV Ag^{+8} ions to a fluence of 5.0×10^{14} ions/cm^2, (a) and (b), respectively. The direction of the ion beam is indicated by the black arrows.

4. Discussion

As pointed out in the experimental section, the projected ranges of the ions at the applied energies are far beyond the location of the spherical Au NPs. Thus, the elongation of such metal NPs must be a result of the ion passage through the SiO_2-Au-containing layer.

Systematic investigations of the deformation of NPs in response to swift heavy ion (SHI) irradiation have allowed us to evidence experimentally the existence of a threshold fluence for elongation, Φ_c. The threshold fluence for elongation as a function of ion energy and NP size

for 15–80 nm Au particles is estimated in **Table 3**. The value of Φ_c has been observed to depend on both ion energy and pristine NP size. In particular, Φ_c decreases with increasing electronic stopping power and increases with the NP diameter. However, as suggested by Klaumünzer [18, 19] and successively experimentally shown by Penninkhof et al. [20, 21], irradiation-induced NP elongation is a complicated issue where both the matrix and the characteristics of the confined NPs play an active role. Here, we put forward three possible mechanisms that could be the origin of the existence of a threshold fluence and its variation with NP size and incident ion energy. These mechanisms are listed as followed:

i. Preparation methodology of the samples.

ii. The compaction of the hosting silica matrix under irradiation.

iii. Occurrence of the irradiation-induced stresses within the silica matrix constrained by a substrate.

iv. Following the process at which our samples are prepared, Au NPs are first assembled on top of a thermally grown SiO_2 film and subsequently confined by sputtering of a secondary layer of SiO_2 that is reactively sputtered on top of the first layer. The final configuration of the active region of the samples indicates that Au NPs are embedded in a single plane 200 nm far from the surface of the sample. Chemically, gold is known to have a fairly poor wetting affinity with the SiO_2. Consequently, the mechanism of how precisely the oxide layer is formed around the Au NP during the deposition process is basically unknown. Following the process, our SiO_2 top film is grown at zone 1 at the low adatom mobility growth mode [22] and relatively low ion bombardment energy [23]. Within this sputtering scheme, most likely voids will form near the lower half of the NP in the growing oxide. The latter is attributed due to shadowing effects. On the other hand, during X-TEM analysis, none of the aforementioned voids were imaged. Therefore, it is plausible that a certain compaction of the SiO_2 surrounding the NP is required before the deformation process is activated.

v. It has been mentioned in literature that under irradiation with swift heavy ions at low fluences, the SiO_2 matrix exhibits a compaction of about 3%. At higher irradiation fluences, an anisotropic growth dominates the compaction phase [24–27]. Rearrangement of the SiO_2 ringlike material into smaller compact ring volume leads to densification of the silica matrix [28, 29]. For swift heavy ion irradiation, within each individual cylindrical ion track, the virgin material density is irreversibly modified. Subsequent ion impact within the same region does not produce any further density changes [24]. In this view, the fluence required to achieve

Ion energy	Nanoparticle size (nm)	Threshold fluence (ions/cm^2)
18 MeV Ag^{+4}	15	5×10^{13}
25 MeV Ag^{+5}		3×10^{13}
18 MeV Ag^{+4}	30	7×10^{13}
25 MeV Ag^{+5}		5×10^{13}

Table 3. The threshold fluence for elongation as a function of ion energy and NP size for 15–80 nm Au particles.

the compaction corresponds slightly to a compromise where all incident neighboring tracks exhibit mutual overlap in such way that the perturbed area covers the overall sample surface.

vi. As mentioned in our experimental part, our grown silica film is not free standing films but constrained by underneath silicon substrate. The stress state of a constrained silica film as an effect of the ion irradiation has been intensively studied in literature [25–27]. Two extremely opposite stress situations depending on the irradiation fluence have been reported as follows: (1) under irradiation at low ion fluences, the initially compressive stress turns into a tensile stress. The latter, which is related to the mechanism of compaction, leads to the structure to a higher equilibrium density state. The maximum value for this equilibrium is reached at the end of the matrix densification for fluences up to few 10^{13} ions/cm^2. (2) Under irradiation with fluences larger than 10^{14} ions/cm^2, anisotropic material deformation becomes quiet prominent in the further evolution of the system. The latter effect is associated with the tensile stress reduction and the buildup of a compressive stress for the constrained film.

Considering mechanisms (i) and (ii), we presume that the NP elongation is limited to the accomplishment of the structural transformation of the silica matrix. With the latter in mind, we try to correlate the threshold deformation evolution with the energy of the incident ions. As the end of SiO_2 matrix compaction implies the situation whereas the sample surface becomes entirely covered by the mutually overlapping ion tracks, it is conceivable that the resulting deformation threshold depends on the incident ion track diameter. In that sense, the larger the track radius is, the lower the deformation threshold fluence will be. In literature, a number of experimental and theoretical publications have already reported on the ion track cross sections in SiO_2 matrix [30–33]. In these publications, the track size is calculated from the thermal spike model and already found to correspond to the region that melted in the wake of the passing heavy projectile [34]. In our current results, the applied ion energies of 18, 25, and 54 MeV Ag, the corresponding electronic stopping powers in SiO_2 amount to 5.4, 6.7 and 9.7 keV/nm). The corresponding track diameters for these energies in the silica are approximately 3, 4, and ~5 nm, respectively. The calculated corresponding complete overlap of the ion tracks at the surface of the sample is found at fluences of 2.0×10^{13}, 1.0×10^{13}, 0.7×10^{13}, and 0.5×10^{13} ions/cm^2, respectively.

Putting on mind that (i) the swift heavy ion irradiation follows random statistics and that (ii) the compaction fluence for a silica matrix containing partially wetted metallic NP can be different from that of pure silica film, our calculations account pretty well for the reported reduction of the deformation threshold when the incident ion energy is increased.

In our results, we show that the inertia against NP elongation increases with size. In other words, NPs with larger diameters require higher electronic stopping powers to be deformed. Since the macroscopic stress induced by heavy ion irradiation in planar constrained films can reach larger values (several hundreds of MPa) [26], we presume that that mechanism (iii) can actively participate in deformation process of the embedded Au NPs. The aforementioned scenario of (iii) has already been introduced by Roorda et al. [12] for verification of the shape change of Au NPs confined within a silica shell and suggested to remain solid during the irradiation. However, this indirect mechanism alone is not enough to correlate the observed deformation of embedded solid NPs [18]. The metallic NP must have an active participation in the elongation process. In other words, the elongation process will only take place when

the temperatures of both the metallic NP and the surrounding dielectric matrix exceed their individual melting temperatures [18, 19]. In literature, it has been argued that the melting of metallic NPs with diameters in the range of nearly similar range to our NPs of the current study (6 and 20 nm) cannot be invoked with energy deposition corresponding to the electronic stopping powers in the current work [35]. Particles with relatively larger diameters are not expected to completely melt and virtually are not observed to deform under SHI irradiation, [18, 35, 36]. Awazu et al. [35] report that Au NPs with diameter of about 50 nm are not subject to deform under irradiation with 110 MeV Br ions to a fluence of about 1.0×10^{14} ions/cm^2. For this class of NP size, it is conceivable that a minimum compressive stress is needed to activate the NP deformation. On the other hand, it is necessary to mention that the threshold fluence cannot be directly regarded to the individual track-generated stress [37–39]. This is because the deformation threshold would be only dependable on the electronic stopping. Consequently, macroscopic stress should be invoked to clarify the observations. In this sense, direct correlation between minimum compressive stress and NP size could be established. The larger NP size requires larger (minimum) compressive stress to activate the NP elongation process leading to larger fluence necessary to reach it. The latter hypothesis accounts quiet well for our results for the deformation dependence on initial NP size, ion energy, and irradiation fluence. Furthermore, the variation of the embedded NP areal density has led to identification of two distinct fluence regimes for the NP elongation under swift heavy ion irradiations as follows:

i. For low irradiation fluences, Au NPs deform into ion beam-aligned nanorods. This morphology transformation occurs under volume conservation. In other words, the ion-shaping mechanism is an individual mechanism, where each pristine NP deforms into a single oblate nanorod. As this behavior is observed for all values of the NP areal density, in this first stage which is represented by the region A, the ion-shaping process can be seen as an *individual process* as far as the nanoparticles are concerned.

ii. For irradiation fluences above—somewhat critical threshold—of 1.0 x10^{14} ions/cm^2, RBS analysis indicates that the deformation rate is sensitive to the initial NP areal density. With increasing the NP areal density, the deformation rate increases. In this deformation's secondary stage, high-resolution TEM images show long Au nanowires aligned in direction of the ion beam accompanied by strong signs of Au disintegration and/or fragmentation. As the volume of the longer nanowires visualized is about five to six times the volume of the originally spherical NP, the NP elongation process in this fluence-dependent region necessitates the contribution of several individual nanostructures. Within this fluence region, the elongation process might be identified in terms of a *collective process* where some of already-deformed NPs, or even some of the aligned nanowires, dissolve under the irradiation, while other nanowires continue to grow by integration of the atoms from the dissolving particles. The mechanism behind the driving force identifies which nanowire should dissolve and which nanowire should grow remain unknown. Consequently, there is a need for more detailed experimental and theoretical approach to verify it.

The mechanism governing the growth of Au nanowires most likely involves the diffusion through the silica matrix of the gold solute from the dissolved/fragmented nanoparticles toward the growing ones. The task to identify the physical origin of the driving force for preferred Au diffusion from shorter Au nanorods to longer ones, which causes a kind of Ostwald ripening, is difficult.

Some insights can be obtained from **Figure 11(c)** (the inset) and **Figure 14a**, **b** where small fragments are clearly visualized. In fact, those small fragments were not imaged before irradiation; thus, they must be a product of the ion beam irradiation. The energy deposited within the NP subsystem may have allowed the Au atoms and/or species to dissolve in silica. Upon local fluctuation of the solute concentration, the supersaturation of the solid solution then evolves toward the precipitation of the satellite particle phase. Under swift heavy ion irradiation, these small precipitates become unstable [40], and thus they dissolve by subsequent impinging ions (track by track) through the silica matrix. In other words, the diffusion of such nanostructures is driven by the transient melted region formed in the wake of the impinging ions. Dais et al. [41] report on direct observation of the gold diffusion within the ion track. As this process depends on the amount of the available solute sources, i.e., the NP concentration, the lower their relative distance the shorter the diffusion time and the longer the nanowires, as shown in **Figure 13c**, **d** and **Figure 14a**, **b**. On the other hand, when the NP areal density is low, the particle growth is limited by the too long distance between the metal particles. This effect accounts for the relatively low saturation length observed in the samples having the lowest NP areal density. If metal solute may diffuse only within the thermal spike region, for each ion impact, the lateral diffusion distance will be of the order of magnitude of the track size. In the current study, the calculated ion track radius corresponding to the applied ion energies ranges between 3 and 5 nm. Considering the minimum calculated interparticle distance of NPs of about 50 nm, and assuming that the minimum fluence needed for the sample surface overlap is about 1.0×10^{13} ions/cm^2, approximately ten ion impacts within the region are necessary to diffuse over 50 nm. Therefore, the minimum fluence required for solute metal atoms to diffuse from one particle to the nearest one is about 1.0×10^{14} ions/cm^2. The latter accounts quiet well with the fluence necessary to pass from the individual deformation region (*denoted as A*) to the collective deformation process region (*denoted B*) in our results.

Thus, the possibility to grow Au nanowires under swift heavy ion irradiation requires basically the possibility for original NPs to deform and the availability of short-distance solute sources to achieve an effective mass transport. It seems further required that the particles have a certain nanorod shape before the nanowire region is entered or that, alternatively, a certain fluence is applied to enter this region. For Au NPs larger than 30 nm diameter, the mechanism governing nanowire creation requires greater total energy deposition than the value applied here. We note a tendency that the elongation rate diminishes at a higher nanorod length for a higher areal density. For Au NPs of 15 and 30 nm diameter and with increasing irradiation fluence, the minor axis of the elongated nanorods reaches a saturated width at 8 nm. Much in standing with, Giulian et al. [36] report on the elongation process of Pt NPs with size of about 7 nm diameter in a SiO_2 matrix. In this study, the minor axis of the elongated Pt NPs is found to reach a saturation at an increasing fluence, while the saturation value of the minor axis increases with increasing the incident in energy. The latter is attributed due to the NP confinement within a well-defined molten track radius in the amorphous SiO_2 matrix. On the other hand, Pt NPs with size smaller than 7 nm diameter did not show any sign of deformation but mostly indicate a decrease in size as a result of dissolution. In addition, Au nanocrystals (NCs) [42] with size between 1 and 6 nm diameters further grow in size under SHI irradiation with 100 MeV Au^{+8} ions to fluences of 5×10^{12} and 2×10^{13} ions/cm^2. These Au NCs were produced by implantation of 4×10^{16} ions/cm^2 of the 32 keV Au ion into silica glass. With increasing the irradiation fluence to 1×10^{14} ions/cm^2, the amount of Au nanocrystals retained in the silica matrix dropped to about 20% of its initial value as a result of dissolution. These observations

suggest that smaller NPs have the tendency to fragmentation and/or disintegration. With the latter in minds, a hypothesis could be that when the minor axis of the aligned nanostructures (nanorods and/or nanowires) is reaching a critical value (maybe in the order of about 8 nm), such nanostructures will disintegrate under subsequent direct ion impact. Due to the parallelism of such nanostructures with the ion beam direction, such ion impact does immediately affect the entire nanowire. Besides, a minimum value for the minor axis of the nanorods and/or nanowires implies that these aligned nanostructures can only be further elongated when atoms from the matrix are collected. In additions, the mutual ion impacts determine which nanowires disintegrate and which grow. In this frame, the NP disintegration and growth are treated as a continuous process, extending also in the region of the collective growth (region B). Eventually, and in view of the decreasing density of the nanowires, the rate of disintegration with fluence decreases and so does the rate of elongation until ultimately a saturation length is reached.

5. Conclusion

In this chapter, we have shown that the shape of originally spherical Au NPs embedded in a single plane within a SiO_2 matrix can be modified by swift heavy ion irradiations. Under Ag swift heavy ion irradiation, spherical Au NPs undergo anisotropic deformation into single prolate nanorod with their long axis parallel to the ion beam direction. Systematic experimental investigation has led to the existence of the so-called threshold fluence for deformation. The extent of the latter has been carried out by variation of both NP size and ion energy. In addition, we have shown that the NP size and areal density have a substantial influence on the characteristics of the ion-induced elongation of confined NPs. In that respect, a well-defined size-dependent NP elongation below a certain irradiation fluence (region A) is identified. In this region, all the NPs elongate following *individual elongation process* depending only on NP size. Under irradiation with fluence above a certain critical value of 1.00×10^{14} ions/cm^2, region B at which the deformation is regarded as *collective mechanism* is defined. In this region, longer nanowires are created as a product of several metallic NP contribution to the nanowire growth. Furthermore, in region B, the NP deformation increases with increasing initial NP areal density, i.e., the higher the initial NP areal density is, the longer the nanowires are grown.

Author details

Elmuez A. Dawi

Address all correspondence to: e.dawi@ajman.ac.ae

Ajman University, Ajman, UAE

References

[1] Mayer JW. Ion implantation in semiconductors. Electron Devices Meeting, 1973 International, 1973; Vol. 19. pp. 3-5

[2] Cheam DD, Bergstrom PL. ASC manuscripts. 2008; M/MP-2

[3] Nastasi M, Mayer JW, Hirvonen JK. Ion-Solid Interactions: Fundamentals and Applications. Great Britain: Cambridge University Press; 1996

[4] Klaumünzer S, Schumacher G. Physical Review Letters. 1983;**51**(1987)

[5] Klaumünzer S, Ming-dong H, Schumacher G. Physical Review Letters. 1986;**57**(850)

[6] Benyagoub A, Löffler S, Rammensee M, Klaumünzer S, Saemann-Ischenko G. Nuclear Instruments and Methods in Physics Research Section B. 1992;**65**(228)

[7] van Dillen T, Polman A, Fukarek W, van Blaaderen A. Applied Physics Letters. 2001; **78**(7):910

[8] Toulemonde M, Dufour C, Meftah A, Paumier E. Nuclear Instruments and Methods in Physics Research Section B. 2000;**903**:166-167

[9] Gerardy JM, Ausloos M. Physical Review B. 1982;**25**:420

[10] Penninkhof JJ, Polman A, Sweatlock LA, Maier SA, Atwater HA, Vredenberg AM, Kooi BJ. Applied Physics Letters. 2003;**83**(20):4137

[11] Quinten M, Kreibig U. Applied Optics. 1993;**32**:6173

[12] Roorda S, van Dillen T, Polman A, Graf C, van Blaaderen A, Kooi BJ. Advanced Materials. 2004;**16**:235

[13] Gonella F, Mazzoldi P. Handbook of Nanostructured Materials and Nanotechnology. Vol. 4. San Diego: Academic Press; 2000

[14] Kooij ES, Brouwer EAM, Wormeester H, Poelsema B. Colloids and Surfaces A: Physicochem. Engineering Aspects. 2003;**222**:103

[15] Zhong O, Inniss D, Kjoller K, Elings VB. Surface Science Letters. 1993;**290**:L688

[16] Digital Instruments, Santa Barbara, CA

[17] Ziegler JF, Biersack JP, Ziegler MD. SRIM–A version of the TRIM program, The Stopping and Range of Ions in Matter (2008). Available from: http://www.srim.org

[18] Klaumünzer S, et al. Nuclear Instruments and Methods in Physics Research Section B. 2006;**244**:1

[19] Klaumünzer S, et al. Nuclear Instruments and Methods in Physics Research Section B. 2004;**225**:136

[20] Penninkhof JJ, Graf C, Van Dillen T, Vredenberg AM, Van Blaaderen A, Polman A. Advanced Materials. 2005;**17**:1484

[21] Penninkhof JJ. PhD Thesis. Utrecht University, September, 25th (2006)

[22] Messier R, Venugopal VC, Venul PD. Journal of Vacuum Science and Technology. 2000; **A 18**:1538

[23] van Hattum ED, Palmero A, Arnoldbik WM, Rudolph H, Habraken FHBM. Applied Physical Letters. 2007;**91**:171501

[24] Benyagoub A, Klaumünzer S, Toulemonde M. Nuclear Instruments and Methods in Physics Research Section B. 1998;**146**:449

[25] Snoeks E, Weber T, Cacciato A, Polman A. Applied Physics. 1995;**78**:4723

[26] Brongersma ML, Snoeks E, van Dillen T, Polman A. Journal of Applied Physics. 2000;**88**:59

[27] van Dillen T, Siem MYS, Polman A. Applied Physics Letters. 2004;**85**:389

[28] Primak W. Studies in Radiation Effects in Solids Gordon and Breach. Vol 4. New York; 1975

[29] Devine RAB. Nuclear Instruments and Methods in Physics Research Section B. 1994;**91**:378

[30] Meftah A, Brisard F, Constantini JM, Dooryhee E, Hageali M, Hervieu M, Stoquert JP, Studer F, Toulemonde M. Physical Review B. 1994;**49**:12457

[31] Meftah A, Djebara M, Khalfaoui N, Toulemonde M. Nuclear Instruments and Methods in Physics Research Section B. 1998;**146**:431

[32] Kluth P, Schnohr CS, Sprouster DJ, Byrne AP, Cookson DJ, Ridgway MC. Nuclear Instruments and Methods in Physics Research Section B. 2008;**266**:2994

[33] Rotaru CC. Ph.D. thesis. University of Caen, 2004. Available from: http://tel.archives-ouvertes.fr/tel-00005399

[34] Toulemonde M, Dufour C, Paumier E. Physical Review B. 1992;**46**:14362

[35] Awazu K, Wang X, Fijimaki M, Tominga J. Physical Review B. 2008;**78**:054102

[36] Giulian R, Kluth P, Araujo LL, Sprouster DJ, Byrne AP, Cookson DJ, Ridgway MC. Physical Review B. 2008;**78**:125413

[37] Trinkaus H, Ryazanov AI. Physical Review Letters. 1995;**74**:5072

[38] Trinkaus H. Nuclear Instruments and Methods in Physics Research Section B. 1998;**146**:204

[39] Kluth P, Schnohr CS, Pakarinen OH, Djurabekova F, Sprouster DJ, Giulian R, Ridgway MC, Byrne AP, Trautmann C, Cookson DJ, Nordlund K, Toulemonde M. Physical Review Letters. 2008;**101**:175503

[40] D'Orléans C, Stoquert JP, Estournès C, Grob JJ, Muller D, Guille JL, Richard-Plouet M, Cerruti C, Haas F. Nuclear Instruments and Methods in Physics Research Section B.2004; **216**:372

[41] Dais C, Bolse T, Bolse W, Shubert-Bischoff P, Lindner JNK. Nuclear Instruments and Methods in Physics Research Section B. 2006;**245**:239

[42] Joseph B, Ghatak J, Lenka HP, Kuiri PK, Sahu G, Mishra NC, Mahapatra DP. Nuclear Instruments and Methods in Physics Research Section B. 2007;**256**:659

Chapter 3

Ion Beams for Materials Analysis: Conventional and Advanced Approaches

Vladimir Egorov and Evgeny Egorov

Additional information is available at the end of the chapter

http://dx.doi.org/10.5772/intechopen.76297

Abstract

Ion beam material diagnostic possibilities are discussed. Experimental data of H^+ and He^+ ion beams interaction with material for the energy range 0.8–1.6 MeV are presented. There are described the conventional ion beam analytical complex facility and some peculiarities featured for Sokol-3 IMT RAS one. Common characteristics of ion beam analytical methods are described. Specific attention is focused on the ion beam methods use for real objects investigations. It is shown that these methods are very effective for the light element diagnostics. New technology for the element surface analysis on base of the PIXE method modification by the planar X-ray waveguide-resonator application is elaborated. Attention is drowning to facts that all ion beam experimental methods are nondestructive and the Rutherford backscattering spectrometry is real quantitative analytical procedure.

Keywords: ion beam, ion beam scattering, Rutherford backscattering, RBS, ions stopping, ion acceleration, ion beam channeling, nuclear reactions, particle-induced X-ray emission, PIXE, ion beam-induced luminescence, depth elements profiles, nuclear elastic recoil spectrometry, vacuum systems, target chamber, X-ray fluorescence yield, X-ray detector

1. Introduction

It is well known that the interaction of ion beams—high energy charged particles fluxes with material is accompanied by the complex of specific effects [1]. The interaction with the solid material electron subsystem leads to uniform stopping of high energy charged particles. This interaction is not elastic owing to the atomic ionization effect initiation. Ion collisions with the atomic nuclei can have the elastic as well as inelastic character. Main channels of the interaction are presented in **Figure 1**. These channels can be used for the nondestructive quantitative analysis of studied target element composition and some features of its structure [2]. In result

IntechOpen

© 2018 The Author(s). Licensee IntechOpen. This chapter is distributed under the terms of the Creative Commons Attribution License (http://creativecommons.org/licenses/by/3.0), which permits unrestricted use, distribution, and reproduction in any medium, provided the original work is properly cited.

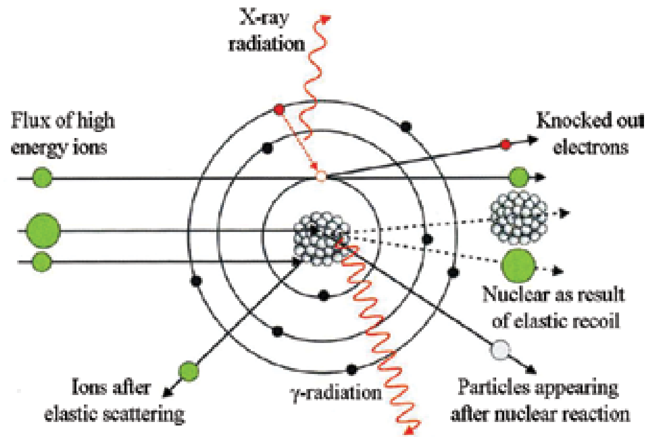

Figure 1. Products of the high energy charged particles interaction with atoms flux.

of the ion beam stopping the material, electron subsystem comes into the excited state. The excited state relaxation can happen by the radiation mechanism through luminescence. The optical luminescence spectra analysis allows to characterize some features of the studied material band structure [3–5]. More high energy relaxation leads to the X-ray characteristic fluorescence irradiation. Collection of X-ray fluorescence spectra is the subject of the particle-induced X-ray emission (PIXE) spectrometry [6–8].

The elastic interaction of high energy ion with atomic nucleus is described by the Rutherford expression, which presents fundamental basis for the Rutherford backscattering (RBS) spectrometry [8–14]. This type of ion-nucleus collision allows to create the nucleus elastic recoil spectrometry [15, 16]. The inelastic ion-nucleus collision leads to the nucleus excitation and the nuclear reaction provoking [17, 18]. Specific peculiarity of the ion-nucleus interaction is the nonRutherford scattering effect [19]. This effect is connected with the increase in time interaction and change in scattering conditions. It must be taken into account to use the proton beam scattering on nuclear of light elements at energy range 0.5–2.0 MeV. In such cases, this effect can be used for the increase in analytical efficiency for the light element diagnostics.

The above enumerated techniques based on interaction of chargedparticles beams with substance are indifferent to the material structure peculiarities. At the same time, experimental investigations showed that the monocrystalline and epitaxial targets study by ion beam analytical methods demonstrate specific deviations from results characteristic for polycrystalline and amorphous ones. The monocrystalline structure is characterized by long-range open spaces through the ionsthat can propagate without significant scattering and diminished stopping. Ions can spread to these open channels by glancing collisions with the atoms rows or planes, hereby extending the final ion distribution deeper into target. This effect was called the ion beam channeling, which can be the axial or planar one [20, 21]. The axial channeling of ion beam is visualized in**Figure 2**. The channeling effect can be used to the trace impurities diagnostics in single crystal and epitaxial targets, the structure defects analysis and for the position determination of impurity atom in the structure. Moreover, this method can allow to define the relative angular orientation of the unit cells axis within the layers of multilayer

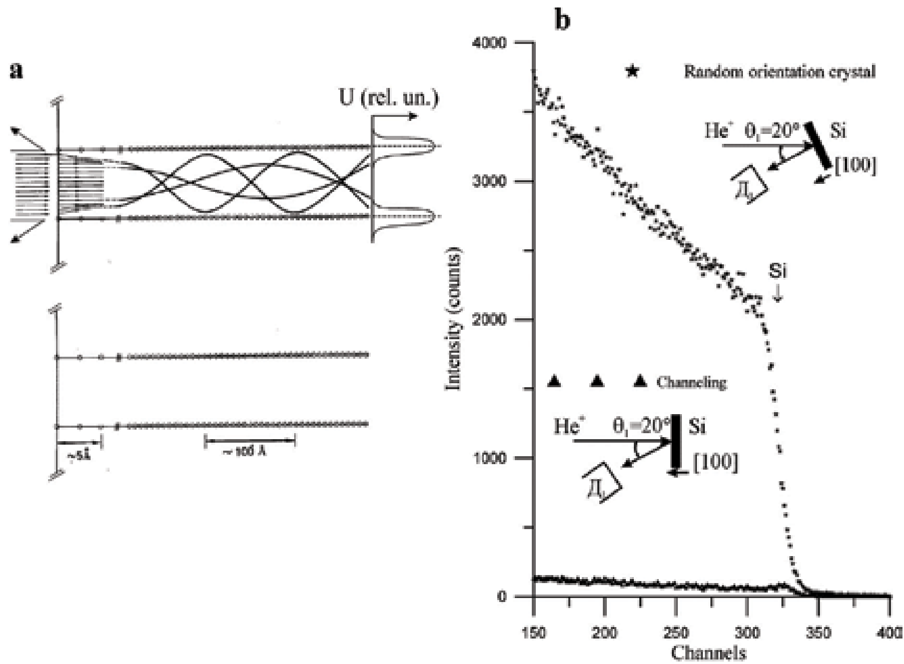

Figure 2. The model of He^+ ions flux axial channeling through Si monocrystal along [100] crystallographic axis (a) and RBS spectra He^+ ions flux for Si crystal in random position about the ion beam propagation direction and in conditions of the ion beam channeling along [100] its axis (b).

heterostructures [22]. The ion beam channeling is accompanied by the excitation processes efficiency reduction connected with inner atomic electrons of the target. X-ray fluorescence yield intensity excited by high energy beams comes down. At the same time, the intensity of ionoluminescence increases. In the ion beam channeling conditions, the nuclear reaction efficiency and probability of the nuclear recoil effect reduce to a minimum.

Ion beam experimental methods of the material diagnostics are realized by use of ion beams analytical complexes Sokol-3. This complex is in our disposal and will be shortly described in the next section.

2. Experimental setup for ion beam measurements

Common arrangement of the Sokol-3 units is presented in **Figure 3**. The Van de Graaff electrostatic generator, which can generate H^+ and He^+ ion fluxes in the energy range 0.05–2.0 MeV with energy dispersion $\Delta E = 0.1/0.3$ keV, is the most important device of the ion beam analytical complex. The generator allows to vary of the ion beam current magnitude from 0.1 to 50,000 nA (from $6 \cdot \times 10^8$ to $3 \cdot \times 10^{13}$ ions/s) in the beam spot on studied target with diameter 0.1–5 mm. The ion beam current magnitude stability is 3–5%. The analytical complex is equipped by the vacuum system with total volume near 1 m^3. The clean vacuum environment in ion guides and experimental chambers is provided by turbomolecular and magnetic-discharge pumps

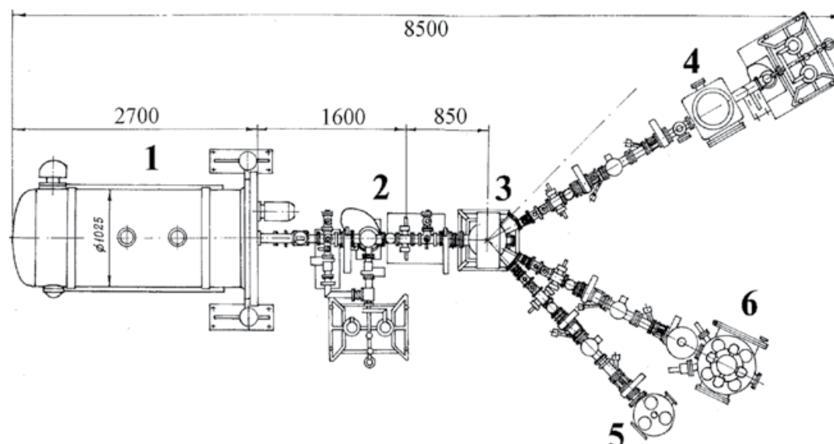

Figure 3. Units arrangement of Sokol-3 ion beam analytical complex facility. 1. Van de Graaff accelerator ESU-2; 2. Vaccum ion guide; 3.Analytical electromagnet; 4.RBS chamber; 5.Chamber for nuclear recoil spectrometry; 6.Chamber for PIXE and ionoluminiscence measurements.

working in a pair with additional use the liquid nitrogen freezing out. In the result, the medium residual pressure in the vacuum system is usually near 1×10^{-6} torr (7×10^{-4} Pa). At the same time, experimental investigations in the complex chambers are accompanied by C-H film appearing in the ion beam spot. It is connected with great number of the vacuum joints with rubber-like gaskets. Any ion beam analytical complex must be provided by the analytical magnet for the ion beams turning into experimental chambers. Our analytical complex is equipped by three experimental chambers for the RBS, nuclear reaction, and channeling measurements, for the registration of the nuclear recoil effects and for the PIXE and ionoluminescence spectrometry. The Rutherford backscattering is characterized by the original system of the studied target scattered ions registration. It has two detectors for the ions fluxes parallel registration on angles $\theta_1 = 167°$ and $\theta_2 = 125°$ to the initial direction of ion beam propagation as shown in **Figure 4**. Furthermore, the figure presents experimental and theoretical RBS spectra of He^+ions for Nb/Si target obtained for the angles pointed above. It is very important that two independent RBS spectra represent the target element distribution. The spectra approximation carried out by RUMPP computer program built on base of the RUMP software modification [23] allowed to obtained the target depth element concentration profile. The depth element profile of this target is very simple and the double detector registration system application in this case has an excessive character. But the approximation of two RBS spectra allowed to increase precision of the Nb thin film thickness. Application of two detector systems for RBS investigations and for registration of the nuclear reaction products allows to avoid possible errors at the experimental data interpretation.

We used the original construction for the PIXE measurements modification. **Figure 5a** presents chamber for conventional PIXE measurements execution. The conventional PIXE spectrometry allows to characterize the volume element composition of studied target. The method modification by application of the planar X-ray waveguide-resonator (PXWR) presents possibilities of the target surface element composition study [24]. **Figure 5b** shows the measurement scheme dedicated for the surface element study. PXWR can transport X-ray

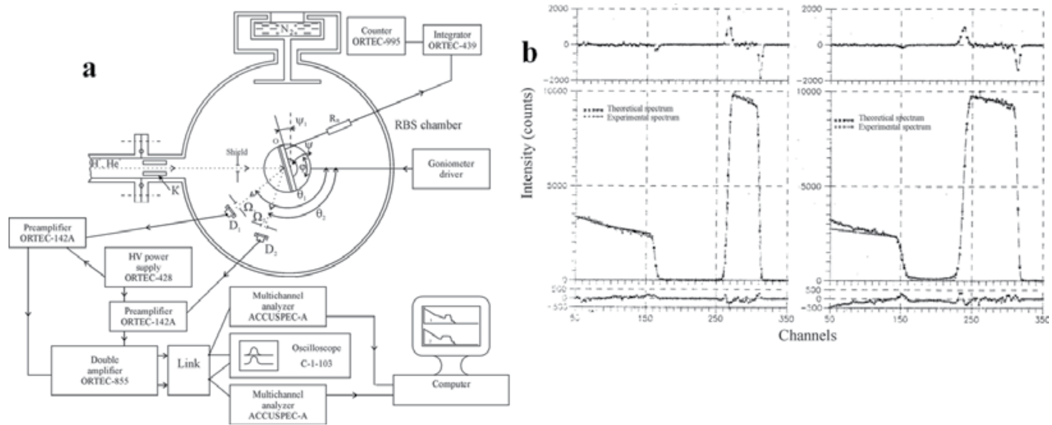

Figure 4. Schematic design of RBS chamber of Sokol-3 analytical complex equipped by two charge particle detectors (a) and pattern of application for study of Nb thin film with thickness t=135.20.7 nm on Si substrate (b).

quasimonochromatic radiation according to the waveguide-resonance mechanism of radiation flux propagation [25]. The waveguide-resonator showed in **Figure 5b** is formed by the Be polished reflector and surface of the studied target. The distance between Be reflector and target surface is equal 0.15 μm. Be reflector has the hole for the exciting ion beam propagation to the target. The extended slit clearance formed by Be reflector and target surface captures radiation from the target X-ray fluorescence yield corresponding to the surface atoms fluorescence yield and transports it into SDD X-ray detector. Similar measurement geometry for the surface elements diagnostics at ion beam excitation presents

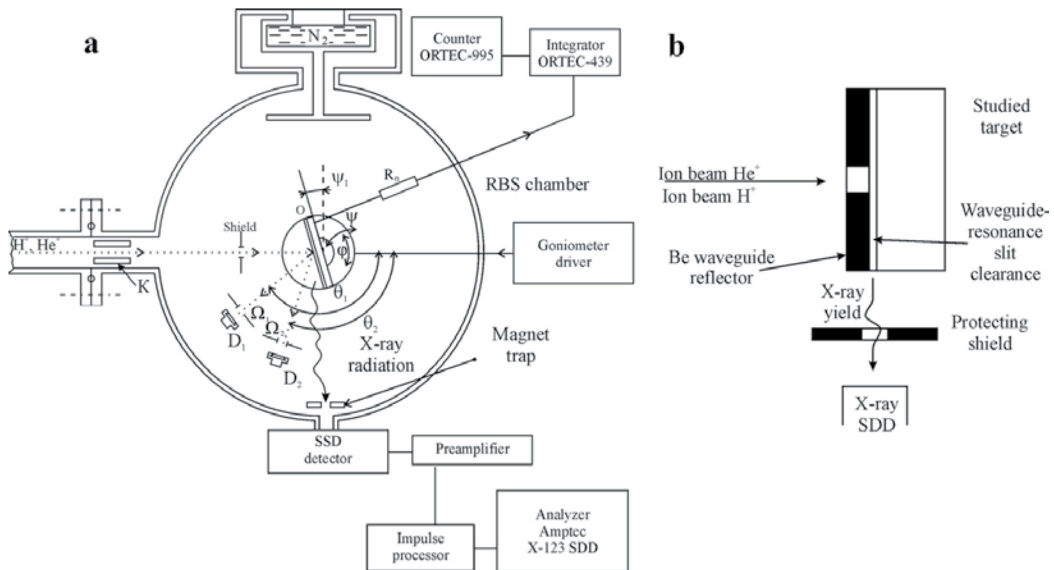

Figure 5. Experimental chamber for the PIXE conventional measurements (a) and scheme of the modifies PIXE one allowed to study of the surface element composition (b).

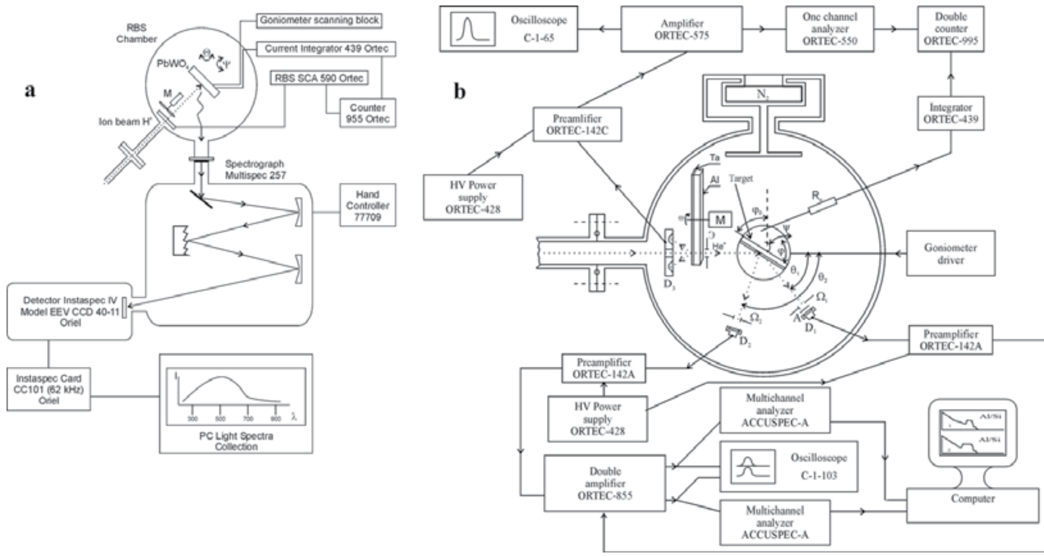

Figure 6. Schemes of experimental setups for yield registration of the light luminescence from the studied target at ion beam excitation (a) and for the target parallel investigation by RBS and the elastic nuclear recoil methods (b).

new experimental method, which was named as the total X-ray reflection fluorescence at particle excitation (TXRF PE).

Figure 6 shows the experimental chamber arrangement for the ionoluminescence and the nuclear recoil spectrometry. These investigation methods are realized in frame of the Sokol-3 facility in conventional arrangement.

Experimental investigations of the ion beam channeling can be executed in any chambers of the analytical complex. But most part of these experiments is carried out by using the RBS chamber.

3. Rutherford backscattering spectrometry as the basic method of material ion beam diagnostics

3.1. Common principles of the method

The Rutherford backscattering conception is based on possibility of the energy losses direct calculation for ion beams interacting with electron and atomic nuclear material subsystems. The energy redistribution in the ion-nucleus collision is defined by the kinematical factor expression [10]:

$$E_1 = E_0 \left[\frac{\sqrt{M_2^2 - M_1^2 \sin^2\theta} + M_1 \cos\theta}{M_1 + M_2} \right] \tag{1}$$

where E_0 and E_1 are energies of ion pre- and post-collision, M_1 and $M_2$are masses of ion and nucleus accordingly and θ is the angle of ion deviation from its initial propagation direction.

There is discussed the "backscattering" situation because the kinematical factor maximum magnitude is obtained for θ near 180°. In this case, we have the best mass resolution.

Probability of the ion-nucleus collision is defined by the Rutherford famous formula in form of the scattering average differential cross-section σ, which can be presented in the laboratory coordinates system by the next expression [8]:

$$\sigma = \frac{Z_1 Z_2 e^2}{2E} \frac{\sqrt{1 - x^2 \sin^2\theta} + \cos\theta}{\sin^4\theta\sqrt{1 - x^2\sin^2\theta}} \tag{2}$$

where x is M_1/M_2 relation, Z_1 and Z_2 are changes of ion and nucleus, e is the electron charge and E is the ion pre-collision energy. The charge particle detector registers the total particles quantity A_i, which defines by the collision cross-section, the total quantity of charged particles interacted with the studied target q, the detector spatial angle Ω, the volume atomic concentration N_i and the layer thickness t connected with the RBS spectrum discreteness degree and can be presented by the expression [8]:

$$A_i = q\Omega\sigma N_i t \tag{3}$$

Total Rutherford backscattering spectrum presents aggregate of similar magnitudes outlined in the diagrammatic form. Sample of this similar diagram is shown in **Figure 7**. RBS spectra of He^+ and H^+ ion beams obtained for the $SrTiO_3$ stoichiometric target are presented. These spectra are diagrams reflecting dependences of the ion beams scattering yield on the energy of scattering particles. Every channel of the diagrams reflects the ions number scattering on nuclei the target atoms (Eq. (3)). An energy scales of the spectra are connected with the depth

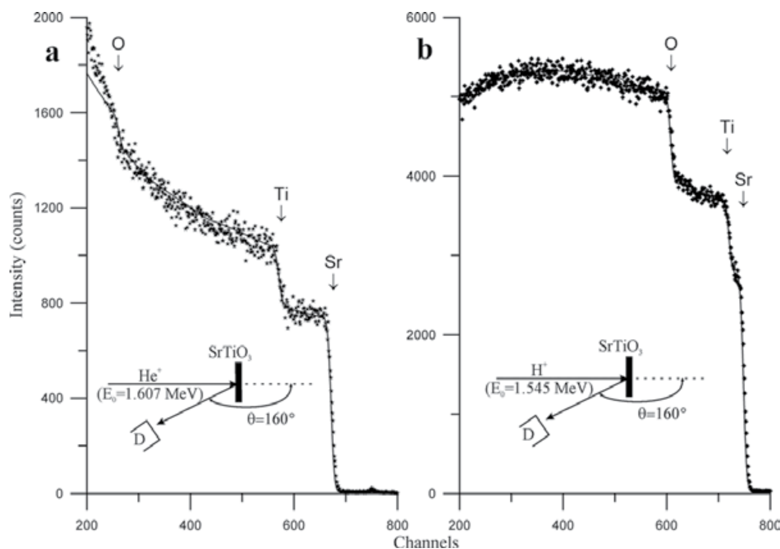

Figure 7. RBS spectra of He^+ (a) and H^+(b)ion beams obtained for the $SrTiO_3$ stoichiometric target. Experimental spectra are approximated by RUMPP program and the theoretical spectra are superposed with experimental ones. The arrows designate the scattering energies corresponding to atoms on the target surface. The measurement geometry is shown on the inserts. The energy step is 1.9 keV/channel.

elements distribution profile for the studied target. The scattering energy for surface atoms is defined by the kinematical factor, only. These energies are connected to steps edges of the diagrams. The scattering description of ion beams on nuclei of the internal atoms demands taking into account the ions stopping as pre- and post-scattering act. The stopping energy losses ΔE on the distance Δx are usually described by the Bohr formula:

$$-\frac{\Delta E}{\Delta x}=\frac{4\pi Z_1^2 e^4 n}{mv^2}\ln\frac{2mv^2}{I} \tag{4}$$

where Z_1 and v are the charge and velocity of the stopping ion, e and m are the charge and mass of electron and n is the studied material electron density. I is the ion average energy loss for the electron excitation (near 30 eV). I and n parameters are not constants and depend from very much factors. As a result, the decision was made to present the stopping losses in the tabular form [26]. This approach allowed to calculate the energy losses by introduction of the $[\overline{\varepsilon}]$ effective stopping cross-section accordingly to the expression [27].

$$\Delta E = [\overline{\varepsilon}]Nt \tag{5}$$

where N is the atomic density (atoms/cm^3). In case of the multielement material, the stopping cross-section is defined accordingly to the Bragg rule:

$$\varepsilon^{AmBn} = m\varepsilon^A + n\varepsilon^B \tag{6}$$

Accuracy of tabular magnitudes for the material stopping cross-section is limited by value near 1%. In the result, the material parameters determination accuracy cannot be better of this value. In the practical work, the stopping cross-section data are fed into a computer program providing the RBS spectra approximation [23, 27]. As a result, we have that every channel of the spectrum is connected with a planar layer of the target with thickness t and average element concentration N. The rise steepness of steps in the RBS spectrum is defined by the detector energy resolution used for the spectrum registration. The resolution of He^+ ions scattering fluxes is near 10 keV thatcorresponds to the depth resolution 10–12 nm at the ion beam vertical incidence on the studied target and up to 2 nm at the sliding incidence.

The Rutherford backscattering spectrometry is very effective method of the thin film structure analysis. **Figure 8** demonstrates experimental and theoretical spectra of RBS He^+ ion beam for $SrTiO_3$ thin film on the silicon substrate with oxidizing layer. The experimental spectrum theoretical approximation showed that the film is characterized by the stoichiometric composition with thickness t = 230 nm. Theoretical approximation of the spectrum did not involve some difficulties, because the film material contained elements with high atomic masses, and substrate, on the contrary, contained light elements. Similar situation can be observed in **Figure 9**. It demonstrates experimental and theoretical RBS of He^+ and H^+ ion beams spectra for the Hf/Cr/Al multilayer target. Theoretical approximation of these spectra showed that the Hf film had thickness t = 120 ± 5 nm and contained 11% of Sr atoms and 14% of Ti atoms. Cr film had not admixture. It was characterized by the thickness t = 40 ± 7 nm. Interdiffusion zone between these films had the thickness near 25 nm. The surface roughness of the coating was

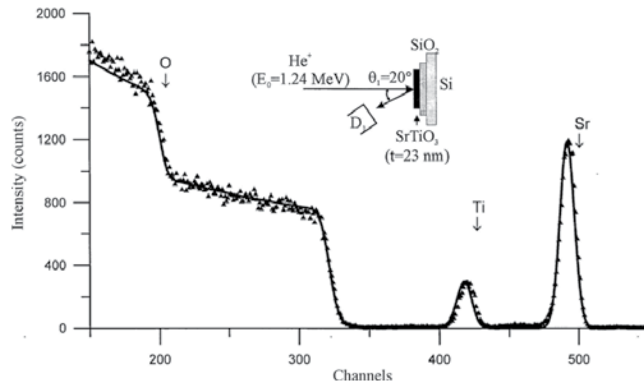

Figure 8. Experimental and theoretical RBS He^+ ions (E_0 = 1.24 MeV) spectra for the $SrTiO_3/SiO_2/Si$ thin film structure. Arrows show the ion scattering energies on nuclei of atoms located on the target surface. Measurement geometry is shown on insert. Energy step 1.9 keV/channel.

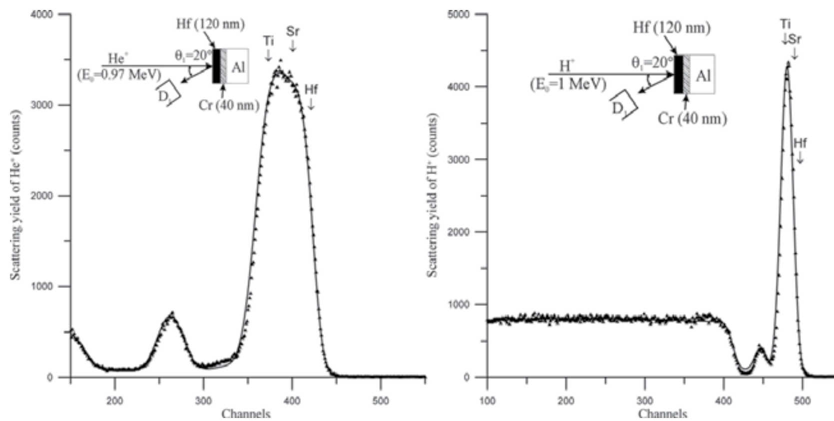

Figure 9. Experimental and theoretical RBS He^+ and H^+ ions spectra for the Hf/Cr/Al multilayer target. Arrows show the ion scattering energy on nuclei of atoms located on the target surface. Measurement geometry is shown on inserts. Energy step 1.9 keV/channel.

near 20 nm. Last parameter was evaluated on base of the steepness evaluation of step increasing for Hf(Sr, Ti) partial spectrum in comparison with this parameter for the Nb/Si standard target with roughness smaller 5 nm. The surface roughness Δr can be evaluated by the next expression [10]:

$$\Delta r = \frac{\sqrt{\Delta E_{\mathrm{exp}}^2 - \Delta E_d^2}}{N_t[\overline{\varepsilon}]} \tag{7}$$

where ΔE_{exp} is the half width of the curve obtained as a result of the step rise steepness differentiation, ΔE_d is the detector energy resolution, N_t is the target atomic density and $[\overline{\varepsilon}]$ is the average value of the target atomic cross-section. Comparison of the RBS spectra obtained

for the same object shows that the He^+ ion beam application allows to have the better resolution and the H^+ ion beam use takes possibilities to test object on the more depth.

3.2. Possibilities of the RBS elements diagnostics

The RBS investigations of target with the heavy elements high content have evident problems. **Figure 10** presents RBS H^+ and He^+ ions beam spectra for the $W_{0.45}C_{0.43}C_{0.12}$ target characterized by the tungsten atoms high concentration. The scattering cross-section of ions on the W nuclei is higher in comparison with these parameters for C and Co atomic nuclei. The alloy target composition had been gained in the result of the four spectra joint approximation obtained for He^+ and H^+ ion scattering beams collected for $\theta_1 = 167°$ and $\theta_2 = 125°$. The nonRutherford scattering effect was taken into account in the calculation. Owing to the necessity of this effect inclusion, specific investigation were executed [18, 19]. Sample of similar investigations of $^{12}C^6$ nucleus nonRutherford scattering factor is presented in **Figure 11**. Comparison of the Rutherford scattering cross-section and magnitudes of this parameter obtained in the experiments shows a great difference especially for the energy E = 1735 keV. The nonRutherford scattering factor value depends on the registration angle, and it is a need to get the factor experimental data for the selected measurement conditions. Similar work of the nonRutherford factor determination for carbon and boron atoms was executed preparatory to approximate RBS spectrum presented in **Figure 12**. The approximation of this spectrum is not simple procedure. Chief problem of the approximation is connected with the nonRutherford factors energy variation for carbon and boron atoms. The approximation result is presented in the table. Total thickness of the coating is 1.75 μm. Including the second RBS spectrum into approximation procedure does not improve the final result because this procedure demands additional investigations for receiving the nonRutherford factors energy dependences for the additional scattering angle. At the same time, the nonRutherford factor can be very useful for the

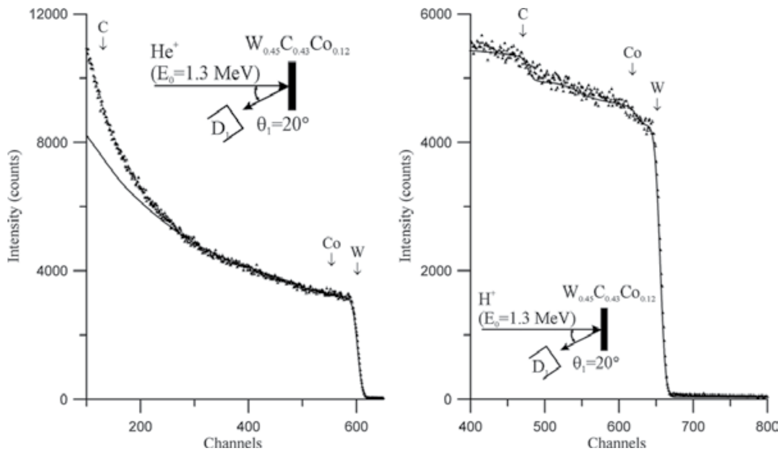

Figure 10. Experimental and theoretical RBS He^+ and H^+ ions spectra for the $W_{0.45}C_{0.43}Co_{0.12}$ high temperature alloy. Arrows show the ion scattering energies on nuclei of atoms located on the target surface. Measurement geometry is shown on inserts. Energy step 1.9 keV/channel.

http://dx.doi.org/10.5772/intechopen.76297

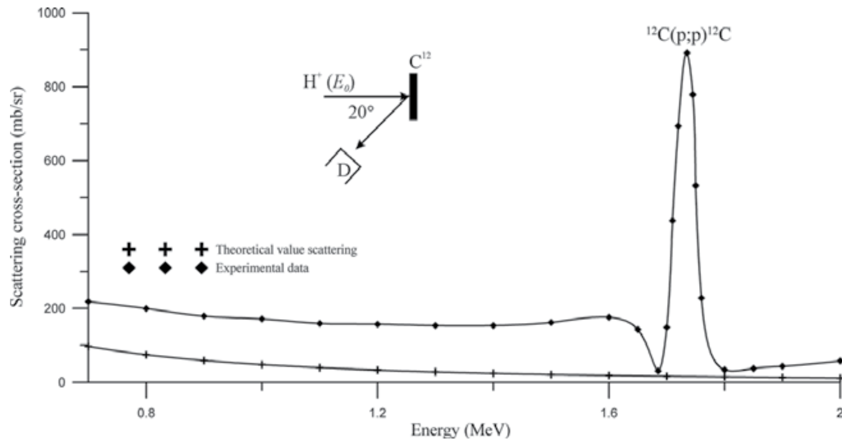

Figure 11. Theoretical and experimental energy dependences of H^+ ion beam scattering cross-section on ^{12}C nuclei for the collection angle θ = 167°.

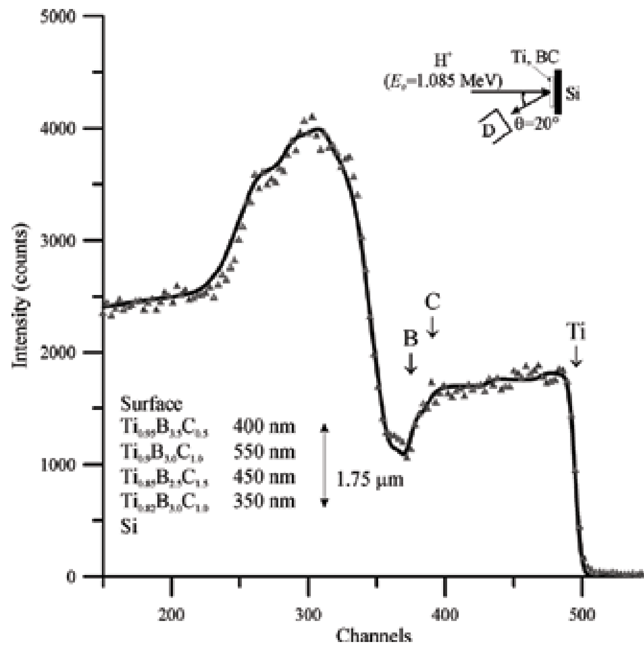

Figure 12. Experimental and theoretical RBS H^+ ions (E_0 = 1.085 MeV) spectra for Ti-B-C film deposited on Si substrate in result of the Ti_2CB_{10} sample magnetron sputtering (a) and table with the approximation results. Arrows show the ion scattering energies on nuclei of atoms located on the target surface. Measurement geometry is shown on insert. Energy step 1.9 keV/channel.

targets study containing light element. As the sample, RBS spectra of the polished beryllium disk are presented in **Figure 13**. The spectrum of the He^+ ions scattering in selected energy range does not distort by the nonRutherford factor. It shows that the target possesses the surface oxide film

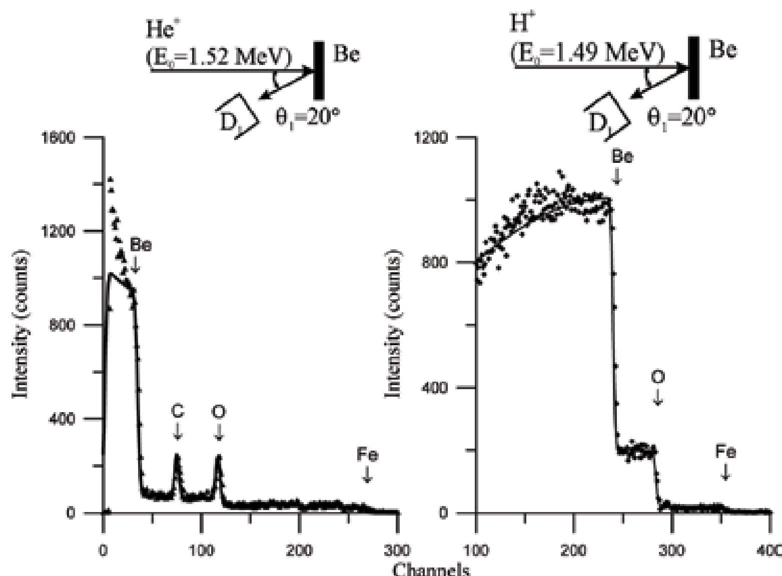

Figure 13. Experimental and theoretical RBS He^+ and H^+ ions for the polished Be disk. Arrows show the ion scattering energies on nuclei of atoms located on the target surface. Measurement geometry is shown on inserts. Energy step 3.8 keV/channel.

with thickness near 10 nm and the carbon hydrogen snuff with similar thickness appearing in result of the ion bombardment. The beryllium material contains 5% of the oxygen atoms, 0.1% of the iron atoms and 0.002% of the tungsten atoms. RBS spectrum of H^+ ions confirms these results. But its approximation is more difficult and it does not show the oxide film on the disk surface. At the same time, its registration time is more short in comparison with the He^+ spectrum collection.

Be polished disks can serve beautiful substrates for study of the solution dry residues and structures prepared by the specific procedure. Sample of the similar investigation is presented in **Figure 14**. This target is studied by RBS method and by application of the elastic nuclear recoil spectrometry. The main element composition of the petroleum film is $H_{0.07}C_{0.90}S_{0.028}N_{0.002}$. The film admixture composition defined by PIXE method will be discussed below. RBS spectrometry can be used for the medical preparation element diagnostics. **Figure 15** shows experimental and theoretical of RBS spectra for the solution dry residue of pantocrine in form of the film on Be substrate. The element composition knowledge is not chief problem for the pharmacology, but RBS, PIXE and nuclear reaction analysis can help for the specific element diagnostics of medical preparations.

Figure 16 shows experimental and theoretical RBS spectra for the graphene oxide film deposited on the Be substrate in the hydrothermal conditions. The technology of the grapheme oxide preparation is not perfect. As a result, the film contains Na and Ca atoms in the macro concentration. At the same time, RBS measurements allow to control the admixtures macro concentration presence and the film constitution. RBS method is useful for the target study containing other light element. **Figure 17** presents experimental and theoretical RBS He^+ and H^+ ions spectra for the hexagonal BN target. Mathematical approximation of the spectra shows

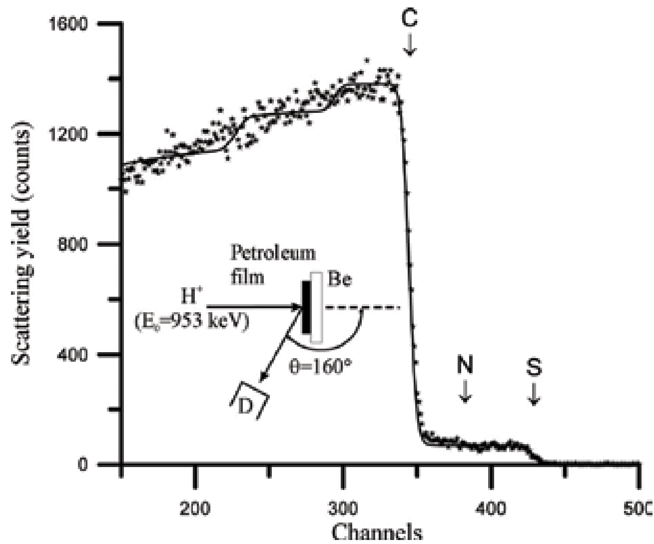

Figure 14. Experimental and theoretical RBS H^+ ions (E_0= 0.953 MeV) spectra characterizing the petroleum film on Be substrate. Film composition is $H_{0.07}C_{0.9}S_{0.028}N_{0.002}$ (on mains elements). Arrows show the ion scattering energies on nuclei of atoms located on the film surface. Measurement geometry is shown on insert. Energy step 1.9 keV/channel.

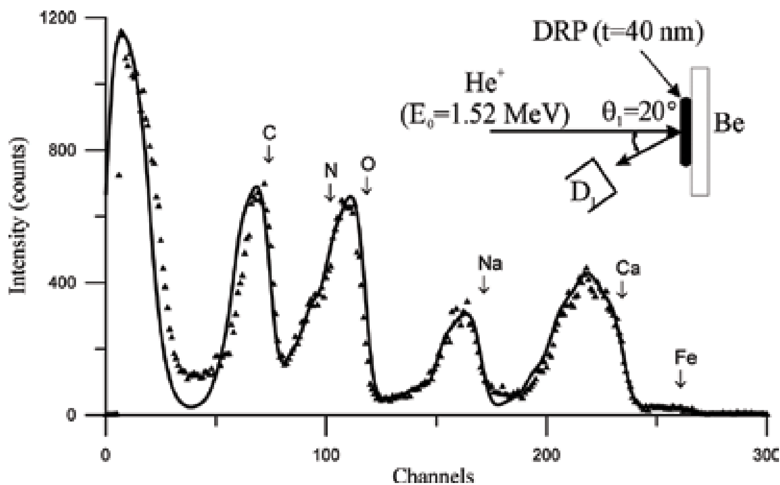

Figure 15. Experimental and theoretical RBS He^+ (E_0 = 1.52 MeV) ions spectra for the dry residue of pantocrine (DRP) aqueous solution on Be substrate. Arrows show the ion scattering energies on nuclei of atoms located on the dry residue film surface. Measurement geometrics and the pantocrine element compositions are presented on inserts. Energy step 3.8 keV/channel.

that the surface layer of the target has the boron increasing concentration. The spectrum of H^+ ions scattering showed that the scattering process is accompanied by the $^{11}B(p,\alpha)^8Be$ nuclear reaction course. The approximation has some problem in the context of $^{10}B^5$ and $^{11}B^5$ boron two isotopes existence in comparison concentrations. Every isotope is characterized by its own

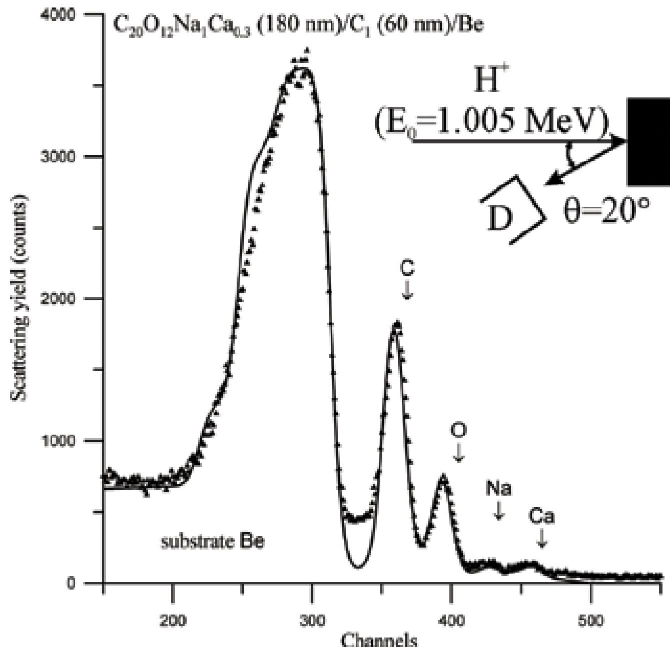

Figure 16. Experimental and theoretical RBS H^+ (E_0 = 1.005 MeV) spectra for the graphene oxide film deposited on the beryllium substrate in hydrothermal conditions. Arrows show the ion scattering energies on nuclei of atoms located on the film surface. Measurement geometries and the film parameters are presented on insert. Energy step 1.9 keV/channel.

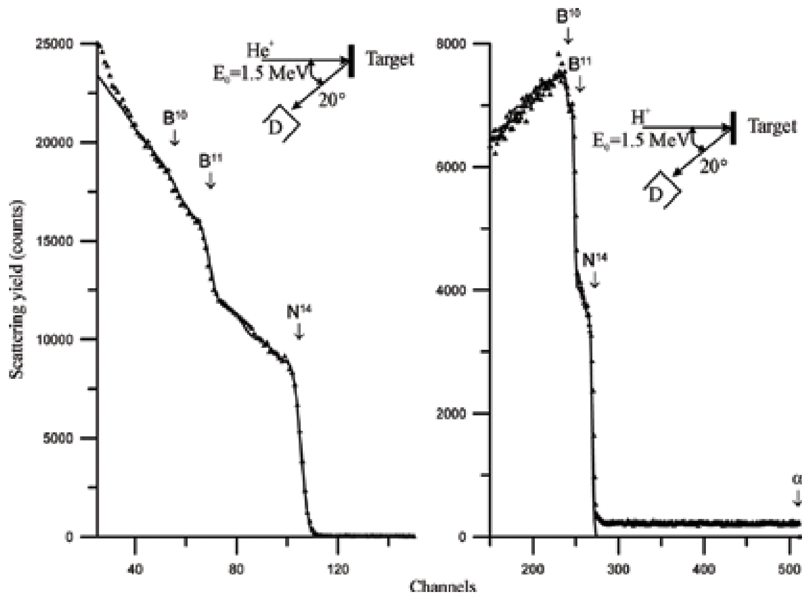

Figure 17. Experimental and theoretical RBS He^+ and H^+ ions (E_0 = 1.5 MeV) spectra for the Boron-Nitrogen target prepared by chemical exfoliation method in form of the free plate. Arrows show the ion scattering energies on nuclei of atoms located on the plate surface. Measurement geometry is shown on insert. Energy step 3.8 keV/channel.

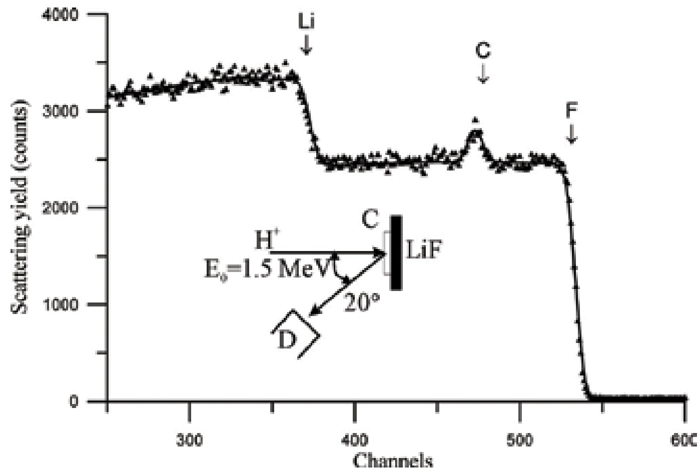

Figure 18. Experimental and theoretical RBS H^+ions spectra for the LiF natural specimen. Surface carbon film with thickness t = 12 nm appeared during of the measurements process. Arrows show the ion scattering energies on nuclei of atoms located on the target surface. Measurement geometry is shown on insert. Energy step 1.9 keV/channel.

nonRutherford factors for the proton beam scattering. The nuclear reaction existence can be used for the boron concentration diagnostics in materials.

The Rutherford spectrometry can help to analyze the lithium atoms presence in materials. **Figure 18** shows RBS spectrum for the LiF stoichiometric target. This approximation required the nonRutherford data collection in the selected energy range for the H^+ ion beam scattering on Li and F atomic nuclei. But owing to the nonRutherford factor for Li, N, O and F atomic nuclei is not great the diagnostic of its atoms in targets with high concentration of heavy atoms presents some difficulties (see **Figure 10**). PIXE and ion beam channeling methods can help in this problem solution.

3.3. Atomic diffusion study by RBS method

Study of atomic diffusion peculiarities in solid material is the main branch of the solid state physics [28]. The wide use of thin material films has direct relation to study the material transport in thin films and coatings, since the density of short-circuit diffusion paths, especially grain boundaries (GBs) in its compositions is higher as compared with massive materials [29]. In our work, we used RBS spectrometry possibilities for the interdiffusion study in the Au/Cu bimetallic structure. **Figure 19** presents RBS He^+ spectra of the bimetallic structure pre and post treatment used different thermal actions [30]. At the long thermo treatment, the main interdiffusion mechanism was connected with the bulk diffusion (**Figure 19a**). In this case, the Au/Cu interface disappears and the intermediate layer arises. In case of the short high temperature treatment, we can see the copper atoms on the target surface, and Au atom from the initial interface dissolves in the Cu film. As a result, it is possible to obtain bulk and GB diffusion factors for different bimetallic combinations and to evaluate magnitudes of the possible segregation effect [31]. Particular significance for the diffusion practice can have the element isotopic investigation with the nuclear reaction application.

Figure 19. Experimental and theoretical RBS He^{+}ions spectra for the Au/Cu bimetallic structure pre and post-treatment of the thermal action. The long time treatment at T = 493 K during 2400 sec of Au (44 nm)/Cu (190 nm) led to bulk interatomic diffusion (a). The short time treatment at T = 523 K during 300 sec showed the grain boundary diffusion, only. Second case is illustrated the table of the depth element distribution. Energy step 3.8 keV/channel.

3.4. Special features of the material density analysis

The material atomic density is a principle parameter of the substance condenses state. This parameter magnitude is usually defined by direct measurement of the subject mass and volume. But this method is not suitable for the material density determination of thin film structures. The Rutherford backscattering method can help to solve this problem. The atomic density distinction must lead to variation of the RBS yield intensity. **Figure 20** shows that the

Figure 20. Experimental RBS H^{+} ions (E_0 = 1.557 MeV) spectra for diamond (ρ = 3.52 g/cm^3) and glassy carbon (ρ = 2.21 g/cm^3) sample. Measurement geometry is shown on insert. Energy step 1.9 keV/channel.

expected effect takes place, really. RBS H^+ ions spectra for the diamond crystal and for the glass carbon sample are not equivalent. The diamond structure is characterized by a more compact atomic packing and demonstrated the enhanced scattering yield in the RBS spectrum. Its effect can be used for study of the porous structures. **Figure 21** shows the sample of the Rutherford backscattering study of the Al film in conditions after its preparation and in the result of thermal treatment [32]. Initial spectrum demonstrates the smaller scattering intensity yield in comparison with the theoretical spectrum (a). It is connected with the structure vacancy concentration near 6%. The thermal treatment let to the Al film, thickness decreasing from 300 to 284 nm (see the diagram (c)). The comparison of initial and finishing experimental spectra demonstrates the thickness decreasing and the atomic density increasing up to the normal structure value. Similar investigations is very important because the thin film preparation is no the equilibrium thermodynamic process.

The material atomic density variation can be connected with not only the structural vacancy appearing. Material in the nanostructure state is characterized by the increase in interatomic distance [33]. **Figure 22** demonstrates the Rutherford backscattering yield decreasing for the Ag thin films deposited on the silicon substrate. There are presented two RBS He^+ (E_0 = 1.27 MeV) ions spectra collected by our double detector system (θ_1 = 160°, θ_2 = 120°). Theoretical approximation of these spectra showed that the Ag film thickness is equal 48 nm but the evident discrepancy between Ag theoretical and experimental partial spectra was discovered. In this case, it was nearly equal to 6%. Moreover, the discrepancy increases as the Ag film became more slender and disappears when it will be large 100 nm. Our diffraction measurements confirmed supposition about the atomic density decreasing as aresult of the interatomic distance growth. Similar RBS investigations can be very useful for the material atomic density evaluation in multilayer structures.

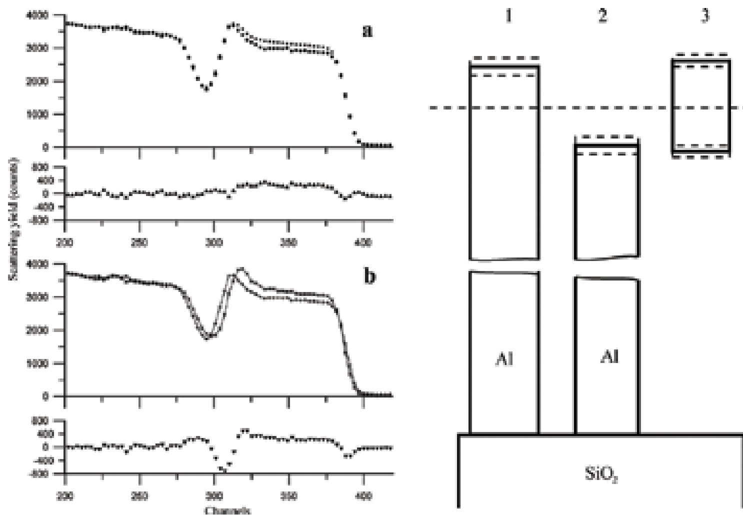

Figure 21. Experimental and theoretical RBS He^+ (E_0 = 1.5 MeV) ions for Al/SiO_2 structure pre (a) and post-thermal treatment (b) and the experimental diagram of the Al thin film thickness variation in result of the thermal treatment influence. Scattering angle is 160°. Energy step 1.9 keV/channel.

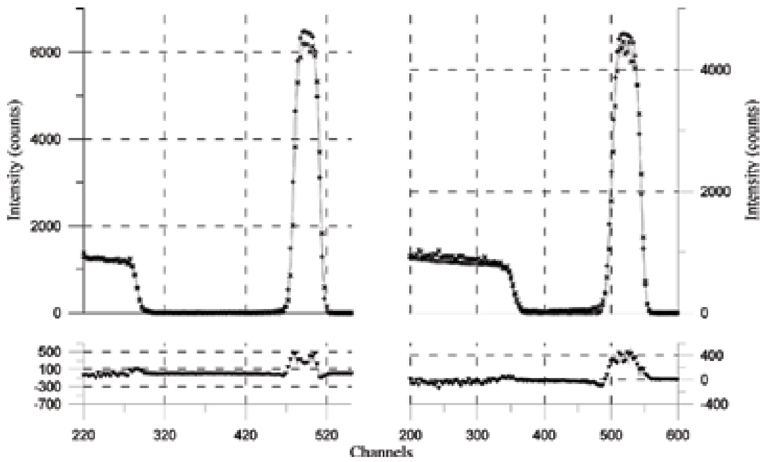

Figure 22. Experimental, theoretical and subtraction RBS He^{+} (E_0 = 1.27 MeV) ions spectra for the Ag thin film deposited on Si substrate. Spectra were collected by the double detector system (θ_1 =160° and θ_2 = 120°). Measurement geometries is presented on inserts. Energy step 1.9 keV/channel.

4. Particle-induced X-ray emission

4.1. Common principles of the method

Particle-induced X-ray emission is an ion analytical method, which utilizes the X-ray characteristic yield induced by ion beam interacting with the electron subsystem of target atoms. X-ray characteristic energy depends on Z atomic number of the target atom. PIXE method similar to other X-ray fluorescence diagnostic technologies collects the characteristic lines yield corresponding to K, L and M radiation series. At the same time, the main distinguishing of the

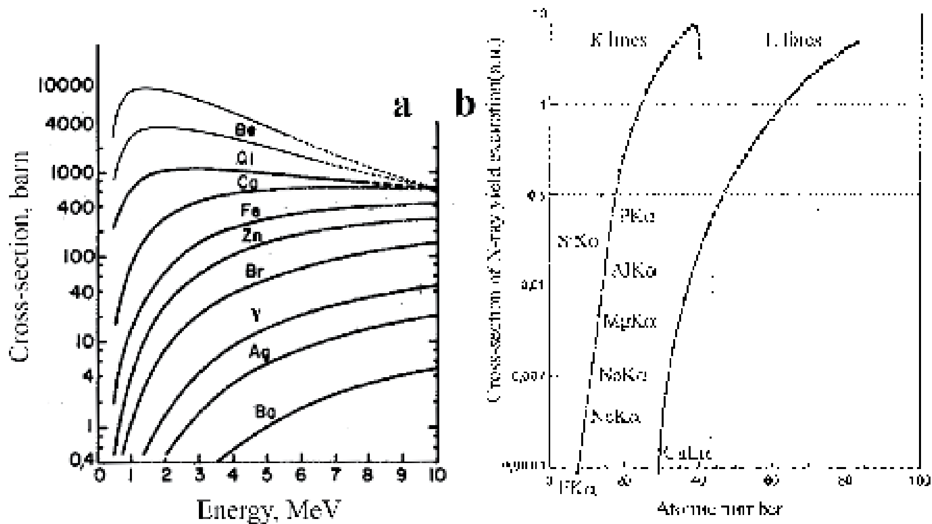

Figure 23. Cross-section of the X-ray fluorescence excitation by proton beam [34] (a) and MoKα radiation flux (b).

ion beam excitation method from X-ray, electron beams and gamma radiation ones is the very high efficiency of the low energy characteristic radiation excitation. In this plane, it is very interesting to compare the X-ray fluorescence yield excitation cross-section at use the X-ray high energy flux (MoKα, E = 17.4 keV) and the proton high energy beam. These data arepresented in **Figure 23** [34]. Cross-sections of X-ray low energy lines excitation by the MoKα radiation flux use are characterized by very small magnitudes. At the same time, these parameters in conditions of the proton beam use demonstrate high values, especially for the low energy lines excitation. Comparison of YKα and AlKα fluorescence excitation cross-section in case of the MoKα radiation flux application shows that the yttrium fluorescence excitation efficiency is higher as the aluminum one on three orders. Similar comparison of these elements fluorescence excitation cross-sections at the proton beam excitation with energy E_0 = 1 MeV shows that the situation will be changed on the reverse one. So, it is evident that the light element diagnostic difficulties at the X-ray beam fluorescence application can be compensate by use the PIXE method [35, 36]. The X-ray fluorescence excitation by ion beams is more effective not only in comparison with the X-ray hard radiation flux application. PIXE bears some similarity to the fluorescence yield electron beam excitation but it characterizes by smaller values of the bremsstrahlung photon intensity yield. As a result, PIXE measurements are distinguished by the background lower level in comparison with the electron excitation. This fact is illustrated in **Figure 24** [7]. The spectra

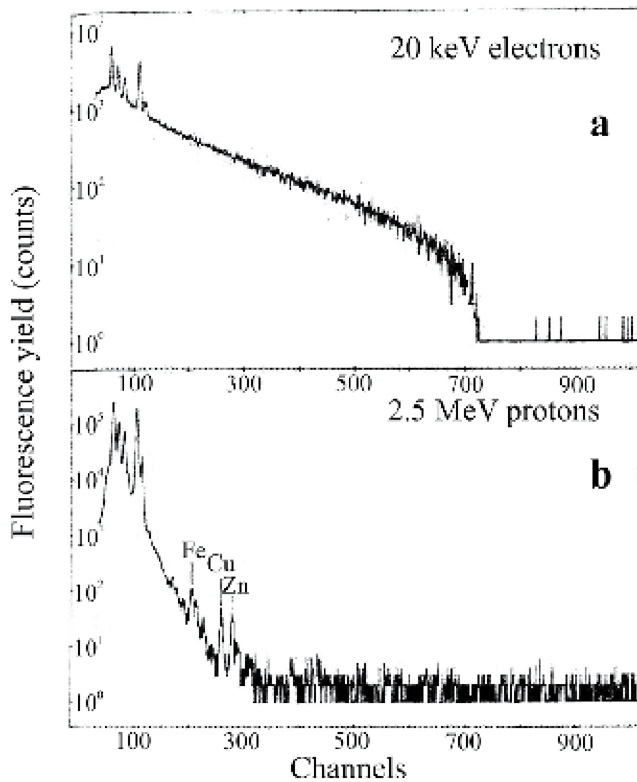

Figure 24. X-ray fluorescence spectra of the human brain tissue collected in conditions of the electron beam (E_0 = 20 keV) excitation (a) and the proton beam (E_0 = 2.5keV)application (b) [36].

comparison shows that the ion beam excitation leads to the background intensity decreasing in result of the bremsstrahlung photon yield reduction. In the presented data, the ion beam excitation application allows to registrate Fe, Cu and Zn atoms presence in the studied target. In the result, one can establish that the PIXE method is characterized by very low magnitudes of detection levels. At the same time, it should be emphasized that the PIXE spectrometry is not the quantitative analytical method. PIXE measurement results are controlled by the matrix effect [37] and by the specific factor connected with the absorption cross-section distinction for different characteristic lines. The last factor is defined by the material layer thickness responsible for the line X-ray fluorescence yield. (This factor can be eliminatedby usingthe planar X-ray waveguide-resonator, see **Figure 5**.)

PIXE element diagnostics, in addition to the matrix and absorption effects, must take into account specific peculiarities of the X-ray fluorescence yield registration by the energy dispersion detector. Any X-ray detector is equipped by the input window, which absorbs the collected radiation. Moreover, X-ray detector is characterized by the reduced efficiency at the high energy photon registration. **Figure 25** presents the experimental diagram reflectingthe X-ray radiation efficiency registration for the wide range of photon energy. Best results of the light element diagnostics can be obtained with X-ray detectors equipped by C_1 and C_2 superfine windows because it allow to collect PIXE spectra up to the photon energy E ≅ 0.1 keV. As a whole, the PIXE spectrometry is very beautiful supplement to the RBS spectrometry.

4.2. PIXE for the material element analysis

Distinction in the X-ray fluorescence yield excitation cross-section demonstrated in **Figure 23** can be illustrated by the direct experimental measurements. **Figure 26** shows spectra of the

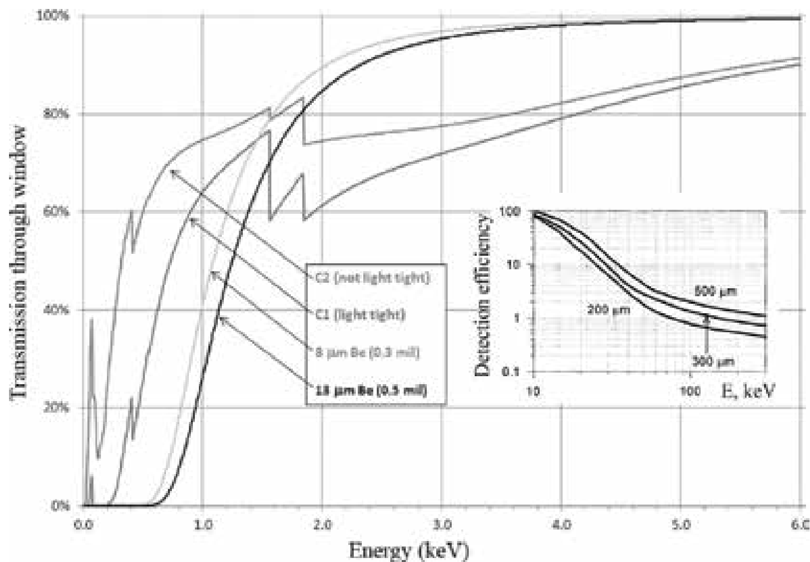

Figure 25. X-ray radiation energy efficiency of the SDD detector equippedby different input windows. Insert shows the efficiency dependence on the detector working plate thickness.

http://dx.doi.org/10.5772/intechopen.76297

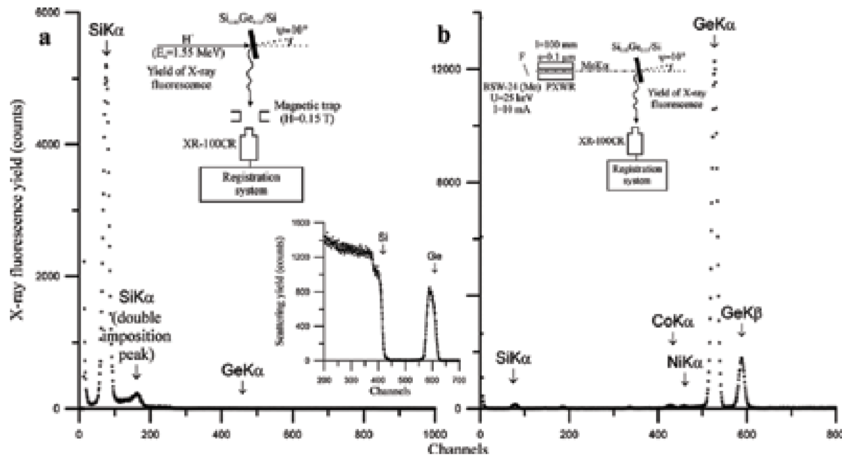

Figure 26. Comparison of X-ray fluorescence yield for $Si_{0.85}Ge_{0.15}$/Si epitaxial structure collected in conditions of the proton beam (a) and the MoKα radiation flux excitation (b). Arrows shows the energy position of X-ray characteristic lines collected by X-ray pin detector. Insertions show the measurements geometry and RBS He^+ (E_0 = 1.525 MeV) ions spectrum for the target. Energy steps for ones 1.9 keV/channel.

X-ray fluorescence yield excited by the proton beam and the MoKα radiation flux. For the reference, the figure presents experimental and theoretical RBS spectra of the target. The target is the silicon-germanium epitaxial film with thickness 112 nm on the silicon monocrystal substrate. Experimental spectrum was collected in the target random position. Comparison of X-ray fluorescence spectra collected in conditions of the different excitation methods use shows that the PIXE approach is more effective for the light element diagnostics in materials, but the X-ray fluorescence excitation is more preferable in case of the heavy element analysis. It is very important to notice that the ion beam excitation provokes the X-ray characteristic fluorescence yield by very high intensity. The spectrum excited by the proton beam with current I = 2 nA (1.2×10^{10} ion/sec) was registeredfor 5 seconds, at the same time, the time registration of spectrum excited by the MoKα radiation flux (N = 4×10^5 photon/sec) was equal 300 s. High intensity of the X-ray fluorescence yield characteristic for the first spectrum is borne out by the double imposition peak appearance. So, in the last experiments, we use SDD silicon detector in frame of the Sokol-3 ion beam analytical complex facility, which can work at the enhanced pulse loading without double imposition peaks.

High efficiency of the PIXE light element diagnostics was used in our investigations of the geological object. **Figure 27** shows the proton-induced X-ray emission spectrum of the $(Mg_{0.93}Fe_{0.07})_2SiO_4$ natural olivine. Host composition of the mineral was defined by RBS method. Experimental and theoretical spectra of the object are presented in the figure, too. PIXE measurements allow to fix in the target structure the Ca, Cl, S, Al and Na elements set existence. Quantitative analysis of the target contamination can be carried out by the TXRF spectrometric method [38].

PIXE spectrometry can be used for petroleum contamination analysis. **Figure 28** shows TXRF and PIXE spectra demonstrating the contamination set existence in the petroleum film deposited on Be substrate. RBS spectrum of the film is shown in **Figure 14**. TXRF spectrum allows to

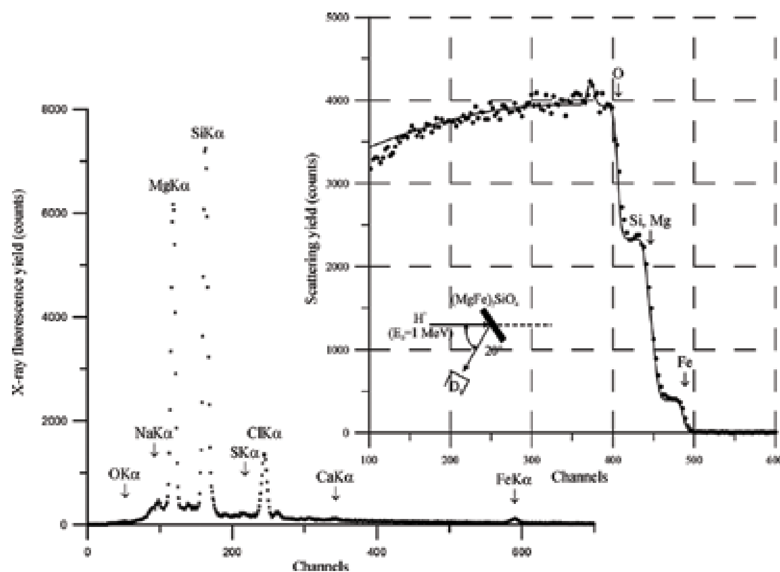

Figure 27. PIXE spectrum of the olivine natural crystal collected in result of H^+ ion beam excitation. Arrows shows the energy position of X-ray characteristical lines collected by SDD silicon detector. Rutherford backscattering spectrum of the target is presented on insert. Energy step for PIXE spectrum 10.9 eV/channel, for RBS 1.9 keV/channel.

produce the quantitative analysis of the contamination concentration that used the sulfur atomic content as the internal standard. TXRF and PIXE spectra confirm the vanadium atoms presence in the petroleum sample. At the same time, the La atoms concentration diagnostics is inaccessible for the total X-ray external fluorescence spectrometry. PIXE analysis is able to fix the La atoms presence in the petroleum sample. The lanthanum atomic content was evaluated by usingthe comparison method with data for Ca and V atom concentration. It is 0.0005 if the sulfur concentration is elected as a one. PIXE diagnostics of the solution dry residue is the very perspective application for this specific target.

PIXE measurements can be used for the nonstandard element analysis. **Figure 29** shows RBS and PIXE spectra collected for the leather processing material by usingthe proton beam excitation. RBS spectrum allows to evaluate the host elements concentration (except hydrogen atom), at the same time, the PIXE investigation takes possibilities to fix the contamination element presence in the leather processing material. How showed experience of the leather goods manufacturing the chromium and contamination concentrations defines quality of different products manufactured from the leather. The quantitative contamination analysis can be executed by TXRF method application. But if the TXRF spectrometry sensitivity is not enough, it is possible to use the planar X-ray waveguide-resonator for the trace surface element diagnostics in frame of the PIXE excitation of the X-ray fluorescence yield. The experimental scheme for such measurement execution is presented in **Figure 5b**, and the diagnostic method has name – TXRF PE.

Figure 30 presents the experimental data characterizing the method possibilities on base of the old coin study. PIXE spectrum shows X-ray fluorescence lines initiated by surface and

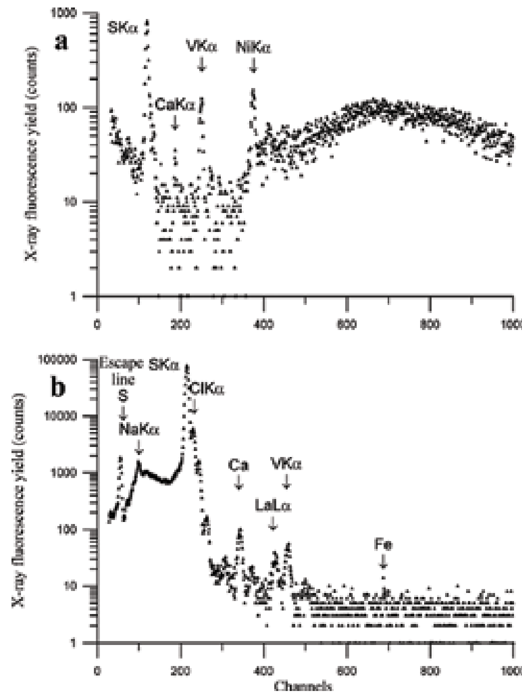

Figure 28. X-ray fluorescence spectra collected for the petroleum film deposited on Be substrate by use the TXRF and the PIXE spectrometry. Energy step for TXRF spectrum 20 eV/channel, and 10 eV/channel for PIXE spectrum. TXRF fluorescence yield was excited by the MoKα flux, PIXE – by the proton beam with energy E_0 = 0.953 MeV. Arrows show the energy position of X-ray characteristic lines collected by SDD silicon detector.

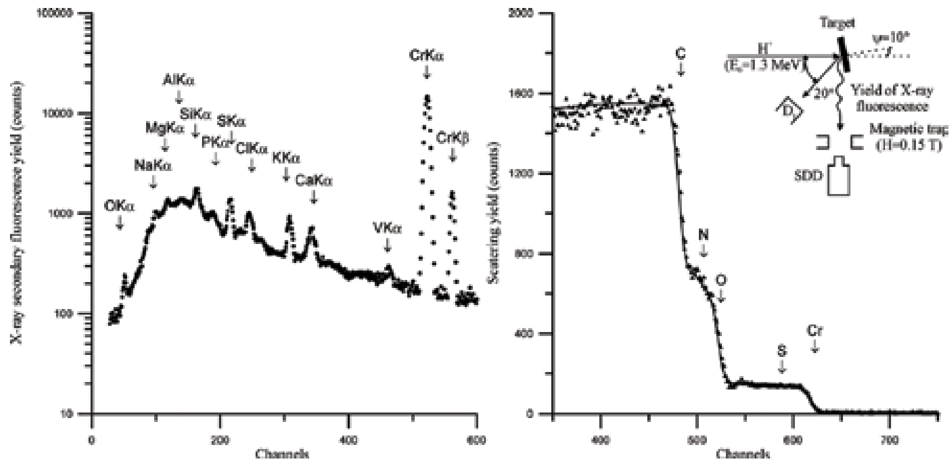

Figure 29. Experimental and theoretical RBS H^+ (E_0 = 1.3 MeV) ions for the sample of thin leather – processing material and PIXE spectrum of the one collected in the same experiment. Arrows on the RBS spectrum show the ion scattering energies on nuclei of atoms located on the sample surface, and on the PIXE spectrum show the energy position of X-ray characteristical lines collected by SDD silicon detector. Energy step for RBS spectrum 1.9 keV/channel, for PIXE one 10 eV/channel. Insert shows the measurement geometry.

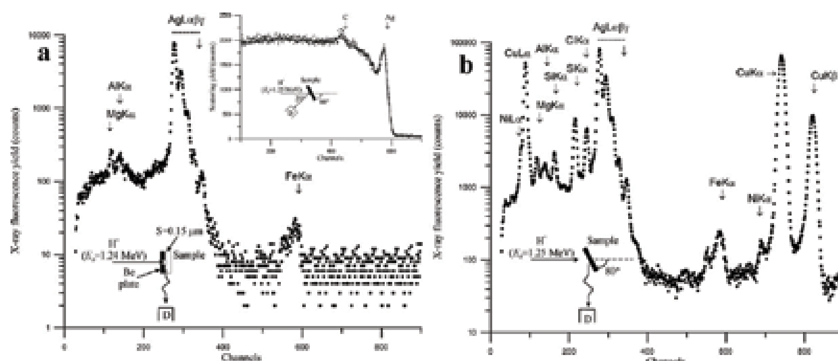

Figure 30. TXRF PE (a) and PIXE (b) spectra of the half copeek old coin fabricated from copper with the surface Ag coating (t= 170 nm) collected by SDD silicon detector in conditions of the X-ray fluorescence excitation by the proton beam (E_0 = 1.25 MeV). Inserts show measurements geometry and RBS H^+ ions spectrum of the target. Arrows on fluorescence spectra show of the energy position of X-ray characteristical lines and on RBS one ion scattering energies on nuclei located on the coin surface. Energy step for fluorescence spectra 10.5 eV/channel for RBS one 1.9 keV/channel.

volume atoms of the target. In its turn, TXRF PE spectrum reflects X-ray fluorescence lines characteristic for the coin surface. (Carbon peak on the Rutherford backscattering diagram is connected with the C-H film appearing in process of the proton beam scattering in the measurement period.) The X-ray fluorescence spectra comparison allows to conclude that the Mg, Al and Fe atoms contamination are typical for the Ag coating. This conclusion was confirmed by the TXRF direct study. So, new experimental method can be recommended for the trace light elements diagnostic in addition to the standard TXRF experimental measurements.

5. Nuclear elastic recoil for the hydrogen diagnostics

It is known, that the hydrogen atoms diagnostic can be carried out by using the direct resonance nuclear reaction, for example, $^{1}H(^{15}N;\ \alpha,\gamma)^{12}C$ and $^{1}H(^{19}F;\ \alpha,\gamma)^{16}O$, or by the nuclear elastic recoil (NER) method [16]. The resonance method has a limited spearing because its application demands ion beams with the enhanced energy. For example, the low energy resonance of $^{1}H(^{15}N;\ \alpha,\gamma)^{12}C$ reaction has value 3.35 MeV. So, the nuclear recoil spectrometry is more accessible while less informative. The experimental scheme for the nuclear recoil method is presented in **Figure 6b**. The measurement scheme assumes the surface target installation on the $\theta_1/2$ small angle about of the helium ion beam propagation line and the recoil and scattering ion detector placing under the θ_1 angle. The detector must have a collimator and the thin film absorber. The absorber thickness must provide a total absorption of the helium ions scattering flux. In these conditions, the recoil hydrogen atoms undergo the noticeable straggling [10–16]. The straggling effect is characterized by the ion beam average energy decreasing attended by increasing of the ΔE energy dispersion. Moreover, it is a need to take into account the adsorbed layer existence on the any material surface, which contains some hydrogen quantity. As a rule, the hydrogen surface concentration is higher in comparison of the hydrogen target volume content.

http://dx.doi.org/10.5772/intechopen.76297

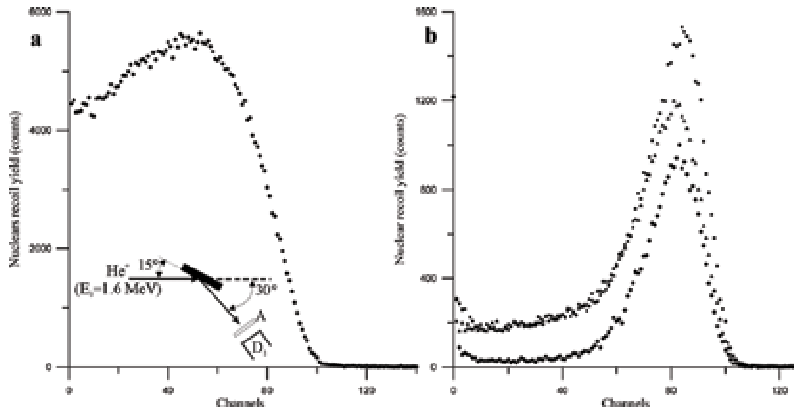

Figure 31. Nuclei elastic recoil spectra of the $TiH_{0.98}$ weighting etalon (a) and some perovskite structures (b) collected in the specific geometry allowed to fix the hydrogen atoms recoil. Hydrogen recoil spectrum for $SrTiO_3$monocrystal (●), for BSTO film on MgO substrate (▲), for BSTO film Si substrate (♦). Measurement geometry is presented on insert. Energy step 3.8 keV/channel.

The nuclei recoil spectrometry, similar to the RBS method allows to produce the absolute analysis. At the same time, it is possible to use standard samples attested by the precision weighting. We used $TiH_{0.98}$ as the similar etalon. **Figure 31** shows NER spectra of the etalon and some perovskite structures. Data obtained from the etalon spectrum allows to evaluate the hydrogen content in studied perovskite structures. It is very strange but the hydrogen atoms concentration in the $SrTiO_3$ monocrystalline structure was near 4% at. Similar hydrogen content was detected in the BSTO film deposited on MgO substrate. The BSTO film deposited on the silicon substrate had smaller hydrogen atoms in its structure (near 1% at.). Evaluation of the hydrogen atoms in surface absorbed layers shows that the film has the C_1H_1 composition. NER measurements are characterized by specific conditions. The helium ion beam energy must be higher as 1.5 MeV. At smaller energy of the beam some experimental and interpreting difficulties appear.

6. Nuclear reaction analysis application for the material study

Nuclear reactions excited by high energy ion beams can have the resonance nature and can demonstrate the threshold characteristics[39]. It is the isotopically sensitive methods. Some nuclear reactions have the practical significance. It is the $^{27}Al(p,\gamma)^{28}Si$ famous resonance reaction, which uses for the ion beam accelerator calibration [40]. Nuclear reaction analysis (NRA) is mostly used for the light element diagnostics in material. In our work we applied the $^{11}B(p,\alpha)^{8}Be$ nuclear reaction for study of the electro-rocket engine function peculiarities [41]. The main investigation task of the study was the elements spatial distribution determination in the engine output jet. The engine discharge chamber was manufactured from the material elaborated on the BN base composition. So, it is expected that the main admixture element in the xenon jet will be boron. For the boron spatial distribution in the engine jet, we used the Be plates set arranged on different angles about the jet propagation line. The deposit on the Be

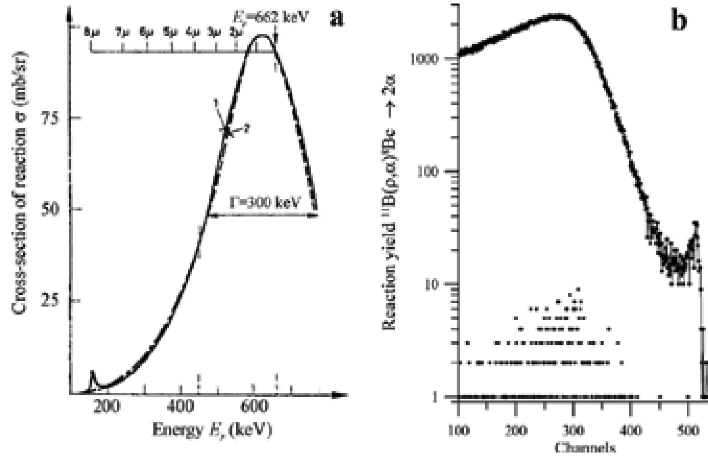

Figure 32. Cross-section energy dependence of the ^{11}B(p, α)^{8}Be nuclear reaction (a) [43], and the reaction yields for the $B_{0.4}N_{0.45}X_{0.15}$ engine ceramic, for the Be plate with deposited film, which was arrangement on angle 59 about the jet propagation line and for the Be clean plate.

Isotope	Content in nature, %	Nuclear reaction	Energy of proton, keV	Cross-section of reaction, mb/sr	Width of resonance, keV	Emission product E_γ, E_α, MeV	Limits detection, at.%
^{6}Li	7.62	—	—	—	—	—	—
^{7}Li	92.58	^{7}Li(p.γ)Be^{8}	441	6	12	17.65; 14.75	$\sim$100 ppm
^{9}Be	100	^{9}Be(p,α)^{6}Li	330	4	1.5	8.5; 14.2	$\sim$50 ppm
^{10}B	19.61	^{10}B(p,γ)	1146	0.01	570		$\sim$10 ppm
^{11}B	80.39	^{11}B(p,α)^{8}Be	650	90	10	-; 3.7	$\sim$10 ppm
^{12}C	98.89	^{12}C(p,γ)^{13}N	459	0.13	40	2.36; –	$\sim$120 ppm
^{13}C	1.11	^{13}C(p,γ)^{14}N	550	1.44	32	8.6; –	$\sim$100 ppm
^{14}N	99.64	^{14}N(p,γ)^{15}O	278	$\sim$0.01	1.6	6.8	$\sim$100 ppm
^{15}N	0.36	^{15}N(p,γ)^{12}C	898	800	2.2	4.43	$\sim$10 ppm
^{16}O	99.8	—	—	—	—	—	—
^{18}O	0.2	^{18}O(p,α)^{15}N	730	15	10	3.4	$\sim$10 ppm
^{19}F	100	^{19}F(p,γ,α)^{16}O	872	661	4.5	6.13	$\sim$1 ppm
^{23}Na	100	^{23}Na(p,α)^{20}Ne	592	4	45	2.238	$\sim$20 ppm
^{24}Mg	78.6	^{24}Mg(p,γ)Al^{25}	1200	$\sim$0.01	<10	3.44; 1.83; 1.61	$\sim$200 ppm
^{25}Mg	10.2	^{25}Mg(p,γ)Al^{26}	317	$\sim$0.01	12	6.19; 4.86; 0.82	$\sim$500 ppm
^{26}Mg	11.2	^{26}Mg(p,γ)Al^{25}	661	$\sim$0.01	<10	7.88; 6.68; 5.9	$\sim$500 ppm
^{27}Al	100	^{27}Al(p,γ)^{28}Si	992	0.1	0.05	1.77; 7.93; 10.78	$\sim$10 ppm

Table 1. Resonant nuclear reaction parameters for light element isotopes initiated by proton beams.

plates was analyzed by the boron resonance reaction. Cross-section energy dependence of the reaction is presented in **Figure 32a** [42]. **Figure 32b** shows the pattern of our measurements, which allowed to evaluate the boron spatial distribution in the jet of electro-rocket engine. Similar investigations are very effective but are very expensive. At the same time, it is useful to have a grasp about possibilities of NRA methods application and atomic detection limits determination on base of the real nuclear reaction use. **Table 1** presents the information about the most useful reaction applied for the light element diagnostics.

7. Some peculiarities of the ion beam optical luminescence excitation

Our active investigations in the optical scintillation field at ion beam excitation were connected with the $PbWO_4$ and LaF_3 luminescence response study [43–45]. Interest to the $PbWO_4$ luminescence characteristic study was initiated by the fast component existence in the luminescence response at the proton beam excitation. There was the specific interest to fix the luminescence distinction between yields in the random and the channeling orientation of the crystal and to study kinetic of the luminescence yield dependence on the absorbed radiation doze. Results of these investigations are shown partially of **Figure 33**. The luminescence spectrum obtained in the channeling proton beam condition demonstrates some integral intensity yield increasing [43] and is characterized by some spectrum variation. Dosimetric data showed that luminescence yield intensity reduces as the radiation doze increases up to some critical value J_∞. After

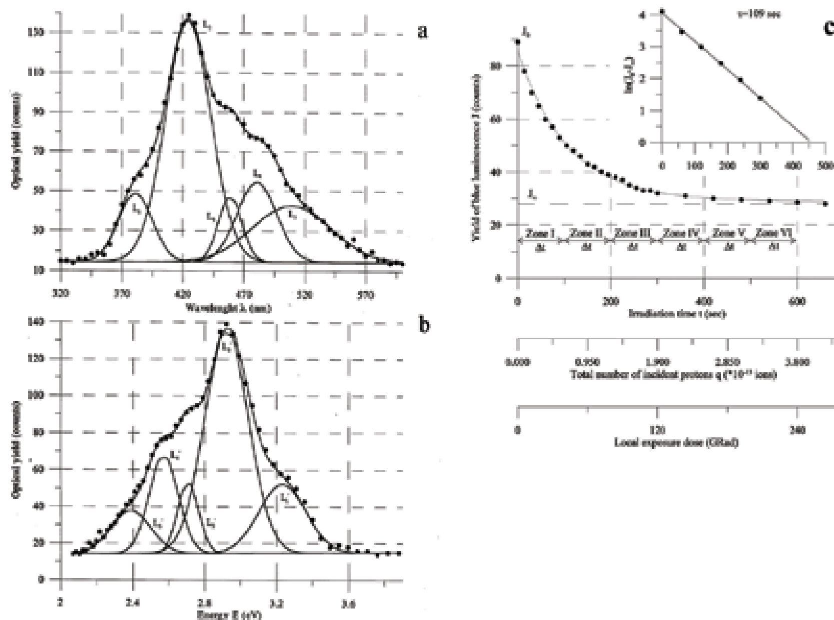

Figure 33. Luminescence yield optical spectra for random (a) and channeling along [001] axis (b) of $PbWO_4$monocrystal target executed by H^+ ions beam (E_0 = 0.9 MeV), and the kinetic function of random spectrum blue component (λ_0 = 412 nm) on the absorbed radiation dose.

warning at t = 100°C during τ=600 s, the $PbWO_4$ target had got the critical radiation doze returned into the initial state. Total interpretation of the experimental data is very difficult, but some results of our investigations were found useful for the elaboration of the $PbWO_4$ monocrystal great size preparation technology. The experimental arrangement used for our luminescence study in conditions of the ion beam excitation is presented in **Figure 6**. The ion luminescence investigations does not have wide spread use owing to the interpretation problems existence. At the same time, it is a need to understand that the ion beam luminescence excitation mechanism is different from the X-ray, gamma ray and electron beam excitation one. In case of the $PbWO_4$ excitation by the proton beam, we can observe the L_1 luminescence line being absent at any other excitation types.

8. Monocrystalline and epitaxial structures study by the ion beam channeling method

How it was discussed early peculiarities of the ion beams interaction with materials is defined by the material structure features. Experimental investigations of very much crystals confirmed the Starks assumption about possibility for high energy ions to propagate through the crystal almost without scattering in case of its movement along ordered atomic chains [46]. This effect was called the ion beam channeling in crystals. Fundamental features of the effect and its possible practical application were discussed in details in the specific monograph [20]. Some features of the effect were studied in our investigation. **Figure 34** shows this effect observation for the monocrystalline synthetic diamond target prepared by the temperature gradient method realized at the high hydrostatic pressure conditions. Ion beams axial channeling along [100] axis of the target demonstrates the high perfection structure (χ_{exp} = 0.23 at χ_{tcor} = 0.09). W atoms are the main admixture of the target. The hydrogen ion channeling allows to evaluate the channeling effect depth for the diamond. SiO_2 thin film presents on the diamond surface. It is the result of polishing procedure. The studied diamond target has noticeable sizes (0.5 × 5 × 5 mm^3). It can be used as the substrate for the power integral circuits

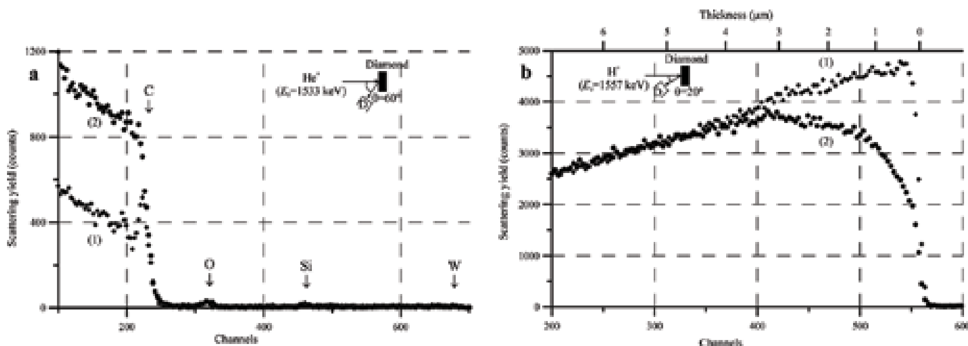

Figure 34. Experimental RBS He^+ and H^+ ions spectra for the random position (a) and the channeling orientation through [100] axis (b) of the diamond monocrystal. Arrows show the ion scattering energies on nuclei of atoms located on the target surface. Measurement geometries are shown on inserts. Energy step 1.9 keV/channel. (1) Random orientation. (2) Channeling.

http://dx.doi.org/10.5772/intechopen.76297

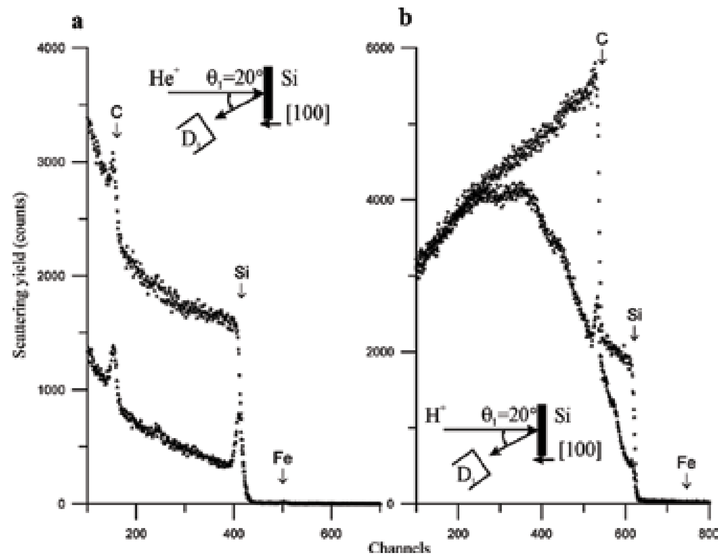

Figure 35. Experimental RBS He^+(a) and H^+(b) ions spectra for theSiCmonocrystal in the random position and the channeling condition along [001] axis. Arrows show the ion scattering energies on nuclei of atoms located on the target surface. Experimental geometries is shown on inserts. Energy step 1.9 keV/channel.

preparation and the X-ray tube windows manufacturing owing to its high thermal conductivity. Other sample of the ion beams axial channeling is shown in **Figure 35**. It demonstrates patterns of He^+ and H^+ ion beams channeling along [001] axis of SiC monocrystal prepared by the Lely method [47]. RBS measurements executed for the random and oriented conditions showed that the silicon carbide crystalline structure has high perfection (χ = 0.36). The target structure is characterized by the 6H hexagonal polytype with crystallographic parameters of the cell a = 0.308 nm, c = 1.512 nm. Because the preparation method is connected with molten metals, Fe atoms are a chief contamination of the target. The technology preparation of SiC monocrystalline boules is very important for the nanophotonics because the silicon carbide material is very suitable for manufacture of light emitting diodes (LED) on base of the high energy-gap semiconductors. In the context of this, very interesting works of Prof. Kukushkin are connected with combination of the silicon and the silicon carbide technologies [48]. He elaborated the technology of SiC/Si epitaxial heterostructure preparation. The ion beam analysis application showed that the SiC/Si heterostructure is characterized by low perfection but the crystallographic epitaxy existence [49]. Moreover, on base of the SiC/Si substrate,they were able to prepare the effective light emission structure. So, the ion beam analysis application to the compositions diagnostics having the SiC structure has the direct practical application.

The living practical interest is connected with perovkite crystals and its heterostructures investigations. It is well known, that multielement oxide films fabricated on base of the doped barium titanate ($BaTiO_3$) are assumed to be promising material structures for the development of micro and nanoelectronic and electro-optical devices. Such coatings are potentially applicable as electro-optical modulators and phase shifter, switching devices, optical microprocessors, surface waveguide-acoustic transducers and capacitive elements in dynamic memory. Experimental investigations showed that the epitaxial coatings on single crystals substrates with appropriate

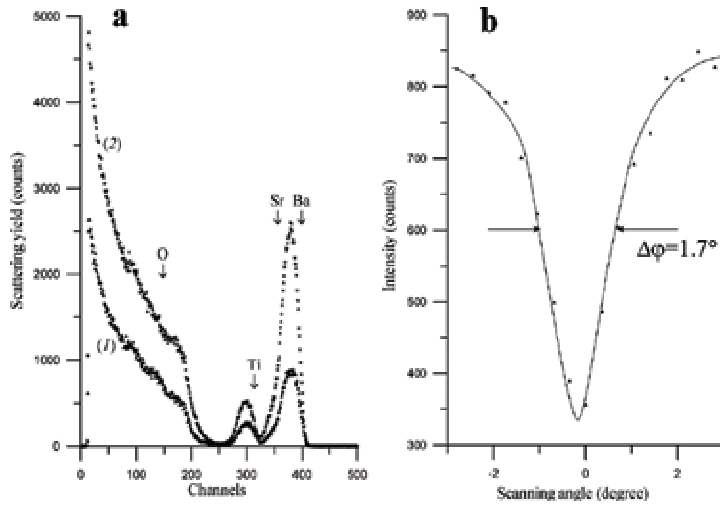

Figure 36. Experimental RBS He^+ions spectra for $Ba_{0.8}Sr_{0.2}TiO_3$/MgO epitaxial structure in the random position and the channeling condition along [100] structure axis (a) and the rocking resette near the channeling axis (b). Arrows show the ion scattering energies on nuclei of atoms located on the target surface. Measurement geometry is presented on the insert. Energy step 1.9 keV/channel.

crystallographic parameters exhibit the best electro-optical properties. So, the BSTO films study deposited on different substrates were one of our priority films study deposited on research direction. **Figure 36** shows experimental RBS spectra of the $Ba_{0.8}Sr_{0.2}TiO_3$/MgO epitaxial heterostructure collected for the target random position and in conditions of He^+ ion beam channeling along [100] direction. Comparison of He^+ ion scattering spectra collected in the random and channeling target disposition shows that the scattering yield proportional decreasing for the film and substrate atoms takes place. Moreover, rocking rosettes obtained for film and substrate atoms showed the identical form. At the same time, it is a need to notice that the χ experimental factor for the target is twice as much as the theoretical magnitude χ_{min} = 0.18. It is showed that the target structure is characterized by some nonperfection. But the ion beam channeling along the sole crystallographic axis does not always reflect real degree of the target structure perfection. Similar information can be accessible at the channeling data use for some crystallographic axis. Sample of such situation is presented in **Figure 37**. It shows experimental and theoretical RBS He^+ ions spectra for the $Si_{0.8}Ge_{0.2}$/Si epitaxial structure obtained for random target positions and oriented states and the rocking rosettes of the ion beam channeling near [100] and [110] axis [50]. The minimum yield for the He^+ ion beam channeling along [100] axis is near this parameter theoretical magnitude (χ_{min} = 0.03). One can expect on base of the RBS channeling spectrum that the thin film epitaxial structure is characterized by the almost ideal perfection. But the ion beam channeling spectrum along [110] crystallographic axis does not confirm the similar expectation. Experimental magnitude of the minimum yield parameter for the [110] silicon crystallographic axis is higher as the theoretical one on two times. This discrepancy is connected with the elastic stress owing to the magnitudes difference of film and substrate unit cells. In this case, the structure distortions have an anisotropic character. The stress value is dependent on the film composition and its thickness. Thick films demonstrate the exfoliation trend. The channeling method can be used with success for the light element diagnostic

http://dx.doi.org/10.5772/intechopen.76297

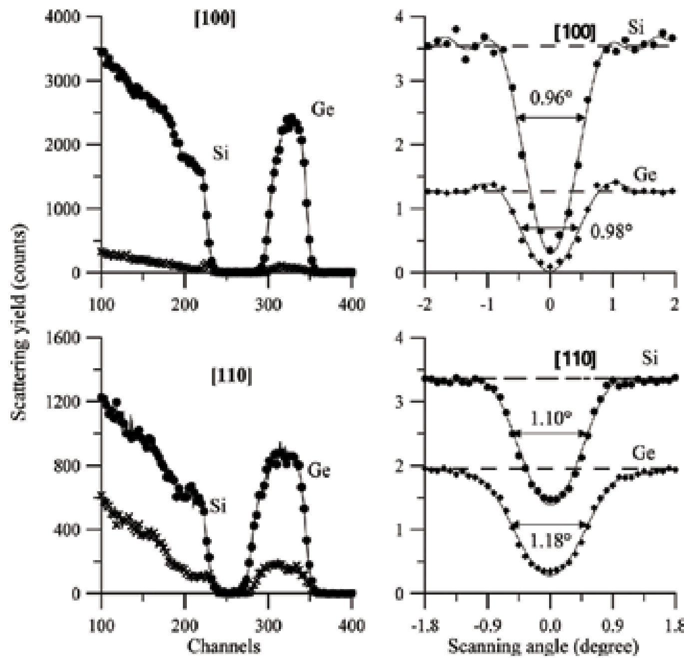

Figure 37. Experimental RBS He^{+}ions spectra for $Si_{0.8}Ge_{0.2}$/Si epitaxial structure in the random positions and the channeling conditions along [100] axis, [110] axis and the rocking rosettes near the channeling axis. Arrows show the ion scattering energies on nuclei of atoms located on the target surface. Measurement geometries is shown on inserts. Energy step 1.9 keV/channel.

implanted into the monocrystalline objects. It has possibilities to study the structure defects types and its distribution [22]. But it is a need to notice that the channeling method is very expencive.

9. Conclusion

Short review of the ion beam spectrometry and analytical method built on base of the ion beams interaction with material shows that the methods application is very useful and in some cases unique. All ion beam analytical methods are the nondestructive technique. RBS spectrometry is the only instrumental method being not demanded analytical standards and etalons. Complex application of the material ion beam analysis allows to present the total description of the material properties. But the cost of its use is very high.

Acknowledgements

We are grateful to Prof. S.A. Kukushkin and Dr. M.S. Afanas'ev for helpingthis work. The work was partially supported by Russian Foundation for Basic Researches (project #16-07-00665) and state task #007-00220-18-00. This paper received partial financial supported by the Ministry of Education and Science of the Russian Federation on the program to improve the

competitiveness of Peoples' Friendship University of Russia (RUDN University) among the world's leading research and education centers in the 2016–2020.

Author details

Vladimir Egorov[1*] and Evgeny Egorov[1,2]

*Address all correspondence to: egorov@iptm.ru

1 Institute of Microelectronics Technology Russian Academy of Science (IMT RAS), Chernogolovka, Russia

2 RUDN University, Moscow, Russia

References

[1] Schmidt B, Wetzig K. Ion Beam in Material Processing and Analysis. Wien: Springer; 2013. p. 418

[2] Bird JR, Williams JS. Ion Beams for Material Analysis. Sidney: Academic Press; 1989. p. 719

[3] Townsend PD. Optical effect of ion implantation. Reports on Progress in Physics. 1987;**50**: 501-558

[4] Pop SS, Belikh SF, Drobnich VG, Ferleger VK. Ion-Photon Metal Emission. Tashkent: FAN; 2000. p. 200 (In Russian)

[5] Huddle JR, Grant PG, Ludington AR, Foster RL. Ion beam-induced luminescence. NIM. 2007;**261**:475-476

[6] Koljada VM, Zaychenko AK, Dmitrenko PV. X-Ray Spectral Analysis at the Ion Beam Excitation. Moscow: Atomizdat; 1978. p. 248 (In Russian)

[7] Johansson SAE, Campbell JL. PIXE: A Novel Technique for Element Analysis. New York: Wiley; 1988. p. 347

[8] Instrumentation for PIXE and RBS. Special Issue of International Atomic Energy Agency (IAEA). IAEA-TECDOC-1190. Vienna: IAEA; 2000. p. 83

[9] Petrov NN, Abrojan IA. Surface Diagnostics by Ion Beams Application. Leningrad: LGU Press; 1977. p. 160 (In Russian)

[10] Chu WK, Majer JM, Nicolet MA. Backscattering Spectrometry. New York: Academic Press; 1978. p. 384

[11] Shipatov ET. Background Scattering of Fast Ions, Theory, Experiment, Practice. Rostov-on-Don: Rostov State Univ. Press; 1988. p. 155

[12] Tesmer JR, Nastasi M, editors. Handbook of Modern Ion Beam Material Analysis. Pittsburg: MRS Published; 1995. p. 704

[13] Hellbord J, Whitlow HJ, Zhang Y. Ion Beams in Nanosize and Nanotechnology. Heidelberg: Springer; 2009. p. 457

[14] Nastasi M, Mayer JW, Wang Y. Ion Beam Analysis, Fundaments and Application. Boca Raton: CRC Press; 2015. p. 434

[15] Chernov IP, Shadrin VN. Analysis of Hydrogen and Helium Concentration by the Nuclei Recoil Method. Moscow: Energoatomizdat; 1988. p. 129 (In Russian)

[16] Hofsas H. Forward Recoil Spectrometry. New York: Plenum; 1996. p. 278

[17] Amsel G, Lanford WA. Nuclear reaction techniques in material analysis. Annual Review of Nuclear and Particle Science. 1984;**34**:435-460

[18] Ehmann WD, Vance DE. Radiochemical and Nuclear Methods of Analysis. New York: Wiley; 1991. p. 531

[19] Rauhala E. Proton elastic scattering cross-section of carbon, nitrogen and silicon for backscattering analysis in the energy range 0.7-2.5 MeV. NIM. 1985;**12**:447-452

[20] Feldman LC, Mayer JW, Picraux ST. Material Analysis by Ion Channeling. New York: Academic Press; 1982. p. 300

[21] Shipatov ET. Ions Channeling. Rostov-on-Don: Rostov State Univ. Press; 1986. p. 144 (In Russian)

[22] Gotz G, Gartner K, editors. High Energy Ion Beam Analysis of Solids. Berlin: Acad. Verlag; 1988. p. 342

[23] Doolittle LR. Algorithm for the rapid simulation of Rutherford backscattering spectra. NIM. 1985;**9**:344-351

[24] Egorov V, Egorov E, Afanas'ev M. TXRF spectrometry at ion beam excitation. IOP Publishing; IOP Conf. Ser.: Journal of Physics: Conf. Ser. 2017;**808**:012002. DOI:10.1088/1742-6596/808/1/012002

[25] Egorov V, Egorov E. Waveguide-resonance mechanism for X-ray beam propagation. Advances of X-ray Analysis. 2003;**46**:307-315

[26] Zieglar JF. The Stopping and Ranges of Ions in the Matter. New York: Pergamon Press; 1977. p. 367

[27] Mayer M. SIMNRA: simulation of RBS, ERD and NRA spectra [Internet]. 1999. Available from: http://home.mpcdf.mpg.de/~mam/Mayer-AIP-Conference-Proceedings-475-(1999)-541.pdf [Accessed: 2018–02-19]

[28] Mehrer H. Diffusion Is Solids, Fundaments, Methods, Materials, Diffusion-Controlled Processes. Berlin: Springer; 2007. p. 651

[29] Poate M, Tu KN, Mayer JW, editors. Thin Film Interdiffusion and Reactions. New York: Wiley; 1978. p. 578

[30] Aleshin AN, Egorov VK, Bokstein BS, Kurkin PV. Study of diffusion in thin au/cu films. Thin Solid Films. 1993;**223**:51-55

[31] Aleshin AN, Bokstein BS, Egorov VK, Kurkin PV. Segregation effect on grain-boundary diffusion in thin metallic films. Thin Solid Films. 1996;**275**:144-147

[32] Egorov VK, Kononenko OV, Kondratiev OS. Porosity of film coatings in Rutherford backscattering. Surface Investigation. 1988;**13**:729-741

[33] Natelson D. Nanostructures and Nanotechnology. Cambridge: Cambridge Univ. Press; 2015. p. 630

[34] Cahill TA. Proton microprobs and partical induced X-ray analytical system. Annual Review of Nuclear and Particle Science. 1980;**30**:211-252

[35] Folkman F, Gaarde G, Huus T, Kemp K. Proton induced X-ray emission as a tools for trace element analysis. NIM. 1974;**116**:487-499

[36] Johanson SAE, Campbell JL, Malquist KG. Particle Induced X-Ray Emission Spectrometer (PIXE). New York: Wiley; 1995. p. 451

[37] Seppala A, Raisanen J. Matrix effects in particle induced X-ray emission channeling measurements of ZnSe/GaAs heterostructures. Applied Physics Letters. 1999;**75**(6):820-822

[38] Klockenkamper R. Total Reflection X-Ray Fluorescence Analysis. New York: Wiley; 1997. p. 245

[39] Verma HR. Atomic and Nuclear Analytical Methods. Berlin: Springer; 2007. p. 375

[40] Scharf VH. Particle Accelerators Application in Technology and Research. Somernet: Res. Stud. Press; 1989. p. 663

[41] Arbatskii VM, Nadiradze AB, Chirov AA, Shaposhnikov VV, Egorov VK. The study of the angular distribution of doped elemental composition in a jet of an electro-rocket engine by ion beam methods. Surface Investigation. 2001;**16**:875-888

[42] Golicheff I, Locullet M, Engelman C. Analytical application of the direct observation of nuclear reactions induced by low energy protons and leading to the emission of gamma-photons which are measured. Journal of Radioanalytical Chemistry. 1972;**12**:233-250

[43] Egorov VK, Zuev AP, Egorov EV. Scintillation response of monocrystal $PbWO_4$ to random and channeled ions. NIM. 1996;**119**:418-424

[44] Egorov V, Zuev A, Egorov E. Light output of scintillation upon ion excitation of surface layers of $PbWO_4$ single crystal in oriented and nonoriented positions. Surface Investigation. 1997;**12**:717-731

[45] Egorov VK, Egorov EV. Luminescence kinetics of $PbWO_4$ crystal at excitation by H^+ ion beam. NIM. 2001;**179**:536-542

[46] Stark J. Bemerkung uber strahlen zerstreuung und absorption von beta strahlen und rontgenstrahlem in kristallen. Physikalishce Zeitschrift. 1912;**13**:973-988

[47] Lely JA. Darstellung von einkristallen von silicium carbide und beherrschung von art und menge der eingebauten verunreinigungen. Berichte der Deutschen Keramischen Gesellschaft. 1955;**32**:226-264

[48] Kukushkin SA, Osipov AV. New method for growing silicon carbide on silicon by solid phase epitaxy, model and experiment. Physics of the Solid State. 2008;**50**(7):1238-1245

[49] Egorov VK, Egorov EV, Kukushkin SA, Osipov AV. Structural heteroepitaxy during thermochemical transformation of silicon to silicon carbide. Physics of the Solid State. 2017;**59**:135-141

[50] Vyatkin AF, Egorov VK, Egorov EV. Study of strain relaxation in epitaxial structure $Ge_{0.2}Si_{0.8}$/Si at thermo-implantation treatment by ion beam channeling. Materials Research Society Symposium Proceedings. 2000;**585**:183-189

Chapter 4

Ion Beams for Space Applications

Sokeng Ifriky Tadadjeu, Balla Diop Ngom,
Shane Martin, Robert Ryk Van Zyl and Malik Maaza

Additional information is available at the end of the chapter

http://dx.doi.org/10.5772/intechopen.76993

Abstract

This chapter uses an active space mission as well as current and ongoing research work to showcase the role of ion beams in the advancement of space science and technology. It uses the mission objectives of the ZACUBE-2 space mission developed at the Cape Peninsula University of Technology in Cape Town, South Africa, to predict the space environment it will encounter when in orbit. These predictions are then used to show how ion beam parameters for single event effect testing are selected, and how trade-offs are made to achieve a cost effective use of beam time. An experiment is detailed, showcasing the role of ion beams in the investigation of the shielding capabilities of coatings obtained from the pulsed laser ablation of W_2B_5/B_4C for solar panel applications in space. The results of this experiment show that indeed this is a potential shield capable of reducing solar panel degradation due to low energy protons. By using ZACUBE-2 and coatings made from W_2B_5/B_4C, this chapter takes a practical and current approach to demonstrate the central role played by ion beams in advancing space technology. More importantly, it eases the conversation between the satellite and the ion beam communities.

Keywords: ion beams, space applications, ZACUBE-2, W_2B_5/B_4C, radiation damage

1. Introduction

The objective of this chapter is to ease the conversation between satellite engineers, ion beam operators and contributors to fundamental science for whom ion beams are either a research tool or the very subject of their work.

Space is a very hostile environment for technology. Before sending any piece of technology to space, one must consider its likelihood to survive this environment made up of high energy

IntechOpen

© 2018 The Author(s). Licensee IntechOpen. This chapter is distributed under the terms of the Creative Commons Attribution License (http://creativecommons.org/licenses/by/3.0), which permits unrestricted use, distribution, and reproduction in any medium, provided the original work is properly cited. CC BY

ionising and non-ionising radiation. Spacecraft engineers consistently turn to ion beams to create environments similar to those in which their spacecraft are designed to dwell. The main reason for this is to ascertain the functionality of their technology in space. This can either mean testing existing/established technology for use under specific space conditions, or determining whether new technology can be space applicable.

Using a rather practical approach, this chapter brings to light the main aspects that are taken into account from a space science and technology point of view, when it comes to using ion beams to ensure the success of space missions and the advancement of space-related technology. It utilises an ongoing university space mission and related research and development to describe the role of ion beams in a typical space program.

The first step towards using ion beams for space related testing, is clarifying the space mission objectives. To describe this, the ZACUBE-2 satellite currently being tested prior to its launch scheduled for a June 2018 launch window, is used. This mission is designed by the French South African Institute of Technology (F'SATI) Space Program, which is housed at the Cape Peninsula University of Technology (CPUT) in Cape Town, South Africa [1].

The primary objective of ZACUBE-2 is the tracking of vessels within the South African continental shelf. The secondary objective is imaging applications such as ocean colour monitoring and fire tracking [1]. In order to meet these objectives, the satellite will have to be in a 550 km sun synchronous orbit with a 98° inclination for an estimated 2–4 years. ZACUBE-2 has an extremely important indirect objective, which is to demonstrate technology and serve as a precursor to a constellation of low earth orbit satellites whose mission will be continuous maritime vessel tracking and fire detection/monitoring. It is important to predict the space environment in which ZACUBE-2 will dwell in order to define appropriate test/experimental conditions for the future constellation satellites. This is because they will have similar orbit parameters, and each satellite is foreseen to carry at least one experimental/scientific payload. As will be mentioned further in this chapter, one of the future experimental payloads will be the in-orbit testing/measurement of the performance of novel and smart nanomaterials which have shown the potential to significantly increase functionality per unit mass in space. Knowing the space environment of ZACUBE-2 therefore informs the earth-based experiments carried out prior to the constellation design, one of which will be described in this chapter.

In space, a satellite is exposed to radiation from the Van Allen radiation belts (trapped particles), the sun (solar particles), and the galaxy (galactic cosmic radiation (GCR)). Thanks to in-orbit measured data it is now possible to model and predict the space environments that satellites are likely to encounter with relatively high levels of confidence. This can be done using software packages such as SPENVIS [2] or OMERE [3]. These models provide the individual contributions from each of the 3 main radiation sources for specified orbits. GCR are made up of particles ranging from protons to Uranium nuclei, with about 83.3% protons, 13.72% alpha particles, 2% electrons and 0.98% heavier nuclei. Their energies can vary from a few MeV/nucleon to a few GeV/nucleon [4, 5]. The sun emits mainly protons and electrons with energies ranging between about 100 eV to about 3.5 keV for protons [4]. Trapped particles consist of electrons of up to about 7 MeV, protons of up to about 600 MeV and heavier ions of less than about 50 MeV/nucleon [4]. It should be mentioned

http://dx.doi.org/10.5772/intechopen.76993

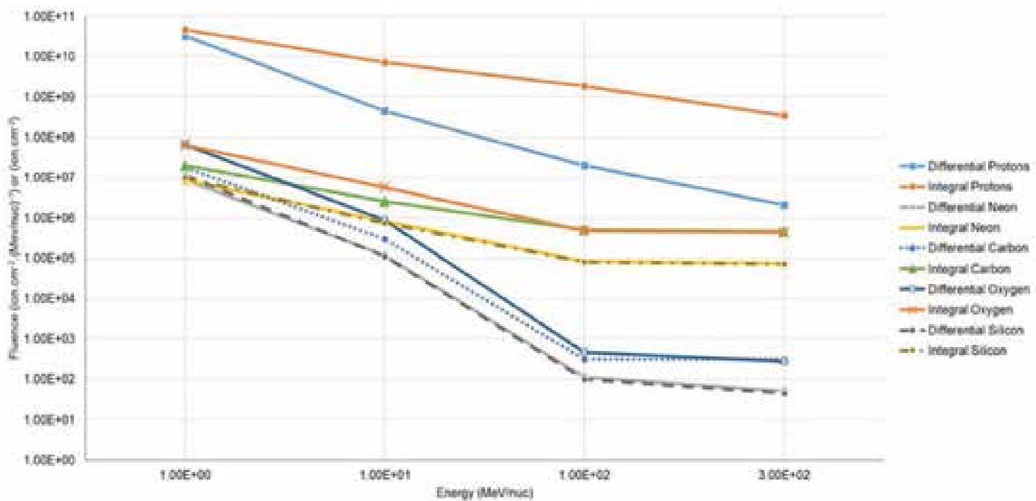

Figure 1. Expected proton, carbon, oxygen, neon and silicon total fluences as a function of energy for the ZACUBE-2 space mission for 4 years in orbit.

that sometimes considerable amounts of neutrons can be encountered in Low Earth Orbit (less than 1000 km altitude). When they occur, they are albedo neutrons coming from earth as a result of the interaction of GCR with the earth atmosphere [6].

In the case of ZACUBE-2, the predicted total fluence of protons, Carbon, Oxygen, Neon and Silicon from all radiation sources is shown in **Figure 1**. Although the range of ions present in the predicted environment for ZACUBE-2 includes more than only these ions, these are very likely to be used for testing purposes. Indeed, protons are the principal source of degradation in space due to ionising particle. This is either directly at low energies (direct ionisation of SRAM memory cells, or solar cell degradation for instance), or indirectly at high energies (by generating secondary heavier ions within devices, which in turn degrade the device functionality). A curve similar to **Figure 1** can be generated for any ion predicted to be present in the intended space mission. This can help define test conditions based on the capabilities of specific ion beam facilities.

2. Ion beams towards space radiation testing

With a clear prediction of the total fluence of protons and heavy ions of various energies that ZACUBE-2 will encounter during an estimated 4 years in orbit, one would seek out test facilities capable of providing protons and other test ions of the appropriate energy ranges. It is indeed after similar simulations and predictions that satellite engineers typically seek out and book time at selected ion beam (accelerator) facilities among the many that are available around the world. The radiation tests, which are in fact single event effect (SEE) tests when they involve damaging electronic devices, are then planned and prepared as a collaborative effort between ion beam operators and mission engineers (typically the radiation engineer or space radiation

subject matter expert). This planning ensures the test hardware, software, and ion beam configuration are optimal to ensure the most cost effective use of the booked beam time.

While the dosimetry is generally carried out by the party providing the ion beam, engineers may or may not need to double check the dosimetry. A quick way to do this can be seen in [7]. That being said, for ions, a simple calculation can be performed to determine the particle flux as a function of the beam diameter and the beam current.

$$Flux(particles/s/cm^2) = \frac{IN}{\pi\left(\frac{d}{2}\right)^2} \tag{1}$$

where I is the beam current in Ampere (Coulomb/s), $N = 1/|particle\ charge|$ is the number of particles per Coulomb (ions/Coulomb) of charge in the beam, and d is the beam diameter in cm. If, for instance, the beam is a proton beam, then $N_{protons} = 1/1.6 \times 10^{-19} = 6.25 \times 10^{18}\, protons/Coulomb$.

Such an analytical particle flux can always be validated by using a thermoluminescent dosimeter (TLD) to measure the particle fluence (in particles/cm^2) for a specified duration.

Mission engineers can use Eq. (1) to work out specific requirements to be sent to beam operators in terms of determining the best trade-off between the flux and the time it takes to achieve the desired fluence, given the beam time available and the nature of the test to be carried out. To test for single event latch-up (SEL), for instance, it is important that the flux be low enough to characterise the SEL cross section, yet high enough to complete the experiments (achieve the desired total fluence) within a reasonable time frame [7].

Before 2013, SEE testing was mainly done at energies higher than 60 MeV, be it for protons or heavy ions. It was in October 2013 that standards for proton testing at energies below 5 MeV were first published in JEDEC's JESD234 release. At the time this chapter is written, there is no commonly accepted standard for heavy ion SEE testing at energies in the 5 MeV range. Be that as it may, when it comes to testing with heavy ions or with low energy protons, it is very important to know as much as possible about the materials that constitute the device being tested. This is because the devices to be tested must be delided (either by wet or dry etching), and this requires knowledge of the materials that constitute the device lid and overlayers. Furthermore, Monte Carlo based simulation packages such as SRIM [8] can be used to calculate the linear energy transfer (LET) of ions as they traverse different layers of materials. This is because even after etching, it is highly likely that there will still be a certain thickness of material left. In order to estimate the energy at which incident ions reach the actual device die, such simulation packages require prior knowledge of the stoichiometry of the traversed materials. Relatively precise knowledge of the chemistry of the layers of materials that are in the device can be acquired by the use of a combination of certain ion beam characterisation methods. This would require sacrificing a device by carefully cutting it in two to expose a vertical cross-section of the interior. A combination of micro-scale particle induced x-ray emission (micro-PIXE) and Rutherford backscattering (RBS), for instance, can provide a detailed knowledge of the elements present within each layer of material and their relative atomic percentages. This should be enough to run a meaningful SRIM simulation. Should there be a need for more precision, further material characterisation such as x-ray diffraction (XRD) and/or x-ray photoelectron spectroscopy (XPS) can be performed on the device cross-section.

http://dx.doi.org/10.5772/intechopen.76993

3. Space applicability of innovative technology solutions

CPUT, through F'SATI and the African space innovation (ASI), has a very strong innovation agenda when it comes to space science and technology. The research activities that result from this drive appropriately illustrate the role ion beams can play when it comes to advancing satellite technology.

With a focus on the space applicability of innovative technology solutions, there are ongoing collaborative research projects being carried out between CPUT/F'SATI/ASI and the National Research Foundation iThemba Laboratory for Accelerator Based Sciences (NRF/iThemba LABS). One of the experiments from this collaboration is detailed in this section to give a practical illustration of how central ion beams have been so far.

Scientific payloads are being designed to investigate the in-orbit performance of two coatings. These are vanadium dioxide (VO_2) coatings and coatings made from W_2B_5/B_4C ceramic composite. While VO_2 smart coatings can provide entirely passive thermal regulation (no power or circuitry is required), coatings made from W_2B_5/B_4C are promising potential nanoscale space radiation shields. Both materials will most likely be part of the scientific payloads in the constellation for which ZACUBE-2 is a precursor. It is therefore necessary to investigate how they are affected by radiation. This is done by irradiating the coatings with particles that are predicted to be encountered, and at the energies at which they are predicted to be encountered. The results of similar experiments can be seen in [9–14].

For this chapter, an experiment is described in which a coating obtained from the pulsed laser ablation of W_2B_5/B_4C was irradiated with 1 MeV protons. This energy is justified by its relatively large proton population predicted in **Figure 1**. Indeed, **Figure 1** indicates that ZACUBE-2 will be exposed to about 8×10^9 protons/cm^2 1 MeV protons (differential fluence over 4 years), and about 9×10^{10} protons/cm^2 of energies greater than 1 MeV (integral fluence over 4 years). One as-deposited sample was used as control sample and three were irradiated at fluences of 1×10^{15} protons/cm^2, 3×10^{15} protons/cm^2, and 5×10^{15} protons/cm^2. While these fluences are higher than those predicted in **Figure 1**, they are large enough to have a deeper understanding of the coating. The structural effects of the incident protons, and the optical transmission measurements in the Ultraviolet, Visible and near Infrared range were investigated. This was to find out whether this coating showed any indication that it could potentially shield solar panels from 1 MeV protons in space.

3.1. Experiment material and methods

The coating was synthesised using a technique called pulsed laser deposition (PLD). With PLD, a target material is ablated with a laser into a plasma plume which then grows as a film/coating onto a substrate. The target used for this deposition was the same B_4C/W_2B_5 pellet used in previous related experiments [9, 10]. The composition of this target was confirmed using XRD [9, 10], and its purity was investigated using yet another ion beam technique called heavy ion elastic recoil detection analysis (ERDA) [15]. The heavy ion ERDA revealed an oxygen contamination of about 10% in the target [9, 10].

The substrates were cut from soda lime corning glass and were approximately 1 × 1 cm in dimension. They were cleaned using a BRANSONIC ultrasonic cleaner (70 W, 42 kHz, ±6%). They were immersed in methanol, acetone, trichloroethylene, distilled water and methanol again for 5 minutes each in an ultrasound water bath. Although for the targeted applications the coatings are to be deposited directly on solar panels, glass was used as substrate for coating characterisation purposes.

The PLD was done using a Q-switched 3rd harmonic Nd − Y AG (Spectra Physics) laser with a wavelength of 355 nm and a frequency of 10 Hz. The laser fluence was $3.265 J/cm^2$. The deposition time was 5 minutes for four identical samples. The target was 3.7 cm away from the substrate in a vacuum chamber at $4 \times 10^{-5}\ mbar$. The deposition was carried out at room temperature.

The samples were irradiated with a focused proton beam emanating from the standard Van De Graaf accelerator based at the materials research department of iThemba LABS (this has been upgraded to a tandetron accelerator). The proton energy was set to 1 MeV, the beam diameter was 6 mm and the beam current was maintained at 10 nA. The proton flux was 2×10^{11} protons/cm^2/s and three samples were irradiated at fluences of 1×10^{15} protons/cm^2, 3×10^{15} protons/cm^2, and 5×10^{15} protons/cm^2 at room temperature in a vacuum chamber at 5×10^{-6} mbar. The fourth sample was not irradiated and was used as control sample.

Scanning electron microscopy (SEM) was used to study the structural effects of the proton irradiation on the coatings. This was done with a Zeiss Auriga field emission gun SEM (FEG-SEM) operated at 5 kV for secondary electron imaging, using an inlens detector and 20 kV for energy dispersive spectroscopy (EDS) analysis. The EDS spectra were collected using an Oxford Instruments X-Max solid-state silicon drift detector.

3.2. Results and discussion

The XRD characterisation of the synthesised coating was consistent with the coatings deposited in [9], where a good understanding of the coating (which do not have the same stoichiometry as the target) can be found.

Figure 2a–d shows the SEM images of the control sample and the samples irradiated at 1×10^{15} protons/cm^2, 3×10^{15} protons/cm^2, and 5×10^{15} protons/cm^2 respectively. One can notice the absence of the droplets that characterise PLD in all the samples. This means that during deposition, the laser beam energy was low enough that there was no sub-surface melting when the laser interacted with the target. Also noticeable are the cracks on the surface of the coatings. These cracks appear on all the samples, meaning they are not caused by irradiation.

Figure 2a shows a sample of the rods that are formed on the coating during deposition. These rods are, on average, about 10 μm long and about 1 μm wide, except for a few, like the rod in **Figure 2b**. On average, there are only about 2 rods in every 100 μm^2. One can suggest that the W content of the coating coupled with the high temperatures inherent to the PLD process might have favoured the formation of these rods [16–20]. However, their formation mechanism is not fully understood yet, mainly because of the way in which they melt under proton irradiation. Indeed, after a fluence of 1×10^{15} protons/cm^{2}as seen in **Figure 2b**, the surfaces of the rods appear to weaken, revealing a rough pattern from underneath. This is the first of

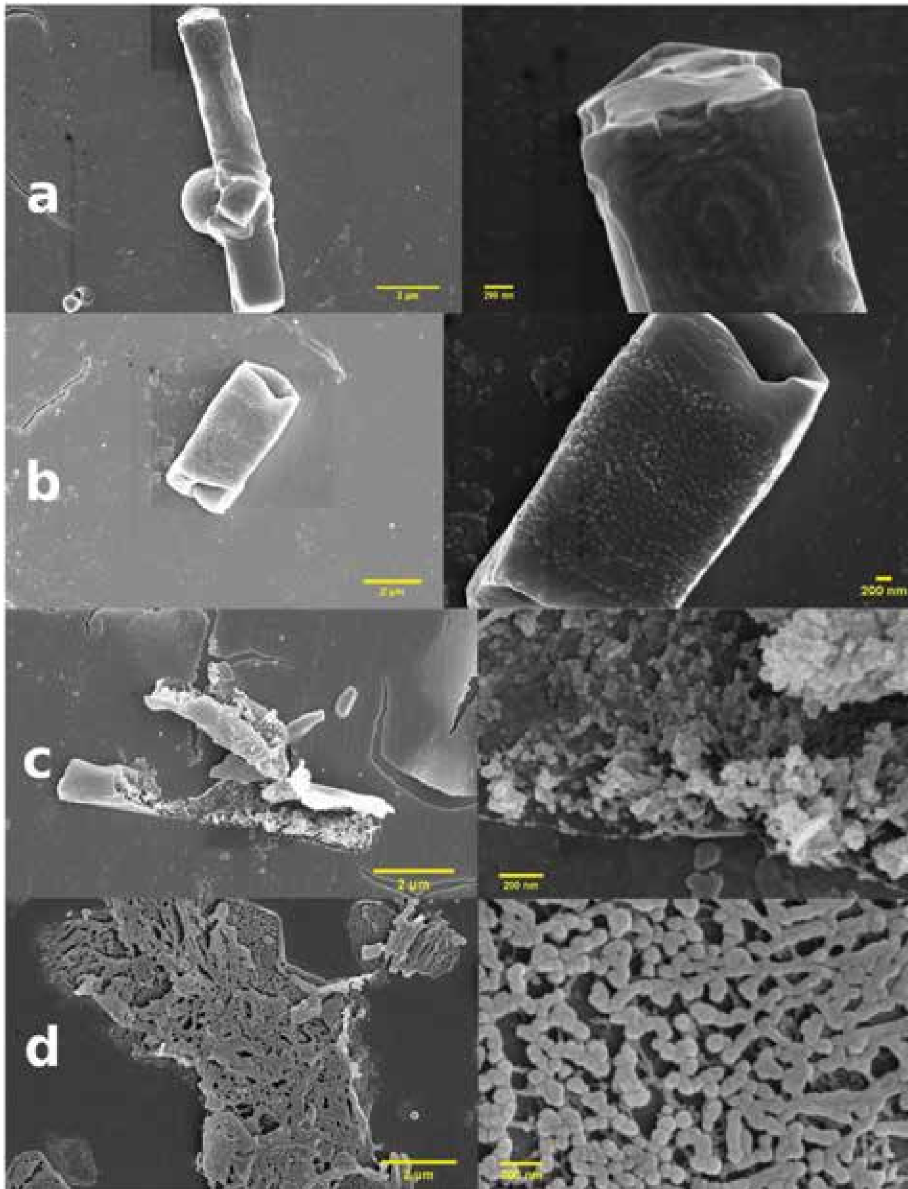

Figure 2. SEM images of non-irradiated and irradiated coatings. (a) as deposited, (b) at 1×10^{15} protons/cm^2, (c) at 3×10^{15} protons/cm^2, (d) at 5×10^{15} protons/cm^2.

three peculiar phenomena observed during the melting of these rods. **Figure 2c** shows the second phenomenon, which occurs after a fluence of 3×10^{15} protons/cm^2. The rod `skins' break open, exposing a very large amount of clustered nanospheres about 60 nm in diameter each. This observation suggests that the rods were in fact sealed enclosures containing nanospheres, analogous to coffee shop sugar sachets if they were completely full. It would be rather speculative to plausibly propose how such rods may have formed a this stage. The third phenomenon

is the melting of the exposed nanospheres into the floor of the coating, as shown in **Figure 2d**. These nanospheres also appear to merge as they melt. As with a previous experiment involving 900 keV proton irradiation, these observations also show strong evidence of lateral diffusion of the energy lost to the coating by the incident protons [10]. It is, however, difficult to predict what would happen at higher proton fluences. Intuitively one may suggest that the nanospheres would completely melt and disappear into the coating, but it is not impossible that unexpected phenomena occur, similar to the rod growth described by Tadadjeu et al. [10].

The atomic percentages of, respectively, B, C, W and O, on top and beneath the cracked surface are approximately the same. This observation strongly suggests a layer-by-layer growth as proposed by Frank and Van der Merwe [21]. There is, however, an inconsistency in that Frank-Van der Merwe growth generally occurs in homoepitaxy, which is not the case of this coating since the substrate and the coating are made up of different materials. A Volmer-Weber growth [22], however, is consistent with heteroepitaxy but does not account for the observed layers. The latter observations and remarks are a very strong indication of a different growth mechanism, the reversed Stranski-Krastanov growth mode. In this mode, unlike in the Stranski-Krastanov growth mode [23], the early stages of the growth starts with nucleation, island formation and coalescence (consistent with heteroepitaxy and with the work

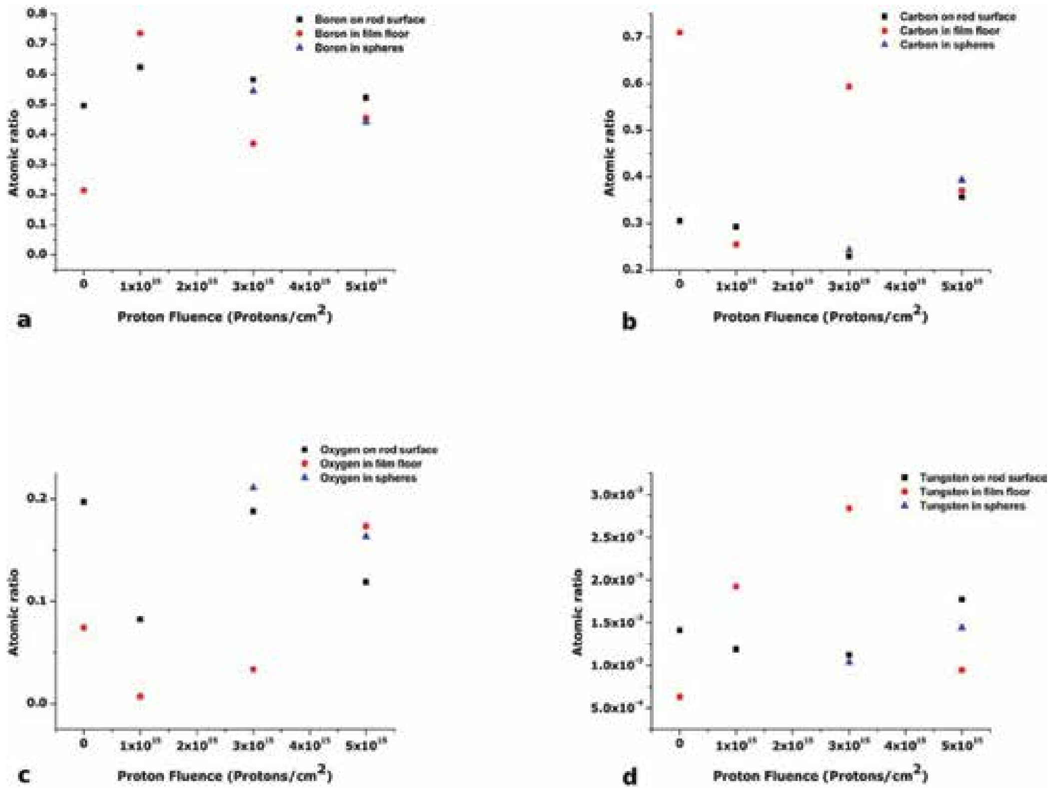

Figure 3. Atomic percentage distribution per element as a function of proton fluence. (a) B atomic percentage distribution, (b) C atomic percentage distribution, (c) O atomic percentage distribution, (d) W atomic percentage distribution.

published by Tadadjeu et al. on the same coating [9]). After coalescence, the film surface becomes an apparent homoepitactic substrate, favouring a Frank-Van der Merwe growth. Chen et al. reported this mode to grow GaN films on Si(111), but he had to induce it through temperature ramping to 1050°C [24]. In this work, this growth mode occurs at room temperature under the specified deposition conditions.

Figure 3a–d shows the atomic percentages of B, C, O and W in the coatings as a function of proton fluence. It is difficult to explain the trends in atomic percentages before the rods break open. This is because the phenomenon in itself is not yet explained. Of particular interest, however, is what happens after the rods break open (at 3×10^{15} protons/cm^2). In **Figure 3a**, B is seen to steadily reduce in the rod surface and in the nanospheres, while at the same time increasing in the floor as the proton fluence increases. O follows the same trend as seen in **Figure 3c**. This trend is to be expected from melting nanostructures, and was previously observed [10]. In **Figure 3b**, C increases steadily in the rod surface and in the nanospheres as it decreases in the floor with an increase in proton fluence. W follows the same trend as seen in **Figure 3d**. These trends suggest that it is possible that nanostructures start forming at higher fluences, just like they did when the atomic percentage of W increased in the nanorods in Tadadjeu et al.'s observations [10]. Indeed, protons lose energy to matter through ionising processes, and non-ionising processes such as the thermal excitation of atoms [25]. Thermal excitation has been reported to favour the growth of nanorods in the presence of Zinc [26] and Tungsten [16] as catalysts. Furthermore, WC nanorods were reported to be synthesised in processes where WO_3 nanorods and thermal treatment played a key role [17–20].

In a broader observation, the melting and the evidence of potential nanostructure formation suggest that at least part of the energy lost by the protons to the coating is dissipated in its

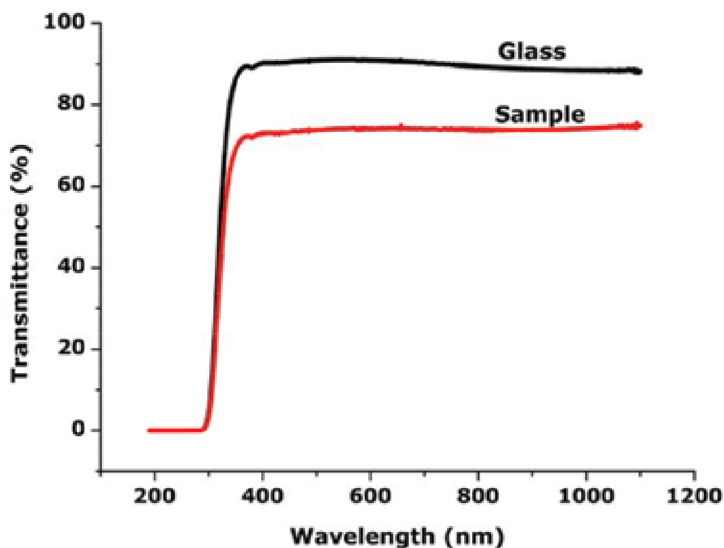

Figure 4. Percentage transmittance of the control sample relative to the glass substrate in the UV–visible and near-IR ranges.

surface rather than being transferred across itself. This makes the coating a promising shield against low energy protons in space.

Given that this experiment was geared towards solar panel shielding, it was necessary to investigate the transparency of the coating. This is to verify that the coating does not compromise the power yield of the panel it is meant to protect. **Figure 4** shows the percentage transmittance of the control sample relative to the glass substrate used at room temperature. While the substrate was about 90% transmitting across the near ultraviolet through the visible to the near infrared spectrum, the coating was about 73% transmitting in the same range. This is promising for solar panel applications in space, as it shows that this coating can be used as a shield to reduce the contribution of low energy protons to solar panel degradation, if its transmittance is deemed acceptable. The implementation of this application, however, would require further testing and optimisation, including the post-irradiation optical characterisation of the coating.

4. Conclusion

This chapter used a space mission and related research work, both active and ongoing at the time it was written, to showcase the role of ion beams in the advancement of space science and technology. The thought process and the factors that guide the specificity of beam parameters for space related testing were described using ZACUBE-2. An experiment that investigated the shielding capability of coatings made from W_2B_5/B_4C for solar panel applications in space was described in details. This experiment showed how a novel space applicable material can be investigated both at a fundamental level and at an application level with the help of ion beams. With a very practical, fresh and current approach, this chapter provides information that can help:

- Satellite engineers to better plan their SEE and related tests, and communicate their needs to ion beam facilities
- Ion beam facilities to better understand and serve the needs of the space community
- Satellite subsystems and device designers to understand how ion beams can contribute to the advancement of their technologies
- The satellite engineering and the ion beam communities to have a broader awareness of each other, which can enhance collaborative and innovative work

Acknowledgements

We thank the French South African Institute of Technology / Cape Peninsula University of Technology and iThemba LABS-National Research Foundation for providing the necessary sponsorship and experimental facilities for this work.

We also wish to thanks Dr. Francious Cummings for his assistance in the SEM and EDS measurements, and Dr. Abdoulaye Diallo for his assistance with UV–Vis transmittance measurements.

Finally we thank the masters students from the 2017 F'SATI course titled "Engineering for the Space Environment" for their simulation of the ZACUBE-2 space environment. While this was part of their course work, it did add value to this chapter. They are: Mr. Shane Martin, Ms. Nicole Drive, Mr. Caleb Hillier, Ms. Mataele Damane, and Ms. Odette Sandrine Bakam.

Conflict of interest

We, the named authors of the paper titled "Ion Beams for Space Applications", confirm that the chapter contains nothing defamatory, and that it may be submitted to IntechOpen with a view to publication as a chapter in the book titled "Ion Beams".

We declare that this manuscript is original, has not been published before and is not currently being considered for publication elsewhere. We wish to confirm that there are no known conflicts of interest associated with this publication.

There are no other persons who satisfied the criteria for authorship but are not listed. We further confirm that the order of authors listed in the manuscript has been approved by all of us. We confirm that we have given due consideration to the protection of intellectual property associated with this work and that there are no impediments to publication, including the timing of publication, with respect to intellectual property. In so doing we confirm that we have followed the regulations of our institutions concerning intellectual property.

We understand that the Corresponding Author is the sole contact for the Editorial process (including Editorial Manager and direct communications with the office). He is responsible for communicating with the other authors about progress, submissions of revisions and final approval of proofs. We confirm that we have provided a current, correct email address which is accessible by the Corresponding Author.

Author details

Sokeng Ifriky Tadadjeu[1,2]*, Balla Diop Ngom[2,3], Shane Martin[1], Robert Ryk Van Zyl[1] and Malik Maaza[2,3]

*Address all correspondence to: ifriky@gmail.com

1 Department of Electrical, Electronics and Computer Engineering, French South African Institute of Technology/Cape Peninsula University of Technology, Bellville, South Africa

2 Nanosciences African Network (NANOAFNET), iThemba LABS-National Research Foundation, Somerset West, Western Cape Province, South Africa

3 UNESCO-UNISA Africa Chair in Nanosciences/Nanotechnology College of Graduate Studies, University of South Africa (UNISA) Muckleneuk Ridge, Pretoria, South Africa

References

[1] Van Zyl R R, de Villiers D, Jansen E, Silberbauer M, Labuschagne A. Nanosatellites as catalyst toward sustainable maritime domain awareness for the African continent. In: Small Satellites System and Services; 21 May – 3 June 2016; Valetta, Malta

[2] Heynderickx D, Quaghebeur B, Wera J, Daly EJ, Evans HDR. New radiation environment and effects models in the European Space Agency's Space Environment Information System (SPENVIS) Space Weather. 2004;**2**:S10S03. DOI:10.1029/2004SW000073

[3] OMERE. 2018. Available from: http://www.trad.fr/en/space/omere-sotftware/

[4] Reitz G. Characteristic of the radiation field in low earth orbit and in deep space. Zeitschrift für Medizinische Physik. 2008;**18**:233-243

[5] Badhwar GD. The radiation environment in low earth orbit. Radiation Research Supplement: Space Radiation Damage and Biodosimetry. 1997;**148**:S3-S10

[6] Clowdsley MS, Wilson JW, Shinn JL, Badavi FF, Heinbockel JH, Atwell W. Neutron Environment Calculations for Low Earth Orbit. 2001;SAE 01ICES2327

[7] Schwank JR, Shaneyfelt MR, Dodd PE. Radiation hardness assurance testing of microelectronic devices and integrated circuits: Test guideline for proton and heavy ion single-event effects. IEEE Transactions on Nuclear Science. June 2013;**2013**:2101-2118. DOI: 10.1109/TNS.2013.2261317

[8] Ziegler JF, Ziegler MD, Biersack JP. SRIM–The stopping and range of ions in matter. Nuclear Instruments and Methods in Physics Research Section B. 2010;**268**:1818-1823. DOI: 10.1016/j.nimb.2010.02.091

[9] Tadadjeu SI, Ngom BD, Msimanga M, Nuru ZY, Kotsedi L, Maaza M, Van Zyl RR. Coatings synthesised by the pulsed laser ablation of a B_4C/W_2B_5 ceramic composite. Thin Solid Films 2015;5935-5939. DOI: 10.1016/j.tsf.2015.09.030

[10] Tadadjeu SI, Ngom BD, Cummings F, Kotsedi L, Msimanga M, Maaza M, Van Zyl RR. Proton-induced nanorod melting in a coating obtained from the pulsed laser ablation of W_2B_5/B_4C. Nuclear Instruments and Methods in Physics Research Section B: Beam Interactions with Materials and Atoms. 2015;**344**:70-75

[11] Madiba IG, Émond N, Chaker M, Thema FT, Tadadjeu SI, Muller U, Zolliker P, Braun A, Kotsedi L, Maaza M. Effects of gamma irradiations on reactive pulsed laser deposited vanadium dioxide thin films. Applied Surface Science. 2017;**411**:271-278. DOI: 10.1016/j.apsusc.2017.03.131

[12] Sechogela T, Kotsedi L, Nkosi M, Sandt C, Madjoe R, Przbylowicz W, Bharuthram K, Maaza M. 2 MeV proton irradiation effects on ZnO single crystal. Surface Review and Letters. 2014;**21**. DOI: 10.1142/S0218625X14500127

[13] Mathevula L. Deep Space Radiations-like Effects on VO_2 Smart Nano-Coatings for Heat Management in Small Satellite [Thesis]. University of South Africa; 2014

[14] Mtshali C, Kotsedi L, Ngom B, Ndlangamandla C, Ndwandwe O, Maaza M. Structural investigation of 2MeV proton-irradiated fullerene nanorods. Nuclear Instruments and Methods in Physics Research Section B: Beam Interactions with Materials and Atoms. 2013;**296**:22-25

[15] Msimanga M, Wamwangi D, Comrie C, Pineda-Vargas C, Nkosi M, Hlatshwayo. The new heavy ion ERDA set up at ithemba LABS gauteng: Multilayer thin film depth profiling using direct calculation and Monte Carlo simulation codes. Nuclear Instruments and Methods in Physics Research Section B: Beam Interactions with Materials and Atoms. 2013;**296**:54-60. DOI:10.1016/j.nimb.2012.11.015

[16] Ngom B, Sakho O, Manyala N, Kana J, Mlungisi N, Guerbous L, Fasasi A, Maaza M, Beye A. Structural, morphological and photoluminescence properties of w-doped Zno nanostructures. Applied Surface Sciences. 2009;**255**:7314-7318

[17] Yan Y, Zhang L, Qi X, Song H, Wang J, Zhang H, Wang X. Template-free pseudomorphic synthesis of tungsten carbide nanorods. Small. 2012;**8**:3350-3356

[18] Shanmugam S, Jacob D, Gedanken A. Solid state synthesis of tungsten carbide nanorods and nanoplatelets by a single-step pyrolysis. Journal of Physical Chemistry. 2005;**109**:19056-19059

[19] Li N, Yan Y, Xia BY, Wang JY, Wang X. Novel tungsten carbide nanorods: An intrinsic peroxidase mimetic with high activity and stability in aqueous and organic solvents. Biosensors and Bioelectronics. 2014;**54**:521-527. DOI: 10.1016/j.bios.2013.11.040 URL http://www.sciencedirect.com/science/article/pii/S0956566313008269

[20] Yan Z, Cai M, Shen P. Nanosized tungsten carbide synthesized by a novel route at low temperature for high performance electrocatalysis. Scientific Reports. 2013;**3**:1646. DOI: 10.1038/srep01646

[21] Frank F, Van der Merwe J. One-dimensional Dislocations. 1. Static Theory. In: Proceedings of the Royal Society of London. Series A, Mathematical and Physical Sciences; 1949. pp. 205-216

[22] Volmer M, Weber A. Keimbildung in übersättigten gebilden. Zeitschrift für Physikalische Chemie. 1926;**119**:277-301

[23] Stranski NI, Krastanov L. Theory of orientation separation of ionic crystals. Sitzungsberichte/Akademie der Wissenschaften in Wien. Mathematisch-Naturwissenschaftliche Klasse Abteilung IIB. 1938;**146**:797-810

[24] Chen NC, Shih CF, Chang CA, Chiu AP, Teng SD, Liu KS. High quality GaN films grown on Si(111) by reversed Stranski-Krastanov growth mode. Physica Status Solidi B. 2004;**241**:2698-2702

[25] Shockley W. Problems related to p-n junctions in silicon. Czechoslovak Journal of Physics. 1961;**11**(2):81-121

[26] Wang N, Cai Y, Zhang R. Growth of nanowires. Materials Science and Engineering. A Review Journal. 2008;(1-6):1-51. DOI: 10.1016/j.mser.2008.01.001

Section 3

Focused Ion Beam Applications

Chapter 5

Ion Beams for Nanoscale Optical Data Storage

Tania Tsvetkova

Additional information is available at the end of the chapter

http://dx.doi.org/10.5772/intechopen.77976

Abstract

The ion beam techniques have been investigated as a novel approach for properties modification and optimization of wide-bandgap materials with view of their uses in submicron lithography and high-density data storage for archival purposes. Focused ion-implantation has been used to write nanoscale optical data into wide-bandgap amorphous materials (hydrogenated amorphous silicon carbide (a-SiC:H) and tetrahedral amorphous carbon (ta-C) films). Scanning near-field optical microscopy is proposed as a novel technique for characterizing the ion-implanted patterns fabricated in amorphous silicon carbide (a-SiC:H). Although a considerable thickness change (thinning tendency) has been observed in the ion-irradiated areas, the near-field measurements confirm increases of optical absorption in these areas. The results are discussed in terms of the competition between the effects of ion implantation and surface milling by the ion beam. The observed effects are important for amorphous silicon carbide and tetrahedral amorphous carbon thin films as extremely stable materials in adverse environments to be used for permanent data archiving. The observed values of the optical contrast modulation are sufficient to justify the efficiency of the method for optical data recording using focused ion nanobeams.

Keywords: focused ion beams, optical data storage, data archiving, ion beam lithography, wide-bandgap amorphous materials

1. Introduction

The use of ion beam techniques is a very attractive method to modify and control material properties [1]. A major aim of materials research has been to develop new solid media and working tools. Joint efforts by industry and research institutions have advanced the use of these developments in the important social area of information technology serving many

IntechOpen

© 2018 The Author(s). Licensee IntechOpen. This chapter is distributed under the terms of the Creative Commons Attribution License (http://creativecommons.org/licenses/by/3.0), which permits unrestricted use, distribution, and reproduction in any medium, provided the original work is properly cited. (cc) BY

fields of our social and cultural life. In these computer-related technologies, rapidly advancing progress has always demanded improved solutions for mass data storage.

Present-day digital memories are subject to lifetime limitations of the order of some 10 years due to physico-chemical deterioration effects at ambient temperatures, so that an enormous effort in continuously rewriting library archives onto freshly prepared media is anticipated. This is true for both recording techniques presently in main use: magnetic and optical disks are affected by thermal, mechanical and chemical events. In addition, magnetic information can also be destroyed by electromagnetic fields. Thus, for cultural values of all kinds to be preserved for future generations, other ways have to be found providing unlimited lifetimes. Safe archival data storage has become an urgent issue. Electronic libraries already constitute an important issue in this field. Foreseeable total storage volumes approach the order of 1 Eb, or 10^{18} b. Thus, it is of paramount interest to find a truly permanent recording technology with the additional condition of higher storage density. The steadily increasing amount of digital data of global order of zetta bytes will require novel storage techniques of ultra-high density, possibly in the nanoscale [2].

The main aim of this chapter is to present some novel approaches to this problem. The reading of such digital data with nanometer dimensions is also subject to further technical progress. In this chapter, how ion nanobeams are used to write data bits of nanometer diameter into new generation storage materials is presented and photon near-field technology is employed to read this novel kind of digital memory.

2. Optical contrast formation in wide-bandgap materials

During many years of development, ion beams have found important applications to the modification of materials. While ion-implantation technology has revolutionized the industrial production of electronic devices, optical applications have so far been scarce. This state of affairs is quite astonishing, since optical changes in certain wide-bandgap materials, in particular in semiconductors, are very pronounced and easily produced. Both physical processes and applications to the optical modification of certain insulators have been reviewed in a dedicated publication by Townsend et al. [3].

Recently, ion beam-induced optical modification of wide-bandgap materials has been successfully employed for the development of novel methods for high-density data storage [4, 5]. There have been two markedly different kinds of approaches: a method based on ion beam-induced amorphization of wide-bandgap crystalline materials [4] and a method based on ion beam optical modification of wide-bandgap amorphous materials [5], both using highly focused ion nanobeams.

2.1. Ion beam-induced amorphization of wide-bandgap crystalline materials

The optical properties of crystalline insulating materials can markedly be modified by irradiation with energetic ions. Radiation damage causes dramatic changes of the optical absorption in the bandgap energy regime of crystalline insulating materials. In particular, if the state of amorphicity can be introduced, absorption changes will be strongest. The exposed areas of

such materials absorb and reflect light more strongly than non-irradiated ones. In this way, optical contrast is created between irradiated and non-irradiated areas, if suitable masks are applied or alternatively, computer-controlled focused ion beam (FIB) equipment is used [6].

With modern equipment, ion beams of sufficient intensity can be focused to submicron dimensions. Thus, both analog and digital information can be recorded with pixel densities of Gbit/cm^2 to Tbit/cm^2. Initially, focused ion beams of inert gas ions (Ar^+, Ne^+, Xe^+), produced by gas-field ion sources (GFIS), were employed to generate optical patterns of both kinds in wide-bandgap crystalline materials. This is demonstrated in **Figure 1**, showing digital data storage (ionographic process) in crystalline films of group-IV elements of the periodic system and in **Figure 2**, where analog information storage in polycrystalline silicon carbide (pc-SiC) by focused Ne^+ beam is presented. Usually, this type of optical data storage is read in light transmission mode (**Figure 3**), hence highly transparent optical substrates are used, like Al_2O_3 (sapphire).

Crystalline films of group-IV elements of the periodic system, such as Si, SiC and C_D (diamond), are best suited for this novel data recording process, due to the marked differences in their absorption coefficient in the two different phases—crystalline and amorphous (**Figure 4**). As shown, due to their higher bandgap energies, the optical "contrast window" for SiC and C_D (diamond) is shifted toward the ultra-violet part of the spectrum.

2.2. Ion beam modification of wide-bandgap amorphous materials

Since the crystalline-amorphous contrast-based data storage in thin film crystalline materials is usually read in light transmission mode, it requires the use of solid transparent substrates, for example, quartz or sapphire that meet certain requirements. To produce analog patterns in pc-Si on sapphire written by focused Ar^+ or Ne^+ beam (**Figure 2**) the procedure starts first with plasma deposition of a-SiC:H film with moderate absorption. To achieve the needed initial high film transparency for the aimed high optical contrast after irradiation, the next step is

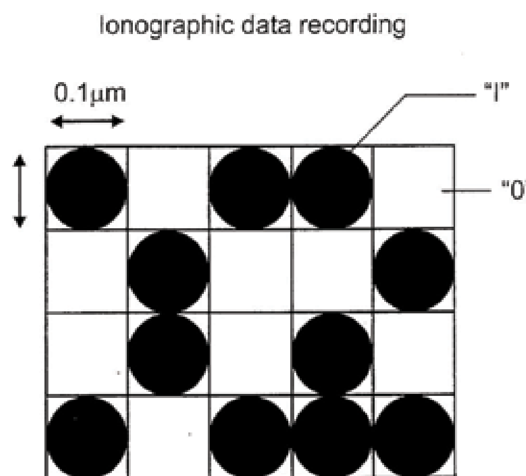

Figure 1. Crystalline-amorphous digital pattern obtainable by writing with a focused ion beam into a thin film of Si, SiC or C_D [5].

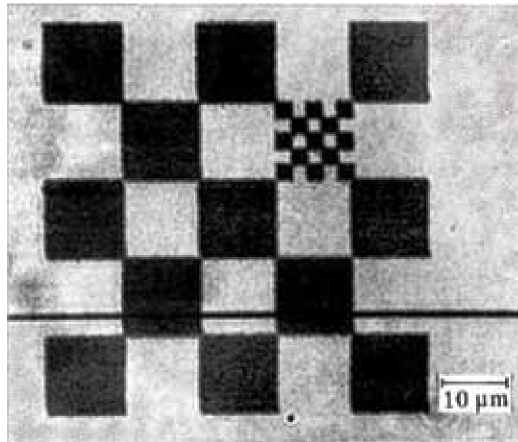

Figure 2. Crystalline-amorphous analog pattern in poly-crystalline SiC on a sapphire substrate by using a 20 keV focused Ne beam [5].

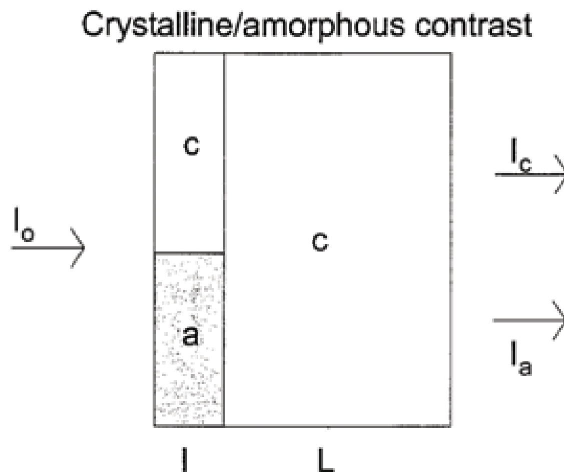

Figure 3. Principle of crystalline-amorphous contrast. Incident light of intensity I_0 traverses a thin layer l of material consisting of crystalline and amorphous areas on a thick transparent substrate. The transmitted beams I_c and I_a have different intensities [5].

to produce low absorption pc-SiC by crystallizing the a-SiC:H film in a special hot furnace at temperatures as high as 1400°C. This high temperature requires the use of high-quality expensive sapphire substrates. Only after this costly technological step the ion irradiation is performed to achieve the aimed optical contrast (**Figure 5**) and generate optical information patterning of the pc-SiC (**Figure 2**) [7].

On the other hand, although these investigations have shown the feasibility of this method for achieving the initially stated goals for permanent safe archival dense data storage, it has been stressed that the whole process requires also further high-technology processing steps, for example, the use of Ar^+, Ne^+ and Xe^+ nanobeams of nA intensity, the equipment systems

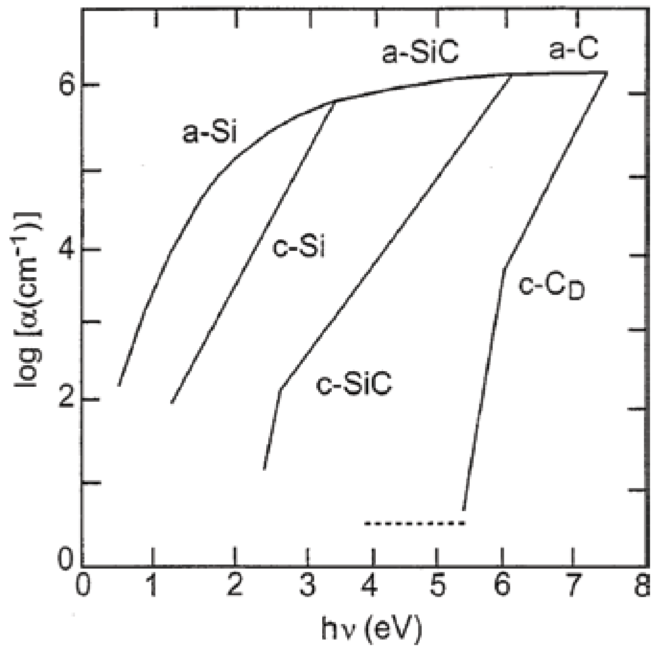

Figure 4. Working range of different group-IV semiconductors for crystalline-amorphous contrast. Note that the amorphous phases follow a common curve, whereas the crystalline phases are distinctly different [5].

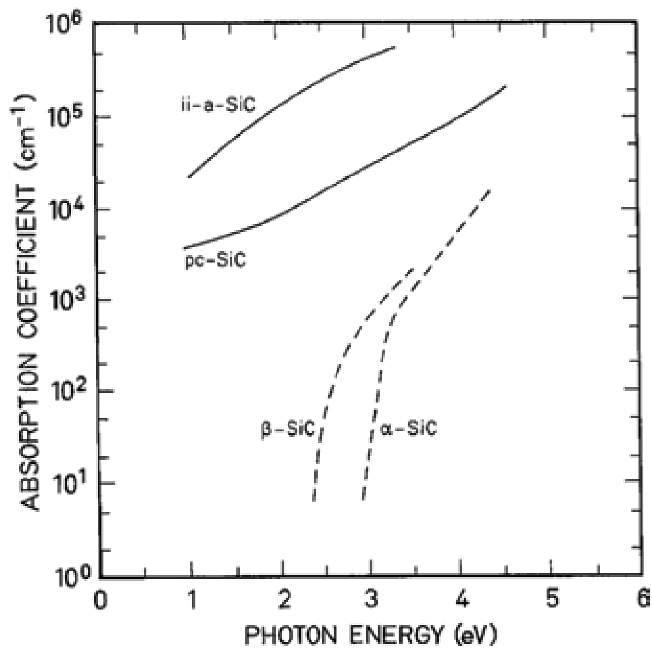

Figure 5. Optical absorption coefficient of SiC films (full lines) as obtained after poly-crystallization (pc-SiC) and irradiation with Ar^+ ions (ii-a-SiC). The dashed lines refer to monocrystalline α- and β-SiC [5].

for which are rare to find. The authors have admitted that such equipment is not yet commercially available even though, depending on the importance of the respective data, costs nevertheless look affordable [8].

The above costly requirements have been later avoided with the development of yet another optical data storage method, using the ion beam-induced optical contrast in wide-bandgap amorphous materials by their structural-and chemical-based optical modification. Previous investigations of Tsvetkova et al. [9] on the optical effects of Ar^+, N^+ and O^+ bombardment of thin chalcogenide films of the As-Se system at comparable implantation conditions, have shown that the chemically active N^+ and O^+ species have a more pronounced effect on the optical characteristics of the films, even though Ar^+ has a higher mass and hence would yield higher amounts of radiation defects. The effect of the higher changes in the absorption coefficient and refractive index, induced by the N^+ and O^+ implantation as compared to the Ar^+ bombardment, has been attributed, apart from the increased amount of radiation defects, also to their chemical modification by reacting with the As-Se host atoms and creating new bonds, affecting the amorphous material electronic structure and hence modifying the optical properties.

In the case of the a-SiC:H amorphous material, used as a source material for the crystallization step to produce a highly transparent pc-SiC film and thus achieve maximum optical contrast with the Ar^+ ion irradiated a-SiC, a new route has been suggested to avoid the crystallization step and start with as transparent as possible initial a-SiC:H material even though it will be somewhat less transparent than the pc-SiC. Indeed, the optical bandgap width of a-$Si_{1-x}C_x$:H is known to be easily controlled by controlling its stoichiometry (x) and may vary between 1.8 and 3.0 eV [10].

On the other hand, for the achieved optical contrast, it is not the absolute values of the optical absorption of the initial material and the irradiated one but the relative difference between the two absorption coefficients. Thus, even though this coefficient for the starting a-SiC:H material is higher than the one for pc-SiC, if the ion irradiated a-SiC:H can be rendered still more absorbing by using instead of Ar^+ bombardment some more chemically effective ion species, competing results can be easily achieved with the ones for the method based on crystalline-amorphous contrast. Such chemically active dopants have been known to be Ge and Sn, effectively reducing the optical bandgap of a-SiC:H, when added during the deposition process [11].

A considerably higher optical effect has been achieved in a-SiC:H films by ion implantation of Ge and Sn as compared to the effect of Ar bombardment [12], as shown in **Figure 6**. (The sample preparation conditions of the a-SiC:H films for this study, together with the parameters of the ion implantation processing of the samples employed, are described elsewhere [12, 13]; it is worth though to mention here that simple Corning glass was used for the transparent substrates instead of sapphire.) This effect is manifested by an optical transmission edge shift to the larger wavelengths, accompanied by a decrease in the transmission coefficient, as a result of the ion implantation.

The registered difference in the optical effect for the three types of ions is attributed to the different chemical nature of the implanted elements rather than to the radiation effect difference due to the varying parameters of the implanted species. This has been ensured by

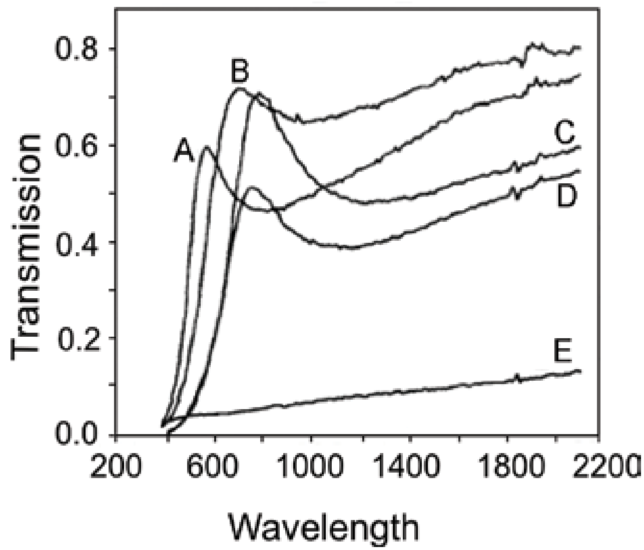

Figure 6. Transmission spectra of unimplanted (A) and implanted with Ar^+, Ge^+ and Sn^+ at D = 10^{17} cm^{-2} (spectra B, D and E, respectively) and with Sn $^+$ at D = 10^{16} cm^{-2} (C) a-$Si_{0.82}$ $C_{0.18}$:H films [12].

	Ar	Ge	Sn
E (keV)	30	50	75
R_p (nm)	37.1	34.3	38.0
ΔR_p (nm)	14.8	12.1	11.5

Table 1. Energies, normalized projected range R_p and standard deviation ΔR_p for the three types of implanted ions [12].

an appropriate choice of the film thickness (d = 100 nm) and ion energies, so as to match the resulting projected ranges R_p and standard deviation ΔR_p for the three elements, as estimated approximately using LSS theory and SRIM program [14]. (See **Table 1** [12]).

Figure 7 demonstrates the changes of the absorption coefficient α with the dose both for Ge^+ and Sn^+ (**Figure 7a** and **b**, respectively) implantation in a-SiC:H films. It is easily noticed that the ion implantation increases α and shifts the absorption edge to the lower energies even for the lowest dose (D = 10^{15} cm^{-2}). Saturation is reached gradually when increasing the dose. Determination of the absorption coefficient α for the highest implantation dose of Sn^+ (D = 10^{17} cm^{-2}) is hampered by the drastic decrease of transmission (**Figure 6**), related to certain metallization in this case, and hence it is not presented in the figure.

The results for the dose dependence of the Tauc optical gap E_g for the cases of ion implantation with Ge^+ and Sn^+ are shown in **Table 2** [12].

The observed optical properties modification effects induced by the ion implantation of a-SiC:H films signify a change in the energy spectrum of the electronic states. The observed change could be related to breaking of bonds and increase of disorder due to ion bombardment for the three elements (Ar, Ge and Sn), and for the case of Ge and Sn—also to some

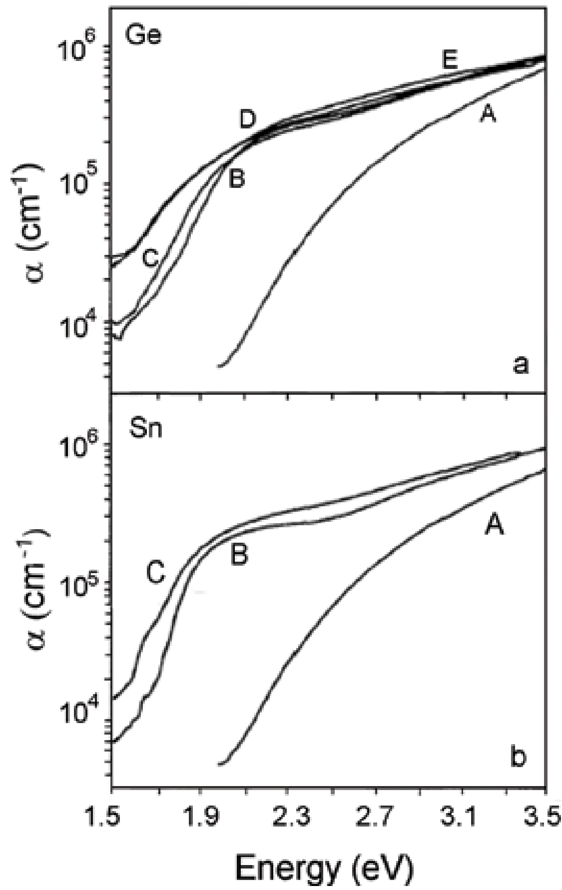

Figure 7. Absorption coefficient α of unimplanted (A) and implanted with Ge^+ (a) and Sn^+ (b) a-$Si_{0.82}C_{0.18}$:H films at doses (in cm^{-2}): 10^{15}(B), 10^{16}(C), 5×10^{16}(D) and 10^{17}(E) [12].

Eg [eV]				
	x = 0.18		x = 0.35	
D [cm^{-2}]	Ge	Sn	Ge	Sn
0	2.08	2.08	2.32	2.32
1×10^{15}	1.64	1.66	2.05	1.85
1×10^{16}	1.58	1.53	1.99	1.77
5×10^{16}	1.22	—	1.83	0.89
1×10^{17}	1.22	—	1.68	0.23

Table 2. Tauc optical gap E_g of Ge^+ and Sn^+ implanted a-$Si_{1-x}C_x$:H films with different carbon content (x = 0.18 and x = 0.35) at different doses [12].

accompanying formation of additional bonds between the implanted ions and the atoms of the alloy host material, as confirmed by vibrational spectroscopy (IR and Raman) [13], X-ray photoelectron spectroscopy (XPS) [15] and Mössbauer spectroscopy analysis [16].

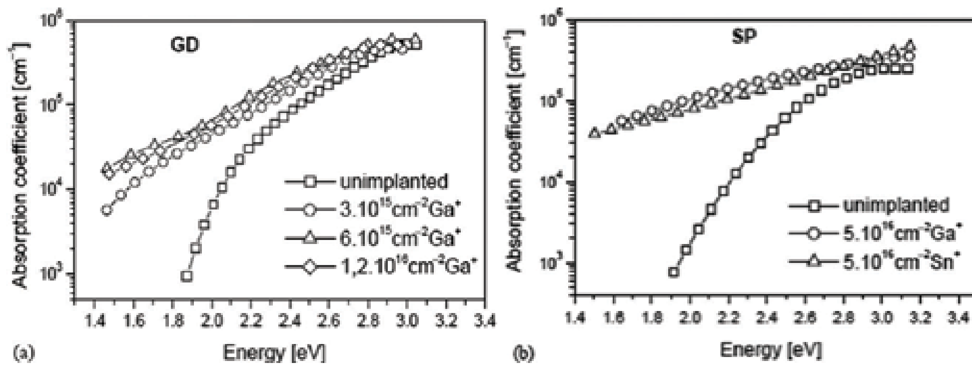

Figure 8. Absorption coefficient α of a-$Si_{1-x}C_x$:H (x = 0.15) films implanted with: (a) Ga^+ at a dose $D_1 = 3 \times 10^{15}$ cm^{-2}, $D_2 = 6 \times 10^{15}$ $cm^{-2}$and $D_3 = 1.2 \times 10^{16}$ cm^{-2}; (b) Ga^+ and Sn^+ at a dose $D = 5 \times 10^{16}$ cm^{-2} [17].

As has been noted about the results presented in **Figure 7**, they clearly show that the ion implantation of Ge and Sn in a-SiC:H films increases α and shifts the absorption edge to the lower energies even for the lowest dose (D = 10^{15} cm^{-2}) and saturation is reached gradually when increasing the dose. Thus, the absorption coefficient change may reach ~ 2 orders of magnitude in the visible light range of the spectrum even applying quite moderate ion doses, allowing for a choice of lower ion doses aiming at a reduced cost. However, to proceed to optical patterning of a-SiC by focused Ge^+ or Sn^+ ion beams, some specially designed focused ion beam (FIB) systems have to be used. And although such custom-built Ge^+ and Sn^+ FIB systems do exist and are available at request, it appeared desirable to explore the possibility to use instead the much more widely spread commercial FIB systems, using Ga^+ focused ion beams for patterning.

Hence, further experiments were focused on the achievable optical contrast in a-SiC:H films by Ga^+ ion implantation, using a wide range of ion doses [17]. The results are presented in **Figure 8**, which clearly shows that the optical effects for the Ga^+ implantation are comparable with the ones for Ge^+ and Sn^+ for similar range of ion doses (**Figure 8b**). It is also demonstrated that for the case of Ga^+ as well, lower doses of the order of 10^{15} cm^{-2} may be sufficient to justify the requirements for optical patterning of a-SiC for optical data storage (**Figure 8a**). Possible applications of these results in the area of submicron lithography and high-density optical data archiving have been suggested with regard to the most widely spread focused microbeam systems based on Ga^+ liquid metal ion sources.

3. Optical patterning of wide-bandgap amorphous materials

The work on the optical patterning of wide-bandgap amorphous silicon carbide for nanoscale archival data storage and submicron lithography constitutes a further step to extend the use of optical crystalline materials, as data storage media, to the new class of wide-bandgap amorphous materials with their numerous technological and ecological advantages. It also extends the use of the FIB systems based on gas-field ion sources (GFIS), implemented as a patterning tool, to the use of the more versatile and widespread FIB systems based on liquid-metal ion sources (LMIS), which are also preferred in many practical applications for some of their superior features.

3.1. Focused ion beam (FIB) systems used for nanoscale patterning

Nanoscale focused ion beams (FIBs) represent one of the most useful tools in nanotechnology, enabling nanofabrication via milling and gas-assisted deposition, microscopy and microanalysis and selective, spatially resolved doping of materials. These instrumentation developments, that have come to play a central role in nanotechnology, have made it possible to create a beam of ions focused to a spot size on the order of just a few nanometers [18].

The ion source is a core part of a FIB system, and its function is to produce an ion beam. [19] There are, indeed, various types of ion sources and a wealth of different ion species, some of which are commercially available, and others that exist in custom-built research laboratory setups only, to be used in niche applications or to be further developed. The state of the ion source technology is historically an enabling factor for FIB instruments.

Beginning in the late 1970s, ion sources with the necessary characteristics began to appear, and one type that soon came to dominate was the liquid metal ion source (LMIS).With an extremely simple construction, high brightness and robust performance, the LMIS has become a central driver in the widespread adaptation of focused ion beam techniques in nanotechnology [20].

In the manufacturing process of the LMIS, a tungsten needle with the tip diameter of 5–10 μm can be made by electrochemical corrosion and then adhere molten liquid metal on the tip of tungsten needle. An electric field is applied on the tip; then the liquid metal on the tip is formed to Taylor cone under the strong electric field force. The electric field intensity of Taylor cone can be as high as 10^{10}V/m, and the metal ions in the surface layer of liquid metal would escape in the form of field evaporation, resulting in the ion beam. The schematic diagram LMIS with a two-lens system is presented in **Figure 9**.

Another type of field-ionization sources (discovered earlier than LMIS) is based on ionizing molecules adsorbed from their gas phase. These gas field ion sources (GFIS) are in use for producing ion beams of hydrogen and noble gases by condensing them first, followed by electric field ionization on an atomically sharp needle, this way creating very small (sub-nm) diameter

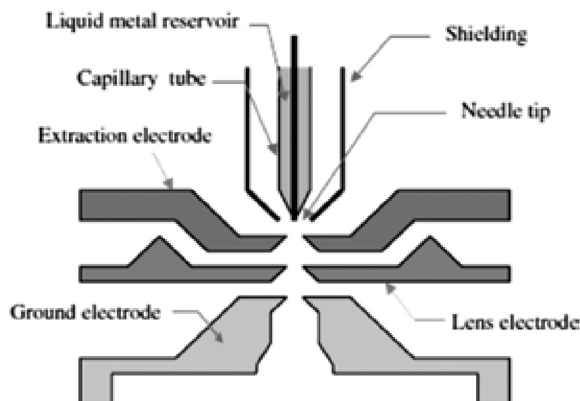

Figure 9. LMIS in a two-lens system.

http://dx.doi.org/10.5772/intechopen.77976

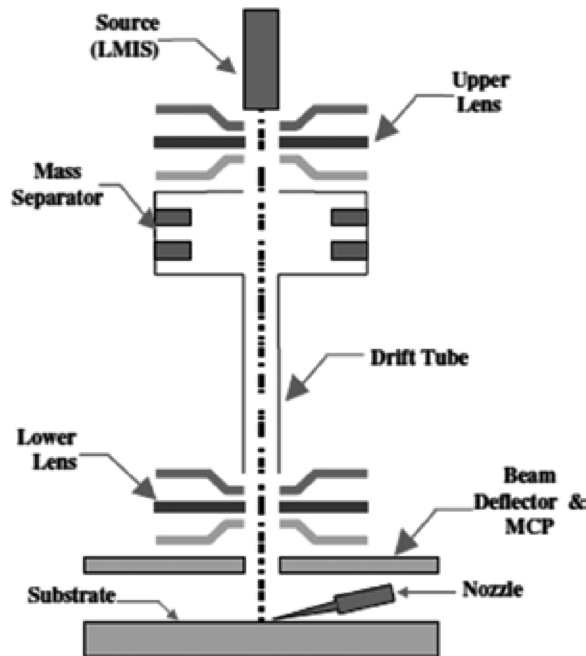

Figure 10. Schematic diagram of LMIS-based FIB.

and small current beams. Major drawback of GFIS though is that it produces very low current on final focal spot [21]. For many practical applications, LMIS-based FIBs are the preferred choice.

The schematic diagram of the LMIS-based FIB is presented in **Figure 10**. The focusing and scanning equipment is generally constituted by a double electricity lens system, beam blanking assembly and quadruple deflection electrode. The sample station includes the sample stage, the detector and the gas injection system. The sample can move along with x, y, z axis, rotate around z axis and move obliquely in five degrees of freedom when it is placed on the stage. In order to improve the controllability and the speed of the nanofabrication, a gas injection system is also introduced in the sample chamber. Further results presented in this work are implemented using the LMIS-based FIB.

3.2. Amorphous silicon carbide and tetrahedral amorphous carbon materials

Hydrogenated amorphous silicon carbide (a-SiC:H) alloy films have great technological potential as structural materials for high-temperature electronics and for various optoelectronic elements and devices designed to operate in aggressive environments (acid vapors, radiation, open space, etc.) [22, 23]. An important feature underpinning the material's environmental robustness is the comparatively wide bandgap which may be tailored in the range 1.8–3.0 eV.

The material can be prepared in thin-film form on different substrates by chemical vapor deposition [24] or by employing a radio-frequency reactive magnetron sputtering method [25]. Reactive sputtering is a convenient method to prepare a-SiC:H films where low-density-of-states

material is not required, as is very often the case. Mechanical, optical and electrical parameters of the material can be controllably varied by changing the relative composition of the constituent elements. In addition, control of electronic and optical properties of such materials can be achieved using ion implantation [26, 27].

Thin films of amorphous carbon (a-C) also referred to as diamond like carbon (DLC), have received considerable attention due to their intrinsic highly attractive properties. Amorphous carbon (a-C) is a disordered phase of carbon without long-range order, containing carbon atoms mostly in graphite-like sp2 and diamond-like sp3 hybridization sites. Depending on the relative concentrations of sp2- or sp3- hybridized carbon, a-C has shown excellent physical properties such as high hardness, low friction coefficient, chemical inertness, relatively high thermal conductivity and optical transparency [28]. The term tetrahedral amorphous carbon (ta-C) is used to describe amorphous carbon films with a large percentage of *sp*3 bonding (up to 87%). The films are manufactured using a variety of techniques, including filtered cathodic vacuum arc (FCVA), pulsed laser deposition (PLD) and mass selected ion beam deposition (MSIBD) [28, 29]. The high *sp*3 content in the films results in unique properties that include extreme hardness (~70 GPa), chemical inertness, high electrical resistivity and wide optical bandgap. These properties also offer some advantages as compared to another wide optical bandgap material—silicon carbide (SiC)—for uses in nanoscale optical data recording for archival information storage using focused ion beams (FIB) techniques.

3.3. FIB optical patterning of a-SiC and ta-C films

The use of ion implantation as a method of introducing additional elements to modify the material chemically and hence its electronic characteristics (the bandgap and the related optical and electrical properties) is an attractive means to control these properties. It is particularly of interest in connection with the emerging techniques of easily operated ion microbeams and the possibilities they reveal for fabricating various sophisticated planar structures [30].

Recently, using the fast developing technology of ion microbeams, promising results have been obtained for the possible application of thin polycrystalline silicon carbide films in high-density optical data storage and submicron lithography [6–8]. This approach has been further developed by implementing ion doping of amorphous silicon carbide films with focused ion beam (FIB) systems that use Ga^+ or other chemically active ion species as implants [12, 17].

The widespread use of FIB systems based on Ga^+ LMIS has prompted special attention to the choice of Ga^+ as the implant species in further experiments. Investigations on Ga^+ broad-beam implanted a-SiC:H films have shown various structural and chemical modification changes, resulting in an effective optical bandgap decrease and considerable optical absorption coefficient increase [17]. The underlying mechanism, as studied by IR and Raman measurements, involves breaking of Si–H and C–H bonds and apparent loss of H. An increased Si–C bond breaking is revealed and formation of Si–Ga bonds, implying that Ga substitutes for the C atom in the C–Si–H bond due its lower electronegativity [31, 32]. Yet, due to the low melting point of Ga (Tm = 29.8°C), some part of the implanted Ga ions are apparently incorporated as Ga-clusters rather than directly bonded to host atoms [33].

The computer-controlled focused ion-beam system IMSA-100 [34] working with a Ga^+ LMIS was used to create a preliminary chosen optical pattern in a-SiC:H films [17]. The

computer-generated pattern, shown in **Figure 11**, consists of several line series and chess-board-type fields with different sizes and doses of implanted Ga^+. The shorter line series LS1 (size 2.5/2.5/20 mm) and the longer ones LS2 (size 5/5/40 mm) were obtained with Ga^+ ion doses in the range $D = 5 \times 10^{15}–2 \times 10^{17}$ cm^{-2}. The big chess-board-type field (BCF) (size 20 mm) and the smaller chess-board-type fields SCF1 and SCF2 (size 10 mm) were obtained with doses $d_1 = 2.5 \times 10^{16}$ cm^{-2} (BCF and SCF1) and $d_2 = 4 \times 10^{16}$ cm^{-2} (SCF2). The figure shows the potential of this method for different applications as diverse as high-density optical data storage and direct writing of submicron lithographic masks for microelectronics and optoelectronics.

Similarly, programmable computer-controlled focused ion-beam system, working with a Ga^+ LMIS, was used to create a preliminary chosen optical pattern in ta-C films [35]. Samples of

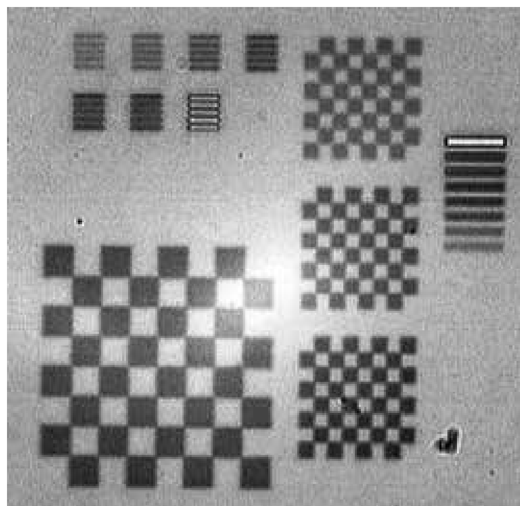

Figure 11. Micron-scale pattern on an a-SiC:H film written with the FIB using a 15 pA Ga^+ − ion beam. The size of the big chess field is 20×20 mm^2 [17].

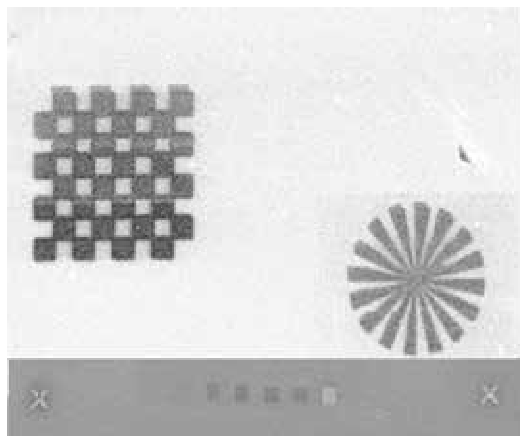

Figure 12. Contrast images in ta-C film, written with the FIB using a 15 pA Ga^+ − ion beam, and dependence of absorbance of implanted areas on Ga^+ fluences (squares 10×10 μm^2): 1e14, 5e14, 1e15, 5e15, 1e16, 5e16 cm^{-2} [35].

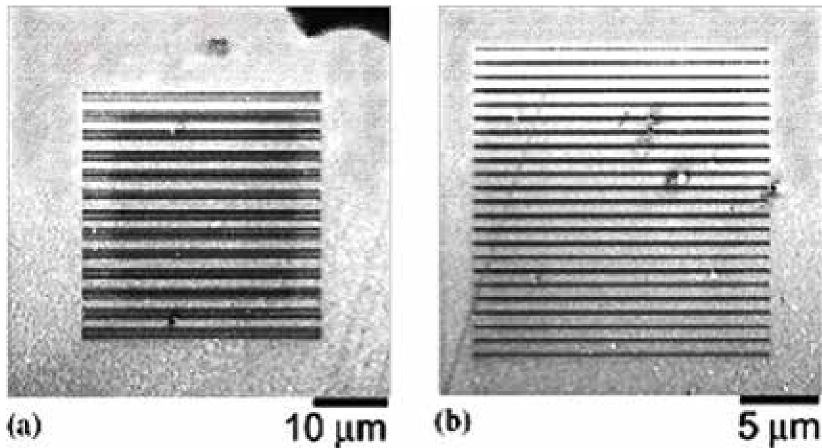

Figure 13. Secondary ion image of (a) triplet lines pattern (100 nm width, 300 nm separation between adjacent lines in each triplet and 1000 nm separation between triplets) and (b) low-density set of single lines (100 nm width and 900 nm separation), in an Al-coated a-SiC:H thin film, written with FIB system using focused Ga^+ ion beam [36].

thin ta-C films (d~40 nm) were deposited on Corning glass substrates using a commercial FCVA system (Commonwealth Scientific Corporation). The Ga^+ focused ion beam (FIB) patterning was performed with NVision 40 Crossbeam System (Zeiss) using 1, 10, 80 pA Ga^+, 30 keV and a range of Ga^+ ion doses (**Figure 12**).

Some further results of the experiments at the nanoscale by patterning a-SiC:H samples with Ga^+ FIB are demonstrated in **Figure 13** [36]. The secondary ion images recorded immediately after the FIB implantation in the vacuum chamber are shown in the figure. Each pattern consists of a set of lines with 100 nm width separated differently. The secondary ion images show that a line thickness as small as 100 nm has been realized.

4. Near-field technique uses for reading nanoscale optical data

The optical properties of nanoscale structures need to be characterized with a "super-resolution" technique, for example, near-field techniques. Additionally, the ion irradiation induced sputtering may cause ablation of the a–SiC:H film, resulting in changes in the surface topographic features. Hence, a technique mapping the topographic features of the patterns, such as atomic force microscopy (AFM) [37, 38], is also needed to characterize the modified surfaces. From these points of view, scanning near-field optical microscopy (SNOM), supplied with shear force technique providing also topographic data, is a promising method that can simultaneously obtain optical and topographic images of the samples [38–41].

Atomic force microscope (AFM) (Dimension 3000 Digital Instruments) was used to analyze the topography of the fabricated patterned samples in these studies [39]. Scanning near-field optical microscope (SNOM) was used to study the changes in local optical absorption of the irradiated (patterned) areas as compared to the nonirradiated ones [42].

A schematic diagram of the SNOM equipment used is presented in **Figure 14** [42]. An unpolarized He-Ne laser (633 nm) beam is used to illuminate the sample from its nonpatterned

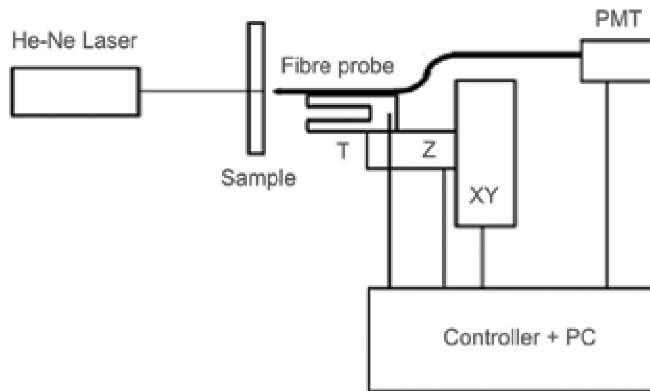

Figure 14. A schematic diagram of SNOM set-up. Photomultiplier tube (PMT); quartz tuning fork (T); piezoelectric stage for scanning (XY); piezoelectric actuator (Z) [42].

side of the transparent substrate. The transmitted light is then collected with a sharpened optical fiber tip positioned in near-field proximity to the patterned surface and is measured with a photomultiplier tube (PMT). The tip is raster scanned across the sample while kept at a constant tip-surface distance, and topographic data and optical images are recorded simultaneously. The tip-surface distance is monitored with nonoptical detection technique using shear-force feedback, where the tip is oscillated by a quartz tuning fork (T) and oscillation amplitude is monitored as variations of the electric impedance of the tuning fork. While the tip scans the sample, the piezoelectric actuator (Z) moves it so as to keep the oscillation amplitude constant, tracing the topography. The typical diameter of the fiber tip end, fabricated by chemical etching, is 100 nm and this determines the optical resolution.

4.1. Atomic force microscopy characterization of FIB patterns

These near-field techniques were used to study Ga^+ FIB patterns in a-SiC:H films [42]. Sample preparation was as follows: thin films of a-$Si_{1-x}C_x$:H (x = 0.15) were deposited by RF (13.56 MHz) reactive magnetron sputtering onto Corning glass substrates. The composite target, comprising of mono-crystalline (100) silicon wafer with chips of pure graphite placed on top, was sputtered in an Ar-20%H_2 gas mixture. The deposition conditions typically were RF power of 150 W, power density 1.91 W/cm^2, total gas pressure 1P, substrate temperature 275°C and graphite-to-silicon target ratio 0.025. Talystep profilometer and optical measurements were used to determine the film thickness d~200 nm. The carbon content (x) of the films was determined by Rutherford backscattering spectrometry (RBS) to be 0.15.

Computer-operated FIB system, using focused Ga^+-ion beam implantation, was applied to produce various pre-designed optical patterns in these samples. The FIB system used was IMSA-Orsay Physics, supplied with a “charge neutralizer” (e^- beam shower). The obtained patterns are presented in **Figure 11**. The figure represents an optical micrograph of a a-SiC:H thin film with a variety of FIB-created patterns. They consist of chess-board-like (CBL) patterns and series of lines with different doses (SL). The optical density of the irradiated areas is increased due to the ion implantation; hence, they are seen as dark regions.

Topographic images of the irradiated areas were recorded with AFM before conducting the SNOM experiments. The results for the recorded CBL and SL structures are shown in **Figure 15**.

The AFM analysis of these results reveals that the irradiated areas are topographically lower. This is supposedly due to the ion beam-induced ablation of the thin film. A cross-sectional view of the AFM image of a SL is presented in **Figure 15(b)**. The dose of the ions is highest on the left-hand side (3.2×10^{16} cm^{-2}), decreasing toward the right-hand side (0.8×10^{15} cm^{-2}). The higher doses are shown to cause larger variations of the topography, as expected.

4.2. Scanning near-field optical microscopy (SNOM) of FIB patterns

As already mentioned in the previous paragraph, SNOM can provide simultaneously an optical image of the corresponding topographic image. As a demonstration of its potential, CBL patterns with different doses are investigated with SNOM. The obtained topographic data and corresponding optical images are demonstrated in **Figure 16**. Compared with the unpatterned areas at the left-hand side of the image, the areas irradiated with ion beam are topographically lower, while being optically more opaque. The observed trend of the topographic features of the irradiated areas are the same as that observed with the AFM (cf. **Figure 15**), while the observed trend of optical contrasts obtained with SNOM is qualitatively the same as that obtained with conventional optical microscopy (cf. **Figure 11**).

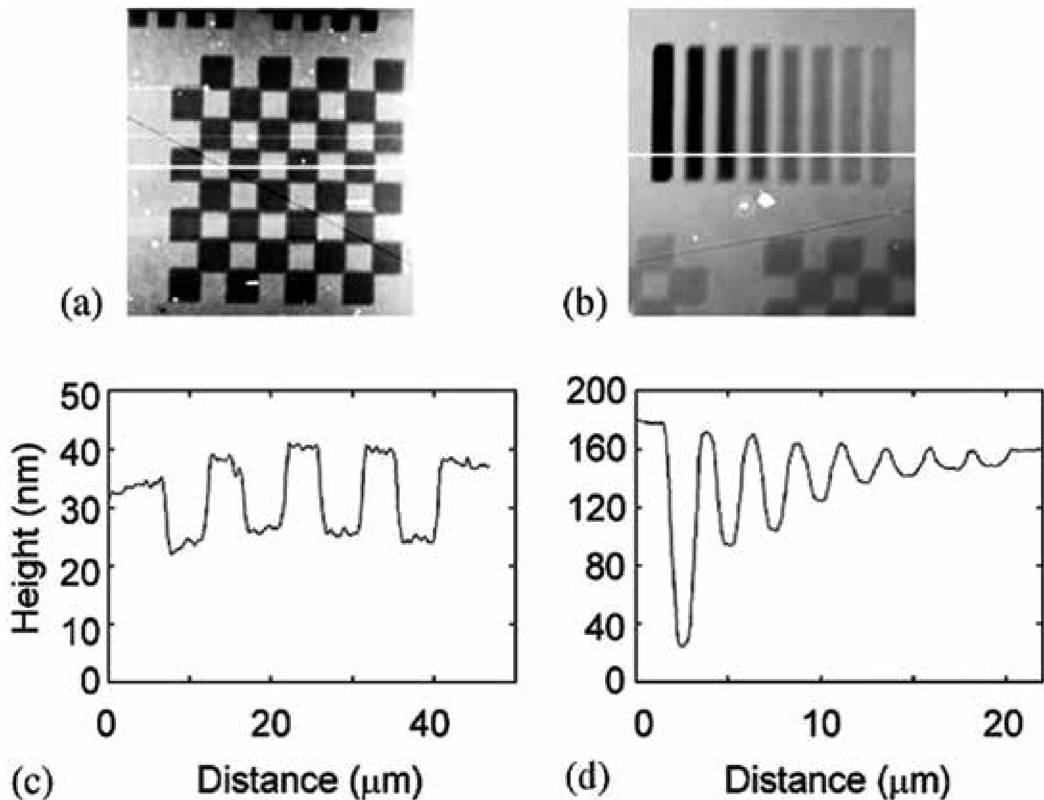

Figure 15. AFM images of (a) CBS and (b) SSL patterns in an a-SiC:H film fabricated by the irradiation of focused ion beam. The cross sections indicated in (a) and (b) are shown in (c) and (d), respectively [42].

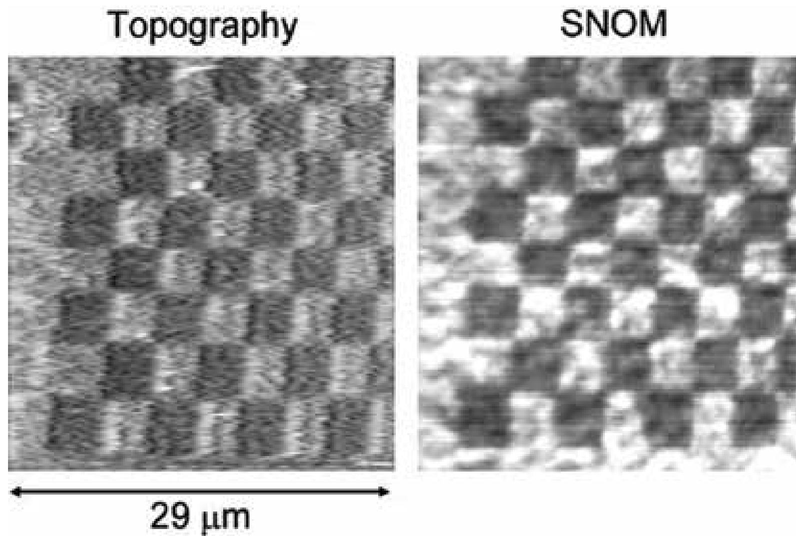

Figure 16. Topographic image (a) and corresponding SNOM image (b) of a CBS pattern created on an a-SiC:H thin film [42].

For the purpose of examining the dependencies of topographic and optical contrasts on the Ga^+ ion dose, three different CBL patterns with doses of 1.3×10^{16}, 0.8×10^{16} and 3.2×10^{15} cm^{-2} have been scanned with SNOM to record topographic and optical images. The obtained results are presented in **Figure 17**. The topographic thickness changes (thinning) of the CBL patterns are measured to be 90, 80 and 50 nm for Ga^+ doses of 1.3×10^{16}, 0.8×10^{16} and 3.2×10^{15} cm^{-2}, respectively. The measured corresponding optical contrasts are 0.5, 0.4 and 0.2. It is thus shown that it can be qualitatively concluded that a higher dose causes both higher optical and higher topographic contrast. It has to be noted, though, that this correlation is an average one, for example, in **Figure 17(C)**, the CBL pattern in the optical image is smeared, while topographic features are still being observed. Since the value of the lowest optical contrast of 0.2 obtained here is rather high, the inhomogeneous optical images of **Figure 17(C)** may be attributed to the inhomogeneous optical property of the material due to contamination or some interference effects associated with the formation of two-dimensional periodic structures. Such information can be used to set optimal dose condition to achieve maximum optical contrast with minimum topographic contrast and less artificial optical features.

4.3. Optimal optical contrast in FIB-patterned amorphous silicon carbide structures

The optical density of ion implanted regions is determined by two competing contributions, mechanical thinning of the a–SiC:H film due to ion beam milling and modification of the film properties (i.e. increased optical absorption) due to ions implanted in the film. Thus, studies of both topographic and optical properties of thin films are important to optimize the ion implantation processing for optical data storage applications. Such investigations have been carried out by simultaneous mapping of topography and optical contrast of Ga^+ FIB optical stripes patterns in a-SiC:H with varying ion dose using a SNOM instrument [43].

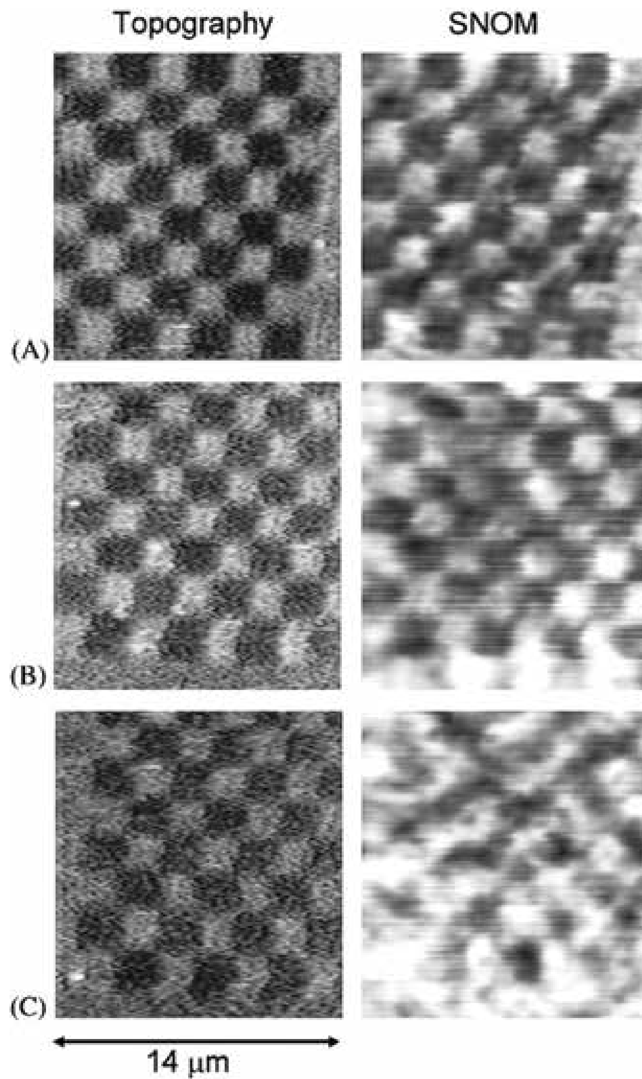

Figure 17. Variations of topographic and near-field optical contrasts of CBL patterns fabricated with different ion doses: (A) 1.3×10^{16} (B) 0.8×10^{16} and (C) 3.2×10^{15} cm^{-2} [42].

When irradiating a film surface with a beam of accelerated ions, there are two main possible processes involved: implantation of the ions into the film [1, 3] and ablation of the film [1, 44]. The resulting increase of optical density in a-SiC:H is assumed to be caused by the former process, while topographic thinning results from the latter. The maximum optical absorption that can be developed in the film may also be limited by the ablation since sputtering of gallium will define an upper limit to the amount that is retained. Effectively, the number of ions per volume implanted into the irradiated material increases with the dose to a certain saturation point, limited by the ion beam-induced sputtering. At the same time, the amount of film material sputtered away from the solid surface increases with the dose as long as the irradiation continues. The results presented in the work of Takahashi et al. [43] show that at

http://dx.doi.org/10.5772/intechopen.77976

lower doses the ion implantation prevails over the ablation effect. The implantation effect reaches saturation at a dose D = 3.0 × 10^{15} ions cm^{-2}. Then, for higher irradiation doses, the ablation effect starts to override the implantation effect, leading to a slow decrease in the optical contrast, while the topographic thinning still increases.

The key feature which must be noted for a practical device is not the level of absorption achieved by the implant, but the contrast that develops relative to the immediately adjacent regions. Local optical measurements as in this work [43] are of particular importance in this respect as they provide a way to study how sharp the optical contrast change is between the implant zones and nominally unaffected regions between them. It is also noted there, in way of comparison, that the change in the optical absorption in this case is somewhat less than the order of magnitude change obtained in conventional far-field optical measurements in samples implanted with an unfocused, broad ion beam [17]. The large optical contrast in the far-field optical measurements case arises mainly from amorphization changes in the host material, but these are less important here; instead, the transmission changes are more strongly defined by the presence of Ga itself and the formation of nanoscale precipitates [33]. Moreover, surface temperature enhanced sputtering (including that of the Ga implant) from the ion beam irradiated regions will act to limit the transmission change achievable.

5. Conclusions

The results presented here demonstrate the possibility to open up new applications of wide bandgap amorphous materials, such as a-SiC:H and ta-C, as media for high-density optical data storage in the nanoscale range, using focused ion beam techniques. In summary, the optical contrast achieved, even at relatively low doses, is of sufficient magnitude to be useful in nanoscale optical data storage and submicrometer lithographic mask production. These results are particularly important when estimating the cost effectiveness of the method, as relatively low implantation doses appear effective in this case and these imply less costly implantation time. The resolution achievable will be defined by the diameter of the Ga^+ FIB and the region of collateral modification/damage, similar to proximity effects in the case of electron beam patterning, but still should offer a significant improvement over the resolution determined by the diffraction limit of light in the case of optical lithography.

Applying near-field optical techniques, like SNOM, for optical and topographic characterization of Ga^+ FIB patterned surfaces, provided results showing that at lower doses, the ion implantation effect leads to increased optical absorption and, hence, higher optical contrast is dominant. However, the optical absorption saturates at higher implantation doses while further ion beam milling causes a decrease in optical contrast, apparently due to the ablation of the film. Thus, the present study shows the existence of optimal conditions for the ion implantation to achieve large optical contrast with less topographic change in the films. Low ion irradiation doses are effectively sufficient and preferable for achieving strong modification of the optical absorption, which is needed for applications in optical data storage for creating permanent optical archives. The obtained results, given the potential of the FIB technique, could be of use for applications of wide-bandgap amorphous materials, like a-SiC and ta-C, in the area of nanoscale optical data storage and data archiving.

Acknowledgements

The support of the Bulgarian Academy of Sciences and Maria Curie-Sklodowska University in Lublin, Poland, is gratefully acknowledged, as well as the help of the staff of the Ion Beam Center at the Helmholtz-Zentrum Dresden-Rossendorf e.V., a member of the Helmholtz Association, for performing the focused ion beam implantation.

Author details

Tania Tsvetkova

Address all correspondence to: tsvet@issp.bas.bg

Institute of Solid State Physics, Bulgarian Academy of Sciences, Sofia, Bulgaria

References

[1] Townsend PD, Kelly JC, Hartley NEW. Ion implantation, sputtering and their applications. London: Academic Press Inc. Ltd; 1976

[2] The Digital Universe of Opportunities. April 2014. Available: www. emc.com/digital universe

[3] Townsend PD, Chandler PJ, Zhang I. Optical effects of Ion Implantation. Cambridge: University Press; 1994. pp. 24-55

[4] Kalbitzer S. Novel concepts for the mass storage of archival data. Nuclear Instruments and Methods B. 2004;**218**:343-354

[5] Tsvetkova T. Ion beam modification of amorphous silicon-carbon alloys. In: Singh J, Copley S, Mazumder J, editors. Beam Processing of Advanced Materials. ASM International: Metals Park. 1996. p. 207

[6] Kalbitzer S. Generation of optical contrast in insulating materials by irradiation with focused ion beams. Applied Physics A. 2000;**71**:565-569

[7] Ruttensberger B, Krotz G, Muller G, Derst G, Kalbitzer S. Crystalline-amorphous contrast formation in thermally crystallized SiC. Journal of Non-Crystalline Solids. 1991;**137-138**:635

[8] Kalbitzer S. High density optical memories for safe archival data. Physical Science International Journal. 2014;**4**(3):366-371

[9] Tsvetkova T, Amov B, Vateva E, Averyanov V. Ion implantation induced modification of vitreous chalcogenides. Physica Status Solidi (a). 1990;**119**:107

[10] Bullot J, Schmidt MP. Physics of amorphous silicon-carbon alloys. Physica Status Solidi (b). 1987;**143**:345

[11] Demichelis F, Kaniadakis G, Tagliafero A, Tresso E, Rava P. Amorphous hydrogenated silicon-carbon-tin alloy films. Physical Review B. 1988;**37**:1231

[12] Tsvetkova T, Tzenov N, Tzolov M, Dimova-Malinovska D, Adriaenssens G, Pattyn H, Lauwerens W. Optical contrast formation in a-$Si_{1-x}C_x$:H films by ion implantation. Journal of Non-Crystalline Solids. 1993;**164-166**:897

[13] Tzenov N, Tzolov M, Dimova-Malinovska D, Tsvetkova T, Angelov C, Adriaenssens G, Pattyn H. Ion implantation induced modification of a-SiC:H. Nuclear Instruments and Methods B. 1994:**84**:195

[14] SRIM by Ziegler JF, Biersack JP, Ziegler MD. University of California at Los Angeles. CA 90066; 2012 (Available: www.SRIM:org.)

[15] Tzenov N, Dimova-Malinovska D, Tsvetkova T. Modification of magnetron sputtered a-Si_{1-x} C_x:H films by implantation of Sn^+. Materials Research Society Symposia Proceedings. 1996;**396**:243

[16] Barancira T, Moons R, Koops CEJ, Deweerd W, Pattyn H, Tzenov N, Tzolov M, Dimova-Malinovska D, Tsvetkova T, Venegas R, Zhang GL. Study of the ion implantation of ^{119}Sn in a-$Si_{1-x}C_x$:H. Journal of Non-Crystalline Solids. 1999;**244**:189

[17] Bischoff L, Teichert J, Kitova S, Tsvetkova T. Optical pattern formation in a-SiC:H films by Ga^+ ion implantation. Vacuum. 2003:**69**:73

[18] McClelland JJ, Steele AV, Knuffman B, Twedt KA, Schwarzkopf A, Wilson TM. Bright focused ion beam sources based on laser-cooled atoms. Applied Physics Reviews. 2016:**3**(1):011302: DOI: 10.1063/1.4944491

[19] Giannuzzi LA, Stevie FA. In: Introduction to Focused Ion Beams. New York: Springer; 2005

[20] Tseng AA. Recent developments in micromilling using focused ion beam technology. Journal of Micromechanics and Microengineering. 2004;**14**:R15-R34

[21] Nabhiraj PY, Menon R, Mohan Rao G, Mohan S, Bhandari RK. Characterization of compact ICP ion source for focused ion beam applications. Nuclear Instruments and Methods in Physics Research A. 2010;**621**:57-61

[22] Powell JA, Matus L. In: Harris GL, Yang CYW, editors. Amorphous and Crystalline Silicon Carbide. Berlin: Springer; 1989

[23] Kanicki J, editor. Amorphous and Microcrystalline Semiconductor Devices. Boston. London: Artech House; 1991

[24] Heinrich J, Hemeltjen S, Marx G. Analytics of CVD Processes in the deposition of SiC by methyltrichlorosilane. Microchim Acta. 2000;**133**:209

[25] Nagai T, Yamamoto K, Kobayashi I. SiC thin-film thermistor. Journal of Physics E. 1982;**15**:520

[26] Hirvonen JK. Ion implantation and ion beam processing of materials. Amsterdam: North Holland; 1984

[27] Ziegler JF. Ion implantation. New York: Academic Press; 1988

[28] Veerasamy VS, Yuan J, Amaratunga G, Milne WI, Gilkes KWR, Weiler M, Brown LM. Nitrogen doping of highly tetrahedral amorphous carbon. Physical Review B. 1993; **48**:17954

[29] Fallon PJ, Veerasamy VS, Davis CA, Robertson J, Amaratunga GAJ, Milne WI, Koskinen. Properties of filtered-ion-beam-deposited diamondlike carbon as a function of ion energy. Journal of Physical Review B. 1993;**48**:4777

[30] Böhringer K, Jousten K, Kalbitzer S. Development of a high- brightness gas field-ionization source. Nuclear Instruments and Methods B. 1988;**30**:289

[31] Tsvetkova T, Tzenov N, Tzolov M, Dimova-Malinovska D, Adriaenssens GJ, Pattyn H. Optical properties and chemical structure of ion implanted a-SiC:H. Vacuum. 2001;**63**:749

[32] Tsvetkova T, Angelov O, Sendova-Vassileva M, Dimova-Malinovska D, Bischoff L, Adriaenssens GJ, Grudzinski W, Zuk J. Structural and optical properties modification of a-SiC:H by Ga+ ion implantation. Vacuum. 2003;**70**:467

[33] Hole DE, Townsend PD, Barton JD, Nistor LC, Landuyt J. Gallium colloid formation during ion implantation of glass. Journal of Non-Crystalline Solids. 1995;**180**:266-274

[34] Bischoff L, Hesse E, Panknin D, Skorupa W, Teichert J. Writing implantation with a high current density focused ion beam. Microelectronic Engineering. 1994;**23**:115

[35] Tsvetkova T, Berova M, Sandulov M, Kitova S, Avramov L, Boettger R, Bischoff L. Focused ion beam optical patterning of ta-C films. Surface and Coatings Technology. 2016;**306**:341-345

[36] Tsvetkova T, Takahashi S, Zayats A, Dawson P, Turner R, Bischoff L, Angelov O, Dimova-Malinovska D. Fabrication of nano-scale optical patterns in amorphous silicon carbide with focused ion beam writing. Vacuum. 2005;**79**:100-105

[37] Binnig G, Quate CF, Gerber Ch. Atomic Force Microscope. Physical Review Letters. 1986;**56**:930

[38] Friedbacher G, Fuchs H. Classification of scanning probe microscopies. Pure and Applied Chemistry. 1999;**71**:1337

[39] Betzig E, Trautman JK. Near-field optics: microscopy, spectroscopy, and surface modification beyond the diffraction limit. Science. 1992;**257**:189

[40] Pohl DW, Courjon D, editors. Near Field Optics. Dordrecht: Kluwer Academic Publishers; 1993

[41] Richards D, Zayats AV, editors. Nano-optics and near-field microscopy. Philosophical Transactions of the Royal Society. London: 2004;**362**:699-812

[42] Tsvetkova T, Takahashi S, Zayats A, Dawson P, Turner R, Bischoff L, Angelov O, Dimova-Malinovska D. Near-field optical mapping of the ion-implanted patterns fabricated in amorphous silicon carbide. Vacuum. 2005;**79**:94-99

[43] Takahashi S, Dawson P, Zayats AV, Bischoff L, Angelov O, Dimova-Malinovska D, Tsvetkova T, Townsend PD. Optical contrast in ion-implanted amorphous silicon carbide nanostructures. Journal of Physics D: Applied Physics. 2007;**40**:7492-7496

[44] Knystautas E, editor. Engineering Thin Films and Nanostructures with Ion Beams. Boca Raton, FL: Taylor and Francis; 2005

Chapter 6

Nitrogen Ion Microscopy

Marek E. Schmidt, Masashi Akabori and
Hiroshi Mizuta

Additional information is available at the end of the chapter

http://dx.doi.org/10.5772/intechopen.76383

Abstract

The gas field ion source (GFIS) can be used to generate beams of helium, neon, hydrogen, and nitrogen ions, among others. Due to the low energy spread and the atomically small virtual source size, highly focused ion beams (FIB) can be obtained. We discuss the history of the GFIS and explain the field ionization and field evaporation process in general. Then, the unique properties of the nitrogen ionization, originating from the molecular nature, are explained. We show how the nitrogen ion microscopy (N2IM) can be used to image and pattern samples. The unique contrast observed in samples with graphene or carbon is reported. Finally, we conclude with an outlook of the technology and possible key applications such as spatially localized nitrogen-vacancy center implantation.

Keywords: gas field ion source, N2IM, GFIS-FIB, secondary electron

1. Introduction

The development of scanning probe microscopy was driven by the challenge articulated by Richard Feynman [1], namely that it should be possible to write (and read) the *Encyclopedia Britannica* on the head of a pin. By using a focused electron beam to pattern advanced resist materials and later transfer them into solid matter by various processes, this challenge has been overcome. By improving the electron beam, it also became possible to image sub-10-nm-scaled structures in the scanning electron microscope (SEM, relying on the secondary electron generation) or the transmission electron microscope (TEM). The latter technique makes it possible to image individual atoms; however, it is restricted to thin samples. Encouraged by the nanometer scale resolution of the SEM, the replacement of electrons with ions was researched. Since energetic ions generate secondary electrons when interacting with matter, the focused ion beam (FIB) can be used for imaging as well. Due to the lack of other available

IntechOpen

© 2018 The Author(s). Licensee IntechOpen. This chapter is distributed under the terms of the Creative Commons Attribution License (http://creativecommons.org/licenses/by/3.0), which permits unrestricted use, distribution, and reproduction in any medium, provided the original work is properly cited.

ion sources, the first one to gain widespread adaptation was the gallium liquid metal ion source (LMIS), which relies on the formation of the so-called *Taylor* cone. In addition, since ions are significantly slower than electrons for a given energy and their charge-to-mass ratio is smaller, the magnetic lenses in the SEM are replaced by electrostatic lenses. While a sub-5-nm beam diameter for gallium is possible today, the imaging resolution is limited to a few nm due to the immediate surface sputtering by the energetic ion impacts and the requirement to collect sufficient number of secondary electrons [2].

Energetic ions are used in other technological fields as well, such as ion implantation and surface etching (ion milling). These methods can be locally restricted by integrating with a mask; however, this requires several additional process steps, including a lithographic mask, and has limited resolution. Furthermore, this approach has a large initial cost. Instead, FIB can be used to locally mill structures at the nanometer scale with great flexibility. Important parameters are the etch rate and selectivity (difference of etch rate between two different materials for the same milling conditions), which can be improved by the so-called gas-assisted etching. For this purpose, thin needles are introduced close to the beam-sample interaction region, and minute amounts of gas are introduced. While the gas concentration is high at the point of injection, it is quickly evacuated by the pump system of the low-pressure sample chamber. By introducing special volatile precursor gases that are disassociated by the ion beam, the deposition of conducting as well as insulating materials is possible.

Gallium FIB is now widely used for rapid prototyping, circuit editing, lithographic mask repair, and TEM lamella preparation. However, several limitations have become more pressing in recent years:

1. The low milling resolution of the gallium ion (due to the large interaction volume of the heavy ions) is not sufficient for sub-10-nm fabrication, and the repair of next-generation optical masks becomes challenging. Furthermore, reflective UV masks have a higher requirement for defect-free repair.
2. The implanted gallium atoms can degrade the properties of the specimen. This is particularly critical for the preparation of TEM lamellae of certain samples and circuit editing where the semiconducting properties of transistors can change.
3. To improve the resolution of the gallium FIB, very low beam currents in the single-digit pA range are used. At these currents, the low secondary electron yield makes it difficult to do end-point detection, that is, notice when a given layer is fully removed.

In consequence, through meticulous ingenuity, the gas field ion source (GFIS) was commercialized. Initially, work focused on the ionization of helium ions as its ionization field strength clearly distinguishes it from other gases, and the light ions promise a superior imaging resolution while limiting the sample damage. However, today, there is a wide range of gases used, including helium, neon, hydrogen, and nitrogen. We discuss the GFIS in general in Section 2, and focus more on the uniqueness of the nitrogen field ionization in Section 3. In Section 4, we show how the nitrogen ion microscopy (N2IM)[1] can be used for imaging and patterning. Due

[1]The acronym *NIM* is now widely used to refer to the neon ion microscopy.

to the limited space, not all aspects can be discussed in full detail. As there is much overlap with the helium ion microscope, the excellent book edited by Hlawacek and Gölzhäuser [3] should provide answers to outstanding questions.

2. The gas field ion source

The GFIS, as the name suggests, is a type of ion source that works by ionizing gas atoms or molecules in a strong electric field. In this section, first, a short history of the GFIS is given for the interested mind, followed by the fundamental principle of the field ionization and field evaporation in strong electric fields. This also includes the discussion of the fundamental limits. In Section 2.3, the more technical aspects of exploiting the field evaporation and gas etching in order to make a good ion source are discussed. We also summarize some recent ion source developments beyond the GFIS that have been fuelled by the commercial success of the GFIS.

2.1. History of the gas field ion source

The foundation of the GFIS was laid by Müller [4], when he developed the field ion microscope (FIM). In a FIM, individual surface atoms of a metal tip can be imaged with relatively simple methods by applying a strong electrical field in a gas atmosphere. The gas atoms (typically helium) are ionized and are then accelerated away from the metal surface (**Figure 1a**). By allowing these accelerated ions to pass through a hole in the so-called *extraction electrode*, they can be visualized on a detector screen, as shown in **Figure 1b**. As the electric field at protruding atoms is stronger, ionization from these locations is more likely. This setup has to be located in a vacuum chamber to avoid high-voltage breakdown (arcing), and the emitting metal is typically cooled to increase the ionization rate. It quickly became clear that the emission from a single atom could, in principle, facilitate an ion source [5, 6] with unprecedented resolution (as will be discussed in Section 2.3); however, current stability turned out to be a serious issue [7]. In the meantime, the gallium LMIS was developed and offered sufficient performance for the time: a wide range of beam currents from the pA to the nA range, and sufficient resolution to allow prototyping and circuit editing in the semiconductor industry.

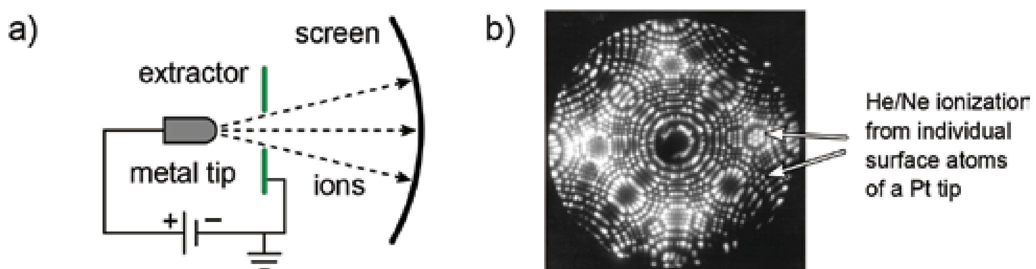

Figure 1. (a) Operation principle of the field ion microscope. (b) FIM image of pt tip (derivative of *platinum* (https://www.flickr.com/photos/dxdt22/315745462) by Tatsuo Iwata licensed under CC BY 2.0).

The development of methods to controllably shape noble metal tips through electrochemical etching, field-assisted evaporation, and etching remained active due to the demand for electron emitters.[2] The effort up until 2005 to develop high brightness, monochromatic noble gas ion sources was reviewed by Tondare [8]. It is now known that sometime in the 1990s, the active development of a GFIS commenced at the *Micrion Corporation*. The goal was to create a next-generation ion source to allow repair of photolithographic masks in the semiconductor industry, and the work was encouraged by the technological advances and the better understanding of the field emission [9]. However, after the first performance values were obtained and the theory had been reexamined, it became clear that in spite of being a source with unprecedented brightness, the overall emission current would not be on par with existing ion sources. The merit of this challenging technology became questionable, and furthermore, the development team was haunted by stability issues of the novel source. Nevertheless, the development team succeeded in forming a GFIS emitter from Tungsten that was terminated by three atoms aligned in a triangle, the so-called *trimer*. The trimer can improve the stability compared to a single atom tip for certain tip materials and crystal orientations; however, only one-third of the total brightness is usable. First results demonstrated that the GFIS would be an ideal candidate for an ion microscope that could excel the SEM with a sub-1-nm beam diameter and favorable beam/sample interaction. However, commercialization was not yet viable.

With this result, Bill Ward continued the improvement of the source stability—the last remaining obstacle before commercialization—after parting with *Micrion* upon their acquisition by the *field electron and ion company* (FEI). After 2 more years of ups and downs, and just as the team had moved to a new location, a demonstration was to be given to potential investors. To the surprise of Ward himself, the stability and performance was significantly better than just before the move. As it later turned out, due to time constraints, a special custom-made gas purifier was not installed to the gas supply in the new location. At some unknown point in the past, a piece of wooden cork had slipped into the tube of the purifier and got stuck. Thus, the gas supplied to the ion source had been passing through the cork during the development time, and this was the root cause for the low stability. However, as Ward recalled during his speech at the 2016 AVS International Symposium & Exhibition in Nashville, Tennessee, commemorating the 10th anniversary of the commercialization of the GFIS [10], during the struggle with the stability of the GFIS, the team gained experience and knowledge that turned out to be indispensable to the commercialization. Would it not have been for the long development time and investment to overcome the instability before realizing the current limitation, the effort to commercialize the GFIS would have likely been dropped earlier in the development.

With investors on board, the Atomic Level Ion Source (ALIS) company went public with its results in 2006 [11, 12]. Shortly after, *ALIS* was acquired by *Carl Zeiss'* Nano Technology Systems Division (NTS), and the *Zeiss Orion* helium ion microscope was the first commercial GFIS tool released in the same year. Development in the time since then progressed; however, the fundamental GFIS technology remains the same, and new tools are now fitted with helium

[2]Technically, the difference between a GFIS and a field emitter gun for electrons is the polarity of the tip with respect to the extractor electrode. Since electrons are supplied through the tip, cooling is not required for electron emission.

http://dx.doi.org/10.5772/intechopen.76383

and neon gas. The events surrounding the development of the HIM at *Micrion* and *ALIS* were also recollected by Economou et al. [13] and Ward himself ([3], Appendix A).

The impressive results achieved by the *Zeiss Orion* certainly renewed the interest in GFIS, and the Japanese gallium FIB specialist *SII Nanotechnology* presented results on their hydrogen and nitrogen GFIS-FIB nanofabrication tool for the first time in 2011. Unprecedented mask repair performance, particularly of reflective UV masks, was reported [14]. Shortly after, at the beginning of 2013, *SII Nanotechnology* was acquired by *Hitachi High-Technologies* and continues operating under the name *Hitachi High-Tech Science*. *Zeiss* and *Hitachi* appear to remain the only commercial manufacturer of GFIS tools. Nevertheless, it is likely that sooner or later other players will enter the field of light gas ion FIB technology. As we show in Section 2.4, this does not have to be necessarily a GFIS.

2.2. Field ionization and field evaporation

To understand the field ionization (gas atoms losing an electron in a strong electric field) and field evaporation (surface atoms detaching due to high electric field), some general knowledge about solid state physics is required. The GFIS is used by scientists and engineers from a broad range of fields, and for the daily use the details that will be explained in this section are not necessary. Nevertheless, it is helpful to understand the potential and limitation of this technology. Therefore, we give an explanation in a way that can be followed by readers from various fields, and details can be found in the excellent books that have been written over the years [15–18].

In solid state physics, there are a few concepts which are prerequisites in this discussion:

1. **Energy versus position** is a common representation of the inner properties of solids as seen by electrons. The position is typically a one-dimensional line through the solid as it contains the essence of the solid and can still be easily interpreted. Two-dimensional (2D) or even three-dimensional (3D) representations exist, but are less common. The energy (sometimes called potential, y-scale) is given in units of electron volt (eV) and defines *relative* energies, that is, there is no zero point as it is irrelevant.
2. **Fermi energy** (E_F) is the highest energy an electron in a given material can have at absolute zero Kelvin. At elevated temperature, some electrons from below E_F are *excited* and gain some additional energy.
3. **Vacuum energy** (E_{vacuum}) is defined as the energy outside of the solid in vacuum.
4. **Work function** is an energy difference that is unique to each individual electron in a solid. It is the energy that has to be added to the electron's energy to make it reach E_{vacuum}, thus separating it from the solid.
5. **Quantum tunneling** is a phenomenon where electrons can cross a potential barrier although they do not have enough energy to reach the top of the barrier (given that the space behind the barrier is unoccupied). Electron energy is conserved. The tunneling probability increases rapidly with the decrease of the barrier width, and the Pauli principle

forbids tunneling into energies below E_F. This phenomenon does not occur in the visible world. A possible image of quantum tunneling could be as follows: Let us imagine a golf ball lying in the grass next to a solid concrete wall. Tunneling would mean that there is a chance that the ball moves to the other side of the wall without being touched.

Figure 2a shows a 2D cut through a large metal, where the atoms are assembled in a regular structure. If we plot the energies along the red line, we obtain **Figure 2b**. Here, + represents the positively charged cores of the individual atoms. They create *energy wells* for electrons through their Coulomb potential, which are filled with some electrons of specific (*quantized*) energy. Since the energy of these electrons is considerably smaller than the top of the barrier between

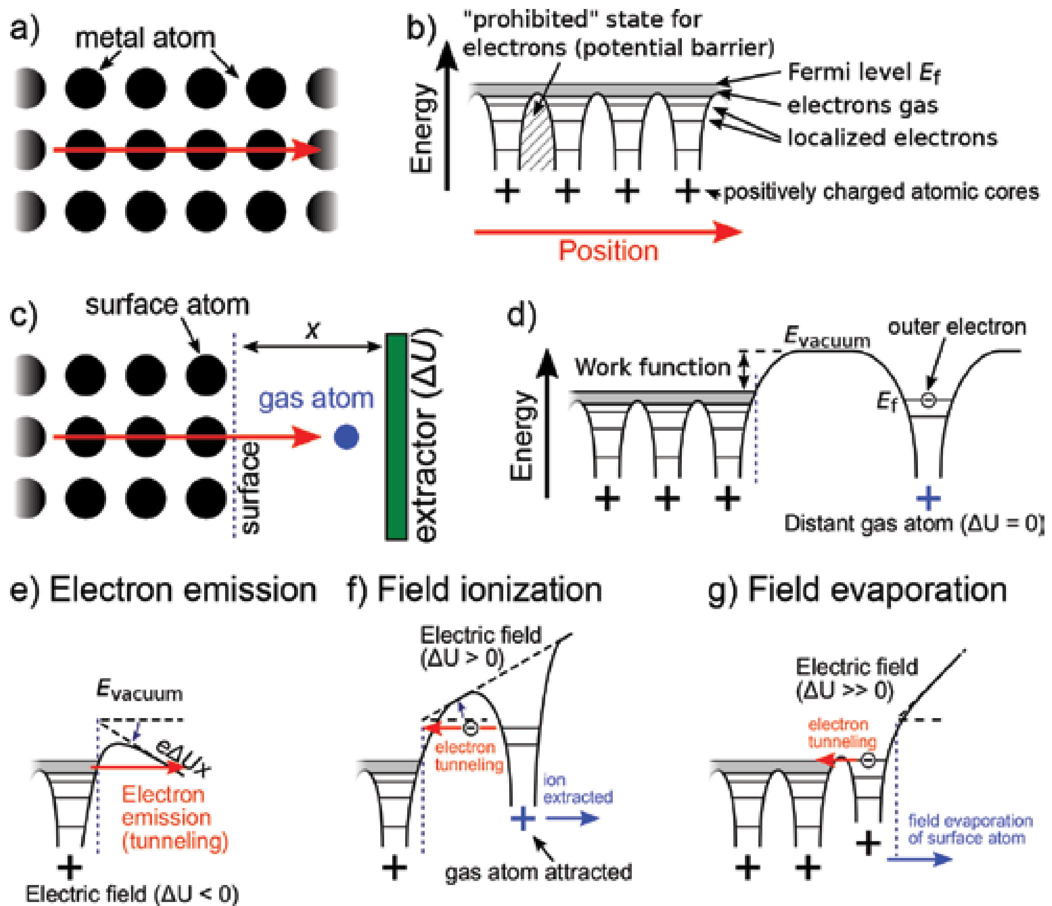

Figure 2. (a) Model of metal atoms inside a bulk metal. The potential along the red arrow is shown in (b). (b) Potential inside bulk metal. Electrons are either localized near the atoms or can move freely if they have sufficient energy. These electrons are referred to as *electron gas* and give metal the high electrical conductivity. (c) Model of metal surface with an extractor electrode at distance x and a gas atom. (d) Potential along red arrow in (c). (e) Narrow potential barrier formed by negative ΔU resulting in electron emission. (f) Positive ΔU causes electron tunneling of outer electron of nearby gas atoms. The ion is immediately accelerated toward the extractor. (g) Further increase of ΔU causes field evaporation of surface atoms.

http://dx.doi.org/10.5772/intechopen.76383

the atoms, they are assumed to be *localized* and do not contribute to electrical conduction. However, since E_F is higher than the barriers (this is only true for metals), there are some electrons that can move freely from left to right. They are part of the so-called *electron gas* which gives metal its high conductivity. Since the metal is periodic, this energy profile is periodic as well.

As pointed out at the beginning of this section, field ionization occurs only at the surface. Therefore, let us see what happens when we cut our metal to create a surface as illustrated in **Figure 2c**. We ignore the extractor for now ($\Delta U = 0$), and observe the energy profile along the red arrow as shown in **Figure 2d**. To the left of the surface, the potentials are unchanged; however, at the surface, a potential barrier reaching up to E_{vacuum} is formed. Thus, the electrons in the electron gas are reflected at the surface and remain inside the metal. Furthermore, a gas atom that is far away from the surface creates its own potential well, and all its electrons are localized. Note that the electron with the highest energy is referred to as the *outer* electron. If we were to observe the gas atom and surface at this condition, we would see that the gas atom moves randomly in respect to the metal surface, but no ionization occurs. Also, since the energy of the outer electron of the gas atom is below E_F of the metal, the electron cannot tunnel to the metal, even if the barrier width was greatly reduced due to collision with the metal surface (Pauli principle). The system is stable.

To actually cause anything to happen, an electric field has to be applied between the metal surface and the extractor electrode. Again, let us first ignore the gas molecule and discuss the electron emission. If we apply a large positive voltage to the extractor (at a distance x) while the tip is grounded,[3] the potential barrier at the surface is deformed as shown in **Figure 2e** and electrons can tunnel from the metal into the vacuum. The slope equals $e\Delta Ux$, where e is the electron charge. As the density of electrons in the metal is high and a virtually infinite supply is available, very high emission currents can occur, and Joule heating of the metal poses the limit.

However, since we are trying to ionize gas, let us go back to the configuration shown in **Figure 2d** and apply a positive ΔU instead (**Figure 2f**). Two things are now happening: first, the vacuum energy increases away from the surface, and second, the energy of the outer electron of the gas atom becomes higher than E_F of the metal. Gas atoms have fluctuating dipole moments as the outer electrons are orbiting around the core, and this causes the gas molecule to be attracted to the metal surface in the strong field. In consequence, all prerequisites for tunneling of the outer electron of the gas atom are fulfilled: the barrier is narrow, and there is space for the electron in the metal at the energy of the outer electron. After tunneling, the now positively charged gas *ion* is immediately accelerated in the strong electric field away from the tip and toward the extractor. The ion has an energy corresponding to ΔU. For the ionization to happen, the field has to be in the range of 10^{10} V/m. For a flat surface, this would correspond to 100 MV at $x = 1$ mm. However, by using a sharp needle instead of a flat surface, the electric field is concentrated at the tip apex, and only 5 kV is required for a tip diameter of

[3]We can also apply a negative voltage to the tip and ground the extractor. Important is the potential difference ΔU. Note that lower potential corresponds to a higher energy. This counter-intuitive definition is of historic origin.

100 nm. Some individual surface atoms that stick out due to the crystal structure cause a localized concentration of the field, and ionization occurs predominantly there (see **Figure 1b**).

By further increasing the electric field, the attractive force of the gas atom is stronger, resulting in a higher tunneling probability (which can be estimated by the *Wentzel-Kramers-Brillouin* approximation). This is directly reflected in a higher ion current. However, an exceedingly large field will cause field evaporation (**Figure 2g**). The potential of the surface metal atom is slightly increased, and one of the localized electrons can tunnel into the bulk. The temporary positive charge of the surface atom can be enough to break it away in the strong electric field. For field ionization, we can therefore conclude that we require enough electric field to attract the gas atom and allow tunneling; however, the evaporation field strength should not be reached. The actual voltage that has to be applied to the extractor depends strongly on the distance x and the shape of the tip. Furthermore, different gases require different field strengths for ionization, with helium being the highest at 4.4×10^{10} V/m [19]. This poses a technological challenge for the control of the ion beam energy: by grounding the extractor electrode and varying the tip potential, the kinetic energy of the ions after passing through the hole in the extractor can be vastly different. This is solved similar to the LMIS and FEG with the introduction of an accelerator electrode that allows extraction control independent of the final beam energy (see **Figure 3a**). The ion column of the GFIS-FIB nanofabrication tool located at the *Japan Advanced Institute of Science and Technology* is illustrated in **Figure 3b**. The microchannel plate that can be inserted into the ion beam is used to image the emission tip in the FIM mode.

2.3. The emitter tip

As discussed in the previous section, to reduce the requirement on the voltage that has to be applied to the extractor, a sharp tip is used. However, this is not the only reason. In the GFIS, the limit of current (i.e., the rate of ionization events) is mostly limited by the supply of the gas atoms. In fact, the main route of gas supply is through the attraction of gas atoms to the shaft of the tip where the electric field is weaker, followed by migration or hopping toward the apex. Thermal vibration of the tip can repel some of the adsorbed gas atoms and constitutes source vibration, thus the cryogenic cooling mentioned earlier. The ionization rate can be directly controlled by the pressure of source gas around the tip; however, exceeding a certain limit might cause arcing between highly charged parts, which has to be avoided. Also, atom-atom collisions reduce the mean free path. It should thus be clear that if a tip has several ionization sites close to each other, they compete with each other for the available gas.

The achievable diameter of a focused ion beam, D, is given by [21].

$$D = 2R = 2\sqrt{(MR_S)^2 + \left(\frac{1}{4}C_{si}\alpha_i^3\right)^2 + \left(\frac{1}{2}C_{ci}\alpha_i\frac{\Delta E}{E}\right)^2}, \tag{1}$$

where R is the beam radius, M the magnification of the optics between the source and the sample (between 0.3 and 2), R_S the source size, α_i the beam cone angle, C_{si} and C_{ci} the spherical and chromatic aberration coefficients, respectively, and E the acceleration voltage. ΔE is the

http://dx.doi.org/10.5772/intechopen.76383

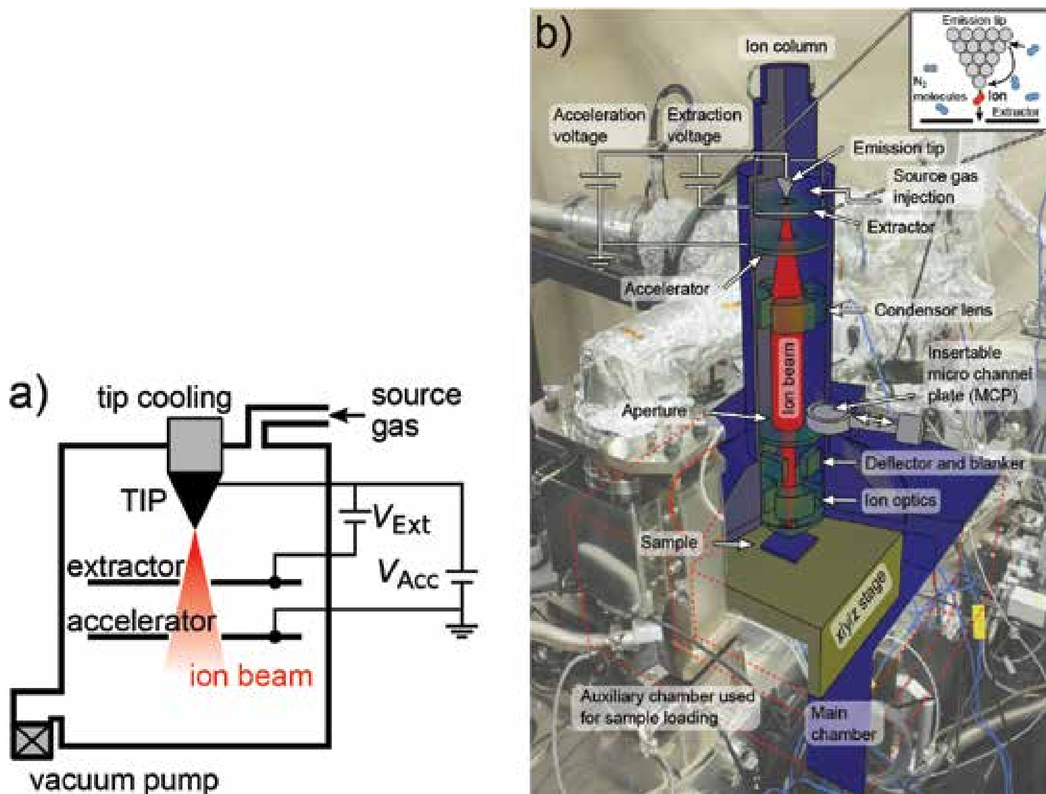

Figure 3. (a) Configuration of emission tip, extractor, and accelerator electrode in the GFIS. (b) Schematic illustration of the ion column of the GFIS-FIB nanofabrication tool. The field ionization process is illustrated in the inset. Reproduced with permission [20].

energy spread, which is the variation of energy of individual ions. To minimize D and thus have the highest resolution, the atomically small R_S and the low ΔE of less than 1 eV [11] are unique to the GFIS and surpass other ion sources. The beam diameter estimation in Eq. (1) assumes that only the emission from a single emission site is aligned with the microscope column, and the emission from the remaining ionization sites is either lost in the ion optics or filtered by a narrow aperture. There had been considerations to focus emission from multiple sites; however, this has proven to be technically not feasible. For the HIM with the tungsten tip, the *trimer* is a compromise between stability (i.e., the three atoms of the pyramid stabilize each other) and brightness of $\sim 4 \times 10^9$ A/cm^{2}sr which can be achieved [12]. In other cases, a single atom tip (SAT) can be formed [22, 23], which can improve source brightness especially for heavier gas atoms that are not as mobile as helium, and the total supply of gas atoms is the limiting factor.

The formation of good emitter tips requires a high level of specialization. Starting from a thin wire of pure metal with as few crystal defects as possible, electrochemical etching [24] is used to form the nanoscopic shape. Then, while observing the emission in an FIM, field evaporation, gas-assisted etching (surface atoms at the shaft of the tip are removed in oxygen or nitrogen

gas atmosphere at fields above the individual ionization field strengths [25]), and emitter heating (causing migration of surface atoms) are used to form the atomistic tip structure. The latter processes can be performed in situ once the emitter is fitted in a microscope, as well. As the ion emission originates from the tip apex and follows the electric field lines, the positioning requirement of the emitter tip in respect to the ion column is unproblematic.

Recently, it has been demonstrated that a tungsten tip can be coated by a thin layer of iridium [26]. Due to the softness of tungsten, it can be shaped more easily, while the extremely sturdy iridium can improve emission stability.

2.4. Other novel ion sources

The renaissance of the FIB with the significantly improved performance of the GFIS compared to the LMIS, as well as the prospect of a large ion portfolio, has led to intensive research into other ion sources as well. For example, gas atoms can be trapped and cooled in the magneto-optical trap (MOT). After condensing them, another light source is used for photoionization, and the ions are extracted in an electrical field [27]. The gas trapping can also be achieved by laser cooling alone [28]. Although the range of possible gases to be ionized by this method is unlimited, the wavelength of the cooling and ionization lasers has to be adjusted for each species which adds to the cost of the source.

3. The nitrogen ion beam

Nitrogen is unique compared to other source gases used in GFIS, as it forms one of the strongest bonds known in nature (binding energy: 9.79 eV; bond length: 0.11 nm) and naturally occurs only as N_2. Nitrogen can be ionized by electron impact, and the effect of nitrogen ion impact on various materials has been investigated [29]. By annealing exposed silicon samples, the formation of Si_3N_4 was reported [30, 31]. The measurement of electron impact ionized nitrogen mass spectra revealed that while N_2^+ ions dominated, some N^+ ions are generated as well [32]. Since the resolution of ion beams in accelerators is in general no issue, a mass filter is typically added to the beam line that removes unwanted ions and leaves a pure beam of required ions. For the GFIS, where we strive for highest resolution, a mass filter would degrade the beam and the ion beam should be pure "as is," Otherwise, two beams are scanned across the sample with a separation depending on the mass difference and the magnetic field occurring along the ion's path. In this regard, N_2 has the advantage of naturally high isotopic purity.

In Section 3.1, we explain what happens during field ionization of nitrogen and interaction with a silicon sample. Then, the nitrogen GFIS-FIB is compared with other ion species used in the GFIS in Section 3.2.

3.1. Field ionization of molecular nitrogen gas and solid-ion interaction

The possible ionization mechanisms of N_2 gas and how they behave after impact on a solid silicon sample are shown in **Figure 4**. In addition, Monte Carlo (MC) simulation results for

http://dx.doi.org/10.5772/intechopen.76383

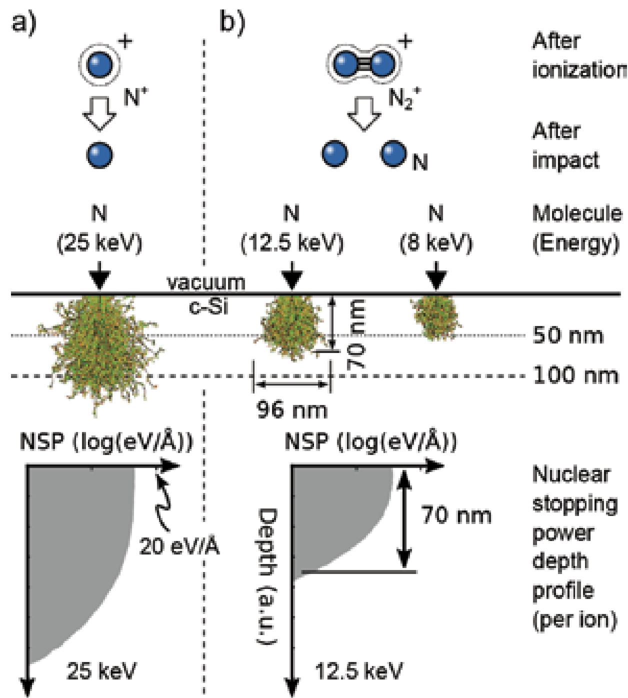

Figure 4. Possible ionization mechanisms of N_2 gas ionized in a GFIS [32, 33] together with MC simulation results for 25-kV acceleration voltage: (a) The molecule splits during ionization and interacts with the sample as an atomic ion with full energy and (b) the molecule stays together during ionization but splits upon impact (modeled as N with 1/2 energy). The interaction volume and nuclear-stopping power depth profiles for the two cases show the different sizes of the expected damage region. In addition, the interaction volume for 16-kV acceleration voltage is shown (modeled as N with 8 keV). Reprinted with permission [39]. Copyright 2017, American Vacuum Society.

these two possibilities with an acceleration voltage of 25 kV are shown. Collision cascades (i.e., the way atoms proceed through a solid after collision) are very difficult to simulate.

The most accurate method is the so-called molecular dynamics (MD) approach, where each individual atom is modeled, and the forces acting onto each other are evaluated accurately. With each additional atom in the simulation model, the complexity increases exponentially, and it is not realistic to simulate a system with several thousand atoms—the number of atoms in the range of the ion—due to the computational cost. Furthermore, the result would be vastly different depending on whether the ion directly collides with a surface atom (possibly resulting in backscattering) or channels along crystallographic directions. Thus, to obtain a complete understanding of the possible effect of the ion beam, a large number of MD simulations would be required where the position and angle in respect to the target crystal are varied. This approach is only viable in special cases, as demonstrated in a study of ion interaction with an atomically thin membrane [35]. MC takes a different approach, which uses probability to simplify complex processes. If an ion is traveling through a medium, it is easy to understand that it has a chance to collide with atom cores or pass between atoms. Instead of explicitly calculating the outcome, a probability of collision is considered that depends on the projectile and the density and composition of the target sample. Furthermore, the possible outcome of

collisions (i.e., the amount of energy lost and the change of direction) can also be assigned to probabilities. Now, to actually perform the MC simulation, a particle with a given direction and velocity is assumed. Based on these parameters, the position of the particle after a certain time τ is calculated. Furthermore, the occurrence and type of interaction is calculated for this time step with the help of the previously mentioned probabilities and a random number generator. With this, we can define a new direction and velocity (which can be unchanged or point to the side) and calculate the position after the next time step. This process is repeated until the particle either left the medium or its velocity dropped below a threshold. Since this result might be far away from the reality as it relies on the random number generator, the outcome of particles with the same initial conditions is repeated for several thousand times, each time with a different outcome. By plotting all the trajectories and evaluating the recorded collision details, the principle shape of the interaction region as well as the mean range can be estimated with small computational cost. For example, we can see that for a N^+ ion at 25 keV (**Figure 4**), damage deeper than 100 nm from the surface will occur. Factors limiting the accuracy of the MC simulation method is the fact that each "shot" is performed onto a pristine target (i.e., no accumulation of damage), and it requires experimental data to model the particle-medium interaction as precisely as possible. SRIM is one software package for MC simulation that has proven useful for many cases [36], but other MC codes exist [37, 38].

To determine which of the two possible ionization mechanisms shown in **Figure 4** is the one that occurs in the GFIS, a crystalline silicon sample is exposed, and the cross section can be observed by TEM, as shown in **Figure 5**. Here, several exposures with different doses were performed with 25 keV and one additional one at 16 keV. As silicon changes from crystalline to amorphous above a well-defined disorder threshold, the observed shape in the TEM is a good indicator of the range of ions. By comparing the shape of the bell-like amorphous region with the MC simulation, it was thus possible to confirm that the N_2 molecules are ionized to N_2^+. As energetic ions are instantaneously neutralized upon impact onto a solid through the pickup of an electron, the impact of a N_2 molecule onto silicon was calculated by atomistic simulation as well [39]. It confirmed that the N-N bond is broken within a few atomic layer, and the N atoms

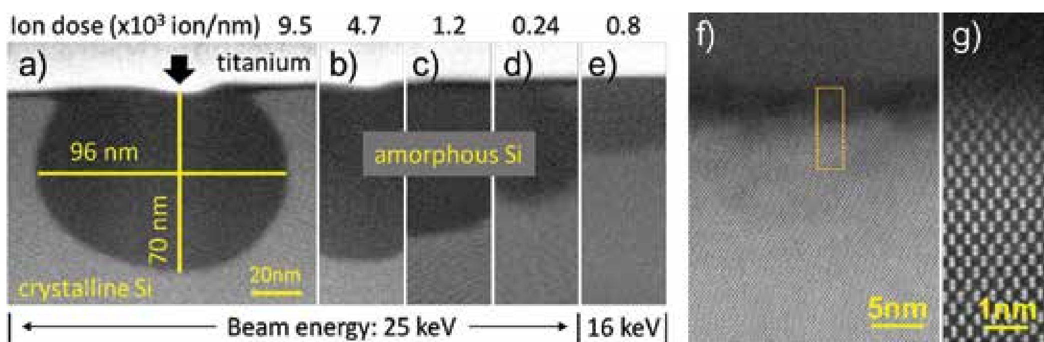

Figure 5. High-resolution HAADF-STEM micrographs of N_2^+ bombarded bulk crystalline Si for 25-keV beam energy at doses of (a) 9.5 to (d) 0.24×10^3 ions/nm, and (e) 16 keV at 0.8×10^3 ions/nm. Scale bar is the same for all images. (f) High-resolution ABF-STEM micrograph of the transition region from crystalline to amorphous Si for the implantation shown in (a). Although some amorphization is observed up to 10 nm away from the amorphous region, the well-defined transition is visible. (g) Atomic resolution HAADF-STEM image of the area indicated by the rectangle in (a), which shows the dumbbell structure of Si(110). Reprinted with permission [39]. Copyright 2017, American Vacuum Society.

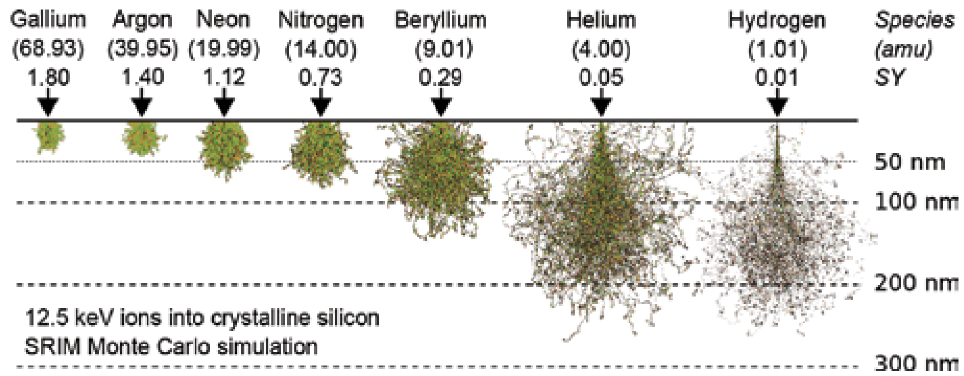

Figure 6. Comparison of interaction volume and sputter yield for Ga, Ar, Ne, N, Be, He, and H for corresponding ion energies of 12.5 keV. Reprinted with permission [34]. Copyright 2017, American Vacuum Society.

continue their path through the sample independently. Therefore, the ion beam with an acceleration voltage of 25 kV in the N_2 GFIS has the same effect on a sample as a N^+ beam with 12.5 keV would have.

3.2. Comparison with other ion species

Previously, various atomic ion species used or potentially usable for FIBs had been compared, based on MC simulation at 30 keV [40]. It impressively shows the advantage of light ions compared to heavier ions, namely the small interaction volume close to the surface, resulting in high milling and imaging resolution. To add nitrogen ions to this comparison, however, some care has to be taken. The MC simulations are based on atomic projectiles. Thus, when simulating the effect of the N_2^+ GFIS-FIB with an acceleration voltage of 25 kV, we have to perform a simulation of N with an acceleration voltage of 12.5 kV instead. If the N_2^+ GFIS-FIB was to be added to the comparison by Tan [40], the acceleration voltage of 60 kV would have to be assumed. This is outside the operation range of FIB microscopes. Therefore, in **Figure 6**, a comparison of different ions for a fixed energy (12.5 keV) is shown instead [39]. As expected from the different masses of the atoms, the penetration depth of nitrogen falls between beryllium and neon, with a sputter yield of 0.73 (i.e., the number of silicon atoms sputtered per impinging ion). It should be noted that this sputter yield considers a single N atom with 12.5 keV; however, the N_2^+ beam will actually yield two of such projectiles. To characterize ion exposure, the number of *primary* ions is typically reported. Thus, if we compare a certain dose of helium ions at 12.5 keV with N^+ at 12.5 keV (actually generated from a 25 keV N_2^+ beam), the nitrogen dose has to be doubled to predict the number of secondary electrons.

4. Nitrogen ion microscopy

Focused ion beams can be used for different types of microscopy. For example, back-scattered ions can reveal details about the atomic mass of target atoms (the imaged target atoms have to

be heavier than the ion species). In the secondary-ion mass spectrometry (SIMS), target atoms are sputtered and characterized in a mass spectrometer. Furthermore, ionoluminescence and transmission of ions through a thin probe can be used for analysis and imaging. However, we focus our discussion on the predominantly used secondary electron imaging due to the simplicity and the good perceptive sense of surface topography in images.

Light ions generate more secondary electrons compared to gallium ions [41]. Therefore, lower doses are sufficient to image a sample compared to gallium FIB, or for low doses visibility is better with light ions. The recent down-scaling of integrated circuits has increased the demand for milling at the single-nm scale, which can only be achieved by gallium FIB with extremely low beam currents. This results in the difficulty to do end-point detection and drives the interest in SE imaging by light ions. A large amount of HIM SE images can be found throughout the literature. The shorter wavelength of helium ions compared to electrons allows a smaller spot, and the small interaction volume at the surface means that the secondary electron generation is restricted to a smaller area on the sample. Regarding nitrogen, Schmidt et al. reported secondary electron images of samples imaged by helium and by nitrogen ions [20].

Secondary imaging is, even with an electron beam in the SEM, almost always a destructive method. Sample chambers in scanning probe microscopes have typical base pressures of $>1 \times 10^{-5}$ Pa due to the fact that rubber o-rings are used to seal some of the large openings that are required to install the sample stage. The ultra-high vacuum alternative is the usage of copper gaskets that, through compression between knife-edge flanges, create extremely good vacuum seals. This increases the cost of the chamber and machine maintenance. Alternatively, it is possible to achieve better vacuum by installing two rubber o-rings, where the space between the rings is evacuated by a separate pump. Such measures would further require ultra-high cleanliness of the images specimen and reduce the machine throughput. The contamination in the chamber is typically hydrocarbons that are emitted from the pump system, and as the beam (again, this applies to electron as well as ion beams) hits the sample, some of the adsorbed hydrocarbons are disassociated, and amorphous carbon is deposited on the sample. This carbon modifies the sample surface and can influence secondary electron emission. In addition, the charging of the sample occurs immediately. Other effects that influence SE emission are as follows:

1. work function,
2. charging (note that ion beams will always cause positive charge due to the implantation of positive ions and emission of electrons, while negative charging can occur in SEM),
3. escape depth of SE,
4. energy spectrum of SE.

Due to all these effects and the fact that imaging is “destructive,” the prediction of SE yield remains impossible even for electrons. Therefore, while secondary electron yield (number of SEs emitted per incident particle) observed in a typical microscope might not be universal, they represent values “appropriate to the actual operational environment” [42]. Comparison of images has to be carefully discussed.

4.1. Unique contrast in carbon-based samples

By imaging samples with carbon-based materials by focused nitrogen and helium ion beams, it was reported that an improved SE contrast is observed by nitrogen [20]. The sample that was imaged is shown in **Figure 7**, which comprises electrically contacted four-layer graphene and graphite on SiO_2 with gold electrodes. Particularly, it was noticed that the graphene, which is pulled-in onto the SiO_2 substrate, is only visible by N2IM. In addition, the authors confirmed that the observed contrast difference was not caused by equipment differences, and re-imaged the structures in the *Zeiss Orion Plus* [42].

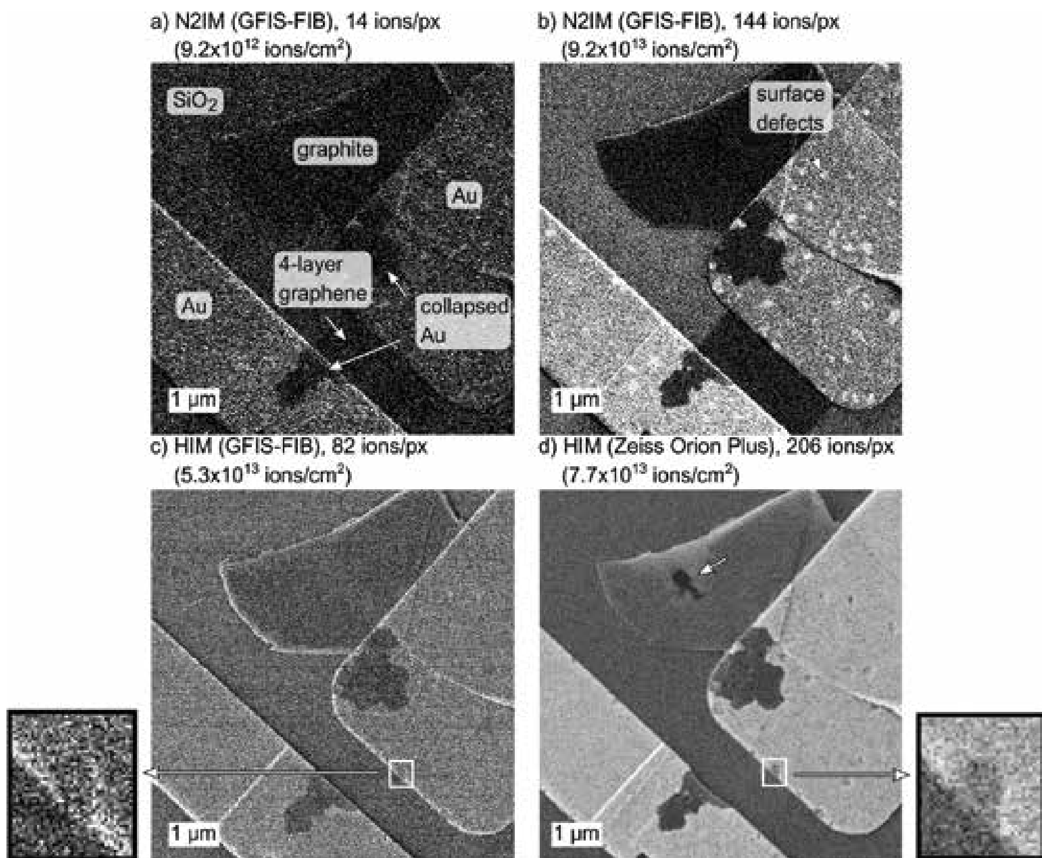

Figure 7. Secondary electron images acquired on identical location on nano-patterned sample. (a+b) N2IM (GFIS-FIB) images with 14 and 144 ions/px imaging dose at 25 keV. Graphite and four-layer graphene have good contrast against SiO_2 and Au electrodes. (c) HIM (GFIS-FIB) image with 82 ions/px at 25 keV. (d) HIM (Zeiss Orion Plus) image with 206 ions/px at 30 keV. The dark area in the graphite (arrow) is only visible in this image and probably formed after the previous imaging. Marek E. Schmidt, Shinichi Ogawa, Hiroshi Mizuta, "Contrast Differences Between Nitrogen and Helium Ion Induced Secondary Electron Images Beyond Instrument Effects," MRS Advances, DOI: 10.1557/adv.2018.33, reproduced with permission [42].

Interestingly, the thick graphite and the SiO_2 substrate had been exposed to a relatively strong oxygen reactive ion etching process, and the contrast difference was not observed for nano-crystalline graphene (NCG), a polycrystalline carbon film that can be deposited via a metal-free plasma-enhanced chemical vapor deposition at the wafer scale [43]. By imaging another sample comprising suspended graphene and electrically contacted graphite that was not exposed to the RIE (**Figure 8**), the contrast difference could be gradually induced by an accumulated nitrogen ion dose of more than 4×10^{14} ions/cm^2 [20]. Although the final cause for the contrast difference is not yet fully understood, it has thus become clear that the surface modification through the RIE process together with the nitrogen beam results in the observed effect. Strangely, however, the contrast difference appears to be temporary while observing with nitrogen. It should be interesting to see if adsorption of the reactive nitrogen atoms to the surface (nitrogen can be ejected from the sample surface, compare **Figure 6**) can cause a temporary change of work function and is removed shortly after imaging is stopped. Nevertheless, any added contrast can enable the imaging of samples that would otherwise remain unobservable. The effect of charging on the contrast is clearly visible in **Figure 8a**. Isolated gold and graphite gradually become darker as it is scanned by the nitrogen beam from top to bottom, while the contacted graphite retains its initial brightness.

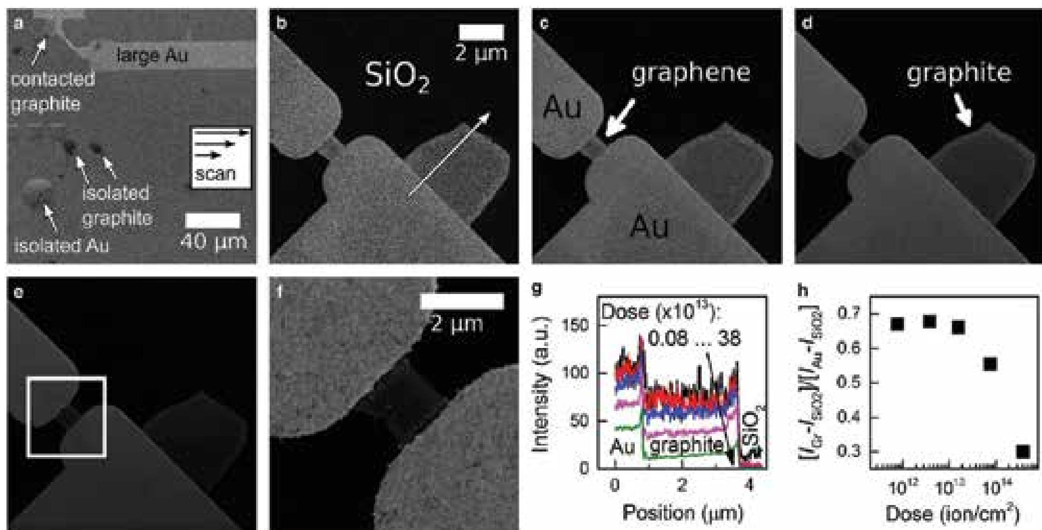

Figure 8. (a) Low-resolution N_2^+ GFIS-FIB image ($\sim 6 \times 10^{10}$ ion/cm^2) of sample C6 showing large Au electrodes with a contacted graphite flake, as well as isolated graphene and Au pattern. The isolated pattern shows decreased brightness from top to bottom caused by charging during the scan (scan direction illustrated in inset). (b–e) Series of images with a gradually increasing dwell time of identical location on sample C6 comprising suspended bilayer graphene and a larger graphite flake. The dose is increased from 6 ($\sim 3.8 \times 10^{12}$ ion/cm^2) to 24, 120, and 600 ion/cm^2. (f) A higher-resolution scan of area indicated by black square in (e) with 120 ion/px ($\sim 8.5 \times 10^{14}$ ion/cm^2). (g) Pixel brightness profile along the arrow shown in (b). (h) Relative graphite brightness as a function of accumulated dose extracted from (g) showing a decrease at high dose. Reproduced with permission [20].

http://dx.doi.org/10.5772/intechopen.76383

4.2. Nanomachining

Nanomachining of nanoscopic structures is one of the main advantages of the FIB over the SEM. At the beginning of this chapter, we discussed the motivation of the light gas ion source development, namely a higher milling resolution than the heavy gallium.

Helium has been demonstrated to offer unprecedented milling resolution of suspended layers [44] with a $\sim$ 5-nm wide graphene nanoribbon (GNR) realized in suspended graphene. As the number of experimental reports with the HIM increased, a serious limitation of the helium beam milling in bulk samples has been observed. Since the helium ion interacts with the surface, a small number of surface atoms are sputtered in a very well-controlled area; however, the ions continue to penetrate into the specimen and are implanted at a depth of 100–500 nm (depending on the energy) and remain there. Helium as a noble gas cannot be absorbed into the target specimen, but can be "squeezed" into the space between atoms. At doses above $\sim 10^{16}$ ions/cm^2, however, the pressure of the helium in the target substrate becomes sufficiently large to break the inter-atomic bonds and form helium nanobubbles [45]. It has been reported that a high-power laser pulse can be used in situ during milling to locally heat the target area and alleviate the damage, but crystal defects and surface deformation remain above 1×10^{18} ions/cm^2, which is the required dose to pattern graphene [46]. For reflection-type UV masks, any defects in the atomically precise adsorber stack will lead to a degradation; therefore, hydrogen (which is small and reactive and thus does not cause significant corruption to the target material [14]) or heavier ion species are preferred.

Figure 9a shows a MoSi film on quartz substrate with a single-line etching with a nitrogen-focused ion beam [47]. The cut width of $\sim$ 9 nm is smaller than what can be achieved by gallium, and vertical side walls are achieved for the whole depth. **Figure 9b** shows how the focused nitrogen beam can be used to correct protrusive defects in the MoSi-adsorbing layer. By careful alignment and control of the milling conditions, the repaired edge is not distinguishable from the non-defective edge—an important requirement for mask repair.

N_2 GFIS-FIB was also used for the successful formation of quantum point contacts in high-in-content InGaAs [48], as shown in **Figure 10**. Here, $\sim$ 30-nm wide trenches were carefully aligned to previously wet-etched areas with an inner separation of down to $\sim$ 30 nm, smaller

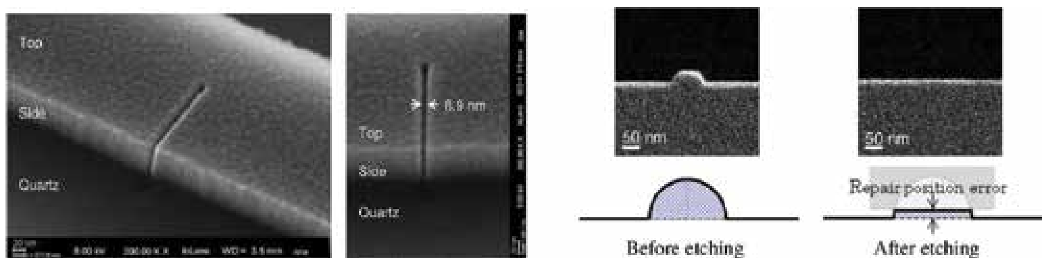

Figure 9. (left) Scanning electron microscopy image of a MoSi film after a one-line etching with the focused nitrogen beam. The width of the deep cut is $\sim$ 9-nm wide. (right) N2IM images showing the removal of protrusive defect in MoSi film on quartz substrate. After removal, the location of the modification is not visible. Reproduced with permission [47].

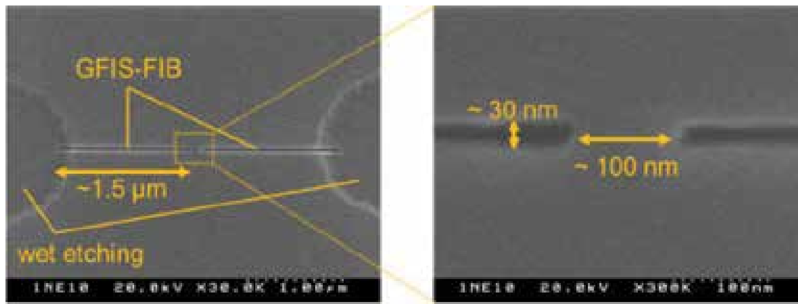

Figure 10. Scanning electron microscopy image of a quantum point contact (QPC) fabricated using N_2 GFIS-FIB. Two horizontal cuts with a width of ~ 30 nm are placed with a separation of ~ 100 nm. Copyright 2014 the Japan Society of Applied Physics [48].

than the size available by electron beam lithography. Half-integer quantized conductance behaviors were observed under magnetic fields, which demonstrates that N_2 GFIS-FIB milling is a promising method to realize quantum devices.

4.3. Other applications

We have shown so far that the N2IM can be used for imaging and milling applications. These can also be performed by helium or neon beams, albeit sacrificing the material contrast discussed in Section 4.1. Nitrogen, however, has a unique effect when implanted into diamond. When a C atom of the diamond lattice is replaced with a nitrogen nearby a vacancy, the so-called nitrogen-vacancy (N-V) center is formed. It has shown to be a scientifically valuable phenomenon as the photoluminescence from a single N-V center can be detected by confocal microscopy [49, 50]. As it turns out, the photoluminescence is affected by magnetic fields [51], electric fields [52], temperature [53], and mechanical stress [54]. Furthermore, N-V centers can be viewed as a basic unit of a quantum computer [55]. To fully exploit these effects, it is necessary to produce N-V centers with nm precision.

To generate N-V centers, either nitrogen implantation followed by annealing is used, or a small amount of nitrogen is added during the chemical vapor deposition of diamond. N-V centers can also be generated by the focused nitrogen ion beam from the GFIS. In this regard, the sub-2-nm beam diameter and variable energy make it a powerful tool. However, some points should be noted about the N-V center generation by ion implantation that needs to be technologically controlled. First, the so-called “conversion efficiency,” which signifies the number of N-V centers per implanted nitrogen, is in the single-digit percentage. Therefore, it is not possible to deterministically control the number of N-V centers. Another (smaller) uncertainty is the minute current fluctuation of the GFIS, which means that repeatedly dwelling the beam for a given time will result in different numbers of nitrogen ions and potentially N-V centers; however, this effect is small compared to the conversion efficiency uncertainty. Second, the trajectory of an ion through a solid is subject to a certain randomness. To implant deep N-V centers (which do not disappear through migration to the sample surface during the required postimplantation annealing), a sufficiently large acceleration voltage is required, and the control over the position is lost. As we saw in **Figure 6**, the horizontal distance the ion can travel from the landing point is significant. For nitrogen in a diamond with 12.5 kV, the range

http://dx.doi.org/10.5772/intechopen.76383

is ~ 50 nm. A possible solution would be the use of a very low acceleration voltage for the GFIS-FIB nitrogen implantation (thus with an accurate spatial control), followed by an in situ deposition of a diamond capping layer without breaking vacuum. This is certainly an interesting technical challenge.

5. Summary and conclusion

We have given an introduction to the nitrogen ion microscopy (N2IM). Starting with the exciting history, development, and principle of the GFIS, which is at the heart of the recent technological advancement in FIB technology, we have discussed how the molecular nitrogen source gas is different from the atomic source gases. We have reviewed the interaction of nitrogen ions with a silicon sample which shows that nitrogen (N_2) is ionized to N_2^+ and splits within few atomic layers after collision with a sample. The unusual contrast of carbon-based films exposed to a high dose of ion damage in SE images was shown. In terms of machining, nitrogen is a good compromise between helium (high-resolution and low sputter yield) that unfortunately leads to sample swelling at higher doses, and the established gallium (low-resolution and high sputter yield). It was shown how quantum point contacts and photolithographic mask repair is enabled by the nitrogen FIB.

Acknowledgements

This work was supported by the Center of Innovation (COI) program of the Japan Science and Technology Agency and the Grant- in-Aid for Scientific Research No. 25220904, 16K13650, and 16K18090 from the Japan Society for the Promotion of Science (JSPS).

Author details

Marek E. Schmidt*, Masashi Akabori and Hiroshi Mizuta

*Address all correspondence to: schmidtm@jaist.ac.jp

Japan Advanced Institute of Science and Technology, Nomi, Japan

References

[1] Feynman RP. There's plenty of room at the bottom. Engineering and Science. 1960;**23**(5): 22-36

[2] Orloff J, Swanson LW, Utlaut M. Fundamental limits to imaging resolution for focused ion beams. Journal of Vacuum Science & Technology B: Microelectronics and Nanometer Structures Processing, Measurement, and Phenomena. 1996;**14**(6):3759-3763

[3] Hlawacek G, Gölzhäuser A. Helium Ion Microscopy. Cham: Springer; 2016. 536pp

[4] Müller EW. Das Feldionenmikroskop. Zeitschrift für Physik. 1951;**131**(1):136-142

[5] Orloff JH, Swanson LW. Study of a field-ionization source for microprobe applications. Journal of Vacuum Science and Technology. 1975;**12**(6):1209-1213

[6] Orloff J, Swanson LW. Angular intensity of a gas-phase field ionization source. Journal of Applied Physics. 1979;**50**(9):6026-6027

[7] Horiuchi K, Itakura T, Ishikawa H. Emission characteristics and stability of a helium field ion source. Journal of Vacuum Science & Technology B: Microelectronics Processing and Phenomena. 1988;**6**(3):937-940

[8] Tondare VN. Quest for high brightness, monochromatic Noble gas ion sources. Journal of Vacuum Science & Technology A. 2005;**23**(6):1498-1508

[9] Knoblauch A et al. Field Electron emission properties of a Supertip. Journal of Physics D: Applied Physics. 1996;**29**(2):470

[10] Ward B. Spectacular collision of entrepreneurial spirit and a doomed technology transforming the impossible into the helium ion microscope. In: AVS 63rd International Symposium & Exhibition; 2016

[11] Morgan J et al. An introduction to the helium ion microscope. Microscopy Today. 2006; **14**(4):24-31

[12] Ward BW, Notte JA, Economou NP. Helium ion microscope: A new tool for Nanoscale microscopy and metrology. Journal of Vacuum Science & Technology B. 2006;**24**(6):2871-2874

[13] Economou NP, Notte JA, Thompson WB. The history and development of the helium ion microscope. Scanning. 2012;**34**(2):83-89. pmid: 21611954

[14] Aramaki F, Ogawa T, et al. Development of new FIB technology for EUVL mask repair. In: Proceedings of SPIE 7969. Extreme Ultraviolet (EUV) Lithography II. Vol. 7969. San Jose; 2011. pp. 79691C-79691C-7

[15] Bowkett KM, Smith DA. Field-Ion Microscopy. Amsterdam: North-Holland Pub. Co; 1970. 274 pp

[16] Gomer R. Field Emission and Field Ionization. Cambridge: Harvard University Press; 1961. 216 pp

[17] Müller EW, Tsong TT. Field ion microscopy, field ionization and field evaporation. Progress in Surface Science. 1974;**4**:1-139

[18] Orloff J. Field emission ion sources for focused ion beams. In: The Handbook of Surface Imaging and Visualization. Boca Raton: CRC Press; 1995. pp. 165-177

[19] Müller EW, Tsong TT. Field Ion Microscopy: Principles and Applications. New York: American Elsevier Pub. Co; 1969. 336 pp

[20] Schmidt ME, Yasaka A, et al. Nitrogen gas field ion source (GFIS) focused ion beam (FIB) secondary Electron imaging: A first look. Microscopy and Microanalysis. 2017;**23**(4): 758-768

[21] Aramaki F, Kozakai T, Matsuda O, Takaoka O, et al. Photomask repair technology by using gas field ion source. In: Proceedings of SPIE 8441. Photomask and Next-Generation Lithography Mask Technology XIX. Vol. 8441. Yokohama; 2012. pp. 84410D-84410D-6

[22] Kuo H-S et al. Gas field ion source from an Ir/W ⟨111⟩ single-atom tip. Applied Physics Letters. 2008;**92**(6):063106

[23] Wood JA et al. Iridium single atom tips fabricated by field assisted reactive gas etching. Applied Surface Science. 2016;**367**:277-280

[24] Lalanne J-B et al. Note: Electrochemical etching of sharp iridium tip. Review of Scientific Instruments. 2011;**82**(11):116105

[25] Rahman F et al. Field-assisted oxygen etching for sharp field-emission tip. Surface Science. 2008;**602**(12):2128-2134

[26] Lai W-C et al. Xenon gas field ion source from a single-atom tip. Nanotechnology. 2017; **28**(25):255301

[27] McClelland JJ et al. Bright Focused Ion Beam Sources Based on Laser-Cooled Atoms. Applied Physics Reviews. 2016;**3**(1):011302

[28] Viteau M et al. Ion microscopy based on laser-cooled cesium atoms. Ultramicroscopy. 2016;**164**:70-77

[29] Schimmerling W, Vosburgh KG, Todd PW. Interaction of 3.9-Gev nitrogen ions with matter. Science. 1971;**174**(4014):1123-1125. pmid:17779399

[30] Pavlov PV et al. Electron microscopic studies of silicon layers irradiated with high doses of nitrogen ions. Physica Status Solidi. 1976;**36**(1):81-88

[31] Yadav AD, Joshi MC. Formation of thin Si3N4 films by nitrogen ion implantation into silicon. Thin Solid Films. 1979;**59**(3):313-317

[32] Stein SE. 2014 Mass Spectra. In: Linstrom PJ, Mallard WG, editors. NIST Chemistry WebBook. Gaithersburg, MD: NIST Standard Reference Database. 2016. Number 69

[33] Zavilopulo AN, Chipev FF, Shpenik OB. Ionization of nitrogen, oxygen, water, and carbon dioxide molecules by near-threshold Electron impact. Technical Physics. 2005;**50**(4):402-407

[34] Åhlgren EH, Kotakoski J, Krasheninnikov AV. Atomistic simulations of the implantation of low-energy boron and nitrogen ions into graphene. Physical Review B. 2011;**83**(11): 115424

[35] Ziegler JF, Ziegler MD, Biersack JP. SRIM – The stopping and range of ions in matter (2010). Nuclear Instruments and Methods in Physics Research Section B: Beam

Interactions with Materials and Atoms. 2010;**268**(11–12):1818-1823. 19th International Conference on Ion Beam Analysis

[36] Mahady K et al. Monte Carlo simulations of secondary Electron emission due to ion beam milling. Journal of Vacuum Science & Technology B, Nanotechnology and Microelectronics: Materials, Processing, Measurement, and Phenomena. 2017;**35**(4):041805

[37] Ohya K, Ishitani T. Monte Carlo study of secondary Electron emission from SiO2 induced by focused gallium ion beams. Applied Surface Science. Proceedings of the Seventh International Symposium on Atomically Controlled Surfaces, Interfaces and Nanostructures. 2004;**237**(1–4):602-606

[38] Schmidt ME, Yasaka A, et al. Interaction study of nitrogen ion beam with silicon. Journal of Vacuum Science & Technology B. 2017b;**35**(3):03D101

[39] Tan S et al. Gas field ion source and liquid metal ion source charged particle material interaction study for semiconductor Nanomachining applications. Journal of Vacuum Science & Technology B. 2010;**28**(6):C6F15-C6F21

[40] Ramachandra R, Griffin B, Joy D. A model of secondary electron imaging in the helium ion scanning microscope. Ultramicroscopy. 2009;**109**(6):748-757

[41] Goldstein JI et al. Scanning Electron Microscopy and X-Ray Microanalysis: A Text for Biologists, Materials Scientists, and Geologists, 2nd ed. Springer US, 1992

[42] Schmidt ME, Ogawa S, Mizuta H. Contrast differences between nitrogen and helium ion induced secondary electron images beyond instrument effects. MRS Advances. 2018:**3**(10): 505-510

[43] Schmidt ME, Cigang X, et al. Metal-free plasma-enhanced chemical vapor deposition of large area nanocrystalline graphene. Materials Research Express. 2014;**1**(2):025031

[44] Pickard D, Scipioni L. Graphene Nano-Ribbon Patterning in the ORION® PLUS. In: Zeiss application note. 2009

[45] Livengood R et al. Subsurface damage from helium ions as a function of dose, beam energy, and dose rate. Journal of Vacuum Science & Technology B. 2009;**27**(6):3244-3249

[46] Stanford MG et al. In situ mitigation of subsurface and peripheral focused ion beam damage via simultaneous pulsed laser heating. Small. 2016;**12**(13):1779-1787

[47] Aramaki F, Kozakai T, Matsuda O, Yasaka A, et al. Performance of GFIS mask repair system for various mask material. In: Proceedings of SPIE. Photomask Technology 2014. Vol. 9235. Monterey; 2014. pp. 92350F-92350F-8

[48] Akabori M et al. High-in-content InGaAs quantum point contacts fabricated using focused ion beam system equipped with N2 gas field ion source. Japanese Journal of Applied Physics. 2014;**53**(11):118002

[49] Gruber A et al. Scanning confocal optical microscopy and magnetic resonance on single defect centers. Science. 1997;**276**(5321):2012-2014

[50] Iwasaki T et al. Direct nanoscale sensing of the internal electric field in operating semiconductor devices using single Electron spins. ACS Nano. 2017;**11**(2):1238-1245

[51] Balasubramanian G et al. Nanoscale imaging magnetometry with diamond spins under ambient conditions. Nature. 2008;**455**(7213):648-651. pmid: 18833276

[52] Dolde F et al. Electric-field sensing using single diamond spins. Nature Physics. 2011;**7**(6): 459-463

[53] Doherty MW et al. Electronic properties and metrology applications of the diamond NV^- center under pressure. Physical Review Letters. 2014;**112**(4):047601

[54] MacQuarrie ER et al. Mechanical spin control of nitrogen-vacancy centers in diamond. Physical Review Letters. 2013;**111**(22):227602

[55] Wrachtrup J, Jelezko F. Processing quantum information in diamond. Journal of Physics: Condensed Matter. 2006;**18**(21):S807

Section 4

Ion Implantation

Ion Implantation as a Tool for Controlled Modification of Photoelectrical Properties of Silicon

Nina Khuchua, Marina Tigishvili, Nugzar Dolidze,
Zurab Jibuti, Revaz Melkadze and Roland Diehl

Additional information is available at the end of the chapter

http://dx.doi.org/10.5772/intechopen.76992

Abstract

The results of our recent studies of controlled modifications of the photoelectrical properties of n-Si due to B^+ ion implantation are supplemented with new data, summarized and analyzed. The starting material was wafers of single-crystalline n-Si and a silicon-on-insulator structures. p-n-Si structures were fabricated by ion implantation of B^+ in doses ranging from 1×10^{13} to 1×10^{15} cm^{-2} and ion acceleration energies of 50 and 32 keV. Subsequent annealing was performed both by steady-state (900 and 1000°C, 20 min) and pulsed photon processing. In such structures, a pronounced photosensitivity is observed in the short-wave infrared range (1.5–2.2 μm), as well as in the ultraviolet region within 0.25–0.40 μm. A well-defined correlation between the structural, electrical and photoelectrical properties and the implantation and annealing regimes, as well as the content of C and O impurities is demonstrated. In the starting material, a damaged layer with a thickness of hundreds of nanometers was found to have a significant effect on the results obtained. The main results are discussed in terms of the formation/transformation of deep-level extended defects in n-Si during B^+ implantation followed by annealing. Innovative application approaches of the technology are obvious.

Keywords: single-crystalline n-Si, damaged near-surface layer, boron ion implantation, annealing regimes, p-n-Si structures, IR and UV photosensitivity, C and O impurities, deep level extended defects

1. Introduction

Studies of the optical and photoelectric properties of semiconductors are in most cases equivalent with respect to their scientific and practical significance. The first aims at a thorough

IntechOpen

© 2018 The Author(s). Licensee IntechOpen. This chapter is distributed under the terms of the Creative Commons Attribution License (http://creativecommons.org/licenses/by/3.0), which permits unrestricted use, distribution, and reproduction in any medium, provided the original work is properly cited. (cc) BY

understanding of the processes involved in a particular material behavior under the influence of electromagnetic radiation (EMR). The second is due to the variety of EMR semiconductor converters used in various fields of technology.

Apart from a more classical point of view which looks at the sensitivity of a semiconductor to various regions of the EMR spectrum depending on the bandgap, materials the initial fundamental properties (structural, electrical, optical) of which are modifiable due to the specific impact of technological processes [1] are of ever increasing interest.

The classical approach cannot solve all the problems that arise when developing detector/sensor systems, e.g. for specific ranges of the infrared (IR) and ultraviolet (UV) spectra. Therefore, new technologies are emerging, in particular the so-called defect engineering. Applying this scientific-technical approach, a number of fundamental semiconductor characteristics are changed due to purposefully creating a variety of defects that modify the material properties. The effective behavior is sometimes difficult to understand - the practical result can be observed immediately, whereas its interpretation turns out to be rather complicated requiring quite a number of various tools and methods of investigation and characterization.

A very attractive and promising material for a variety of applications with respect to modifying its properties is unipolar silicon with its high level of processability and easy availability.

Because silicon is transparent for wavelengths exceeding 1.1 μm, it cannot be used directly e.g. for the development of IR photodiodes. One of commonly applied methods to obtain various structural modifications, is changing the width of the Si bandgap using Ge. Most efficient structures are grown by molecular beam epitaxy (MBE).

In [2], it was shown that, when single crystalline Si is subjected to electropulse treatment, the self- absorption edge of the material shifts to 1.33 μm. This is undoubtedly referred to a change in the band structure of Si allowing for bandgap engineering, but so far the practical application potential of the technology is unclear.

In some cases, ion implantation (II) can be considered as an alternative to the MBE method. II enables the materials' researcher and engineer to tightly control the introduction of impurities into the semiconductor, creating a variety of defects the type, concentration and electrical activity of which are largely determined by the conditions of post-implantation annealing [3, 4]. Altogether, by applying such processes the fundamental properties of the material are changed.

Undoubtedly, this area of technology is not only of scientific but also of practical interest, as it provides access to specific semiconductor electro-optical EMR converters which include detecting devices for various ranges of IR and UV spectra [5, 6].

The II technology is attractive because of its relative simplicity, reproducibility and low-cost potential. However, the physical mechanisms behind the influence of certain defects on the optical and photoelectrical properties of the material are not easily evident. Such defects are not only formed during II, but also transformed by annealing in the subsequent heat treatment process. Therefore, defect engineering requires various techniques to be involved such as Raman and IR spectroscopy, X-ray diffraction, transmission electron microscopy (TEM), photo- and electroluminescence, *deep-level transient spectroscopy* (DLTS), etc.

http://dx.doi.org/10.5772/intechopen.76992

It is known that in silicon technology, boron is one of the widely used impurities, e.g. for the production of single-crystalline p-type material, creation of p-n junctions, etc. A large number of original papers were published and many overviews articles have been devoted to the study and description of defects formed during ion doping of Si with boron (see [7–11], etc.). In general, it is shown that applying the process of II, a wide range of defects is formed, which, due to annealing, evolve from point-like to complex extended defects. For light ions (such as boron) implanted into single-crystalline silicon, for each set of dose-annealing conditions a special type of defects predominate [4].

In [4, 12] it is concluded that the formation of residual extended defects in silicon needs an dose “threshold”. This means that such structural disorder during heat treatment (at least 700°C) arises only if a critical concentration of point defects has accumulated. For boron ions with energies of 10–100 keV this occurs at doses of the order of $1×10^{14}$ cm^{-2}.

It was found that most point defects in Si are annealed at temperatures up to 450°C [4, 7].

Extended defects formed at elevated temperatures are preserved, according to different data, up to an annealing temperature of 1000°C and beyond [15, 16]. In [10], during B^+ implantation with different acceleration energies (10–80 keV) and annealing at 950°C, sufficiently large (30–200 nm) dislocation loops were detected by TEM. It is shown that the acceleration energy does not only affect the depth, but also the size and density of these defects. When introducing B^+ ions with an energy of 75 keV, dose $1×10^{15}$ cm^{-2} and annealing at 700°C, only defects of the road-like {311} were detected by TEM. By increasing the temperature further, these defects are transformed into dislocation loops [11].

In defect formation not only introduced but also unavoidable impurities take part. Oxygen and carbon are one of the main accompanying impurities in Czochralski grown Si crystals The carbon content is estimated to be $5 × 10^{16}$ to $2 × 10^{17}$ cm^{-3} and the oxygen content was found to be $2.5 × 10^{17}$ to $2 × 10^{18}$ cm^{-3} [4, 13].

Altogether, the presence of carbon and oxygen is directly related to the defects formed in n-Si ion-implanted with impurities such as B since the content of impurities and inhomogeneities in the substrate significantly affects the migration of defects induced by II as well as their further evolution.

In the framework of this research, defects with deep levels (DL) are of primary interest.

The analysis of the DL spectrum in the silicon bandgap allows us to conclude that there is no clear correlation between these levels and specific structural defects [14, 15]. In addition, different defects can have very similar or even identical values of the DL activation energy.

Finally, we could not find any information on photosensitivity spectra of boron-implanted silicon, especially in the infrared spectral range. Only sparse data is known on the research of IR and UV photosensitivity in B- and As-implanted Si [16].

As mentioned above, data are incomplete, results partially contradictory and not fully understood. Nevertheless, we can draw the following conclusions:

1. Over the past several decades, the formation of structural distortions in the process of II and their subsequent arrangement due to annealing have been extensively studied both theoretically and experimentally. Disclosing the characteristics of these distortions helps scientists to understand and model the phenomena, such as the transient-enhanced diffusion of impurities and the formation of extended defects. However, many issues concerning the agglomeration of defects and their further evolution during annealing are still unresolved, in particular how point defects are combined to form more stable and complex structures such as clusters of defects, and how the latter evolve into extended defects.

2. Finally, even less information is available about the mechanism of the influence of various damages on the optical and photoelectrical properties of p-n junctions formed by B implantation into n-type single-crystalline silicon. Although the data on the photo- and electroluminescence spectra are well documented in the literature, the absorption/photosensitivity spectra have been studied less comprehensively and are not associated with any type of defects.

In the present work, an innovative approach to B^+ II into Si as a tool for controlled modification of photoelectric properties of silicon was proposed. Such an approach is both of scientific and practical importance. However, the materials science involved has been less studied so far. The new resolved issues allow one to gain a deeper insight into the processes of defect formation/transformation in p-n structures obtained by B^+ implantation followed by annealing (hereinafter p-n-Si(B) structures). From the application point of view, this opens up new opportunities for the development of IR and UV photodetectors as a part of the silicon technology.

In this article we summarize the results of our studies of the structural, electrical, and photoelectrical properties of p-n-Si(B).The extensive experimental material described earlier [17–22] is supplemented with new data and findings.

2. Experimental

2.1. Formation of p-n-Si(B) structures

p-n-Si(B) structures were formed by ion implantation (implanter Vesuvii 3 M) with different doses of 1×10^{13}, 1×10^{14}, 4×10^{14}, 6×10^{14}, 8×10^{14}, and 1×10^{15} cm^{-2} and acceleration energies of 50 and 32 keV. For the energy 50 keV the projected range, R_p, and range straggling ΔR_p, calculated using stopping and range of ions in matter (SRIM) software, were 0.175 and 0.055 μm, respectively, and for the energy 32 keV – $R_p = 0.120$ μm and $\Delta R_p = 0.052$ μm. Post-implantation annealing was carried out mainly in a steady-state regime in argon atmosphere at temperatures of 900 and 1000°C for 20 min. For comparison, some samples were subjected to pulse photon annealing (PPA). The design of our system allows illumination of the specimen surface with UV light, and of the reverse side with a halogen lamp.

Figure 1 shows a schematic view of the processed p-n structures of two types. In the case of **Figure 1a**, (100) n-Si single-crystalline wafers with resistivity of about 70 or 10 Ohm·cm and

http://dx.doi.org/10.5772/intechopen.76992

thickness of 250 μm (University Wafer, USA) were used as a starting material. According to **Figure 1b**, the specimens were silicon-on-insulator (SOI) structures with the working layer of single-crystalline 2 μm n-Si with resistivity up to 30 Ohm·cm. The dielectric layer was also 2 μm thick (manufacturer—Ultrasil Corporation, USA).

After B^+ implantation and annealing, a metal composition Ti/Pt/Au (100/100/1000 Å) or Ti/Au (100/1000 Å) was deposited (through a mask or by lift-off photolithography) in the electron-beam evaporation system Temescal. The alloying was performed in the 210 HEATPULSE system at 350°C (15 s). The first type structures (**Figure 1a**) had a continuous reverse contact, and a point contact for the p-type layer. In the SOI structure (**Figure 1b**), both contacts were formed on the active layer. The mesa structure was obtained by wet etching in a fluorine-containing solution using an acid-resistant photoresist mask.

2.2. Specimen characterization techniques

Diagnostics of the structure of the near-surface layers of the initial and ion-doped material was carried out using two-crystal X-ray diffraction on the Dron-4 installation. The first crystal was the studied sample, and the second was the perfect LiF crystal. Diffracted reflection occurred from the lattice plane hkl (531) oriented at an angle of 2°46' to the primary ray. $Co_{k\beta}$ radiation was used for the experiment.

Raman-spectra were recorded by a Raman-microscope (Renishaw) under He-Ne laser excitation with the wavelength λ_{ex} = 632.8 nm. The thickness of the tested layer was about 1.3 μm, and the wave number reproducibility was 0.1 cm^{-1}. For data analysis the software WiRE3.4 was used.

The surface morphology and elemental composition of the structures to a depth of 1 μm was studied on a YEOL ISU-6510LV scanning electron microscope (SEM). This method providing of sensitivity 0.01% and less was used to determine the C and O composition in Si, averaged over the sample surface.

To measure the I-V characteristics of the diodes the semiconductor parameter Analyzer L2–50 was used.

IR reflection spectra were recorded using a Bruker IFS 66 Fourier-spectrometer within the range of 4000–400 cm^{-1} with a resolution of 0.4 cm^{-2} and wave number accuracy of 0.01 cm^{-1}. For spectra processing the software OPUS 5.5 was used.

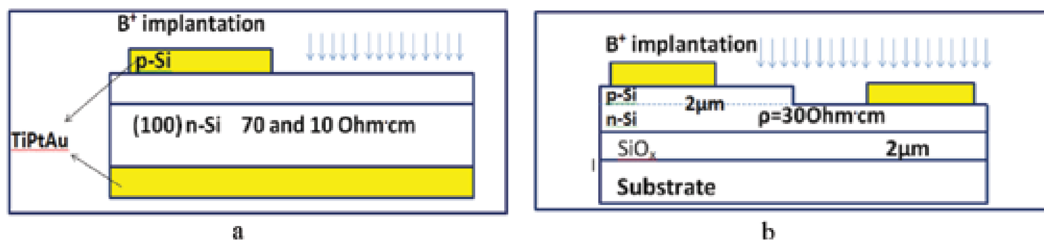

Figure 1. Schematic view of the p-n structures after processing: (a) on n-Si wafers with different resistivity (Si70) and (Si10); (b) on SOI, a, b.

The photosensitivity of the p-n-Si (B) samples in the spectral range 1.0–2.5 μm was measured on a MDR-2 monochromator and IR optical filters.

Since, under real conditions, the photosensitive element is exposed to a beam of light of a limited wavelength range rather than to a non-monochromatic light, we developed a genuine technique and created a setup called "Polychromator," enabling illumination of samples with "packets" of non-monochromatic light. The source of radiation are halogen or mercury lamps, which provide irradiation of samples with light of a wide spectral range (200–4100 nm). This range is regulated by optical filters (altogether 21) selected in such a way that their application allows for varying the spectral ranges by consistently "cutting off" shorter wavelengths.

In our case, the short-circuit current through the element is measured and the quantity

$$\frac{I_n - I_{n+1}}{I_o}, \tag{1}$$

is estimated, where I_o is the current in the sample onto which the entire illumination spectrum is incident, I_n is the current corresponding to the previous filter and I_{n+1} is the current measured for a given particular filter (n = 0, 1, 2, 3, etc.).

Below, the photosensitivity measured by this method will be referred to as "integral" as compared to the data obtained by a monochromator. Such a technique allows one to qualitatively separate the influence of the intensity and spectral composition of the incident illumination on the electrical signal. The value determined by formula (1) may adopt in certain cases a zero or even a negative value.

All measurements were carried out at room temperature, except for the photosensitivity spectra using a monochromator, where the sample was placed into liquid nitrogen.

3. Results

For the samples of both the untreated and boron-implanted silicon with a dose of 1×10^{14} cm^{-2} after stationary annealing (1000°C, 20 min), the diffraction reflection curves were measured. From these curves, the intensity of the diffraction reflection signal, the line half-width, the lattice parameters, the relative lattice deformation, and the interplanar spacing were calculated for each case (**Table 1**).

From the signal line width the degree of crystallinity of the sample structure can be derived: the smaller the width, the more perfect the crystal. On the contrary, a lower intensity of the signal indicates heavy damages of the crystal structure. It is clear that the degree of crystallinity of the ion-implanted and annealed material deteriorates as compared with the untreated one. In the ion-implanted material, an increase of interplanar spacing and of the lattice constant is observed [17].

Figure 2 shows the Raman-spectroscopy results for p-n-Si (B).

The position of the band maximum of the starting material (519.4 cm^{-1}) indicates a shift towards lower wave numbers as compared to the classical value for silicon (520 cm^{-1}), which

Sample	Lattice parameter, Å	Relative lattice deformation, ΔB/d·103	Interplanar spacing, A	Diffraction line half-width, min	Signal intensity, pulse/s
untreated	5,4304	-	0,91792	14,1	700
II+annealing	5,4311	0,1416	0,91805	17,9	600

Table 1. X-ray diffraction results.

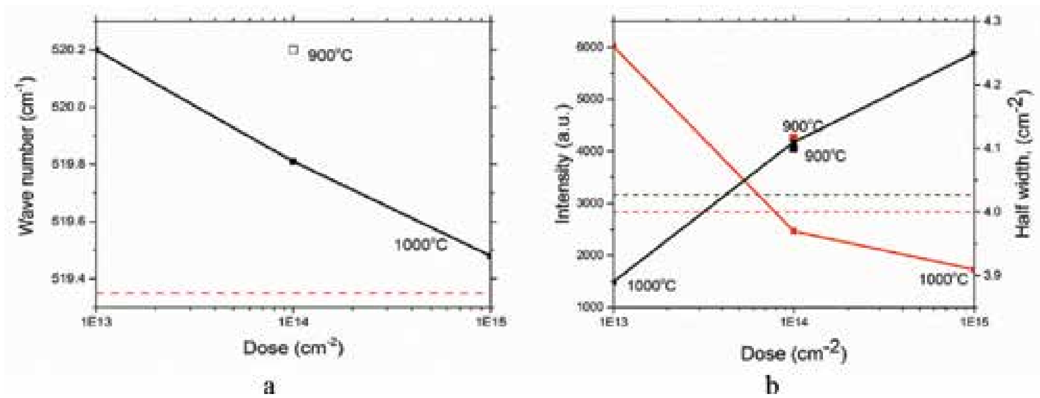

Figure 2. Dose dependence of the Raman spectra parameters: (a) change in the main band position (position of the reference sample maximum is 520 cm^{-1}); (b) intensity (red), half-width (black). The dotted line shows the n-Si data (a,b).

means that n-Si has a near-surface damaged layer. In comparison with the starting material, the maximum of the band for 1×10^{13} cm^{-2} is shifted towards higher values (520.2 cm^{-1}), the intensity becomes twice as much, and the half-width decreases (qualitatively, the same pattern is observed for 1 x 10^{14} cm^{-2} (annealing at 900°C). Increasing the II dose up to 1×10^{15} cm^{-2} and annealing at 1000°C shifts the band towards smaller wave number values, the intensity decreases, and the half-width increases [19, 21].

Figure 3 demonstrates a typical example of SEM measurements for starting n-Si and p-n-Si(B) annealed at 900 and 1000°C. As follows from these data, the n-Si surface is determined by a homogeneous surface morphology (a). This is also characteristic for the surfaces of the "annealed-only" or "implanted-only" Si. At 900°C, defects of different size appear (b), the amount of which noticeably decreases at 1000°C (c). The samples exhibit a similar behavior at all doses.

Figure 4 shows the diode characteristics typical of the investigated structures, implanted with a dose of 4 × 10^{14} cm^{-2} and annealed at 900°C (20 min).

Figure 5 illustrates the behavior patterns of leakage currents at different implantation doses for p-n diodes at a voltage of −2 V (a value frequently used in practice). Of particular interest are the data for the Si70 samples: up to the dose of 6 × 10^{14} cm^{-2} no significant variance in the leakage currents is observed, whereas at higher doses the change exceeds two orders of magnitude. It is remarkable that samples implanted with 1 × 10^{15} cm^{-2} and annealed at 1000°C

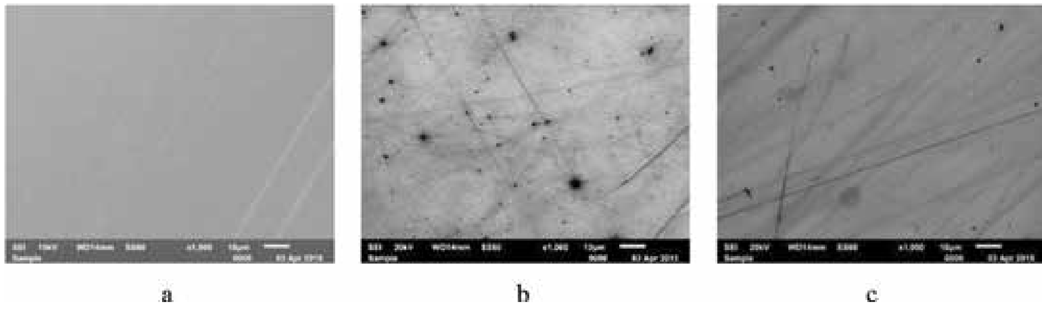

Figure 3. Surface morphology of the samples in SEM: a—starting n-Si; b—900°C; c—1000°C (×1000) (a, b, c).

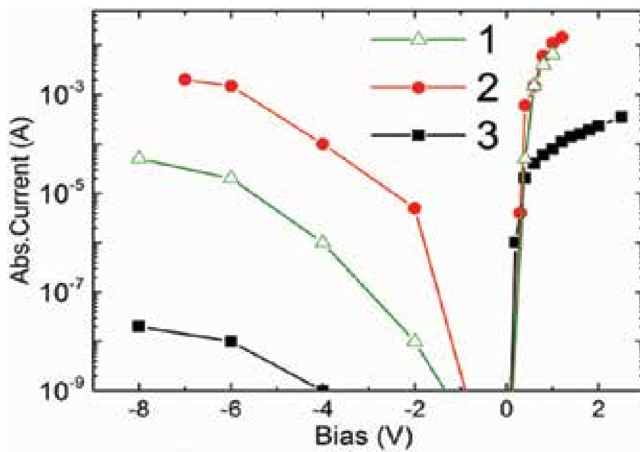

Figure 4. I-V characteristics of the p-n diodes: (1) Si70; (2) Si10; (3) SOI.

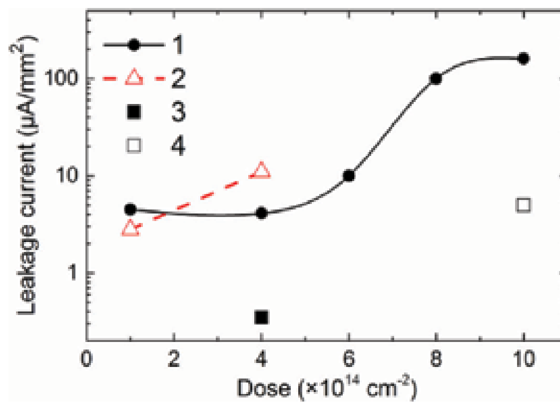

Figure 5. Dependence of the average values of the leakage current density at −2 V on the implantation dose for different samples: (1) Si70, without mesa-etching; (2) Si10 with mesa-etching; (3) SOI with mesa-etching; (4) Si70 after annealing at 1000°C (20 min).

(20 min) exhibit a slight variation of the photoresponse intensity while a drastic (of about 20 times) decrease in the leakage currents is observed. Regarding the Si10 sample, the behavior of the leakage currents can be attributed only to mesa-etched diodes (currents decrease by more than a factor of 80) [22].

Figure 6 shows the IR reflection spectra for the starting n-Si and p-n-Si(B) samples. From these data, the plasma reflection minimum of the untreated silicon wafers is at about 650 cm^{-1}. However, the reflection amplitude is somewhat lower than that corresponding to polished n-Si, probably due to the damaged layer. In the p-n-Si(B) spectra the plasma minimum of the substrate becomes less pronounced and a new minimum appears near 1400 cm^{-1}, which is associated with the presence of a 200–400 nm thick layer with optical parameters different from those of the substrate. The carrier concentration in p-Si is estimated to be of 2×10^{19} cm^{-3}. After implantation and annealing an increase in the band intensity of the Si-O oscillations (1082 cm^{-1}) is observed [19, 21].

Figures 7–13 show the photosensitivity spectra obtained from several samples (Si70, Si10, and SOI) under different conditions of II, annealing, and ion acceleration energies. In addition, for some Si70 samples, the photoresponse spectra were measured at 77°C.

From **Figure 7** it is obvious that the photosensitivity increases for implantation doses of up 6×10^{14} cm^{-2} and then decreases for higher doses. All short-wave infrared (SWIR) spectra exhibit the main maximum corresponding with the wavelength of about 1.8 μm (0.69 eV) and a less pronounced (smoothed) maximum at approximately 1.9 μm (0.65 eV) [20–22].

Figure 8 illustrates an example of the photosensitivity spectra of p-n-Si(B) in the range of 1.5–2.4 μm at 300 K and 77 K for a dose of 8×10^{14} cm^{-2} and annealing at 900°C (20 min). As is evident from the figure, the position of the maxima is practically independent of temperature, whereas their intensity at 77 K is much higher than at 300 K, and the bandwidth is narrowing, especially in the low energy region.

The influence of the annealing temperature on the photoresponse spectra of the Si70 samples implanted with a dose of $1{\times}10^{14}$ cm^{-2} and annealed at different temperatures was studied in [19]. It was shown that the position of the main peak in the SWIR range, similar to the dose dependence, does not depend on the annealing temperature. The photoresponse intensity is maximal for the annealing temperature of 900°C and minimal for 800°C.

For low resistance silicon (Si10) the same picture is qualitatively observed (**Figure 9**): enhancing the dose from 1×10^{14} to 6×10^{14} cm^{-2} (900°C, 20 min), the photoresponse intensity increases. However, in this case, it is significantly lower for each fixed dose as compared to **Figure 7**. The position of the maxima shifts slightly towards higher energies [22].

Figure 10 shows the influence of the thermal treatment on the photoresponse of p-n diodes (Si10) implanted with a dose of 1×10^{14} cm^{-2} [22].

It is seen from the figure that the PPA impact is more effective. The maximum intensity values (curve 1) approximately correspond to the value obtained at a dose of 4×10^{14} cm^{-2} (curve 2, **Figure 9**). This result requires more detailed studies.

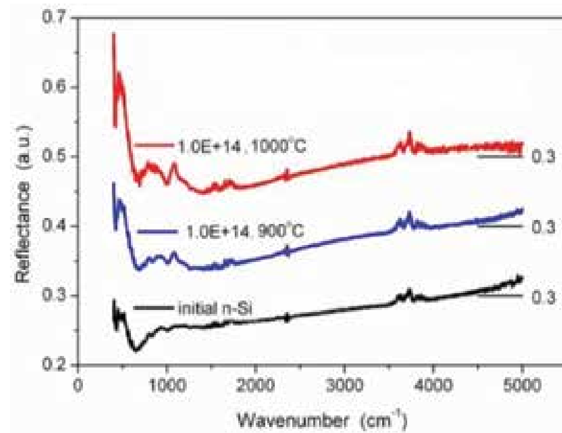

Figure 6. IR reflection spectra (light incidence angle - 16.5°) of the initial and B implanted (dose 1×10^{14} cm^{-2}) samples annealed at 900 and 1000°C.

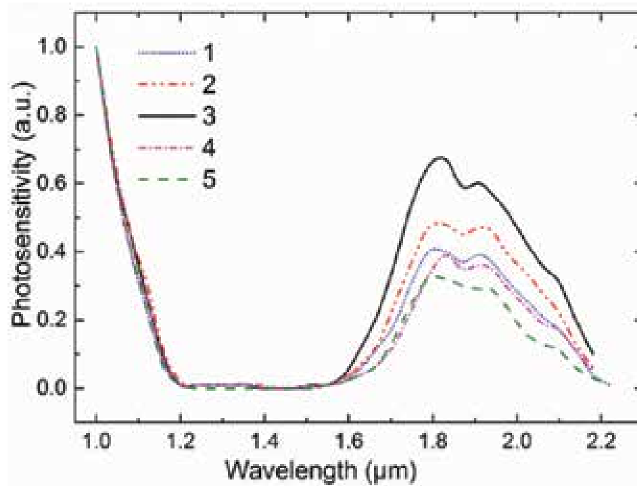

Figure 7. Photosensitivity spectra of the p-n diode (Si70) for different doses: (1) 1×10^{14}; (2) 4×10^{14}; (3) 6×10^{14}; (4) 8×10^{14}; (5) 1×10^{15} cm^{-2}.

In **Figure 11**, a photosensitivity spectrum of the SOI p-n diode is shown. In this case, the character of the dependence differs markedly from the two previous ones: the spectrum is extended, the main maximum is observed at 1.75 μm (0.72 eV), and the second maximum is shifted to the wavelength of 2.04 μm (0.61 eV) [22].

Figure 12 shows the photosensitivity spectra of the p-n-Si(B) structures obtained at an acceleration energy of 32 keV, different doses (1×10^{14} cm^{-2} and 1×10^{15} cm^{-2}) and annealed at 900°C, 20 min.

The comparison of **Figures 12** and **7** shows that the maxima of the photoresponse for 32 keV are approximately 20% higher than the corresponding values for 50 keV.

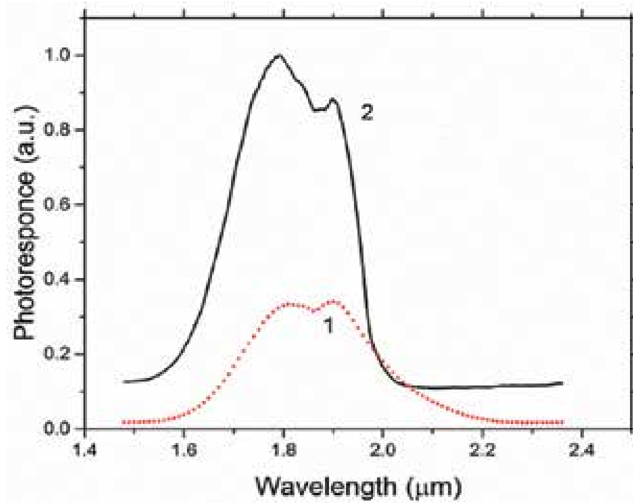

Figure 8. The photosensitivity spectra of p-n diode (Si70) sample implanted with a dose of 8 × 10^{14} cm^{-2} and annealed at 900°C (20 min): (1) 300 K, (2) 77 K.

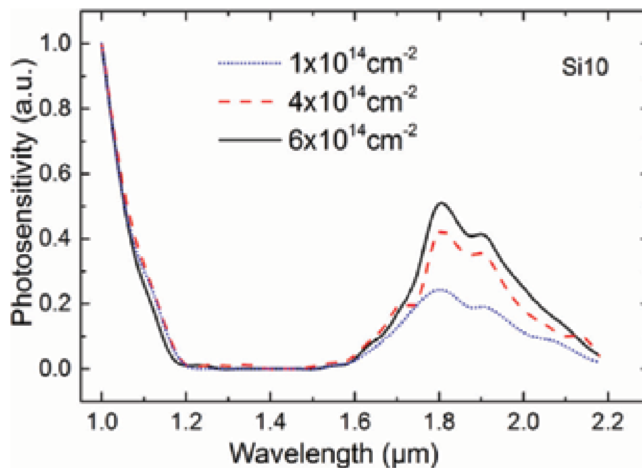

Figure 9. Photosensitivity spectra of the p-n diode (Si10) for different doses: (1) 1 × 10^{14}; (2) 4 × 10^{14}; (3) 6 × 10^{14} cm^{-2}.

Figure 13 shows the photosensitivity vs. the wavelength due to the B^+ implantation with the dose of 1 × 10^{13} cm^{-2} into the untreated material (1) and after the etching of the wafer surface layer to a depth of about 1 μm (2).

As can be seen from the figure, after the etching of the upper layer the photoresponse intensity decreases by a factor of 20, and the main maximum is distinctly less pronounced. The sample with the etched layer behaves in accordance with the proved existence of a threshold dose of 1 × 10^{14} cm^{-2} to form extended defects.

Figure 14 demonstrates an example of the behavior of the p-n-Si(B) photosensitivity in separate spectral regions within 0.2–4.1 μm. The largest photoresponse corresponds to the red,

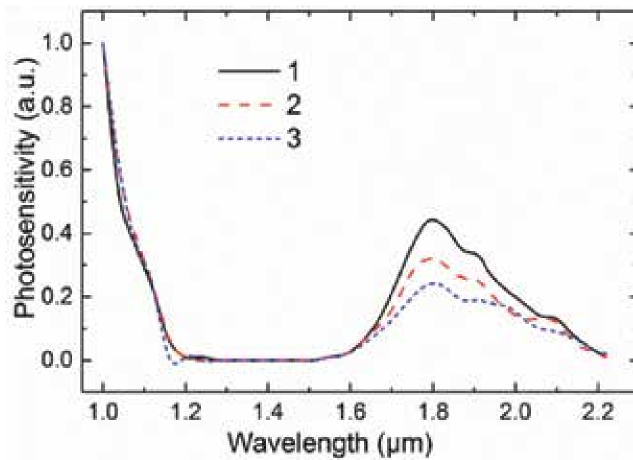

Figure 10. Photosensitivity spectra of the p-n diodes (Si10) for different thermal treatment conditions (dose 1×10^{14} cm^{-2}): (1) PPA at seven 3-s pulses; (2) PPA at three 3-s pulses; (3) in the stationary conditions. Annealing temperature – about 900°C.

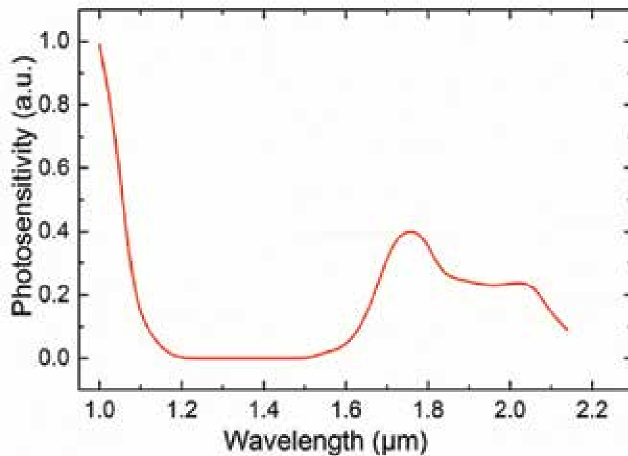

Figure 11. Photosensitivity spectra of the p-n diodes on SOI for the dose of 4×10^{14} cm^{-2}.

near IR and SWIR spectral ranges; a photoresponse is likewise observed in the UV region. It should be noted that, remarkably, areas with zero and negative photosensitivity are detected. These regions are most pronounced for the preselected dose of 6×10^{14} cm^{-2}. The measurement data reported earlier [20, 22] show the dependence of such spectra on the implantation dose and the annealing conditions.

In was shown [21, 22] that in the starting material as well as in n-Si annealed up to 900 and 1000°C or B^+ implanted without annealing only silicon is detected within the SEM sensitivity

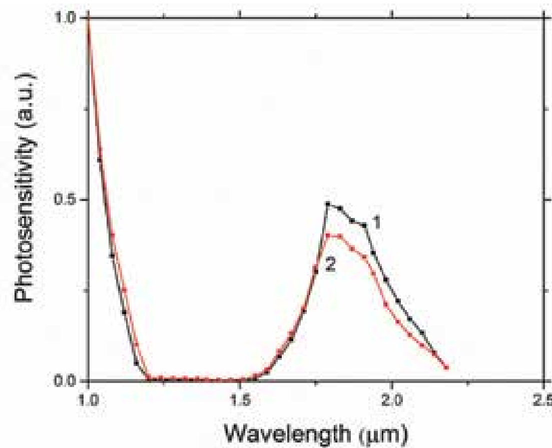

Figure 12. The photosensitivity spectra of the p-n diodes (Si70) obtained at an acceleration energy of 32 keV and different doses: 1–1 × 10^{14} cm^{-2}; 2–1 × 10^{15} cm^{-2} (annealing - 900°C, 20 min).

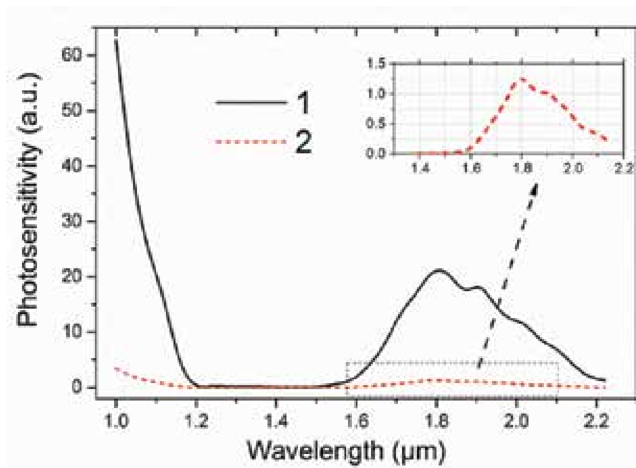

Figure 13. Photosensitivity spectrum for p-n diode (Si70) samples implanted with a dose of 1 × 10^{13} cm^{-2}: (1) the substrate surface is not etched; (2) the surface etched to a depth of about 1 μm; in the upper right corner the dependence of 2 is presented in an enlarged scale.

range. A completely different picture is obtained for the p-n-Si(B) structures (**Figure 15a**): a surprisingly high content of C and O is detected in the samples, depending on the implantation and annealing conditions. For comparison, **Figure 15b** shows the dependencies of the integrated photosensitivity on similar technological conditions.

The detection of C and O after implantation and annealing indicates the gettering of these impurities via the specimen surface. From the concentration levels it is quite likely to assume

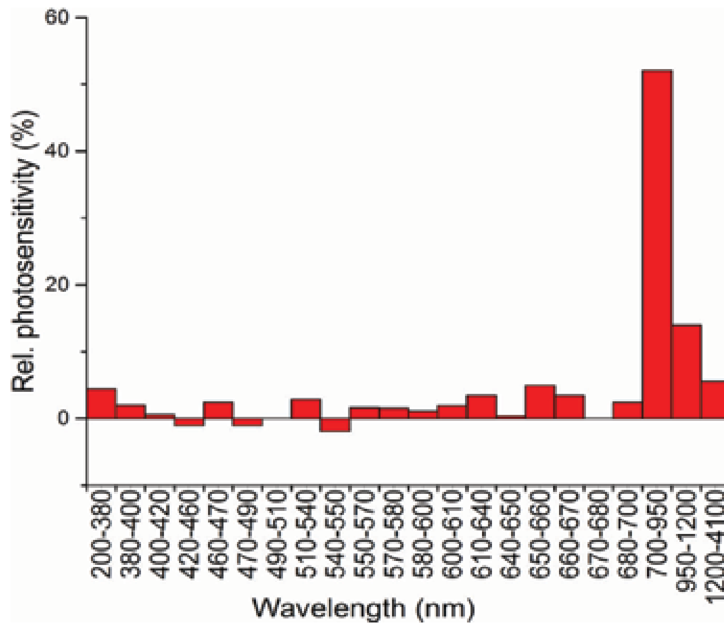

Figure 14. Spectral dependence of the integral relative photosensitivity for the p-n-Si(B) structure at the dose of 6×10^{14} cm^{-2}.

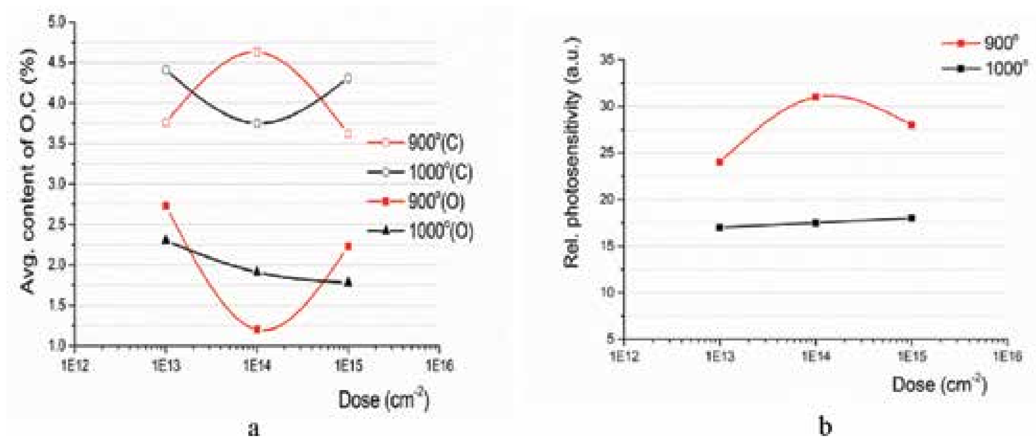

Figure 15. Dose and annealing temperature dependences of: (a) carbon and oxygen content; (b) relative integrated photosensitivity (a, b).

that oxygen has the most critical effect on the formation of defects responsible for the photosensitivity: the lower its content, the higher the photoresponse at both annealing temperatures applied. The C content, though higher than that of O in our case, appears to be less critical.

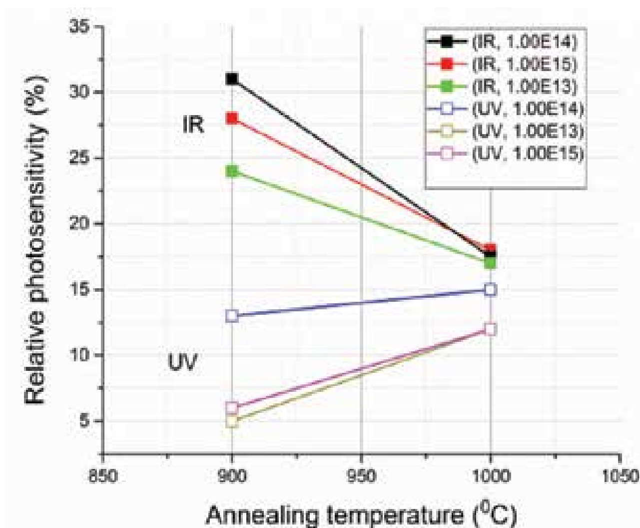

Figure 16. Relative integrated photoresponse for different doses and annealing temperatures in the ranges: UV—0.25–0.40μm; IR—1.0–4.1 μm.

Figure 16 illustrates the presence of a pronounced photoresponse in the UV range for different doses and annealing temperatures, even under EMR of weak intensity. For comparison, similar dependencies for the IR range are also displayed [21].

As indicated by the figure, the annealing temperature has quite a different effect on the photosensitivity in the UV and IR spectral ranges. For both cases the maximum photoresponse is accounted for a dose of 1×10^{14} cm^{-2}, for the UV it slightly depends on the annealing temperature. The behavior of the UV photoresponse for the two other doses applied is almost the same.

It is interesting to note that, in the 1000°C annealing temperature regime, the photoresponse signals in the IR range are practically identical for all three implantation doses.

4. Discussion

From our results of studies of n-Si wafers using Raman (**Figure 2**) and IR (**Figure 6**) spectroscopy we conclude that there is strain in the crystal structure due to the damaged near-surface layer of the material [19, 21]. According to some literature data [23], such a distorted layer can range from hundreds of nanometers to tens of microns, and in our case [21], within the measurement accuracy, it has a depth of several hundred nanometers. Obviously, this layer affects the variance in the characteristics of the material when doped by II. X-ray diffraction data suggest (**Table 1**) that there is no complete restoration of the structure after the II even with an annealing temperature of up to 1000°C.

It is established (**Figures 7–12**) that for all materials under the II and annealing regimes applied in our research work, the photosensitivity is observed in p-n-Si(B) within the wavelength range of 1.5–2.2 μm with two maxima of about 1.8 μm (main) and 1.9 μm (less pronounced) for Si70 and Si10. For SOI they are shifted towards lower and higher wavelengths, respectively.

In an attempt to explain the observed effects, it seems reasonable to rely on a complex physical mechanism indicating that the formation of extended defects with DL in the bandgap, occurs mainly in the damaged layer of the starting material. This assumption is supported by the following experimental results. **Figure 13** illustrates that the presence of the damaged layer can shift the "threshold" conditions of the formation of extended defects from a dose of 1×10^{14} cm^{-2} to 1×10^{13} cm^{-2}. Decreasing the ion acceleration energy from 50 to 32 keV (**Figure 12**) or replacing stationary regimes by PPA (**Figure 10**) leads to a marked increase in the intensity of the photoresponse with II doses unchanged. Apparently, the energy change leads to the change in the size and density of extended defects [10], and during PPA the shift of the p-n junction towards the more distorted near-surface region takes place.

From common knowledge on the formation/transformation of defects in B^+ implanted n-Si at annealing temperatures of 900 and 1000°C that we essentially applied in our studies, it is expected that point defects, small clusters and defects road-like{311} should be completely annealed. However, during the annealing process, defects {311} form dislocation loops of various configurations that persist up to 1000°C and above. Regardless of the doses for Si70 and Si10, some defects form DL in the bandgap with activation energies of about 0.7 and 0.65 eV. The corresponding maxima (main and smoothed) in the photosensitivity spectra are characterized by their intensity that differ with respect to their dose and annealing dependency. The increase in the photosensitivity intensity up to the dose of 6×10^{14} cm^{-2} is associated with the growing concentration of these defects. Increasing the dose further up to 1×10^{15} cm^{-2} the number of electrically active defects decreases and new defects appear that do not affect the photoelectric properties of the material. A sharp intensity increase and a marked band half-width decrease at 77 K indicate an increase in the occupation of DL formed by defects responsible for the photosensitivity (**Figure 8**). Altogether, it is reasonable to assume that, under these implantation and annealing conditions, the electrically active defects are generally evolving dislocation loops [9, 10].

The behavior of leakage currents (**Figure 5**) at high doses of II and annealing at 900°C can be described by the formation of new dislocation-type defects, a part of which leads to generation-recombination processes in the space charge region and affects the reverse current in the diode. At 1000°C these defects are annealed, reducing the leakage currents by a factor of about 20.

The understanding of the defect formation mechanism becomes even more complicated due to the observed correlation between the content of carbon and oxygen impurities in the surface layer and the IR photoresponse at different doses and annealing regimes (**Figure 15**). At this stage, we can only assume that the effect of oxygen on the defects responsible for the photosensitivity is much stronger than that of carbon: for oxygen the shape of the dose dependence curve at 900°C exhibits an opposite behavior to that of the photoresponse at the same temperature. In addition, after implantation and annealing, a change in the band intensity of

the Si-O oscillations (1082 cm^{-1}) with increasing annealing temperature from 900 to 1000°C is observed (**Figure 6**). The role of carbon might rather be indirect, since an increase in the carbon content reduces the concentration of gettered oxygen. The negative effect of oxygen on the photoresponse intensity is also reported in [24]. If annealing occurs at 1000°C, all these processes are much less pronounced.

Another interesting effect is observed on the integrated photosensitivity spectra (**Figure 14**) at EMR energies exceeding the bandgap value of silicon - the appearance of areas of zero and negative photosensitivity. The light absorption coefficient in this spectral region $\alpha \approx (1\text{–}5) \times 10^4$ cm^{-1} and the corresponding absorption depth is of the order of 1 μm. The appearance of areas with negative photoresponse depends on the spectral composition of the incident light, and the intensity at the same annealing temperature (900, 20 min) depends on the II dose, increasing from 1×10^{14} to 6×10^{14} cm^{-2}. The observed negative photosensitivity is apparently due to the presence of surface levels in p-n-Si(B) structures, which are trapping centers of the majority charge carriers. The population of these levels depends on the spectral composition of the light, and their concentration and depth are determined by the processing conditions of ion doping.

It is evident from the data of **Figure 16** that the mechanisms of photoresponse in SWIR and UV regions are completely different. At high energies of the EMR in the UV region, the absorption processes must occur in the surface layer. Most likely, the intensity of the UV photoresponse should increase with the annealing temperature due to a decrease in the concentration of trap centers.

The share of the photosensitivity in the SWIR is estimated to be up to 9%, whereas in the UV region it is up to 7% of the total photosensitivity in the range of 200–4100 nm (**Figure 14** and [18, 19, 21]).

In general, the interpretation of a number of obtained data and the underlying physical mechanisms requires additional clarification.

It is important to note that the technology itself and the measurement results are well reproducible. Hence, using the damaged layer in the starting material, it is possible to realize the controllable photoelectrical properties of p-n structures and propose this process as an innovative approach to the development of SWIR array photodetectors. In this respect, high-resistance n-Si samples implanted with a dose of B^+ 6×10^{14} cm^{-2} and annealed at 900°C (20 min) may find practical application as SWIR pixel arrays. Based on SOI structures, a quasi-planar array can be developed, especially for those cases where a relatively weak output signal is "compensated" by low leakage currents. The development of a UV detector technology is also envisaged.

5. Conclusions

The results of the recent original studies in the field of purposeful modification of the photoelectrical properties of n-Si due to B^+ ion implantation are supplemented with new data, summarized and analyzed.

The starting material was wafers of single-crystalline n-Si with different resistivity (70 and 10 Ohm·cm) and a SOI structure as well. For the fabrication of the p-n-Si(B) structures, ion implantation of B^+ was applied with doses of 1×10^{13}, 1×10^{14}, 4×10^{14}, 6×10^{14}, 8×10^{14} and 1×10^{15} cm^{-2} and acceleration energies of 50 and 32 keV with subsequent annealing in stationary (800, 900 and 1000°C, 20 min) and pulse-photon regimes.

The structural characteristics of the samples were studied by X-ray diffraction, Raman and IR spectroscopy. The surface properties of the samples were analyzed by SEM. The photoconductivity (photoresponse) was studied on a monochromator in the SWIR region (1.2–2.5 μm) and on a special setup that allows samples to be illuminated with a "packet" of waves in the range of 0.2–4.1 μm.

In the studied structures, a pronounced photosensitivity was detected in the range of 1.5–2.2 μm with two maxima of about 1.8 μm (main) and 1.9 μm (less pronounced) for Si70 and Si10. For SOI they are shifted towards lower and higher wavelengths, respectively. A pronounced photoresponse is detected in the UV region (0.25–0.40 μm).

A well-defined correlation between the structural, electrical and photoelectrical properties in SWIR and UV regions on the one hand, and implantation and annealing regimes as well as the content of C and O impurities on the other hand, is demonstrated. In the starting material, a damaged near-surface layer with a thickness of hundreds of nanometers was found to have a significant effect on the results obtained.

The effects observed in the SWIR range are discussed in terms of the formation/ transformation of extended defects with DL (0.7 and 0.65 eV for Si70 and Si10, 0.72 and 0.61 eV for SOI) in the material, most likely dislocation loops. The photoresponse intensity in the UV range seems to be associated with a change in the concentration of trap centers in the near-surface layer of p-n-Si(B) structures. The regions with a negative photoresponse observed on the integrated photosensitivity spectra depend on the spectral composition of the incident light. We attribute this effect to the presence of trapping centers of the main charge carriers in the near-surface layers of the sample.

Taking into account that the technology itself and the measurement results are well reproducible for different monocrystalline n-Si, it is evident that boron implantation permits controlled modification of photoelectrical properties of the material.

The results obtained can be used to develop SWIR pixel and quasi-planar arrays and UV detectors as well.

Acknowledgements

We express our deep gratitude to all co-authors of the previously published research work for their contribution to the development of technology, measurements and discussion of the results obtained, as well as to our colleagues Dr. Tatyana Sakharova and Marina Ashchiyan for their participation in preparing the Chapter.

http://dx.doi.org/10.5772/intechopen.76992

Author details

Nina Khuchua[1]*, Marina Tigishvili[2], Nugzar Dolidze[2], Zurab Jibuti[2], Revaz Melkadze[1] and Roland Diehl[3]

*Address all correspondence to: ninakhuchua@mail.ru

1 RPC “Electron Technology”, Institute of Applied Semiconductor Technology, Iv.Javakhishvili Tbilisi State University, Tbilisi, Georgia

2 Institute of Micro- and Nanoelectronics, Tbilisi, Georgia

3 Fraunhofer Institute for Applied Solid-State Physics (IAF), Freiburg im Breisgau, Germany

References

[1] Milvidskii M, Chaldyshev V. Nanoscale atomic clusters in semiconductors as a new approach to formation of materials properties. Fizika i Tekhnika Poluprovodnikov. 1998;**32**:513-522

[2] Kotov V, Klindukhov V, Cherepasgkin I. Modification of the silicon structure and optical properties by electric pulse treatment. Nano-i Microsistemnaya Tekhnika. 2000;**3**:8-10

[3] Vavilov V, Chelyadinsky A. The ion implantation of impurities crystalline Si single crystals: The efficiency of this method and the radiation damage. Uspekhi Fizicheskikh Nauk. 1995;**165**:347-358. DOI: 10.2267/UFNr.0165.199503g.0347

[4] Libertino S, La Magna A. Damages formation and evolution in ion-implanted crystalline Si. In: Bernas H, editor. Material Science with Ion Beams. Topics in Applied Physics. Vol. 116. Berlin Heidelberg: Springer-Verlag; 2010. pp. 147-212. DOI: 10.1007/978-3-540-88789-8-6

[5] Casalino M. Near-infrared sub-bandgap all-silicon photodetectors: A review. International Journal of Optics and Applications. 2012;**2**:1-16. DOI: 105923/j.optics.2012201.01

[6] Lastkin V, Gavrushko V, Ionov A. An improves silicon UV-photodiode obtained by As implantation. Elektronika: Science, Technology, Business. 2010;**2**:72-73

[7] Eichler S, Gebauer J, Börner F, Polity A, Krause-Rehberg R, Wendler E, Weber B, Wesch W, Borner H. Mint: Defects in silicon after B+ implantation: A study using a positron-beam technique, Rutherford backscattering, secondary neutral mass spectroscopy and infrared absorption spectroscopy. Physical Review B. 1997;**56**:1393-1403. DOI: 10.1103/PhysRevb.56.1393

[8] Feklistov K, Fedina L, Cherkov A. Mint: Boron precipitation in Si at high implantation dose. Fizika i Tekhnika Poluprovodnikov. 2010;**44**:302-305

[9] Duguay S, Philippe T, Cristiano F, Blavette D. Direct imaging of boron segregation to extended defects in silicon. Applied Physics Letters. 2010;**97**:242104-1-242104-3. DOI: 10.1063/1.3526376

[10] Milosavljević M, Shao G, Lourenco M, Gwillian R, Homewood K. Engineering of boron-induced dislocation loops for efficient room-temperature silicon light-emitting diodes. Journal of Applied Physics. 2005;**97**:073512-1-073512-7. DOI: 10.1063/1.1866492

[11] Sobolev N, Emelianov A, Shek E, Vdovin V. Influence of post-implantation annealing on the properties of silicon light-emitting diodes obtained by boron implantation in n-Si. Physika Tverdogo Tela. 2004;**46**:39-43

[12] Cheladinski A, Komarov Ph. Defect-impurity engineering in implanted silicon. Uspekhi Fizicheskikh Nauk. 2003;17:8-46. DOI: 10.3367/UFNr.0173.200308b.0813

[13] Válek L, Śik J. Defect engineering during Czochralski crystal growth and silicon wafer manufacturing. In: Kolesnikov N, editor. Modern Aspects of Bulk and Thin Film Preparation. InTech: Rijeka; 2012. pp. 43-70

[14] Usami A, Katayama M, Mint WT. Diode characteristics and residual deep- level defects of p^+-n abrupt junctions fabricated by rapid thermal boron implanted silicon. Semiconductor Science Technology. 1987;**2**:83-87

[15] Vyzhigin Y, Sobolev N, Gresserov B, Shek E. Influence of the thermal treatment temperature on the formation of deep-level center. Fizika i Technika Poluprovodnikov. 1991; **25**:1324-1331

[16] Gavrushko V, Ionov A, Lastkin V. Analysis of the influence of technological parameters and a type of photodetectors on their photosensitivity in the UV spectral region. In: Proceedings of The 6-th All-Russian Youth School "Materials of Nano- Micro- and Optoelectronic Technology: Physical"

[17] Tigishvili M, Gapishvili N, Gulyaev R, Jibuti Z, Dolidze N, Khuchua N, Melkadze R. Defect engineering in the silicon p-n junction technology. Georgian Engineering News. 2013;**68**:75-79

[18] Khuchua N, Dolidze N, Gapishvili N, Gulyaev R, Jibuti Z, Melkadze R, Tigishvili M. Technology of semiconductor materials sensitive to different regions of the electromagnetic radiation spectrum. Nanotechnology Perceptions. 2014;**4**:91-99

[19] Tigishvili M, Khuchua N, Melkadze R, Dolidze N, Gapishvili G, Jibuti Z, Dovbeshko G, Romanyuk V. Semiconductor material with new optical properties for infrared and ultraviolet photodetectors. In: Proceedings of the 2nd International Conference on Modern Technologies and Methods of Inorganic Materials Science; 20-24 April 2015; Tbilisi Georgia. Tbilisi: Edition of National Academy of Sciences of Georgia; 2015. pp. 288-295

[20] Dolidze N, Jibuti Z, Tigishvili M, Khuchua N, Melkadze R, Gapishvili N. Effect of light spectral composition on photoelectric properties of ion doped silicon. In: Proceedings of the International Conference on Advanced Materials and Technologies; 21-23 October

2015; Tbilisi, Georgia. Tbilisi: Edition of National Academy of Sciences of Georgia; 2015. pp. 63-67

[21] Khuchua N, Tigishvili M, Melkadze R, Dolidze N, Gapishvili N, Jibuti Z, Dovbeshko G, Romanyuk V. Defect formation in ion-implanted Si-approach to controlled semiconductor optical properties. In: Proceedings of the International Conference on Gettering Defect Engineering in Semiconductor Technology XVI; 20-25 September 2015; Bad Staffelstein, Germany. Solid State Phenomena. 2016;**242**:374-379. DOI: 10.4028/www.scientific.net/SSP.242.374

[22] Tigishvili M, Khuchua N, Gapishvili N, Sakharova T, Dolidze N, Jibuti Z, Peradze G, Melkadze R. Impact of damages in monocrystalline n-Si on material photosensitivity. In: Proceedings of the International Conference on Gettering Defect Engineering in Semiconductor Technology XVII; 1-6 October 2017; Lopota Resort, Georgia. Physica Status Solidi. 2017;**C14**:1700094-1-1700094-6. DOI: 10.1002/ppsc.201700094

[23] Mikhajlov A, Belov A, Korolyev D, Timofeeva A, Vasilyev B, Bobrov A, Pavlov D, Tetelbaum D, Shek E. Effect of ion doping on photoluminescence of silicon originated from dislocations formed by Si^+ ion implantation. Physika i Tekhnika Poluprovodnikov. 2014;**48**:212-216

[24] Blynski V, Bozhatkin O, Holub E, Lemeshevskaya A, Shvedov S. Effect of preliminary annealing of silicon substrates on the spectral sensitivity of photodetectors in bipolar integrated circuits. Journal of Applied Spectroscopy. 2010;**77**:478-481

Chapter 8

Characterization and Simulation of p-Type Ion Implantation in MCT

Changzhi Shi

Additional information is available at the end of the chapter

http://dx.doi.org/10.5772/intechopen.77111

Abstract

Ion implantation is one of the key technologies for the fabrication of HgCdTe (MCT) infrared photodiodes. In order to achieve p-on-n type photodiode structure with better performance, the group V elements typically serve as p-type dopants, especially arsenic. In this chapter, ion profiles, defect microstructures, and surface amorphization of implanted group V dopants represented by arsenic into MCT epilayers were characterized by secondary ion mass spectroscopy (SIMS), transmission electron microscopy (TEM), and X-ray diffraction (XRD), respectively. The influences of some significant technological parameters related to ion implantation, such as implant energy, implant dose, ion beam current, barrier layer structure, on the distributions of ions and induced damages are analyzed. In addition, the high-temperature annealing used to eliminate induced damages and activate the electrical activity of ions was subjected to the as-implanted samples, and the ion diffusion profiles and surface microstructures were acquired and analyzed. Finally, the computer simulations on the collision of incident ions and lattice atoms were carried out to study the distributions of ions and recoil atoms numerically. The simulation results are in good agreement with the experimental data.

Keywords: HgCdTe, ion implantation, group V, microscopic characterization, computer simulation, SIMS, TEM, XRD

1. Introduction

In the field of semiconductor and microelectronics, the ion implantation process is the most common technology applied to incorporate dopants. Compared with the other two methods, such as thermal diffusion doping and epitaxy in-situ doping, the ion implantation has

IntechOpen

© 2018 The Author(s). Licensee IntechOpen. This chapter is distributed under the terms of the Creative Commons Attribution License (http://creativecommons.org/licenses/by/3.0), which permits unrestricted use, distribution, and reproduction in any medium, provided the original work is properly cited.

the advantages of simple process, depth controllability, selective and arbitrary concentration doping (not restricted by solid solubility). For MCT, an important narrow gap semiconductor material applied in the field of infrared detection and imaging [1], ion implantation and in-situ epitaxy are both adopted for the incorporation of dopants. In fact, the core element of MCT-based infrared detectors is typically a photodiode based on p-n junction structure, generating a photogenerated potential under the excitation of infrared photons. The p-n junction can be formed either on the p-type absorbing layer or on the n-type absorbing layer, corresponding to n-on-p device [2, 3] and p-on-n device [4], respectively. In the traditional n-on-p device, the in-situ p-type doping can be achieved by Hg vacancy doping [5] and Au or Cu incorporation [6] during epitaxy growth; the n-type doping can be acquired by boron ion implantation. With decades of development, the n-on-p device has provided excellent performance [7]. However, for the infrared detection application of low dark current and low flux in long wavelength infrared (LWIR) and very long wavelength infrared (VLWIR) regions, the p-on-n device has been demonstrated to possess better performances [8–10] such as low dark current, low series resistance, and high operating temperature. For II-VI materials such as MCT, group V elements, especially arsenic, can serve as p-type dopants. Due to its low diffusion coefficient [8] in MCT, the profiles of implanted arsenic ions can be controllable. So far, arsenic has been extensively used as the p-type dopant of MCT. Nevertheless, the implanted arsenic ions usually occupy the cation sublattice and generate a large number of induced damages. Therefore, a high-temperature annealing is necessary to eliminate lattice damages and activate the electrical activity of arsenic ions, that is, transfer arsenic ions from cation sublattices to Te sublattices.

Some studies on arsenic ion implantation in MCT have been reported in several literature studies [4, 8, 11] and our previous work [12–14]. Classically, SIMS is used to acquire the distribution profiles of implanted ions, while the microstructures and distributions of induced damages are observed by TEM. Recently, Rutherford backscattering experiments under channeling conditions (RBS-c) were carried out to extract quantitative damage depth profiles of implanted arsenic ions in MCT [15]. Moreover, the microstructures of the induced damages in the MCT implanted with group V dopants (N, P, As and Sb) were investigated [16]. However, so far, the systematic study on the ion implantation of group V dopants in MCT has not been reported. Therefore, in this chapter, the ion implantation of group V dopants, such as P, As, Sb, in MCT will be analyzed and discussed according to characterization methods. Finally, the computer simulations on the collision of incident ions and lattice atoms will be carried out to study the distributions of ions and recoil atoms numerically.

2. SIMS profile

SIMS is a high-resolution analytic technique for acquiring the element component information in the material. In this section, the depth profiles of group V dopants implanted into MCT will be characterized by this method.

http://dx.doi.org/10.5772/intechopen.77111

2.1. Arsenic

The technological parameters of ion implantation, such as implant energy, implant dose, ion beam current, determine the depth profiles of implanted ions and induced damages. In order to implant heavy ions like arsenic into MCT epilayer, the implant energy should be adequately high to overcome the energy loss in the collision of implant ions and lattice atoms. Here, the MCT epilayers were grown on (111)B CdZnTe substrates by liquid phase epitaxy (LPE). Then, arsenic ions were implanted into MCT epilayers without barrier layers. **Figure 1** provides the SIMS profiles of arsenic ions implanted into MCT at different implant energies before and after high-temperature annealing under saturated Hg vapor pressure. The energy ranges from 350 to 450 keV, while the dose is set to be 2×10^{14} cm^{-2}. The high-temperature annealing was carried out in two steps: the first step at 420°C is used to transfer arsenic ions from cation sublattices to Te sublattices and eliminate induced damages, while the second step at 240°C is to remove Hg vacancies. It can be seen from **Figure 1** that the depth of the end-of-range (EOR) of as-implanted arsenic ions increases with implant energy. Moreover, the average projected range (Rp) increases approximately linearly with energy. After annealing, the indiffusion occurs to the as-implanted arsenic ions, and the diffusion depth also increases with energy.

In addition to implant energy, implant dose is also one of the key technological parameters determine the distribution of implanted ions. The SIMS profiles of the arsenic ions implanted into MCT epilayers without barrier layers at 320 keV with different doses are illustrated in **Figure 2(a)**. The peak concentration of arsenic ions increases with dose; however, the EOR depth is not remarkably influenced by implant dose. **Figure 2(b)** provides the SIMS profiles of as-implanted arsenic ions in MCT with the dose of 5×10^{14} cm^{-2} after Hg overpressure annealing. The profile indicates that the indiffusion of arsenic ions includes three parts: part 1 – in the surface layer, it is considered that the arsenic ions are trapped by the defects in the lattice, thereby resulting in the generation of arsenic complexing; part 2 – beneath the surface layer, the arsenic ions are diffused thermally into the lattice and some of them are activated electrically

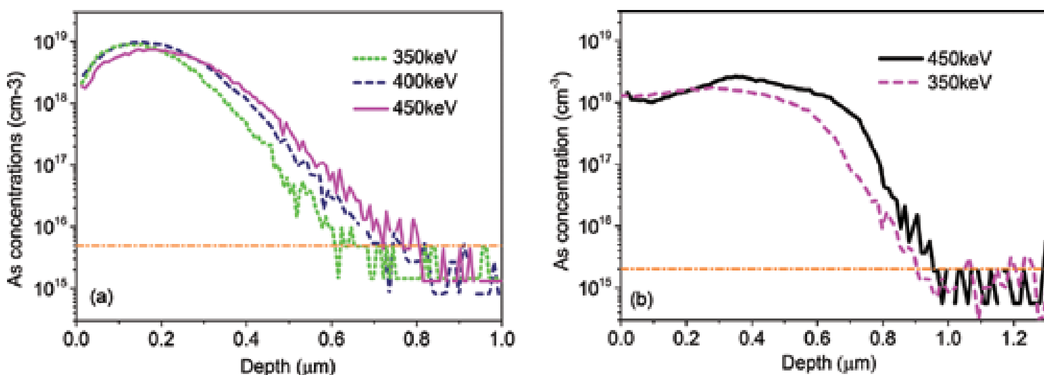

Figure 1. SIMS profiles of arsenic ions implanted into MCT at different energies: (a) before Hg overpressure annealing and (b) after Hg overpressure annealing.

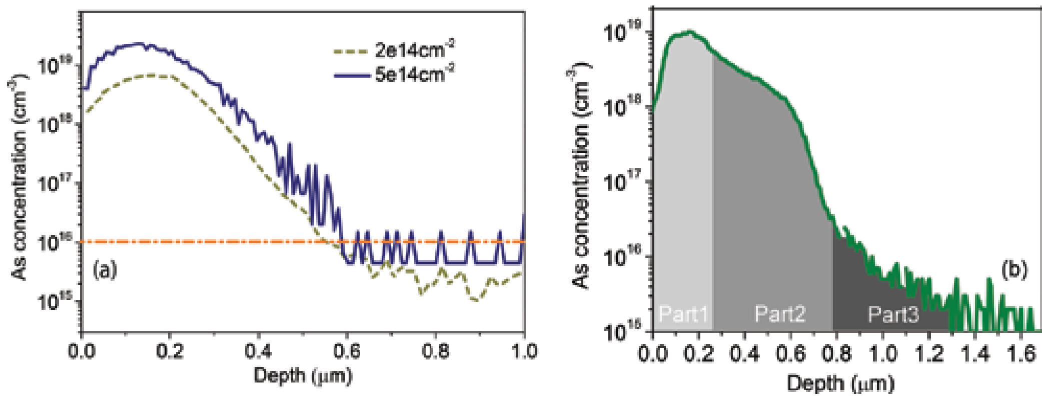

Figure 2. (a) SIMS profiles of arsenic ions implanted into MCT at 320 keV with the doses of 2×10^{14} and 5×10^{14} cm^{-2}, respectively. (b) SIMS profile of arsenic ions in the annealed MCT implanted at 320 keV with the dose of 5×10^{14} cm^{-2}.

by occupying Te sublattices; part 3 – deeper in lattice, there exists a rapid diffusion of arsenic ions due to the channeling effect. This profile is similar to the profiles presented in Refs. [4, 8]. However, the multicomponent indiffusion does not occur to the annealed samples with lower dose as shown in **Figure 1**. It could be due to that the dose of the samples in **Figure 1** is lower than that of the sample in **Figure 2**. It implies that the high dose may aggravate the complexing and the channeling effect of as-implanted arsenic ions.

The ion beam current is another technological parameter to be considered. **Figure 3(a)** shows the SIMS profiles of arsenic ions implanted into MCT epilayers without barrier layers at 320 keV with the dose of 5×10^{14} cm^{-2}, at the beam currents of 100 μA and 300 μA, respectively. It can be seen that the ion profiles are not sensitive to the beam current for arsenic. Even when the span of the beam current is expanded to 50–800 μA, no significant distinction in the ion profiles could be found in **Figure 3(b)**. **Figure 4** provides the SIMS profiles of arsenic ions in the samples in **Figure 3(a)** annealed under saturated Hg vapor pressure. Although the arsenic

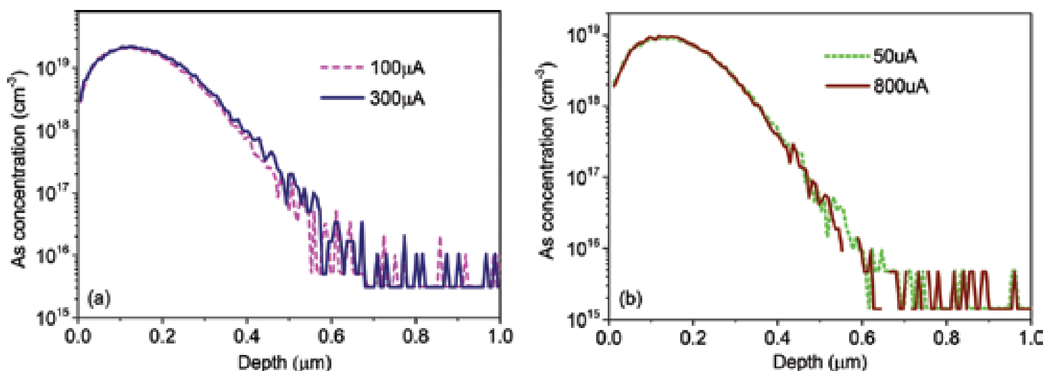

Figure 3. (a) SIMS profiles of arsenic ions implanted into MCT epilayers at 320 keV with the dose of 5×10^{14} cm^{-2}, at the beam currents of 100 and 300 μA, respectively. (b) SIMS profiles of arsenic ions implanted into MCT epilayers at 350 keV with the dose of 2×10^{14} cm^{-2}, at the beam currents of 50 and 800 μA, respectively.

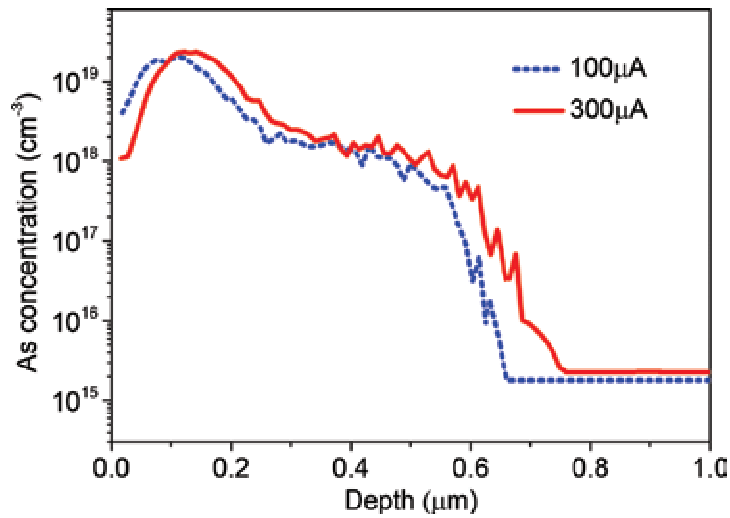

Figure 4. SIMS profiles of arsenic ions in the annealed MCT samples implanted at 320 keV with the dose of 5×10^{14} cm^{-2}, at the beam currents of 100 and 300 μA, respectively.

profiles in the as-implanted samples are sensitive to beam current, the sample with higher beam current presents a deeper diffusion depth than that of the sample with lower beam current. It indicates that the change in beam current gives rise to the different distributions of induced damages, thereby influencing the indiffusion of arsenic ions.

The distribution profiles of as-implanted arsenic ions in bare MCT are discussed above. Nevertheless, in the practical device fabrication, the barrier layers should be prepared on MCT epilayers before ion implantation to avoid the external contamination and absorb the induced damages [17]. Here, the ZnS and CdTe films serve as barrier layers for MCT. Especially, the ZnS and CdTe double-layer films were grown on MCT epilayers by thermal evaporation as barrier layers, respectively, in order to investigate the influences of film materials and interface on arsenic profiles.

Figure 5(a) shows the SIMS profile of arsenic ions implanted into MCT coated by double-layer ZnS barrier layer (80 nm/80 nm) at 400 keV with the dose of 1×10^{14} cm^{-2}. Then, after removing the ZnS layer, the high-temperature annealing was performed at 420 and 240°C. The arsenic SIMS profile of the annealed sample is provided in **Figure 5(b)**. For the MCT sample covered with double-layer CdTe barrier layer (50 nm/100 nm), the arsenic ion implanted at 320 keV with the dose of 2×10^{14} cm^{-2}. In addition, the as-implanted sample was annealed in the same condition as the ZnS-coated sample after removing CdTe. The arsenic profiles of the MCT sample with CdTe barrier layer before and after annealing are illustrated in **Figure 6**. It can be seen that the arsenic ions are accumulated around the ZnS/MCT and ZnS/ZnS interfaces for the as-implanted ZnS-coated sample, and the peak concentration is located near the ZnS/MCT interface. For the as-implanted CdTe-coated sample, the arsenic ions are mainly accumulated at the CdTe/MCT interface. It indicates that the defects at the interface between barrier layer and MCT could serve as the trapping centers to

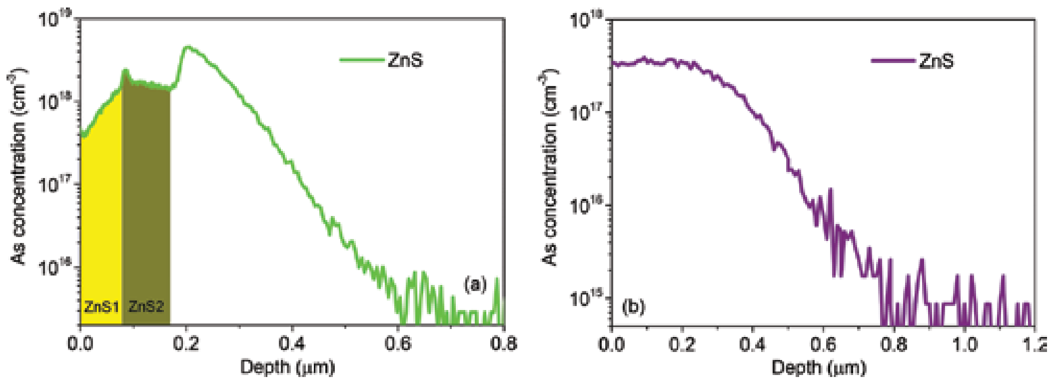

Figure 5. SIMS profile of arsenic ions implanted into MCT coated by double-layer ZnS barrier layer (80 nm/80 nm) at 400 keV with the dose of 1×10^{14} cm^{-2} (a) before annealing and (b) after annealing.

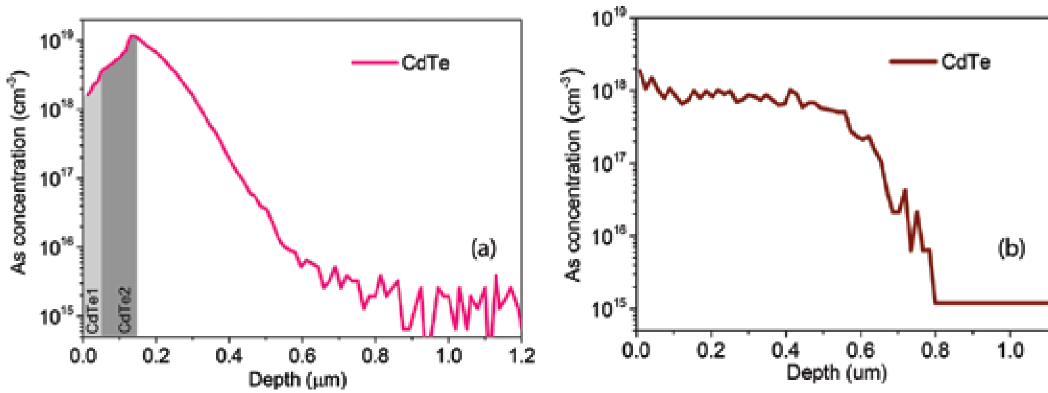

Figure 6. SIMS profile of arsenic ions implanted into MCT coated by double-layer CdTe barrier layer (50 nm/100 nm) at 320 keV with the dose of 2×10^{14} cm^{-2} (a) before annealing and (b) after annealing.

hinder arsenic ions. On the other hand, the shallower EOR depth of the ZnS-coated sample implanted with arsenic ions at higher energy shows that the ZnS layer has stronger barrier ability than CdTe.

2.2. Other dopants

Additionally, the profiles of the other group V dopants implanted into MCT were characterized by SIMS. **Figure 7** provides the SIMS profiles of phosphorus and antimony ions implanted into MCT epilayers, respectively. For phosphorus-implanted samples, the energy is 350 keV, the dose is 2×10^{14} cm^{-2}, and the beam currents are 50 and 800 μA. For antimony-implanted samples, the implant technological parameters are illustrated in **Figure 7(b)**. Dissimilar to arsenic, the phosphorus profiles are sensitive to the change in beam current. It can be seen that the EOR depth increases with beam current, which indicates that the extension of implantation

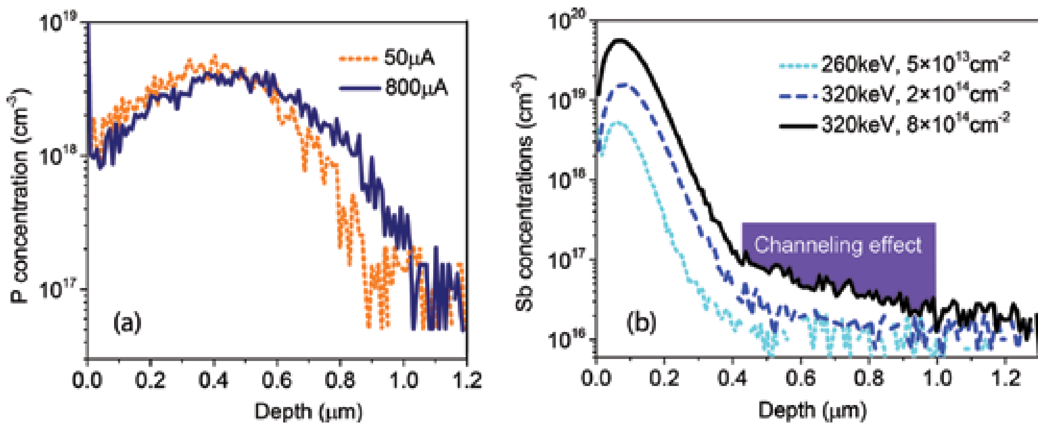

Figure 7. (a) SIMS profiles of phosphorus ions implanted into MCT epilayers at 350 keV with the dose of 2 × 10^{14} cm^{-2}, at the beam currents of 50 and 800 μA. (b) SIMS profiles of antimony ions implanted into MCT.

period for phosphorus ions, as a result of low beam current, gives rise to the increase in the interstitial ions. These interstitial ions could block the implantation of subsequent ions. By contrast, the motion of the arsenic ions implanted into MCT depends mainly on the displacements and replacements of lattice atoms through the collision between ions and atoms. For antimony-implanted samples, it is found that the high dose results directly in the channeling effect due to the large mass of antimony ions.

3. TEM characterization

So far, TEM is one of the most effective methods to characterize the microstructure of defects in materials. Next, the microstructures of the surface amorphization and induced defects in MCT epilayers implanted with arsenic and phosphorus ions will be characterized and analyzed by TEM.

3.1. Arsenic

Figure 8(a) and **(b)** provides the TEM cross-section images of near-surface layers in MCT implanted with arsenic ions at 350 and 450 keV, respectively. The dose is 2 × 10^{14} cm^{-2}. The arsenic profiles of these two samples have been given above. From the TEM observation, the induced damage layer can be divided into two sublayers: the amorphized-MCT (a-MCT) layer near surface, accompany with some long dislocations at the bottom; the short defect layer (SDL) with a large number of short defects. For the 350 keV sample, the thickness of the whole induced damage layer is about 0.45 μm. Therefore, the thicknesses of the a-MCT layer and the SDL are 0.28 and 0.17 μm, respectively. For the 450 keV sample, the whole damage layer is around 0.49 μm thick. Therefore, the thicknesses of the a-MCT layer and the SDL are 0.34 and 0.14 μm, respectively. It indicates that the induced damage to lattice for the sample implanted at higher

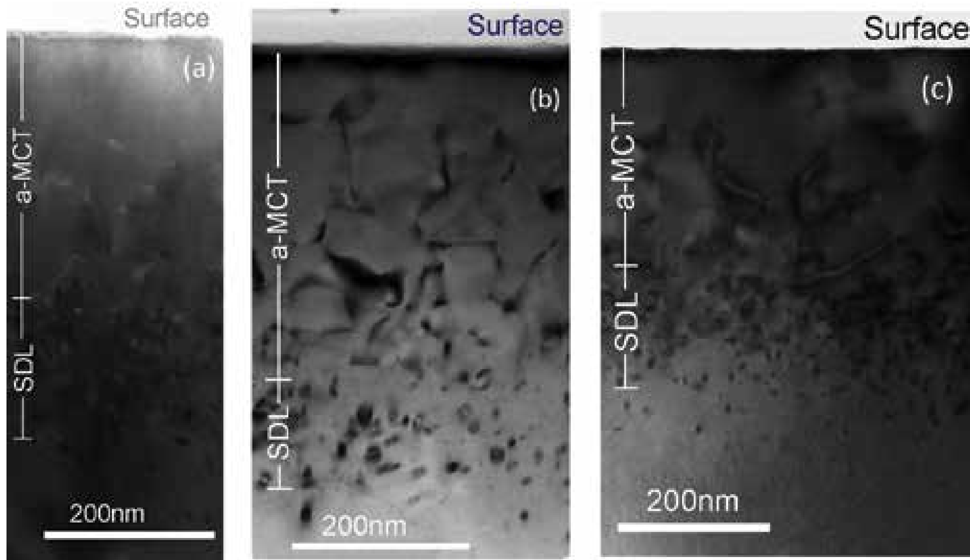

Figure 8. TEM cross-section images of near surface layers in MCT epilayers implanted with arsenic of 2×10^{14} cm^{-2} (a) at 350 keV, 50 μA; (b) at 450 keV, 50 μA; (c) at 350 keV, 800 μA.

energy is more serious than that of the sample implanted at lower energy. That is, the increase in implant energy results in the more energy transfer from implanted ions to lattice with the displacement of more lattice atoms, thereby aggravating the amorphization of surface MCT.

As mentioned earlier, the profiles of arsenic ions are insensitive to beam current. However, the change in beam current leads to the different distributions of induced damages. **Figure 8(c)** provides the TEM cross-section image of MCT implanted with arsenic of 2×10^{14} cm^{-2} at 350 keV and 800 μA. Compared with **Figure 8(a)**, the a-MCT layer and the SDL in the 50 μA sample are about 310 nm and 140 nm, respectively, while the 800 μA sample has a more thinner (260 nm) a-MCT layer and a thicker SDL layer (160 nm). Accordingly, the conclusion could be drawn that a longer period implantation at a low beam current could intensify the amorphization of the surface MCT.

Figure 9 provides the TEM cross-section images of the surface layers in MCT epilayers implanted with arsenic of 2×10^{14} and 5×10^{14} cm^{-2}, respectively. The implant energy is 320 keV. The thickness of the a-MCT layer in the low dose sample is less than that of the high dose sample, while the thickness of the SDL in the former is greater than that of the latter. It indicates that the longer period ion implantation equivalent to higher dose could prompt the amorphization of the surface MCT. Additionally, the insensitivity of the thickness of the whole damage layer to beam current implies that the SDL could be transformed to the a-MCT layer under the successive ion bombardment.

The high-resolution TEM was utilized to characterize the detailed microstructures of the induced defects in the SDL of arsenic-implanted MCT layers. As illustrated in **Figure 10**, the

http://dx.doi.org/10.5772/intechopen.77111

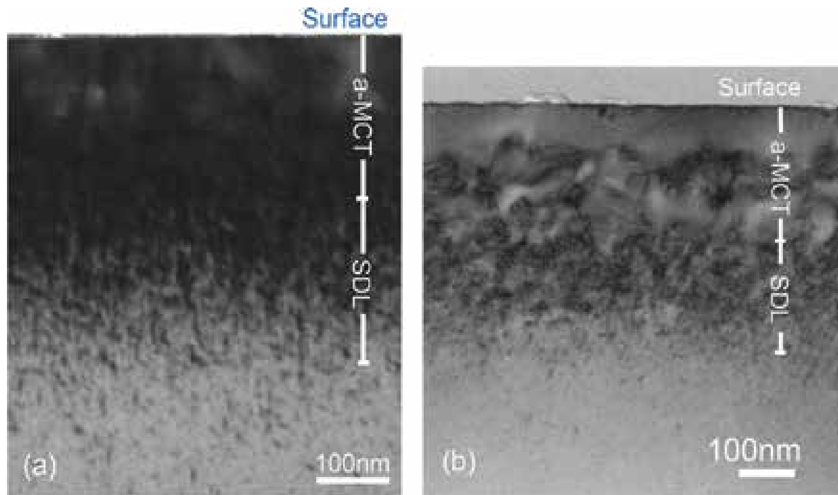

Figure 9. TEM cross-section images of the surface layers in MCT epilayers implanted with arsenic of (a) 2×10^{14} and (b) 5×10^{14} cm^{-2}, respectively, at 320 keV.

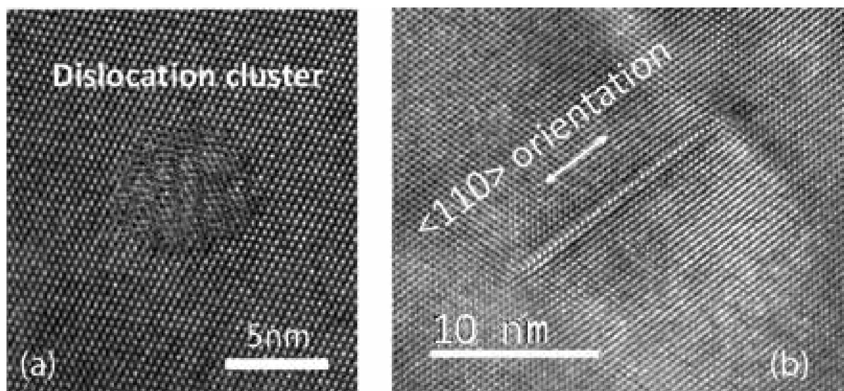

Figure 10. TEM images of induced defects in SDL of arsenic implanted MCT. (a) Dislocation cluster and (b) dislocation line.

short defects in the SDL could be classified into two types: dislocation cluster and dislocation line. Interestingly, most of dislocation lines are along <110> orientation parallel to the surface, which could be attributed to the larger atom spacing along the <110> orientation in MCT with the face-centered-cubic structure. Therefore, the recoil atoms induced by arsenic ions tend to be displaced along the <110> orientation to form dislocation lines.

Specially, the residual defects were discovered around the previous interface between a-MCT layer and SDL for the arsenic implanted MCT at 450 keV after Hg overpressure annealing, forming a belt of point defects, as shown in **Figure 11**. It indicates that the induced defects formed at adequately high implant energy could not be eliminated even after annealing.

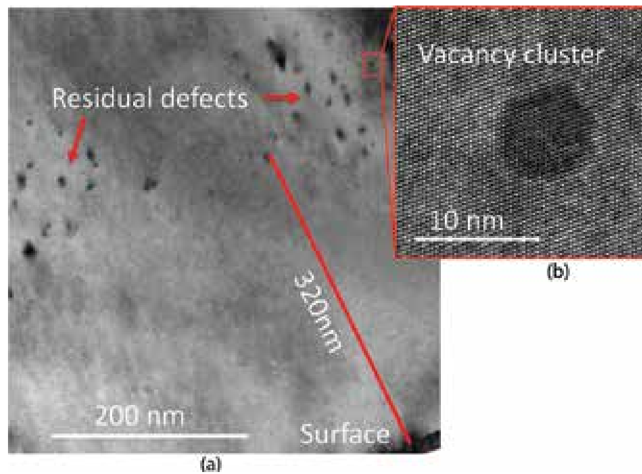

Figure 11. (a) TEM image of a belt of residual point defects in MCT epilayer implanted with arsenic ions at 450 keV after Hg overpressure annealing. (b) Detailed TEM image of residual point defect.

In order to characterize the details of these residual defects, the high-resolution TEM was adopted. It can be seen from the insert chart in **Figure 11** that the point defect is actually a cluster of vacancies. The deduction could be acquired that the ion implantation at too high energy will result in the net loss of lattice atoms.

The barrier layer is deposited to protect the MCT epilayer from the external contamination and absorb the induced damages. However, the thin evaporated CdTe barrier layer was proved to generate the BLICE effect [13]. This effect can be suppressed by increasing the thickness of evaporated CdTe layer and adopting the other barrier layer materials [12]. Here, the TEM cross-section images of the double-layer ZnS-coated MCT epilayer (implanted with arsenic at 400 keV) and the double-layer CdTe-coated MCT epilayer (implanted with arsenic at 320 keV) are provided in **Figure 12** respectively. The a-MCT layers become very thin or almost disappear both in the MCT epilayers of the two samples. In addition, the thinner SDL in the ZnS-coated sample implanted at higher energy demonstrates the stronger barrier effect of ZnS than CdTe. The thickness of the barrier layer can be optimized to adjust the SDL depth.

3.2. Other dopants

The microstructure and distribution of induced defects in the MCT epilayer implanted with the other group V dopants such as phosphorus were also characterized by TEM as illustrated in **Figure 13**. The thicknesses of the a-MCT layer and the SDL in the phosphorus-implanted sample are about 380 and 220 nm, respectively. Obviously, the induced damages of implanted phosphorus ions to lattice are more serious than arsenic ions under the same implantation condition, compared with **Figure 8(a)**. Moreover, in addition to dislocation cluster and dislocation line, the crescent dislocation is discovered in the SDL of phosphorus implanted MCT as shown in **Figure 13(b)**.

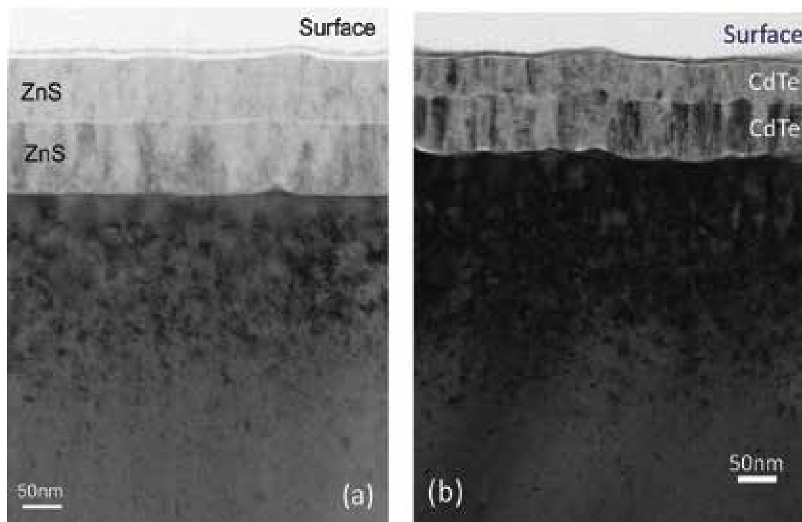

Figure 12. (a) TEM cross-section images of the double-layer ZnS-coated MCT epilayer implanted with arsenic at 400 keV. (b) TEM cross-section images of the double-layer CdTe-coated MCT epilayer implanted with arsenic at 320 keV.

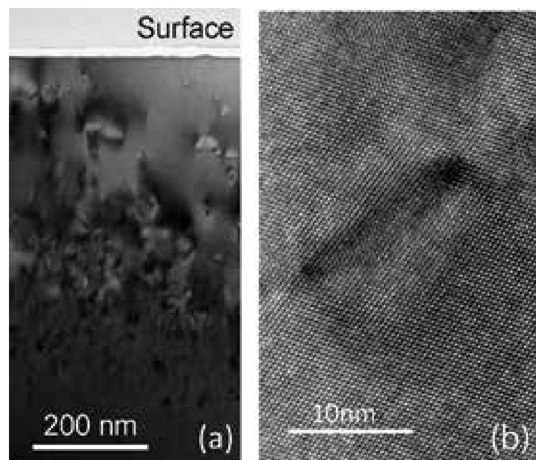

Figure 13. (a) TEM cross-section image of the near surface layer in the MCT epilayer implanted with phosphorus ions of 2×10^{14} cm^{-2} at 350 keV. (b) TEM image of a crescent dislocation in the SDL of the phosphorus-implanted MCT.

4. XRD analysis

XRD usually serves as an analytic method of characterizing the crystallinity and the preferred orientation of materials. Here, it is utilized to characterize the change in the lattice structure of as-implanted MCT epilayers. **Figure 14** illustrates the characteristic diffraction peaks of un-implanted, arsenic implanted, and phosphorus implanted MCT epilayers. It can be seen that the characteristic peak of the un-implanted epilayer is symmetric and the full width at

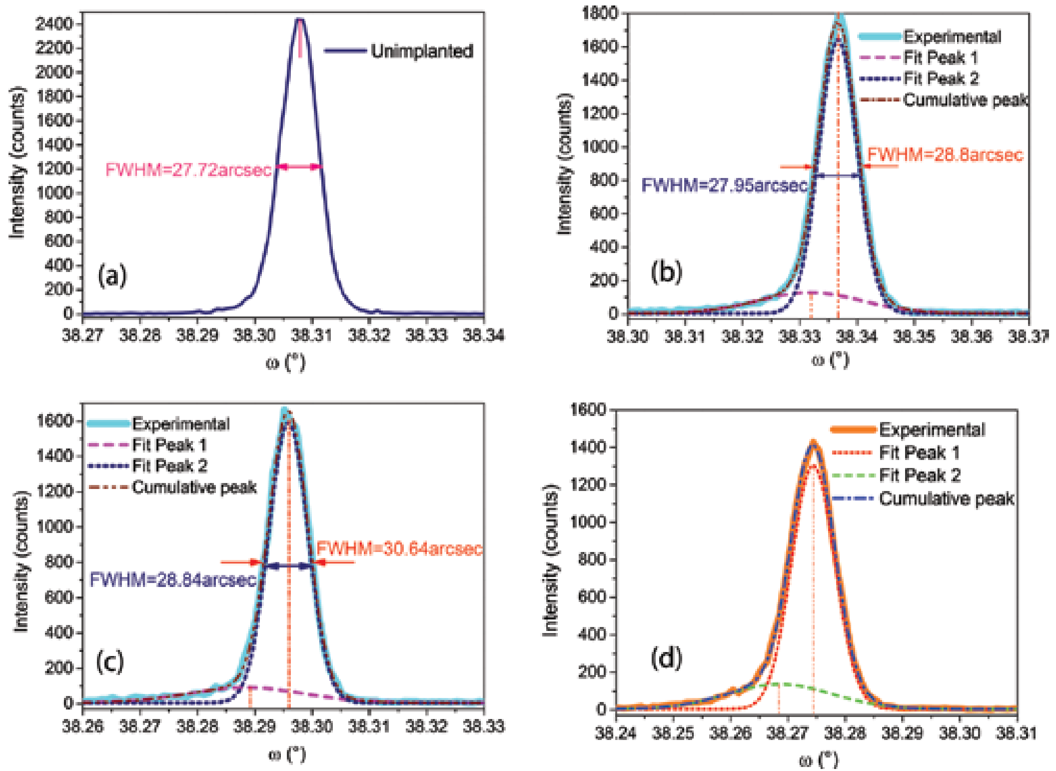

Figure 14. Characteristic diffraction peaks of (a) un-implanted MCT layer, (b) MCT layer implanted with arsenic ions of 2×10^{14} cm^{-2} at 350 keV, (c) MCT layer implanted with arsenic ions of 2×10^{14} cm^{-2} at 450 keV and (d) MCT layer implanted with phosphorus ions of 2×10^{14} cm^{-2} at 450 keV.

half maximum (FWHM) is about 27.7 arcsec. Subjected to ion implantation, the FWHMs of the characteristic peaks of as-implanted MCT epilayers are all broadened. Under the same implant condition, the FWHM of the arsenic implanted sample increases from 27.7 arcsec to 28.8 arcsec, while the FWHM of the phosphorus implanted sample increases from 27.7 arcsec to 33.1 arcsec. Moreover, these peaks become asymmetrical and can be decomposed into two subpeaks by multipeak fitting: a narrow peak with a lower intensity and a broad peak with a very low intensity. The broad peak moves in the direction of the angle ω reduction. It demonstrates that the surface MCT material is amorphized and the corresponding lattice constant increases. Therefore, the FWHM and the position of the broad peak are related to the amorphization of the surface MCT layer. In addition, the position offset and the intensity of the broad peak relative to the cumulative peak should be used to describe the level of amorphization in near surface layer of MCT.

5. Computer simulation

The characterization of ion profiles and induced defects in the MCT epilayers implanted with group V dopants was discussed and analyzed above. Here, some simulation results of

implanted ion trajectories and recoil atom motions in bare and barrier layer-coated MCT epilayers are presented based on the calculation of computer software.

In fact, the trajectories of implanted ions in lattice are random and unrepeatable as shown in **Figure 15(a)**. A number of continuous collisions between an implanted ion and lattice atoms occur, and the ion can stop at a certain position in the lattice. Moreover, the recoil atoms struck by the implanted ion could result in the collision cascades with the other lattice atoms, thereby generating more recoil atoms. The distribution of the recoil atoms corresponding to the ion trajectories in **Figure 15(a)** is illustrated in **Figure 15(b)**. It can be seen that the distribution region of recoil atoms is layer than that of ion trajectories. Therefore, the origin of the induced damages can be considered to be the collision cascade of recoil atoms. On the other hand, both the distributions of ion trajectories and recoil atoms are isotropic for bare MCT implanted with ions. That is, the net loss of lattice atoms could occur due to the short projected range of implanted ions in MCT.

Figure 16 provides the linear density of implanted arsenic and phosphorus ions versus the MCT target depth with the implant energy of 350 keV. From this diagram, the average projected range (R_p) and the ion peak linear density can be acquired. Here, the peak linear densities of arsenic and phosphorus ions are approximately 5×10^4 (at./cm^3)/(at./cm^2) and 2.4×10^4 (at./cm^3)/(at./cm^2), respectively. Calculating with the implant dose of 2×10^{14} cm^{-2} from the samples shown in **Figures 1(a)** and **7(a)**, the theoretical peak concentrations of implanted arsenic and phosphorus ions should be estimated to be ~1×10^{19} cm^{-3} and ~4.8×10^{18} cm^{-3}, respectively, in accordance with the measured peak concentrations of arsenic ions in **Figure 1(a)** and phosphorus ions in **Figure 7(a)**. Therefore, the simulation results should be credible for theoretically calculating the distributions of implanted ions and recoil atoms.

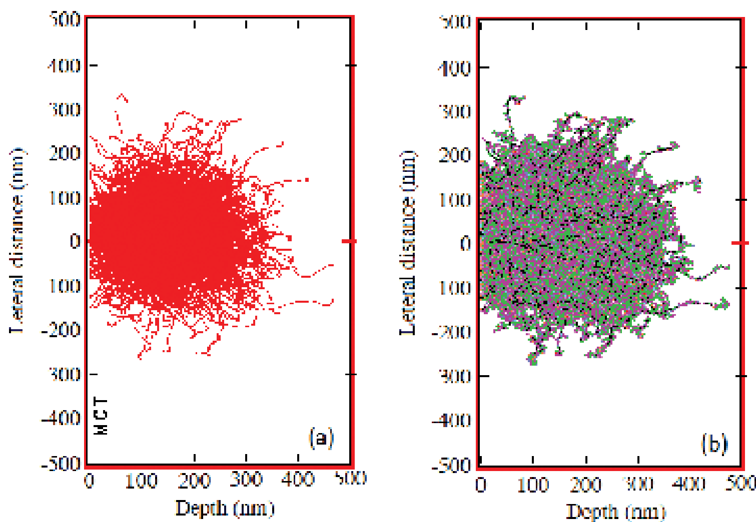

Figure 15. Simulated distributions of (a) ion trajectories and (b) recoil atoms in the bare MCT implanted with arsenic ions at 350 keV based on the computer software.

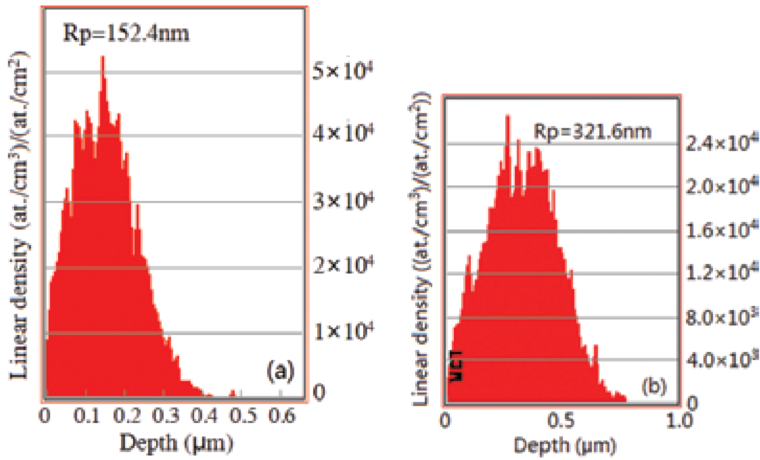

Figure 16. Linear density of implanted arsenic and phosphorus ions versus the MCT target depth with the implant energy of 350 keV acquired from computer simulation. (a) Arsenic ions and (b) phosphorus ions.

Figure 17 shows the histogram of the simulation and experimental values of average projected ranges (Rp) of arsenic, phosphorus, and antimony ions implanted into bare MCT epilayers at different energies. It can be seen that the simulation results are in good agreement with the experimental values. The light ion (P) possesses the largest Rp values, while the heavy ion (Sb) has the smallest Rp values. Additionally, the Rp value increases approximately linearly with implant energy.

Subsequently, the ion trajectories and the recoil atom motions in the MCT epilayers covered by ZnS and CdTe double-layer barrier layers implanted with arsenic ions were simulated, respectively. In the simulation, the density of the evaporated ZnS film is selected to be about 3.3 g/cm^3 [18], while the density of the evaporated CdTe film is set to be 5.83 g/cm^3 [19]. **Figure 18** provides the ion

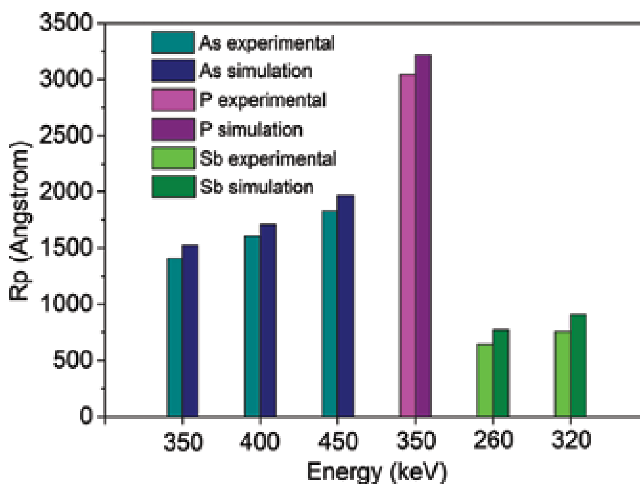

Figure 17. Histogram of the simulation and experimental values of average projected ranges (Rp) of arsenic, phosphorus and antimony ions implanted into bare MCT epilayers at different energies: As~350, 400 and 450 keV; P~350 keV; Sb~260 and 320 keV.

http://dx.doi.org/10.5772/intechopen.77111

trajectories of arsenic ions implanted into ZnS-coated and CdTe-coated MCT targets, respectively. It should be noted that the ion trajectories in the ZnS-coated sample appear to be a little anisotropic, while the ion trajectories in the CdTe-coated sample are still isotropic, similar to bare MCT.

The linear densities of arsenic ions implanted into the MCT covered by ZnS and CdTe barrier layers are illustrated in **Figure 19**. It can be seen that the peak linear densities of arsenic ions in these two targets are both close to the interface between barrier layer and MCT. The peak linear densities of arsenic ions in the ZnS-coated and CdTe-coated samples are approximately 5.5×10^4 (at./cm^3)/(at./cm^2) and 5.6×10^4 (at./cm^3)/(at./cm^2), respectively. Calculating with the dose of 1×10^{14} cm^{-2} from the sample shown in **Figure 5(a)** and the dose of 2×10^{14} cm^{-2} from the sample shown in **Figure 6(a)**, the theoretical peak arsenic concentrations in the ZnS-coated and CdTe-coated samples should be estimated to be ~5.5×10^{18} and ~1.1×10^{19} cm^{-3}, respectively, very close to the measured peak concentrations of ~4.9×10^{18} cm^{-3} in **Figure 5(a)** and ~1.15×10^{19} cm^{-3} in **Figure 6(a)**. **Figure 20** provides the histogram of the simulation and experimental Rp values of arsenic ions implanted into the ZnS-coated and CdTe-coated MCT epilayers, with good consistency between the simulation values and the experimental values.

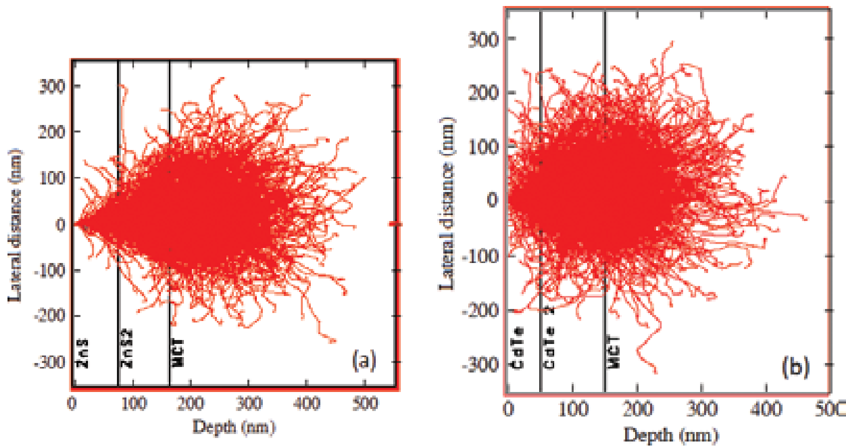

Figure 18. Ion trajectories of arsenic ions implanted into (a) ZnS-coated (implant energy ~ 400 keV) and (b) CdTe-coated (implant energy ~ 320 keV) MCT targets, respectively.

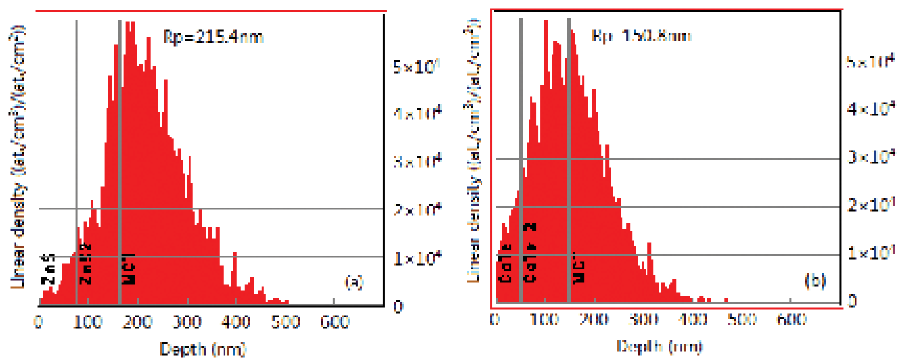

Figure 19. Linear densities of arsenic ions implanted into (a) ZnS-coated (implant energy ~ 400 keV) and (b) CdTe-coated (implant energy ~ 320 keV) MCT targets, respectively.

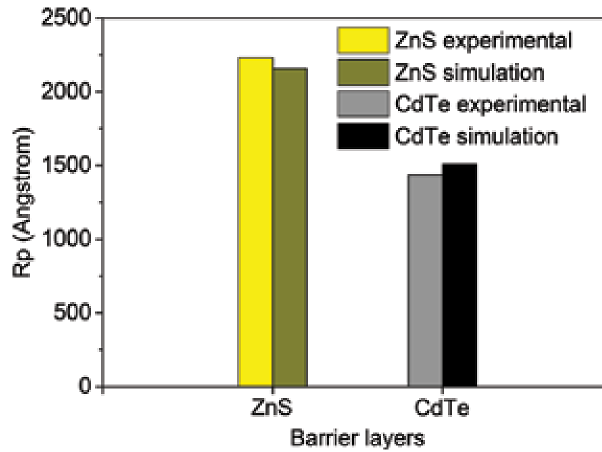

Figure 20. Histogram of the simulation and experimental Rp values of arsenic ions implanted into the ZnS-coated and CdTe-coated MCT epilayers.

6. Conclusion

In this chapter, the p-type (As, P and Sb) ion implantation in MCT epilayer is investigated based on the characterization methods such as SIMS, TEM and XRD. The distribution profiles of arsenic, phosphorus and antimony ions implanted into MCT were measured by SIMS. The influences of some key technological parameters, including energy, dose and beam current, on the distribution and diffusion of implanted ions were discussed and analyzed. Meanwhile, the microstructures of surface amorphization and induced defects in as-implanted MCT were characterized by TEM. The short defects in SDL include dislocation cluster, dislocation line and crescent dislocation. Moreover, the residual point defect belt comprised with vacancy clusters was observed to prove the occurrence of the net loss of lattice atoms under the ion bombardment of too high energy. In addition, XRD was utilized to characterize the variance of lattice structure induced by ion implantation. The position offset of the broad diffraction sub-peaks and the FWHM broadening of the cumulative peaks are attributed to the surface amorphization of as-implanted epilayers. As an important technological structure, the effects of the barrier layers, such as ZnS, CdTe, on the ion profiles and induced defect distributions are studied. Finally, the ion trajectories and recoil atom motions in bare and barrier layer-coated MCT targets were simulated based computer software. The average projected ranges and the peak doping concentrations were calculated theoretically, with good consistency with the experimental values.

Acknowledgements

This work is supported by Innovation Special Fund from Shanghai Institute of Technical Physics (Q-DX-58, Q-DX-84).

Thanks

The author wishes to thank the staff of Research Center for Advanced Materials and Devices at Shanghai Institute of Technical Physics where the sample preparation was completed. Thanks to Prof. Yanfeng Wei for supplying LPE MCT epilayers, and Engineer Chao Yang for ion implantation operation. Special thanks to my mother, Mrs. Xianglan Zhao, for life care and spiritual support.

Author details

Changzhi Shi

Address all correspondence to: shichangzhi@mail.sitp.ac.cn

Research Center for Advanced Materials and Devices, Shanghai Institute of Technical Physics, Chinese Academy of Sciences, Shanghai, China

References

[1] Saur W. Long wavelength mercury-cadmium telluride photoconductive infrared detectors. Infrared Physics. 1968;**8**(3):255-258. DOI: 10.1016/0020-0891(68)90016-X

[2] Wollrab R, Bauer A, Bitterlich H, Bruder M, Hanna S, Lutz H, Mahlein K-M, Schallenberg T, Ziegler J. Planar n-on-p HgCdTe FPAs for LWIR and VLWIR applications. Journal of Electronic Materials. 2011;**40**(8):1618-1623. DOI: 10.1007/s11664-011-1659-0

[3] Gravrand O, DE Borniol E, Bisotto S, Mollard L, Destefanis G. From long infrared to very long infrared wavelength focal plane arrays made with HgCdTe n+n−/p ion implantation technology. Journal of Electronic Materials. 2007;**36**(8):981-987. DOI: 10.1007/s11664-007-0151-3

[4] Bubulac LO, Lo DS, Tennant WE, Edwall DD, Chen JC, Ratusnik J, Robinson JC, Bostrup G. p On n ion-implanted junctions in liquid phase epitaxy HgCdTe layers on CdTe substrates. Applied Physics Letters. 1987;**50**(22):1586-1588. DOI: 10.1063/1.97788

[5] Cooper DE, Harrison WA. Possible negative-U properties of the cation vacancy in HgCdTe. Journal of Vacuum Science & Technology A. 1990;**8**(2):1112-1115. DOI: 10.1116/ 1.576970

[6] Kinch MA, Aqariden F, Chandra D, Liao P-K, Schaake HF, Shih HD. Minority carrier lifetime in p-HgCdTe. Journal of Electronic Materials. 2005;**34**(6):880-884. DOI: 10.1007/s11664-005-0036-2

[7] Rogalski A. HgCdTe infrared detector material: History, status and outlook. Reports on Progress in Physics. 2005;**68**:2267-2336. DOI: 10.1088/0034-4885/68/10/R01

[8] Mollard L, Destefanis G, Baier N, Rothman J, Ballet P, Zanatta JP, Tchagaspanian M, Papon AM, Bourgeois G, Barnes JP, Pautet C, Fougeres P. Planar p-on-n HgCdTe FPAs by arsenic ion implantation. Journal of Electronic Materials. 2009;**38**(8):1805-1813. DOI: 10.1007/s11664-009-0829-9

[9] Mollard L, Bourgeois G, Lobre C, Gout S, Viollet-Bosson S, Baier N, Destefanis G, Gravrand O, Barnes JP, Milesi F, Kerlain A, Rubaldo L, Manissadjian A. P-on-n HgCdTe infrared focal-plane arrays: From short-wave to very-long-wave infrared. Journal of Electronic Materials. 2014;**43**(3):802-807. DOI: 10.1007/s11664-013-2809-3

[10] Baier N, Cervera C, Gravrand O, Mollard L, Lobre C, Destefanis G, Bourgeois G, Zanatta JP, Boulade O, Moreau V. Latest developments in long-wavelength and very-long-wavelength infrared detection with p-on-n HgCdTe. Journal of Electronic Materials. 2015;**44**(9):3144-3150. DOI: 10.1007/s11664-015-3851-0

[11] Mollard L, Destefanis G, Bourgeois G, Ferron A, Baier N, Gravrand O, Barnes JP, Papon AM, Milesi F, Kerlain A, Rubaldo L. Status of p-on-n arsenic-implanted HgCdTe technologies. Journal of Electronic Materials. 2011;**40**(8):1830-1839. DOI: 10.1007/s11664-011-1692-z

[12] Shi C-Z, Lin C, Wei Y-F, Chen L, Ye Z-H. Influences of thicknesses and structures of barrier cap layers on As ion profiles and implant damages in HgCdTe epilayers. In: Proceedings of Infrared Technology and Applications XLII; April 17-21, 2016. Baltimore: SPIE; 2016. p. 981923-1-7

[13] Shi C-Z, Lin C, Wei Y-F, Chen L, Zhu M-X. Barrier layer induced channeling effect of As ion implantation in HgCdTe and its influences on electrical properties of p–n junctions. Applied Optics. 2016;**55**(34):D101-D105. DOI: 10.1364/AO.55.00D101

[14] Shi C-Z, Lin C, Wei Y-F, Chen L. Microstructure characterization of lattice defects induced by As ion implantation in HgCdTe epilayers. In: Proceedings of Infrared Technology and Applications XLIII; April 9-13, 2017. Anaheim: SPIE; 2017. p. 101771C-1-5

[15] Lobre C, Jalabert D, Vickridge I, Briand E, Benzeggouta D, Mollard L, Jouneau PH, Ballet P. Quantitative damage depth profiles in arsenic implanted HgCdTe. Nuclear Instruments and Methods in Physics Research Section B. 2013;**313**:76-80. DOI: 10.1016/j.nimb.2013.07.019

[16] Lobre C, Jouneau P-H, Mollard L, Ballet P. Characterization of the microstructure of HgCdTe with p-type doping. Journal of Electronic Materials. 2014;**43**(8):2908-2914. DOI: 10.1007/s11664-014-3147-9

[17] Ye ZH, Huang J, Yin W-T, Hu W-D, Feng J-W, Chen L, Liao Q-J, Chen H-L, Lin C, Hu X-N, Ding R-J, He L. HgCdTe photodiode arrays passivated by MBE in-situ grown CdTe film. Journal of Infrared, Millimeter, and Terahertz Waves. 2011;**30**(6):495-498. DOI: 1001-9014(2011) 06-0495-05

[18] Bessergenev VG, Ivanova EN, Kovalevskaya YA, Gromilov SA, Kirichenko VN, Zemskova SM, Vasilieva IG, Ayupov BM, Shwarz NL. Optical and structural properties of ZnS and ZnS:Mn films prepared by CVD method. Materials Research Bulletin. 1995;**30**(11):1393-1400. DOI: 0025-5408(95)00150-6

[19] Gschwendtner E, Placidia M, Schmicklera H. Polycrystalline CdTe detectors: A luminosity monitor for the LHC. Nuclear Physics B – Proceedings Supplements. 2003;**125**:363-367. DOI: S0920-5632(03)91017-6

Edited by Ishaq Ahmad and Malik Maaza

Ion beam of various energies is a standard research tool in many areas of science, from basic physics to diverse areas in space science and technology, device fabrications, materials science, environment science, and medical sciences. It is an advance and versatile tool to frequently discover applications across a broad range of disciplines and fields. Moreover, scientists are continuously improving the ion beam sources and accelerators to explore ion beam at the forefront of scientific endeavours. This book provides a glance view on MeV ion beam applications, focused ion beam generation and its applications as well as practical applications of ion implantation.

Published in London, UK

© 2018 IntechOpen
© SafakOguz / iStock

IntechOpen